UNIVERSITY OF READING

Department of Meteorology

Fragmentation and Melting of the Seasonal Sea Ice Cover

Adam William Bateson

A thesis submitted for the degree of Doctor of Philosophy

Submitted October 2020

Declaration

I confirm that this is my own work and the use of all material from other sources has been properly and fully acknowledged.

ADAM BATESON

Abstract

The Arctic sea ice cover is in retreat. Accurate representation of the marginal ice zone (MIZ), the region of the sea ice cover that separates open ocean from the pack ice, is important to capture this retreat in models. The MIZ is associated with complex interactions of the atmosphere, sea ice, and oceans, and a highly heterogenous sea ice cover. Several important sea ice properties and processes that determine the evolution of the MIZ, including lateral melting, momentum exchange, and sea ice rheology, are dependent on floe size. Climate models have historically treated floe size as a fixed parameter, if at all. Observations have shown that floes adopt sizes from scales of metres to kilometres.

Here I investigate two alternative models of the floe size distribution (FSD). The first approach assumes the FSD follows a power law with a fixed exponent and the second approach is a prognostic floe size-thickness distribution model where the shape of the FSD freely evolves. These models are used to understand how variable floe size in the MIZ changes the seasonal retreat of the Arctic sea ice cover, both through the impact on lateral melt volume and on momentum exchange coefficients. I discuss the advantages and disadvantages of each approach, including an assessment of whether either model improves sea ice model performance compared to observations.

I find a high sensitivity to poorly constrained FSD parameters and parameterisations, highlighting the need to better characterise the FSD with observations. I show that winter floe formation and growth processes strongly influence FSD impacts on the sea ice over the melt season. I also demonstrate the need to incorporate brittle fracture in FSD models. I conclude that simple representations of floe size are sufficient to project future sea ice trends, but FSD models are important to capture the spatial distribution of the sea ice.

Acknowledgements

Firstly, I would like to thank my supervisory team at the University of Reading, Prof. Daniel Feltham and Dr David Schröder, for their tireless support and patience in helping me develop as a researcher and to complete the research to produce this thesis. Their scientific input and guidance have been invaluable. I would also like to thank my co-supervisors for the project, Dr Jeff Ridley, Dr Yevgeny Aksenov, and Dr Lucia Hosekova for their significant contributions and support in producing this research

I would also like to thank my Monitoring Committee members, Prof. Ed Hawkins and Prof. Keith Haines, for taking the time to provide frequent feedback and advice on the progress of my research.

I would also like to express my gratitude to members of the wider sea ice community for their help in the progress of this thesis: Dr Stefanie Rynders (National Oceanography Centre, Southampton) and Dr Lettie Roach (University of Washington) for their advice and support in using the FSD models; Dr Byongjun Hwang (University of Huddersfield) and Yanan Wang (University of Huddersfield) for allowing me access to their FSD observations; and Dr Lucy Bricheno (National Oceanography Centre, Liverpool) for preparing her wave projections for use across the Arctic domain.

I would also like to acknowledge colleagues and staff at the Department of Meteorology for the friendly and encouraging environment that the department provides. The SCENARIO DTP has also been a significant source of support over the course of my studentship.

I would also like to note that this research has been funded by a NERC industrial CASE studentship with the UK Met Office (grant no. NE/M009637/1).

Finally, I would like to thank my family for their immense understanding and patience over the course of this thesis, especially during the process of writing-up. The support of my parents and my sister, Hannah, has been essential in getting me over the finish line.

Contents

Chapter 1 - Introduction

1.1. A changing Arctic

The Arctic is a unique environment. It forms part of the global cryosphere; regions of the planet where ice, the solid state of water, is stable under the present climatology. There are two primary components of the Arctic cryosphere: the ice sheet that covers much of Greenland; and the sea ice that forms at the surface of the Arctic ocean when sea water freezes. Sea ice has distinct properties to freshwater ice because of the presence of high concentrations of salts within the water it forms from (Feltham et al., 2006). Freshwater ice usually consists of a single phase with a regular crystalline structure, though this can be disrupted by the presence of gas bubbles or impurities. In contrast, sea ice is a two-phase material that is described as a mushy layer; a rigid matrix of solid ice with low salinity surrounded by a high salinity melt called brine (Feltham et al., 2006).

The Arctic is changing. The global temperature increase associated with anthropogenic climate change is enhanced in the Arctic, a phenomenon known as “Arctic amplification” (Serreze and Barry, 2011). In response to this, the cryosphere is in retreat. Over the period of 1979 – 1999, the trend in the sea ice extent over the winter months has been estimated at -2.4% per decade (Stroeve and Notz, 2018). From 2000 onwards this negative trend in the winter sea ice extent has accelerated, with an estimated average of -3.4% per decade (Stroeve and Notz, 2018). The amplitude of the Arctic sea ice concentration seasonal cycle has also increased abruptly since 2007 resulting in record-breaking minima in the sea ice extent (Stammerjohn et al., 2012; Livina and Lenton, 2013). Kwok (2018) found that the average sea ice thickness near the end of the melt season had decreased by an average of 66% over six selected regions in the Arctic over the period 1958 – 2018. Associated with this general retreat is an increase in the proportion of sea ice that can be classified as first-year ice relative to multi-year ice (Stroeve et al., 2012). First-year ice is ice that formed during the previous sea ice freeze-up season, whereas multi-year ice has lasted through at least one complete summer melt season.

Several animal species have found ways to live upon the Arctic sea ice. Polar bears use the sea ice as a hunting ground, particularly in spring when seals are most vulnerable (Pilfold et al., 2015). The changing sea ice cover is driving positive trends in the number of long-distance swims that polar bears need to complete their usual migratory trajectories (Pilfold et al., 2016), and this expends energy and results in higher mortality rates (Durner et al., 2011). Polar bears are currently listed as a vulnerable species, with sea ice decline the primary reason for this assessment (Regehr et al., 2016). Footprints of climate change can also be seen within the larger Arctic ecosystems (Wassmann et al., 2011). For some species these changes represent a similar threat as they do to polar bears, for example increased sea duck mortality has been attributed to warming and changes in the sea ice cover (Gilchrist and Robertson, 2000). For other species, these changes represent an opportunity, with fish species including cod, snake pipefish, and walleye pollock increasing their northward range (Fleischer et al., 2007; Mecklenburg et al.,2007; Overland and Stabeno, 2004). Several studies have noted an increase in annual primary production in the Arctic ocean associated with lower summer sea ice extent and a longer phytoplankton growing season (Arrigo et al., 2008; Pabi et al., 2008). Model studies have suggested that the increased transmission of light through thinning Arctic sea ice into surface ocean layers is creating increasingly favourable conditions for algal blooms within Arctic environments (Horvat et al., 2017).

For indigenous communities that live within the Arctic circle, sea ice represents a way of life. For example, the Inuit of Igloolik, Nunavut, have a deep knowledge of sea ice that includes an understanding of ocean currents, winds and ice topography (Aporta, 2002). Implicit knowledge of sea ice dynamics and thermodynamics allows these communities to locate large mammals such as seals for food (Aporta, 2011). This knowledge is transferred from generation to generation via oral traditions. Whilst the Inuit can adapt to changing sea ice conditions, the increased unpredictability of winds and sea ice dynamics is making hunting some species such as walrus more dangerous (Laidler et al., 2009). The reduced predictability of the sea ice is also compounding the existing denigration of Inuit knowledge and culture with younger members of the community no longer learning traditional skills (Durkalec et al., 2015). It is not just the direct impact of sea ice loss that poses a risk to communities living in the Arctic. Changes in the Arctic wave climate are expected to increase the general rate of wave-driven erosion along the coast as well as increase the frequency of hazardous extreme

wave events on the coastline by the end of the 21st century (Casas-Prat and Wang, 2020).

The changing distribution of sea ice also presents new opportunities for new trans-Arctic ocean shipping routes. The Northern Sea Route (NSR) from Murmansk in Russia along the Siberian coast to Cape Dezhnev within the Bering Straight saw an average sailing time of 11 days in 2012 – 2013, compared to 20 days in the 1990s (Aksenov et al., 2017). Projections made under the RCP8.5 IPCC emissions scenario suggest that by the 2030 - 2039 period, the North Pole shipping route that traverses the central Arctic ocean will be accessible to certain ship classes with estimated journey times of 13 – 17 days. Projections suggest that the net economic gain from the opening up of the NSR route alone could contribute in excess of a trillion US dollars to the global economy by 2100 under the RCP8.5 and RCP4.5 emissions scenarios (Yumashev et al., 2017). However, changing wind speeds and thinning sea ice are also resulting in positive trends in the sea ice drift speed (Spreen et al., 2011), increasing the risks for ships within the Arctic. Future changes in the wind and wave climate could also increase the rate of sea spray deposition on ship superstructures (Aksenov et al., 2017), which has been identified as the cause for several shipwrecks and other accidents on the NSR (Marchenko, 2012). The increase in Arctic shipping is also projected to have a net warming effect on the climate over this century due to the local impact of shipping emissions on the Arctic environment such as the deposition of black carbon on the snow and ice (Fuglestvedt et al., 2014).

Arctic sea ice is also an important component of the weather and climate system. The sea ice cover moderates high latitude energy transfer and gas exchange between the ocean and atmosphere. Sea ice inhibits direct sensible and latent heat fluxes between the ocean and atmosphere and therefore acts as a partial barrier to thermal energy transfer at high latitudes. As the sea ice thins and retreats, this barrier is reduced in efficacy, enhancing heat transfer between the ocean and atmosphere (Screen et al., 2013). Studies using numerical models that explore the atmospheric response to sea ice retreat have suggested that the increased transfer of heat from the ocean to the atmosphere in autumn and early winter results in changes to local meteorological conditions including increased air temperature, moisture, and cloud cover (Porter et al., 2012; Strey et al., 2010; Rinke et al., 2006) with vertical static stability also reduced (Rinke at al., 2013). These changes have broader implications for weather patterns in both the Arctic and beyond including Europe and North America (Francis et al, 2017;

Screen et al., 2018). Whilst these impacts are complicated and uncertain, suggested changes include increased persistence of mid-latitude weather, a high over Europe resulting in cooler winters in Europe and North East Eurasia, and increased advection of Arctic air masses into North America (Vihma, 2014). Larger scale teleconnections of the Arctic sea ice state to winter surface air temperature and winter extreme weather events in Central and Eastern Asia have also been proposed (Wu et al., 2013). A combination of sparse observational data, imperfect models, and incomplete knowledge of the relevant physical processes means that the magnitude of the impact of Arctic change on the wider climate such as mid-latitude weather is difficult to prove or otherwise (Cohen et al., 2014). Mechanisms that might link Arctic change and mid-latitude severe weather events are particularly disputed (Cohen et al., 2020) with combined model-observational studies reaching very different conclusions on whether the observed coincidence of low sea ice events and cold mid-latitude winters are causal or just correlated (Blackport et al., 2019; Mori et al., 2019).

The sea ice also interacts with the climate via the albedo feedback mechanism. The albedo of a surface is the proportion of incoming solar radiation that a surface reflects rather than transmits or absorbs. Bare sea ice has an albedo of around 0.5 – 0.7, snow covered sea ice has an albedo as high as 0.9, and shallow melt ponds on the sea ice surface have an albedo of 0.2 to 0.4. In comparison, the open ocean has an albedo of 0.06. As the sea ice retreats, the mean albedo of the Arctic system decreases and more of the incoming solar radiation is absorbed rather than reflected. This albedo feedback mechanism is a positive feedback response to global warming and contributes to the Arctic amplification of climate change (Budyko, 1969; Dickinson et al., 1987; Winton, 2006, 2008).

The presence of sea ice also has implications for both the Arctic ocean and wider ocean systems. For example, the presence of sea ice in the Arctic is thought to regulate the spin-up of the Beaufort Gyre via a negative feedback process between ice-ocean stress and surface currents; as sea ice retreats and becomes more mobile, the Beaufort Gyre may then become deeper and faster (Meneghello et al., 2018). In addition to its role in moderating ocean-atmosphere heat and momentum exchange, sea ice also modifies ocean surface properties through changes of state. Brine is rejected from newly forming sea ice, which can destabilise the surface ocean mixed layer and drive convective mixing. The production of sea ice meltwater during the melting season freshens these surface layers, driving stratification and inhibiting

mixing. Sea ice therefore plays a central role in Arctic oceanography and the freshwater cycle within the Arctic ocean (Timmermans and Marshall, 2020). Sea ice may also interact with the wider ocean circulation via the Atlantic Meridional Overturning Circulation (AMOC). It has been suggested that positive buoyancy forcing generated by Arctic sea ice retreat may influence North Atlantic deep-water formation and therefore weaken the AMOC over multi-decadal timescales (Sévellec et al., 2017). Export of sea ice through the Fram Strait may have been a significant source of freshwater required for the AMOC weakening and associated abrupt climate change described as Dansgaard–Oeschger events during the last glacial period (Condron et al., 2020).

Numerical models of the Arctic sea ice are used to understand and quantify the mechanisms that drive changes to the sea ice state and how it is likely to respond to the future changes in climate forcings (Hunke et al., 2015). As additional observations of the sea ice are collected, new processes can be characterised and implemented into these computational models and existing processes and parameters further constrained and refined. These developments are intended to improve the ability of the model to simulate key sea ice metrics including the total and spatial distribution of the sea ice volume. Sea ice models are also coupled to models of the ocean and atmosphere within full climate and Earth system models to understand how these different systems interact together and how the global climate will change in future, particularly in response to anthropogenic forcing.

1.2 The Marginal Ice Zone

The sea ice cover is not homogeneous. Physical properties such as the sea ice concentration and thickness can vary significantly even over small spatial scales of metres and depend on the history and age of the sea ice. It is useful to characterise different regions of sea ice based on these properties, to identify regions of sea ice that would be expected to respond in a similar way to a given change or process.

One such distinction is made between the pack ice and the Marginal Ice Zone (hereafter referred to as the MIZ). The MIZ is defined by the World Meteorological Organisation (WMO) as “the region of an ice cover which is affected by waves and swell penetrating into the ice from the open ocean” (WMO, 2014). Historically, the measurement of wave propagation into the sea ice cover has required in-situ studies

and only recently has progress been made in obtaining wave information within the sea ice cover over larger temporal and spatial scales from satellite derived observations (Horvat et al., 2020). The MIZ will be defined in this thesis as the region with between 15 and 80 % sea ice concentration, which is widely used as a practical alternative definition for the MIZ (Strong et al., 2017). Regions with greater than 80 % sea ice concentration are assigned to the pack ice and regions with less than 15 % are considered part of the open ocean. Figure 1.1 is an aerial photograph of the MIZ, which has been reproduced from Williams et al. (2016). The Seasonal Ice Zone (SIZ) is also a region of interest. The SIZ can be defined as any region within the polar oceans that forms part of the MIZ for at least some of the year. The MIZ varies significantly intra-annually, whereas the SIZ is defined for an annual period.

Figure 1.1: The MIZ (Marginal Ice Zone) is a region where the sea ice cover extends from 15 % to 80 % of the total ocean surface area. It is a region of complex sea ice-ocean-atmosphere interactions. Figure is a reproduction of Fig. 3 from Williams et al. (2016) under CC BY 3.0 (https://creativecommons.org/licenses/by/3.0/us/).

The MIZ is a region of significance for both Arctic sea ice evolution and the wider Arctic system. It marks the interface between the open ocean and pack ice and therefore MIZ processes are key to understanding the seasonal retreat of the Arctic sea ice. As a result, it is important to represent the behaviour of this region accurately in sea ice models, particularly as the MIZ is predicted to occupy a larger fraction of the sea ice cover as it retreats poleward (Aksenov et al., 2017). The observational record indicates small to negligible trends in Arctic MIZ extent over the period 1979 – 2017, however the

retreat of the total Arctic sea ice cover over the same period has resulted in an over 50% increase in the relative August and September MIZ extent as a fraction of the total sea ice cover from 1979 – 2017 (Rolph et al., 2020). The complexity of this region presents a significant modelling challenge due to the numerous interactions between the system components: sea ice, ocean, and atmosphere. Figure 1.2 is a cartoon image that has been reproduced from Lee et al. (2012), which illustrates several of the important interactions and processes that occur within the MIZ. These include:

- Momentum and heat exchange between the sea ice, ocean, and atmosphere.
- The radiative balance. Sea ice has a much higher albedo than the open ocean, so the amount of incident radiation reflected or absorbed by the surface will be highly inhomogeneous over this region.
- Ice advection and divergence influenced by wind forcing and ocean currents.
- The feedbacks between sea ice melt and ocean mixed-layer temperature and salinity.

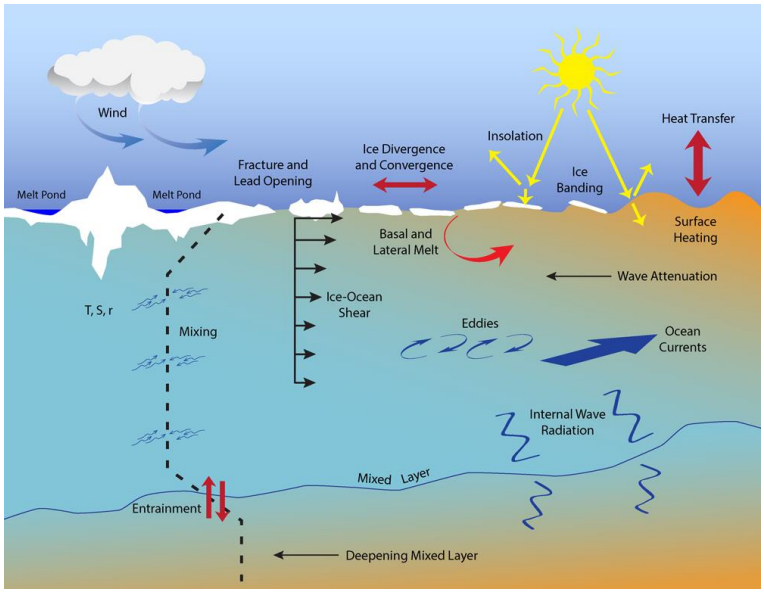

Figure 1.2: A cartoon schematic to illustrate several important processes that determine the evolution and interactions of the MIZ. Figure is a reproduction of Fig. 2 from Lee et al. (2012).

A good example of the complexity of the MIZ interactions is the partial sea ice cover found within the MIZ, which results in a region of intense atmosphere-sea ice-ocean interactions. The interlocking sea ice-ocean cover found within the MIZ results in small

scale inhomogeneities of surface temperature, roughness, and albedo. These factors are all important for the evolution of the Atmospheric Boundary Layer (ABL) (Heinemann, 2008). The exchange of momentum from the atmosphere to the sea ice and ocean is also different within the MIZ. The total 'sea ice edge length' increases in the MIZ, enabling more efficient transfer of momentum from the atmosphere to the sea ice and between the sea ice and ocean (Tsamados et al., 2014). The atmosphere can also transfer momentum to the exposed ocean surface generating waves within the sea ice cover. The ocean state is then perturbed by these interactions, with exposed ocean surface layers vulnerable to turbulent mixing from strong winds. Momentum gradients in the surface layer can be generated from the contrast in aerodynamic drag and wind stress between ice-covered and ice-free locations (Guest and Davidson, 1987). The difference in sea ice-atmosphere and ocean-atmosphere surface stresses at the sea ice edge can generate a strong localised upwelling and entrainment of deep ocean layers (Häkkinen, 1987). The heterogeneity of the sea ice-ocean-atmosphere interface can also influence convective processes. For example, the spatial arrangement of sea ice and open water in the MIZ can impact the strength and distribution of ABL convection (Wenta and Herman, 2019).

The width of the MIZ is an important length-scale for the dynamics of both the sea ice and broader climate dynamics (Strong et al., 2017*)*. This is not only because the width effectively determines the total area of MIZ, but also because the MIZ provides a physical buffer where ocean waves will attenuate, inhibiting these waves from reaching and fragmenting the pack ice. Defining and measuring this width is a non-trivial problem as the MIZ boundaries can be highly irregular (Strong et al., 2017).

1.3 Floes and floe size

The Arctic sea ice is comprised of discrete units called floes. These floes can vary enormously in size. Some can be as small as 10 m, others can be as large as 50 km (Stern et al., 2018a). Floe size has a direct impact on several processes that are important to the evolution of the MIZ, including:

- The melt from the side of floes, or the lateral melt rate (Steele, 1992).
- Momentum exchange between the sea ice, ocean, and atmosphere (Tsamados et al., 2014).

- Moisture flux over the sea ice-ocean surface (Wenta and Herman, 2019).

- The sea ice rheology i.e. the mechanical response of the sea ice to stress (Feltham, 2005; Wilchinsky and Feltham, 2006; Rynders, 2017).

- The clustering of sea ice into larger agglomerates (Herman, 2012).

Sea ice and climate models usually assume that floes adopt a constant floe size. For example the Los Alamos sea ice model, CICE, assumes all floes have a diameter of 300 m. Previous studies have shown a strong sensitivity to the choice of this value, particularly as the floe size reaches values of 50 m and below (Steele, 1992; Tsamados et al., 2015). The assumption of a fixed floe size limits the representation within models of several sea ice processes and interactions within the MIZ, including those described above. The limitations of assuming a singular, fixed floe size have driven several recent efforts to better capture floe size effects within sea ice and related geophysical models, with areas of focus including wave-sea ice interactions (e.g. Williams et al., 2013a, b), floe size impacts on momentum exchange at the sea ice-ocean and sea ice-atmosphere interfaces (Tsamados et al., 2014), and the development of floe size parameterisations or models for use within the thermodynamic component of sea ice models (e.g. Zhang et al., 2015, 2016; Roach et al., 2018 a, 2019).

Observations show that floes adopt a large range of floe sizes, generally with lots of smaller floes and a few larger ones (e.g. Toyota et al., 2006; Stern et al., 2018b). The different sizes that an ensemble of floes adopts is generally referred to as the floe size distribution, hereafter referred to as the FSD. There is not a single method used in the literature to define the FSD, but instead a variety of approaches. The floe number density describes the total number of floes of a specific size within a given area divided by the total given area. The cumulative floe number density describes the number of floes of a specific size or larger, and the floe area density gives the total area of floes of a specific size, both normalised by the total given area. The definition of both floe size and ‘given area’ have multiple definitions, with studies using either floe diameter, radius, or even surface area for floe size and ocean surface area or sea ice surface area for the ‘given area’. Each of these FSD definitions can easily be related to one another using simple mathematical operations, provided the local sea ice concentration is known for some transformations. The choice of FSD definition used depends on both

the context where it is being used and personal preferences, with advantages and disadvantages to each.

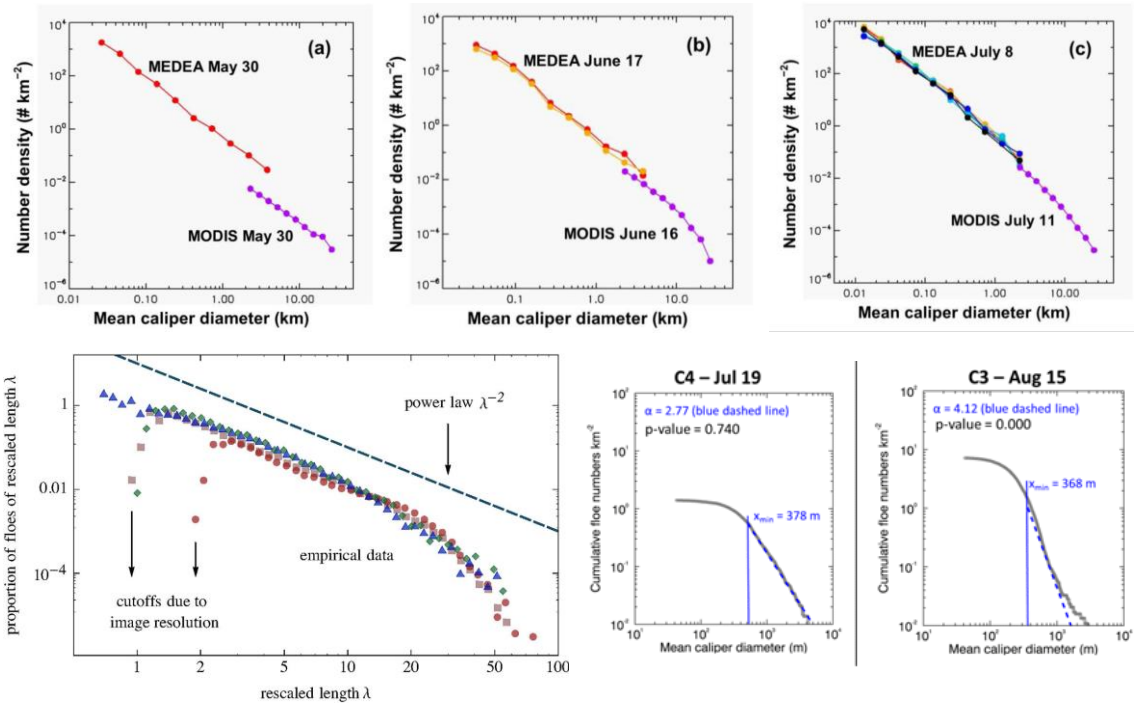

Figure 1.3: Observations of the sea ice floe size distribution can be collected using several methods including directly from a ship, from aerial photography, and from satellite observations. The top three plots are an adaptation of Fig. 12 from Stern et al. (2018b); the bottom left plot is a reproduction of Fig. 2 from Gherardi and Lagomarsino (2015, bottom left); and the bottom right plot is an adaptation of Fig. 1 from Hwang et al. (2017). The x-axis on the bottom left plot was rescaled by eye for each FSD dataset and normalisation constants then recalculated to demonstrate that each FSD collapses onto the same curve. See Gherardi and Lagomarsino (2015) for further details. All plots have been reproduced / adapted under CC BY 4.0 (https://creativecommons.org/licenses/by/4.0/).

Observations of the FSD are often fitted to a power-law distribution. Figure 1.3 displays several examples of observations of the FSD that have been fitted to one or more power law(s). In some cases, a single power law is used to describe the FSD (Stern et al., 2018b). In other cases, two power laws are used to fit the distribution (Steer et al., 2008). Generally, a power law with a less negative exponent is fitted to smaller floes and a power law with a more negative exponent is fitted to larger floes, with a transition between the two regimes ranging from around 50 m – 300 m. The values of exponents reported in different studies generally range between -1.5 to -3.5 (Stern et al., 2018a), though exponents as negative as -7.6 have been reported for floes larger than 40 m in the Weddell Sea in the Antarctic (Toyota et al., 2011). The floe size range over which a power law fit is a valid description of the FSD also varies significantly between observations, for example Toyota et al. (2006) found power law behaviour extending

down to floes of size 1 m, though with a change in exponent reported at a floe size of 40 m, whereas Hwang et al. (2017) found a tailing off behaviour at around 300 – 400 m. These studies use different methodologies with different resolutions, in particular the former uses in-situ observations whereas the latter uses satellite imagery. It is therefore difficult to establish if the minimum limit of the power law behaviour is a physical feature or a product of how the observations have been collected and analysed. Observations also show limited evidence for spatial and temporal variability. Kergomard (1989) shows an increase in the exponent from -2.0 to -2.8 approaching the sea ice edge in the Fram Strait. Both Perovich and Jones (2014) in the Beaufort Sea and Stern et al. (2018b) in the Beaufort and Chukchi Seas report seasonal cycles in the exponent; in particular both found a steepening of the power slope in July, with a maximum steepness in slope reached in August before shallowing in September. The use of a power law fit to represent the FSD is not without controversy. Alternative fits to the FSD have also been proposed, such as the Pareto distribution, which applies an exponential term to the base power law (Herman, 2010). Stern et al. (2018a) provides a complete overview of existing observations of the FSD, including a discussion on the extent to which the different observations can be reconciled.

There are several processes that have been observed to influence floe size or the shape of the FSD:

- Lateral melting and growth at the edges of floes (e.g. Perovich, 2014; Roach et al., 2018 b).

- Break-up of sea ice floes into smaller pieces from ocean wave stress (e.g. Kohout et al., 2014).

- Floes welding together in ocean freeze-up conditions (e.g. Roach et al., 2018 b).

- The dominant formation processes for new floes (Roach et al., 2018 b). New floes form through the consolidation of small crystals of sea ice at the ocean surface called frazil ice. In locations of strong wind and wave activity, this frazil ice agglomerates and forms pancake floes, which are close to circular in shape and usually of several metres in size (Weeks and Ackley, 1986). In calm conditions of low wave and wind activity, frazil sea ice is more uniformly spread

across the ocean surface and freezes together to form large thin sheets of sea ice called nilas ice (Naumann et al., 2012). Floes formed through this process can adopt much larger sizes.

- In-plane brittle fracture (e.g. Wilchinsky et al., 2010).

- Melting along existing cracks and fractures in the sea ice cover to allow break-up of floes by moderate external forcings along these existing linear features (e.g. Perovich et al., 2001).

The shape and variability of the emergent FSD are thought to be some function of these constituent processes.

The immediate prospects for new observations to enable the improved characterisation of the sea ice FSD are promising. In particular, the Arctic expedition “Multidisciplinary drifting Observatory for the Study of Arctic Climate” (MOSAiC; Dethloff et al., 2016) should contribute valuable new in-situ observations to the existing FSD datasets. Similarly, recent studies have demonstrated several novel approaches to improving the understanding of the FSD. For example, Herman et al. (2018) used a laboratory analogue to explore the size distribution of floes that results from wave break-up. Perovich and Jones (2014) combined high-resolution observations of the FSD (obtained using aerial photography) with simple parameterisations of lateral melting and floe breakup by waves to explore whether these processes could be responsible for observed changes in the FSD.

1.4 Waves, the MIZ, and sea ice floes

A common definition of the MIZ is the region of sea ice where waves generated in the open ocean can propagate into and influence the overlying sea ice cover (Dumont et al., 2011). Where waves propagate under the sea ice, the oscillatory nature of waves imposes a bending stress on the sea ice cover. In some cases, the sea ice will fracture in response to this stress to form two or more smaller floes. There is a two-way interaction between the sea ice cover and ocean waves. Sea ice acts as a low-pass filter, preferentially attenuating waves with shorter wavelengths (Kohout et al., 2014). Waves are attenuated both by scattering, where incident wave energy is reflected back into the open ocean through interactions with individual floes, and dissipative

processes such as ice layer interactions and under-ice turbulence, where energy is lost from the waves to other components within the sea ice-ocean-atmosphere system (Squire, 2018; Voermans et al., 2019). There are feedback mechanisms associated with wave propagation and floe break-up derived from the processes that drive the attenuation of waves. For example, as floes break-up into smaller fragments, the number of floe edges available to reflect incident waves and drive further attenuation increases (Williams et al., 2011a). This results in a stronger attenuation of incident waves and reduced propagation of those waves into the sea ice cover. This also has implications for modelling wave – sea ice floe interactions. The wave field cannot be treated as an external forcing to the FSD but instead as something that evolves with the FSD.

The importance of waves to floe size in the Arctic and Antarctic is thought to vary by geographical position of the sea ice. Sea ice in the Arctic is mostly surrounded by continental land mass whereas in the Antarctic the sea ice surrounds the continental land mass with a larger potential wave fetch. This exposes the Antarctic sea ice cover to frequent storm-generated swell waves. These waves have been shown to propagate 100s of km into the sea ice cover and break-up floes (Kohout et al., 2014). A study of the Arctic wave climate over 1992 to 2014 (Stopa et al., 2016) found that Atlantic facing sea ice is exposed to swells generated within the North Atlantic ocean, but isolated and enclosed seas such as the Kara and Laptev sea have an equal mix of swell and wind-driven waves. The shorter wavelengths of wind-driven waves results in a more rapid attenuation of these waves (Meylan et al., 2014). This results in a reduced intensity wave climate in the Arctic where waves have a smaller potential to break-up the sea ice cover. Observations and models have shown the retreat in the Arctic sea ice cover is creating a longer potential fetch within the Arctic ocean resulting in the formation of ocean swell waves with larger significant wave heights (Francis et al., 2011; Thomson and Rogers, 2014). Model studies suggest that this trend is likely to continue for the inner Arctic areas over the 21st century (Khon et al., 2014). Waves may therefore have an increasingly important role in the evolution of floe size in the Arctic MIZ over the next decades.

1.5 Aims of this thesis

In this introduction the importance of the Arctic sea ice has been discussed, the MIZ has been defined, and it has been explained why modelling the MIZ is both important

to understanding the seasonal retreat of the Arctic sea ice and why it presents such a significant challenge. The concept of floe size and the FSD has been introduced, including a description of several processes that can change floe size and mechanisms of how floe size and the FSD can impact the sea ice cover. Wave-sea ice interactions have then been discussed as a specific case of the potential importance of floe size and how this feature is important to the coupling between the sea ice and waves. As mentioned earlier, historically sea ice models have either assumed floes adopt a uniform size or neglect the concept of a floe size altogether. There have been several recent efforts to develop FSD models for use within sea ice models to improve the representation of MIZ processes in these models, often with a specific focus on wave-sea ice interactions.

The general aim of this thesis is to investigate and address important questions relating to the representation of the FSD and FSD feedback processes within sea ice models, particularly regarding the seasonal break-up and melt of the Arctic sea ice. This broad concept can be subdivided into two key themes. The first is to use FSD models to understand the role of the sea ice floe size distribution in the evolution of the Arctic sea ice. There are several key components to evaluate this broader question:

- How does the observed sea ice floe size distribution emerge from the constituent processes that affect the FSD?
- How does the FSD change the seasonal retreat of the Arctic sea ice cover?
- How does inclusion of the FSD impact the overall Arctic sea ice mass balance?

The second theme is to assess how important the inclusion of FSD processes in sea ice models is for the different applications of sea ice modelling. This includes the fully coupled climate models used by organisations including the UK Met Office to understand long term trends in the global climate and to characterise future climate change, where fidelity of simulations must be balanced against the computational cost of additional processes. There will be two additional objectives to consider as part of this overall assessment:

- Does the inclusion of an FSD model improve the simulated sea ice mass balance compared to observations?

- What are the advantages and disadvantages of different approaches to representing the FSD in sea ice models? Is there an ‘optimal’ approach to modelling the sea ice floe size distribution?

1.6 Summary of chapter 1

In this chapter I have introduced the importance and role of sea ice within a changing Arctic and how this change is affecting individuals who live or work within the Arctic. I have explained the importance of Marginal Ice Zone processes in the seasonal retreat of the Arctic sea ice and outlined how this is such a challenging region to model. The concept of floe size and the sea ice floe size distribution is then introduced, including an explanation of how floe size and wave attenuation rates into the sea ice cover are interdependent. Finally, I have outlined the aims of this thesis, which are each designed to develop understanding of how the FSD and related processes can be represented within models.

In chapter 2 I will present a technical discussion of the sea ice model setup that will be used in this thesis, including a description of the model treatment of sea ice-ocean interactions. I will then present a short review of existing studies that consider a variable floe size or FSD and their findings. Finally, I outline the structure to the remainder of this thesis, explaining how the research presented will build on existing knowledge of FSD-sea ice interactions and address the aims introduced in this section.

Chapter 2 – Introduction to models of sea ice and floe size

In this section I present a technical discussion of elements of the modelling of sea ice and the sea ice floe size distribution. This includes a brief introduction to the CICE sea ice model. I also present a summary of the prognostic mixed-layer model and a review of existing approaches to the modelling of variable floe size and the floe size distribution. Finally, a thesis outline will be presented including an introduction to the FSD models that will be used and why these have been selected to address the objectives of this thesis.

2.1 The Los Alamos sea ice model

The Los Alamos sea ice model, hereafter referred to as CICE, is a numerical model of sea ice that has been designed for use within fully coupled climate models. The model consists of several different components designed to produce realistic simulations of the sea ice:

- Thermodynamics: the local rates of sea ice growth or ice and snow melt are calculated from energy budgets using vertical conductive, radiative, and turbulent fluxes.

- Ice dynamics: a momentum balance equation is solved, accounting for atmosphere and ocean drag, internal ice forces, sea surface tilt, and Coriolis force. The internal ice forces are calculated from a model of sea ice rheology. This scheme then allows the velocity field of the sea ice to be evaluated.

- Thickness distribution: the model includes a prognostic ice thickness scheme, with the standard setup consisting of five ice categories. This includes a ridging parameterisation to transfer sea ice between the different thickness categories.

- Advection: sea ice area and volume, along with other state variables, are advected according to an internal transport scheme.

Full details of CICE can be found within the official documentation, Hunke et al. (2015).

Here an overview is provided of how CICE treats sea ice melting and growth in preparation for Chapter 3, where results will be presented on how a floe size distribution impacts the sea ice evolution via changes to the melting behaviour of the sea ice.

As mentioned earlier, sea ice area in CICE is assigned to five separate thickness categories. Each thickness category is taken to be a horizontally uniform column of sea ice and snow, subdivided into a fixed number of snow and ice layers. The thickness of these layers is determined assuming all snow layer and all ice layers have the same thickness respectively. Each snow and ice layer has independently calculated properties including the enthalpy of the layer. The enthalpy is defined as the energy of a unit volume of snow or ice relative to it being in a liquid state at 0°C. This value depends on brine pockets, temperature, and salinity for ice layers, and temperature only for snow layers.

Sea ice growth or melt is subdivided into three separate components within CICE: melt from the upper surface of the sea ice floe (top melt), melt from the bottom surface of the floe (basal melt), and melt from the sides of the floe (lateral melt). Melting at the top surface is calculated as:

$$q\delta h = \begin{cases} (F_0 - F_{ct})\Delta t & if\ F_0 > F_{ct} \\ 0 & otherwise \end{cases}. \tag{2.1}$$

Here, q is the enthalpy of the surface ice or snow layer (with $q < 0$) and δh the change in thickness of the surface layer. The enthalpy of the ice or snow layer, q, is defined as the negative of the energy required to raise the temperature to 0°C and to drive a phase transition from solid to liquid per unit volume of ice or snow. If the entire surface layer is lost during a timestep, the remaining flux is then used to melt subsequent layers. If the entire sea ice cover is lost in a timestep, the remaining energy is then added to the ocean mixed layer. F_0 is the net surface energy flux from the atmosphere to the sea ice and is a function of sensible and latent heat fluxes at the atmosphere-sea ice interface, incoming and outgoing longwave radiation flux, and incoming shortwave radiation flux that is not either reflected by or transmitted through the surface. F_{ct} is the conductive flux from the top surface to the sea ice interior. There is no growth of sea

ice at the top surface due to conductive fluxes however snow-ice can form where the snow cover is sufficiently heavy that the interface between the snow and ice drops below sea level.

At the bottom surface, both growth and melt of sea ice is determined by:

$$q\delta h = (F_{cb} - F_{bot})\Delta t. \quad (2.2)$$

In conditions of sea ice melting, q relates to the enthalpy of the bottom sea ice layer. In conditions of sea ice growth, q relates to the enthalpy of the new ice that forms at a temperature of T_f, the freezing temperature of the ocean mixed layer (calculated as a function of the mixed-layer salinity).

F_{cb}, in Eq. (2.2), is the conductive heat flux to the bottom surface from the ice interior. F_{bot} is the net downward heat flux from the sea ice to the ocean. It is given by the following expression:

$$F_{bot} = -\rho_w c_w c_h u_* (T_w - T_f). \quad (2.3)$$

Here ρ_w is the density of seawater, c_w is the specific heat of sea water, c_h is a heat transfer coefficient (here taking the value 0.006), T_w is the sea surface temperature, and u_* is the friction velocity (with a fixed minimum value). The friction velocity term represents the size of turbulent fluctuations at the ice-ocean interface. It is defined in CICE as the square route of the magnitude of the kinematic Reynolds stress at the ice-ocean interface (Maykut and McPhee, 1995), calculated as $\sqrt{\frac{\tau_w}{\rho_w}}$ where τ_w is the magnitude of the ice-ocean stress vector.

The salinity of the new ice depends on the specific thermodynamic scheme used, either Bitz and Lipscomb thermodynamics or mushy thermodynamics. For this thesis the former approach is used where the salinity of new ice is fixed at S_{max}, a constant with a value of 3.2 ppt. New ice that forms is added to the bottom sea ice layer.

CICE calculates the basal and top melt in terms of sea ice fluxes, whereas the lateral melt volume is explicitly evaluated:

$$\frac{1}{A}\frac{dA}{dt} = \frac{\pi}{\alpha_{shape} L} w_{lat.} \tag{2.4}$$

Here *A* represents the sea ice concentration, such that the term on the left-hand side, $\frac{1}{A}\frac{dA}{dt}$, represents the fractional rate of sea ice area loss due to lateral melt. α_{shape} and L are the floe shape and diameter parameters, set to 0.66 and 300 m respectively in standard CICE. w_{lat} is the lateral melt rate, calculated as a function of $T_w - T_f$. The derivation for Eq. (2.4) uses the approximation that the area lost in a single timestep, ΔA, can be calculated as $P_{floe} \Delta t w_{lat}$, which is a reasonable approximation provided $\Delta t w_{lat}$ is small relative to L. The floe perimeter, P_{floe}, is calculated as πL, making the assumption that the floe shape is convex. The lateral heat flux, F_{lat}, is calculated from the volume of lateral melt.

The melting or freezing potential at the surface ocean-sea ice interface, F_{frzmlt}, is determined by the available ocean heat content. A negative value for F_{frzmlt} is associated with melting of the sea ice. The following condition applies to the lateral and basal flux during periods of melt:

$$|F_{bot} + F_{lat}| \leq |F_{frzmlt}|. \tag{2.5}$$

If this condition is not fulfilled, then F_{bot} and F_{lat} are both reduced by a common factor such that the magnitude of their sum does not exceed the magnitude of F_{frzmlt}.

Where F_{frzmlt} is positive, i.e. in freezing conditions, frazil ice is assumed to form within surface ocean layers. It is assumed that the full freezing potential is used within each timestep. This frazil ice is added to the smallest thickness category within a grid cell, increasing the fractional coverage of this category as necessary according to the volume of frazil ice added. If the maximum possible volume within the smallest category is exceeded or the open water area is nearly zero, then the new ice is spread evenly across all thickness categories (physically this represents frazil ice first accumulating within open water within a grid cell, but once ice covers the whole grid cell the frazil ice instead accumulates across the basal surface regardless of the existing thickness).

An additional mechanism of sea ice gain or loss is through changes of state from solid to gas or vice versa at the atmosphere-sea ice interface. Where the latent heat flux is negative i.e. where latent heat is transferred from the sea ice to the atmosphere, snow or exposed ice can sublimate. If the latent heat flux is positive, the reverse process can happen. The thickness change of such transitions is calculated as follows:

$$(\rho L_v - q)\delta h = F_l \Delta t. \tag{2.6}$$

Here ρ is the density of the surface material (either snow or ice), L_v is the latent heat of vaporisation of liquid water at 0°C, q is the enthalpy of the snow or ice layer (newly formed material is assumed to be the same enthalpy as the existing surface layer), and F_l is the latent heat flux.

An additional mechanism within CICE that forms new ice is where the snow base level falls below the sea level. In such scenarios enough snow is converted to snow-ice such that the base of the snow is at sea level according to the Archimedes principle (when using Bitz and Lipscomb thermodynamics). The snow-ice formation step is carried out at the end of each timestep, after other thermodynamic processes.

After growth and melting processes (but not snow-ice formation), ice and snow layer interfaces are adjusted to reset these layers within each ice thickness category back to equal thickness whilst conserving energy. The overall prognostic thickness distribution is also updated over each timestep in response to both thermodynamically and mechanically driven changes in sea ice thickness. The ice thickness categories have fixed boundaries, and therefore ice area is transferred between these categories where the thickness of a given area of sea ice crosses a category boundary. Full details of how the impact of individual processes such as basal melting or growth are parameterised within the prognostic thickness distribution are available in Hunke et al. (2015).

2.2 The prognostic mixed-layer model

Sea ice-ocean interactions are an important component of calculating sea ice volume change on basal and lateral surfaces. These interactions include a negative feedback whereby a thermodynamic process at the sea ice-ocean interface perturbs the surface ocean state in such a way that reduces the rate of same process subsequently. Sea

ice-ocean interactions are generally investigated using a coupled sea ice-ocean framework rather than a standalone sea ice model. Ocean models such as NEMO (Nucleus for European Modelling of the Ocean) include horizontal and vertical discretisation so that the 3D evolution of the ocean state can be considered. Coupled CICE-NEMO simulations are computationally expensive to run compared to standalone sea ice models. Furthermore, internal ocean processes can obscure and mask sea ice-ocean interactions and feedbacks.

Standalone CICE includes a simplified representation of the ocean mixed layer. This mixed layer incorporates the ocean surface layer i.e. no distinction is made between the surface layer and the mixed layer and is set to a fixed depth (30 m as default). The salinity of this mixed layer is prescribed, and the temperature is prognostic, though can be restored to boundary conditions. This setup also has significant limitations in exploring sea ice-ocean interactions. It is not possible to explore salinity feedbacks within this framework, as the salinity is prescribed rather than prognostic. The mixed-layer depth is also shown to be highly variable in observations. A shallow mixed layer can act to amplify any temperature or salinity-based model feedbacks, whereas a deeper mixed layer can dampen the feedbacks. Processes such as lateral melting can act to change both the salinity, temperature, and depth of the mixed layer through an injection of cool, fresh water and all three impacts may have a role in determining the subsequent feedback on the sea ice lateral melt rate.

The prognostic mixed-layer model of Petty et al. (2014) provides an intermediate step between the complexity and expense of a full ocean model, and the limitations of the standard CICE representation of the ocean as a fixed depth mixed layer. This is a bulk mixed-layer model based on Kraus and Turner (1967) and Niiler and Kraus (1977). In this model, the mixed-layer temperature, salinity, and depth are all evaluated prognostically. The deep ocean below the mixed layer is restored to observations, and the model is zero-dimensional i.e. defined per grid cell without lateral interactions between grid cells. Within this thesis an amended version of the mixed-layer model will be used, adopting some of the modifications described within Tsamados et al. (2015). First an overview of the original mixed-layer scheme will be provided, with full details available within Petty et al. (2014). Then a summary of the modifications included from Tsamados et al. (2015) will also be described.

2.2.1 Petty et al. (2014) mixed-layer model

Figure 2.1 is a reproduction of Fig. 4 from Petty et al. (2014) and it provides an overview of the thermodynamic interactions between CICE and the prognostic mixed-layer model, including the CICE melting and growth processes described in Sect. 2.1. The mixed-layer model considers three separate components to the ocean: a surface layer of a fixed 10 m depth, h_s; a mixed layer of variable depth, h_{mix}; and the deep ocean below the mixed layer. h_s and h_{mix} define a uniform water depth across each grid cell rather than depth of the interface from the surface i.e. the presence of sea ice at the surface does not reduce the total volume of water in the surface or mixed layer.

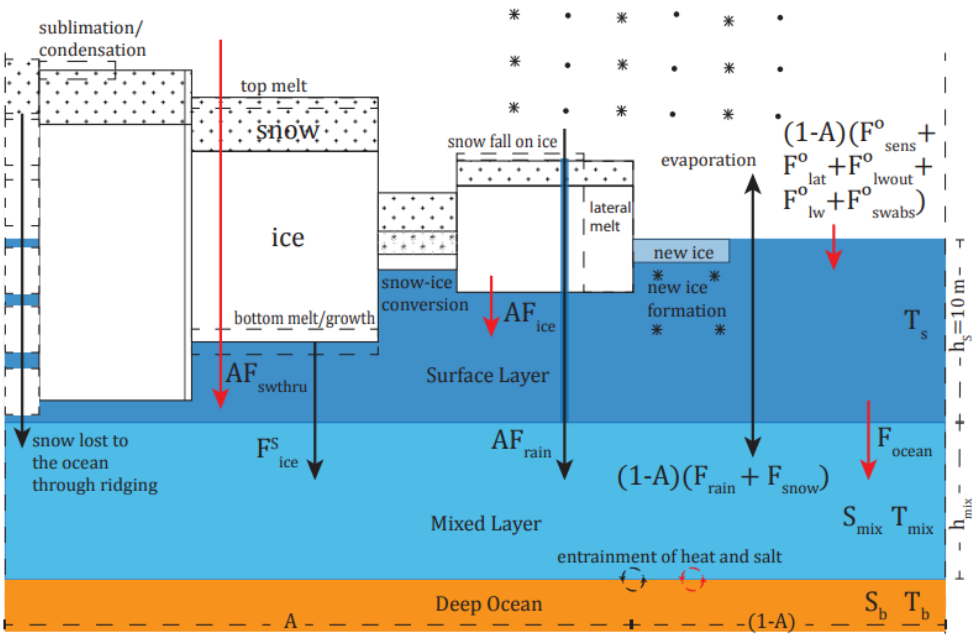

Figure 2.1: A schematic of the main thermodynamic processes included within CICE, including the prognostic mixed-layer model. This figure is a reproduction of Fig. 4 from Petty et al. (2014) under CC BU 3.0 (https://creativecommons.org/licenses/by/3.0/).

Figure 2.1 shows several heat fluxes operating between the atmosphere or sea ice and the surface ocean layer (all positive downwards). These are the sensible heat flux from the atmosphere, F^o_{sens}, latent heat flux from the atmosphere, F^o_{lat}, black-body heat flux of the surface ocean layer (always negative), F^o_{lwout}, downward longwave radiative heat flux (always positive), F^o_{lw}, downward shortwave radiative heat flux (always positive), F^o_{swabs}, heat flux between the sea ice and ocean surface, F_{ice}, and short wave radiative heat flux that transfers through the sea ice cover to be absorbed within the ocean surface layer, F_{swthru}. Each term is multiplied by either A or $1 - A$ depending on

whether the flux is into the sea ice covered section of a grid cell or open ocean and add up to give the total surface heat flux to the ocean surface layer, $F_{surface}$. A is the fraction of the grid cell covered by sea ice.

The heat flux between the ocean surface layer and mixed layer (positive downwards) is calculated as:

$$F_{ocean} = c_p \rho_w u_* (T_S - T_{mix}). \quad (2.7)$$

Here c_p and ρ_w are the specific heat capacity and density of water and T_S and T_{mix} are the temperature of the surface and mixed ocean layers respectively (N.B. S_S and S_{mix} analogously represent the salinity of the surface and mixed ocean layers respectively). u_* is the ocean surface friction velocity calculated in terms of the ice-ocean and atmosphere-ocean stresses, making the assumption that the surface layer is in free drift.

It is assumed that the surface and mixed ocean layers have a uniform salinity and are therefore treated as a single layer for salinity calculations. Five terms contribute to the salinity flux interactions between the mixed layer and overlaying sea ice and atmosphere. F_{salt} and F_{fresh} represent fluxes of salt and freshwater respectively between the sea ice and mixed layer from basal and lateral melting or growth of the sea ice, formation of frazil ice, and melting of snow. F_{snow} and F_{rain} represent prescribed rainfall and snowfall on the open ocean fraction for the former and full grid cell for the latter (it is assumed that rainfall percolates through the sea ice directly into the open ocean). $\frac{F_{lat}^{o}}{L_v}$ represents evaporation from the open surface to the atmosphere, where L_v is the latent heat of vaporisation. These five terms are all treated as either positive or negative virtual salinity fluxes i.e. they are applied with no corresponding change in the total water volume. The net salt flux to the ocean surface layer from sea ice and atmosphere interactions, F_{ice}^{S} and F_{pe}^{S} respectively, can then be calculated from these components.

The mixed layer is distinguished as a region of high mixing such that the temperature and salinity are approximately uniform across the layer. There is an input of mechanical kinetic energy into the mixed layer through wind shear at both the open ocean and sea ice interfaces. The model includes three sources of surface buoyancy flux: salt or

freshwater flux from sea ice growth and melt; salt or freshwater flux from evaporation or precipitation; and heat flux between the surface and mixed layers. Note that each energy input experiences exponential decay with respect to mixed-layer depth (to a fixed minimum for surface buoyancy fluxes). The exponential decay term represents energy loss due to convective dissipation effects through the depth of the mixed layer. The four individual surface contributions to mixing of the mixed layer are summed to produce the total power input per unit density, P_{net} (with units $m^3 s^{-3}$). P_{net} effectively represents the sources of kinetic energy to the base of the mixed layer.

To model the evolution of the mixed-layer depth in response to this kinetic energy input, the change in potential energy from entrainment of deep ocean water or shoaling of mixed-layer water into the deep ocean must be calculated. At a stable interface, kinetic energy is required to drive mixing across the interface, inhibiting mixing across the interface. At an unstable interface, potential energy is released in response to mixing across the interface, favouring deepening of the mixed layer. The difference in buoyancy, Δb, across the mixed-layer base is required to determine the rate in change of the mixed-layer depth:

$$\Delta b = g\alpha(T_{mix} - T_B) - g\beta(S_{mix} - S_B). \tag{2.8}$$

Here α represents the thermal expansion coefficient, β is a saline contraction coefficient, and g is the acceleration due to gravity. T_B and S_B are the temperature and salinity of the deep ocean respectively.

The mixed-layer model must also represent sinks of kinetic energy during the process of mixed-layer shoaling or deepening. Turbulent fluctuations of the mixed layer act as a friction-like sink of energy. This sink is represented in the mixed-layer model by a constant, c_m, the bulk turbulent velocity scale (also referred to as the unsteadiness coefficient). c_m is set to a fixed value of 0.03 ms^{-1}. The power required to entrain water at a given rate i.e. the rate of mixed-layer deepening, P_E, can then be calculated as a function of both the buoyancy difference across the base of the mixed layer and the friction term from turbulent fluctuations:

$$P_E = \frac{dh_{mix}}{dt}(h_{mix}\Delta b + c_m^2). \tag{2.9}$$

The change in h_{mix} can then be calculated by noting that the energy source and sink terms i.e. P_{net} and P_E, must be balanced:

$$\frac{dh_{mix}}{dt} = \frac{P_{net}}{h_{mix}\Delta b + c_m^2}. \tag{2.10}$$

Equation 2.10 describes both entrainment of the deep ocean layer, when $\frac{dh_{mix}}{dt} > 0$, and shoaling, where $\frac{dh_{mix}}{dt} < 0$. Physically, Eq. (2.10) represents the conservation of energy at the mixed layer-deep ocean interface. Input kinetic energy will either be converted to potential energy or taken into turbulent fluctuation sinks through changes in the depth of the mixed layer. The precise ratio of this conversion (including whether the change in potential energy is a source or sink of energy) and whether the mixed layer deepens or shoals, depends on the size and sign of the buoyancy difference, Δb, across the interface between the mixed layer and deep ocean. h_{mix} can vary between a globally defined minimum value, h_{min}, and a maximum value, h_{bath}, determined by observations of the local bathymetry and unique to each grid cell.

The temperature and salinity of each ocean component can then be evaluated:

$$\frac{dT_S}{dt} = \frac{F_{surface} - F_{ocean}}{c_p \rho_w h_S}, S_S = S_{mix}, \tag{2.11}$$

$$\frac{dT_{mix}}{dt} = \begin{cases} \frac{F_{ocean}}{c_p \rho_w h_{mix}} + \frac{1}{h_{mix}} \frac{dh_{mix}}{dt} (T_B - T_{mix}) & \frac{dh_{mix}}{dt} > 0 \\ \frac{F_{ocean}}{c_p \rho_w h_{mix}} & \frac{dh_{mix}}{dt} \leq 0, \end{cases} \tag{2.12}$$

and

$$\frac{dS_{mix}}{dt} = \begin{cases} \frac{F_{ice}^S + F_{pe}^S}{h_{mix}} + \frac{1}{h_{mix}} \frac{dh_{mix}}{dt} (S_B - S_{mix}) & \frac{dh_{mix}}{dt} > 0 \\ \frac{F_{ice}^S + F_{pe}^S}{h_{mix}} & \frac{dh_{mix}}{dt} \leq 0. \end{cases} \tag{2.13}$$

The asymmetry between the entrainment and shoaling expressions in Eqs (2.12) and (2.13) exists because during entrainment mixing between the newly entrained water and mixed-layer water will change the mixed-layer salinity and temperature, whereas

during shoaling no new water mass is introduced to the mixed layer and mixed-layer properties are assumed to be constant at all depths.

The melting potential of the ocean surface, F_{frzmlt}, is calculated using the properties of the surface layer. In freezing conditions, F_{frzmlt} is calculated using the sum of the potential in both the surface and the mixed layers as frazil ice can form in the mixed layer before rising and accumulating at the ocean surface or below existing sea ice cover.

For the deep ocean properties, a 3-D ocean grid is used, with the salinity and temperature defined at specified depths. This grid is defined separately to the mixed layer so deep ocean properties can still be defined where the mixed layer exists. The ocean grid is initialised using a deep ocean climatology. The temperature and salinity values at the top of the ocean grid are assigned to the surface and mixed layers when the model is initialised. The values of S_B and T_B are calculated using a linear interpolation of the vertical ocean grid. Where deep ocean grid points lie above the mixed-layer base, the mixed-layer salinity and temperature are assigned to these grid points. If a water mass is detrained from the mixed layer, it initially retains the mixed-layer properties but is restored at a fixed rate back to the climatology with a timescale of 3 months. There is no exchange of information between neighbouring grid points within the 3-D ocean grid; where grid points have been perturbed from climatology after detrainment of water mass from the mixed layer, they are restored at a fixed rate back to climatology.

2.2.2 Tsamados et al. (2015) modifications

The original Petty et al. (2014) mixed-layer model was set-up for the Antarctic. In the Antarctic the stronger winds and wave activity and larger extent of the MIZ enables a high wind power input into the mixed layer leading to much deeper mixed-layer depths in the Antarctic compared to the Arctic. Tsamados et al. (2015) adjusted the mixed-layer model to ensure reasonable CICE-ML model performance for the Arctic. The three-component model of surface layer, mixed layer, and deep ocean is replaced with a two-component model, with just a mixed layer and deep ocean. Therefore Eq. (2.11) no longer applies, and Eq. (2.12) is updated to:

$$\frac{dT_{mix}}{dt} = \begin{cases} \frac{F_{surface}}{c_p \rho_w h_{mix}} + \frac{1}{h_{mix}} \frac{dh_{mix}}{dt} (T_B - T_{mix}) & \frac{dh_{mix}}{dt} > 0 \\ \frac{F_{surface}}{c_p \rho_w h_{mix}} & \frac{dh_{mix}}{dt} \leq 0. \end{cases} \quad (2.14)$$

Equation 2.13 is the same as before. In addition, the mixed-layer temperature and salinity are restored to the 10 m depth temperature and sea surface salinity from a monthly climatology reanalysis dataset. This restoring is applied at a fixed rate e.g. for salinity:

$$S_{new} = \min\left(S_{clim}, S_{orig} + \frac{S_{clim} \Delta t}{t_{sal}}\right). \quad (2.15)$$

Here t_{sal} is the restoring timescale for salinity, S_{orig} is the initial salinity, S_{new} is the salinity after the timestep of length Δt, and S_{clim} is the salinity prescribed from monthly climatology. An identical restoring approach is used for temperature, but with an independently defined restoring timescale, t_{temp}. t_{temp} and t_{sal} are set to 5 days as standard. This restoring was introduced to represent horizontal advection between adjacent grid cells. The Tsamados et al. (2015) paper also introduced a variable restoring rate depending on how strongly perturbed the mixed-layer temperature was from the neutral value, which has not been adopted for the mixed-layer model used within this thesis.

2.3 Existing floe size models

Chapter 1 outlines that the aims of this thesis are to explore both how the shape of the sea ice floe size distribution, or FSD, emerges from individual floe scale processes and the impact the FSD then has on MIZ processes and the overall sea ice mass balance. These findings will then be used to discuss and make recommendations regarding the use of an FSD model in sea ice and climate models. It has previously been explained that the FSD refers to a set of different definitions, all of which aim to characterise the range of sizes adopted by a given ensemble of floes. There have been several previous efforts to represent either variable floe size or a full FSD within models of sea ice or wave propagation through sea ice. The approaches to modelling floe size or the FSD can be broadly characterised as existing on a spectrum between two endpoints: a fully prognostic approach at the floe scale; or the floe size or FSD is imposed as a

boundary condition with no internal sea ice-FSD feedback. This section will consist of a brief history and critical review into existing efforts within the literature to represent floe size within sea ice models.

Prior to the explicit consideration of floe size, sea ice numerical models evenly divided ocean heat content into reducing the thickness and concentration of the sea ice cover. In these early models, all the incident heat energy from solar radiation into the ocean surface was considered to contribute to the lateral and basal melting of sea ice. Steele (1992) introduced the concept of floe size for use within sea ice numerical models. In this study the FSD was characterised by a single representative floe diameter within an explicit parameterisation of lateral and basal melt. These equations were applied within a 'toy model' setup i.e. a single grid cell was considered as opposed to a network of adjacent grid cells arranged in such a way as to represent a real system. The floe diameter was allowed to change over time in response to lateral melting only. Three initial floe diameters were considered: 30 m, 300 m, and 3000 m. The study concluded that the impact on the sea ice cover was only significant where floes were of a size of order 30 m. The differences in the evolution of the sea ice for floes of either 300 or 3000 m in diameter were found to be small. This study also included the analysis of aerial photography of sea ice, identifying floes of size 30 m and larger. The study noted that only 5 % of the sea ice area was taken up by floes with between 30 m – 300 m in diameter. The sea ice concentration taken up by all the identified floes was calculated as 88 %, suggesting that floes smaller than 30 m, could, at most, take up 12 % of the area distribution. The study therefore concluded that, for this case study, lateral melting was unlikely to contribute significantly to the total basal and lateral melt. Whilst this was a very simplified treatment of floe size, it was the first attempt to consider the importance of floe size in the evolution of sea ice and it also motivated the inclusion of a floe diameter parameter and explicit treatment of lateral and basal melt within CICE. The study also considered the impact of a specific process, in this case lateral melt, on floe size and how that feedback process might be important in the evolution of the sea ice cover.

The sea ice modelling community has not been the only group of researchers interested in representing the sea ice floe size distribution within models. Wave modellers, who want to understand and model the propagation of ocean surface waves into the sea ice cover, are also interested in the floe size distribution. A review paper by Vernon A. Squire, published in 1995, described how "determining an ideal equilibrium

floe size distribution as a function of distance of penetration, ice thickness, and incident wave spectrum" would be an important new development in understanding and modelling the interactions between ocean waves and sea ice (Squire, 1995). Both the size of floes and the frequency with which floe edges are encountered by a wave can impact the attenuation rate of a wave propagating into the sea ice cover. In addition, waves can fracture floes and change the shape of the distribution, leading to a feedback process where a propagating wave can change the attenuation rate of subsequent waves. This has led to a convergence of both the sea ice and wave modelling communities to develop a parametrisation of wave fracture to understand and represent wave-FSD interactions within both sea ice and wave models. As part of the broader research into wave-sea ice interactions in the MIZ, Toyota et al. (2011) developed a simple fragmentation model of wave break-up where floes would be fragmented into k identical subunits with a probability of f, where f takes a value between 0 and 1. This process is then applied again to floes that were broken in the first round and so on to develop a fractal description of the number of floes of each size (noting that possible floe sizes in this setup adopt a discrete distribution). The ratio of floes in adjacent sizes can then be compared to that expected if the distribution followed a power law allowing f, the break-up probability, to be related to α, the exponent. f was taken to represent physically the fragility of the sea ice cover. The value of f was calculated for observations of floes between 2 m and 20 – 40 m in the Antarctic in the north-western Weddell Sea in 2006 and off Wilkes Land in 2007, both in later winter. In both locations f was found to decrease from a value of 0.7 at the ice edge to a value of 0.5 within the interior. Toyota et al. (2011) suggested that the positive correlation between proximity to the ice edge and f in both locations indicated that wave intensity was a key factor in determining the winter FSD. The study also reported a value of 0.93 for f within the Weddell Sea interior during the melting season, away from the ice edge, suggesting that melting was also an important factor in weakening the sea ice and driving the fragmentation of floes. The study concluded that both wave activity and the seasonality of the sea ice strength were important factors to consider in understanding the shape and variability of the FSD.

The concept of a probabilistic fragmentation approach was adopted by Dumont et al. (2011) as a mechanism to define a floe size distribution for use within a 1D representation of waves propagating through the MIZ and breaking-up floes. In this model, the floe size distribution is defined between two limits, D_{min}, taking a fixed value

of 20 m, and D_{max}, which is determined as a function of wave break-up processes. Waves are advected and attenuated through the 1D ice field and a yield criterion for a break-up event defined and tested at each grid interval. Where a wave break-up event is identified, D_{max} is set to the distance between two consecutive maxima in the wave profile. A distribution is then constructed from D_{max} by applying the probabilistic fragmentation scheme of Toyota et al. (2011) for as many steps as possible before the resulting floe size from a fragmentation step is lower than D_{min}. Dumont et al. (2011) use a value of 2 for k, the number of subunits per fragmentation step, and a value of 0.9 for f. The mean floe size is then calculated from the resulting distribution, defined between D_{max} and D_{min}, which is used to calculate the attenuation rate of waves propagating through the grid interval in the subsequent time step. This model is used to characterise the interactions between sea ice floes and waves. They observe a sharp transition moving into the sea ice cover from locations with significant break-up of the sea ice cover to locations without, suggesting this transition separates the MIZ from pack ice.

Williams et al. (2013a, b) used an identical approach to Dumont et al. (2011) to model the FSD, however using a more complex wave advection, attenuation, and break-up scheme. This study performed several sensitivity studies to model details and parameters including the Courant number, dispersion, horizontal resolution, wave attenuation, and ice properties. The Courant number represents the proportion of a grid cell waves traverse within a timestep. This parameter is notable because if a wave does not traverse a full grid cell within a timestep, any breakup events within that grid cell in the prior timestep will result in enhanced wave attenuation in the subsequent timestep. The Courant number therefore serves as a proxy for wave energy loss during a breakup event. Williams et al. (2018 b) found that where waves only travel through a small proportion of broken ice (i.e. where the Courant number is close to 1), the MIZ width was highly sensitive to the exact proportion. However, the MIZ width became insensitive to this proportion once it travelled through over 30% of broken ice (i.e. where the Courant number is less than 0.7). This result was used to suggest that, provided a wave breakup events result in a significant loss in wave energy, the MIZ width is insensitive to the precise amount. The study also found low FSD sensitivity to wave dispersion effects, but high sensitivity to wave attenuation rate, ice thickness, and a breaking strain parameter, highlighting the need to better constrain these processes and parameters using observations. An adapted version of the waves-in-ice scheme

outlined in Williams et al. (2013a, b) is used within the power-law FSD model introduced in chapter 3 to represent wave break-up processes and will be described in more detail in the next chapter.

There have been several further recent studies that specifically explore the interaction between waves and the sea ice floe size distribution. Boutin et al. (2018) adapted the model of Williams et al. (2013a) to explore the dissipation of wave energy as a wave propagates through the sea cover. This study considered three sources of wave attenuation resulting from wave-sea ice interactions: floe size dependent inelastic scattering; basal friction; and dissipation resulting from ice flexure. The study was able to produce a realistic simulation of an ice break-up event close to Svalbard in 2010, noting that the observed transition from strong wave attenuation prior to break-up to weak attenuation subsequently could only be reproduced with the inclusion of nonlinear dissipation. Scattering was found to be particularly important for wave attenuation within the first few km of wave propagation into the sea ice cover and also reduced the average wave speed, broadened the directional spread, and increased the height of waves, with the latter associated with increased break-up of floes. Williams et al. (2017) coupled the modified wave and FSD model of Williams et al. (2013a) to the neXt-generation Sea Ice Model (neXtSIM), a Lagrangian sea ice model, to explore the impact of wave radiative stress (WRS) on the spatial distribution of sea ice and how the weakening and break-up of the sea ice cover by waves contributes to this impact. The study concluded that the WRS associated with wind-driven waves only had small to negligible impacts on the sea ice edge position, with wind stress dominating this impact. Williams et al. (2017) did, however, find that wind waves may have an important role in fragmenting and weakening the sea ice within the MIZ, preconditioning the ice for increased response to wind stress. Herman (2017) used a discrete-element bonded-particle model to explore the induced stress and break-up of sea ice for a variety of wave and sea ice states. Results from this model suggested that the value of maximum stress within sea ice is a function of both wave and ice properties, and hence both components need to be well characterised to identify an ice fragmentation event. Floes produced from wave break-up events in the model adopted close to uniform sizes, with this size a function of ice thickness and strength only and not wave properties. Montiel and Squire (2017) defined an algorithm to explore wave interactions with an array of floes subject to break-up. Wave induced fragmentation events in this framework were found to produce near unimodal normal or bimodal

distributions. Similarly to Boutin et al. (2018), Montiel and Squire (2017) also found that multiple wave scattering can enhance break-up, but only for long wavelengths and thin ice, with the reverse true for short wavelengths and thick ice. The study also found that, for the latter case, a break-up front could be observed progressing into the sea ice cover due to weakening of the sea ice from prior break-up events.

Bennetts et al. (2017) adapted the framework outlined in Williams et al. (2013a, b) into CICE to study the impacts of wave break-up of sea ice in the Antarctic. The wave advection and attenuation component of the original scheme was adapted to account for wave spreading away from the mean wave direction. Note that the wave attenuation coefficient in this approach is based on the empirical model of Meylan et al. (2014) and is not a function of floe size i.e. in this setup the floe size feedback process on wave attenuation is not represented. This model both identifies grid cells where wave break-up could occur, but also calculates the fraction of the grid cell where this is possible by considering the attenuation of the incident wave through the grid cell. The resulting grid cell floe size, D, is then calculated as the average of the floe size of unbroken floes (i.e. the floe size in the grid cell at the start of the time step), D_0, and broken floes, D_{bk}, weighted according to the length of the grid cell where floe breaking waves could not or could propagate respectively. D_{bk} is calculated assuming that the floe size follows a split power-law distribution defined from the minimum floe size, D_{min}, and infinity. This is based on the observation from Toyota et al. (2011), and others, that the floe size distribution in the Antarctic appears to follow different power laws above and below a critical diameter of around 15 – 40 m, D_{cr}, with a more negative exponent above this critical diameter than below. Bennetts et al. (2017) suggested that D_{cr} characterises the smallest floe size that can be broken-up by waves via a flexural mechanism. The study defined the probability density distribution, $p(x)$, for this split power-law approach as:

$$p(x) = \begin{cases} AP_o x^{\alpha_1} & D_{cr} > x \geq D_{min} \\ B(1-P_o)x^{\alpha_2} & x \geq D_{cr}. \end{cases} \quad (2.16)$$

Here x refers to the diameter of floes, A and B are related normalisation constants, α_1 and α_2 are the exponents for the distribution below and above D_{cr} respectively, and P_o is a weighting coefficient. P_o is calculated based on the properties of the waves that have caused the break-up event. D_{bk} can then be calculated as the mean value of the split power-law distribution. After break-up the resulting representative floe size in each

grid cell, D, is also subjected to lateral melting and advection. During freezing conditions, a simple floe bonding scheme is applied, with D doubled where there is a freezing potential until a maximum value, D_{max}, is reached. The study does not clarify the time interval between subsequent applications of this floe bonding scheme. The model is initiated with a floe size of D_{max} everywhere except the edge of the sea ice cover where a value of D_{min} is assigned. It is shown that the inclusion of this FSD scheme into CICE enhances the lateral melt rate up to 100 km into the sea ice cover and can result in changes to the sea ice mass balance not just within the MIZ but also the pack ice.

An alternative framework to explore how floe size influences sea ice-ocean interactions has been developed at the National Oceanography Centre of the UK (NOC) as a part of the EU FP7 project 'Ships and waves reaching Polar Regions (SWARP)' (Hosekova et al., 2015; NERSC, 2016) within a coupled CICE-NEMO setup. The full name for this setup is the NEMO–CICE–Waves-in-Ice (WIM) model. This approach was originally developed to understand the impact of waves on the MIZ and the upper ocean via the thermodynamic and dynamic response. This included a particular focus on the operational forecasting of the MIZ and large-scale coupled sea ice-ocean global modelling, where assuming a power law is particularly practical. The FSD model defines a power law between a maximum and minimum floe size, D_{max} and D_{min} respectively. The exponent is calculated independently for each grid cell as a linear function of the sea ice concentration between a minimum of -2.99 at zero concentration and -1.1 at maximum sea ice concentration. The NOC FSD model includes a wave attenuation and floe break-up model based on the waves-ice model from the Nansen Environmental and Remote Sensing Center (NERSC) Norway, introduced in Williams et al. (2013a, 2013b). However, the NOC setup uses a more efficient upstream advection scheme for wave spectra (to replace the original Lax-Wendroff scheme). D_{max} is then updated after a wave break-up event using the same approach as the NERSC model. The mean floe size, D_{mean}, is calculated as the mean value of the distribution generated with the probabilistic break-up scheme of Dumont et al. (2011). The setup also includes an option to calculate D_{mean} as the numerical mean of the power-law distribution. The NOC model incorporates the following additional features: updates to either D_{mean} or D_{max} in response to lateral melt; advection of D_{max} using a remapping advection scheme following Lipscomb and Hunke (2004); treatment of floe formation and growth processes; calculation of D_{max} from the mean floe size using the

Newton-Raphson method and bisection. A treatment of pancake ice is included in this setup; where D_{mean} drops below 20 m, D_{mean} and D_{max} are assumed to be equal i.e. the FSD consists of floes of equal size.

The NEMO–CICE–Waves-in-Ice (WIM) model developed at NOC was then used in the work of Rynders (2017) alongside a floe size dependent rheology and an updated wave mixing scheme to explore the impact of surface waves on sea ice and ocean in the polar regions. Rynders (2017) used the composite rheology approach of Feltham (2005), which combines the EVP rheology used as a standard rheology in CICE (Hunke and Dukowicz, 1997; Hunke et al., 2015) with a collisional rheology (Shen et al., 1986; Shen et al., 1987). The purpose of this combined rheological approach is to discriminate between behaviour in the pack ice, where the motion of the sea ice is driven by slowly deforming 'granules' of sea ice that interact with each other predominantly through plastic interactions, and MIZ behaviour, where interactions between the neighbouring 'granules' or floes are via rapid, dissipative collisions, which can be modelled overall as a viscous material (Feltham, 2005). The contribution of the plastic and collisional components to the net sea ice rheology is determined as a function of sea ice concentration and granular temperature, which is a measure of the kinetic energy associated with the random fluctuation of floes. The relationship between granular temperature, sea ice concentration, and the net contribution of collisional rheology to the total rheology is non-trivial, but in general collisional rheology dominates within the MIZ whereas EVP rheology tends to dominate within the pack ice, and a higher granular temperature is associated with a larger contribution from collisional rheology (Rynders, 2017). Collisional rheology and granular temperature calculations both require a floe size metric, which in this study is taken as D_{mean}. The relationship between collisional rheology and floe size is again non-trivial, whereas granular temperature increases with floe size for a fixed sea ice concentration because the separation between floes also increases, reducing the rate of energy loss through floe collisions. Rynders (2017) completed global coupled sea ice-ocean simulations to explore the impact of the updates to floe size treatment and rheology on the sea ice cover. The net effect on the sea ice mass balance was a reduction in the sea ice concentration and thickness across the Arctic when averaged over summer months (June, July, and August), though this was attributed to changes in the lateral melt rate from the use of an FSD rather than rheological effects. Significant changes to the motion of the sea ice were also reported. The reduction in sea ice concentration and

thickness from the enhanced lateral melt resulted in accelerated rates of ice drift. The collisional rheology was found to increase ice thickness at the centre of the Beaufort Gyre but decrease it at the outer edges of the Gyre; these changes in thickness were found to persist through to winter and drive an acceleration of the Beaufort Gyre. The study also considered the impact of the updated model physics on the ocean state, finding an increased momentum transfer and freshening to the surface mixed layer associated with the reduced sea ice concentration and increased lateral melt respectively. The net effect of these changes was found to be a deepening of the mixed layer, suggesting the increased momentum transfer was the dominant effect.

The FSD models of Dumont et al., (2011), Williams et al. (2013a, b), Bennetts et al. (2017), and Hosekova et al. (2015), each require assumptions about the shape of the FSD, with the impact of processes such as wave break-up and lateral melt on the FSD characterised within that assumption. In 2015 two new FSD models were introduced, both of which aimed to avoid any assumptions regarding the shape of the distribution and to instead allow the shape to emerge from the model. The first of these was a full prognostic sea ice floe size-thickness distribution, introduced in Horvat and Tziperman (2015, 2017). This approach has been subject to several further developments (Roach et al., 2018a; Roach et al., 2019). An adapted version of this prognostic FSD model will be used within this thesis, with an overview of the model provided in Chapter 6. The second was the prognostic floe size distribution of Zhang et al. (2015, 2016), which assumes that all floe size categories adopt an identical ice thickness distribution (ITD) rather than determining the thickness distribution uniquely for each category. This FSD model is constructed around the following equation to describe the evolution of the FSD:

$$\frac{\partial g_l}{\partial t} = -\nabla \cdot (\boldsymbol{u} g_l) - \frac{\partial (f_l g_l)}{\partial l} + \Phi. \tag{2.17}$$

Here g_l is the FSD function, $\boldsymbol{u}$ is the velocity of the sea ice cover, f_l is the rate of change in floe size, and Φ represents mechanical redistribution of the FSD. l represents the floe diameter. In this expression the first term on the right represents advection and divergence of the FSD and the 2nd term represents changes to the FSD through lateral growth or melting.

In Zhang et al. (2015), the focus is on evaluating the mechanical redistribution term, Φ, and the advection and thermodynamic terms are discarded from Eq. (2.14). Φ is broken down into three components:

$$\Phi = \Phi_0 + \Phi_r + \Phi_f. \tag{2.18}$$

Here Φ_0 is the contribution from the creation of open water (defined to be consistent with the model ITD), Φ_r from ridging, and Φ_f from wave break-up of floes. To evaluate Eq. (2.18), three assumptions are made. Firstly, each floe size category has the same ITD and therefore there is no area transfer between floe size categories during ridging. Then, during wave break-up events, floes of any size smaller than the original floe size have an equal chance of forming. Finally, floes that are larger are more likely to break-up in response to a given applied stress than floes that are smaller. To evaluate Φ_r, a participation factor, c_b, is introduced, taken to be a parameter that captures break-up sensitivity to the ITD, FSD, waves, and wave-ice interactions. c_b determines both whether floe break-up will happen and the proportion of floes that will be broken-up during a given event. For Zhang et al. (2015), c_b is taken as a parameter to be imposed rather than evaluated. The FSD model is then implemented in a simple ITD and FSD description of the MIZ to explore the sensitivity of the emergent FSD to parameters such as c_b. The model is initiated with all sea ice area assigned to the largest floe size category. The results of this first study suggest an upper-truncated power-law distribution can emerge provided small floes can result from fragmentation processes. The study also found that the emergent FSD was not sensitive to the partitioning of the floe size categories.

Zhang et al. (2016) applied the FSD model described in Eq. (2.17) into a full coupled sea ice-ocean model, with a focus on simulating the FSD within the Arctic. The sea ice component of this model also includes an ITD and an ice enthalpy distribution to ensure the thermal energy of the sea ice is conserved. The mechanical redistribution term, Φ, is calculated as in Eq. (2.18). The participation factor, c_b, is now parameterised as a function of wind speed, open water fraction (averaged over local grid cells to mimic fetch), mean thickness, and area-weighted mean floe size, rather than assigned a single value. Note that this approach to representing wave break-up distinguishes this model approach from Horvat and Tziperman (2015) and the other approaches discussed here, in that a wave advection and attenuation model is not

used to determine wave-sea ice interactions, but instead the impact of waves on the FSD is parameterised based on local grid cell conditions. Furthermore, the assumption that there is not a preferential floe size for a given fracture event is not shared by other models. In this iteration of the FSD model, the thermodynamic term in Eq. (2.17) is also included in simulations. In this formulation, the partitioning between the basal and lateral melt is calculated as a function of floe size. The lower the sea ice concentration and smaller the mean floe size, the lower the fraction of the total available heat energy in the mixed layer that goes into basal melt, to a minimum of 0.2. This is motivated by both the idea of a stronger temperature gradient between the side and base of floes during periods of high radiative heat flux into the ocean surface in addition to the higher lateral melt to volume ratio expected for smaller floes. The lateral melt rate is then calculated assuming that the remainder of the heat energy within the mixed layer will contribute to lateral melting. The only other thermodynamic process represented in the FSD model is the welding of floes. Here a very simplified approach is used by assuming all sea ice will be assigned to the largest floe size category where a certain welding threshold is exceeded, with this threshold selected to give the best fit of the emergent FSD to observations. It is not clear from the paper if or how the advection term in Eq. (2.17) is evaluated. The exponents measured for the simulated FSD showed about 32% of the variability seen within observations. The study reached several conclusions regarding the behaviour of the FSD, including that a strong annual cycle could be seen in the area-weighted mean floe size for the pack ice but not within the MIZ. The model also found strong sensitivity of the simulated FSD to c_b throughout the year but only to the floe welding threshold in the winter months. The overall impact of the inclusion of the FSD was to reduce the simulated sea ice thickness, particularly within the MIZ.

Most recently Boutin et al. (2020) imposed a hybrid FSD model, adapting features of both the Dumont et al. (2011) and Williams et al. (2017) FSD models for use within a coupled sea ice-wave model. This adapted framework allows a freely evolving FSD in response to thermodynamic processes but fit the emergent FSD to a power law in response to wave break-up events. Although this approach overrides the existing shape of the FSD in response to wave break-up events, Boutin et al. (2020) explained that this approach was taken to ensure coherence between the sea ice and wave models, since the latter also included a simple internal FSD model to enable the representation of wave-floe size feedbacks. The study focusses on two aspects of

wave-sea ice interactions within the Arctic: the impact of wave radiative stress (WRS) on sea ice drift within the MIZ, and the impact of wave induced break-up of floes on lateral melt. Boutin et al. (2020) found that whilst wave break-up does impact the total lateral melt, the dynamical effects of including WRS have a much stronger impact. This is because the WRS tends to compress the ice edge, lowering the overall sea ice melt.

In this section an overview has been provided of the different approaches to modelling the FSD described in the literature. Several of these models primarily focus on the FSD in relation to wave propagation and do not represent the impact of other processes on the FSD. The more recent examples from Zhang et al. (2016), Bennetts et al. (2017), Rynders (2017), Boutin et al. (2020), and the progression of studies developing the prognostic floe size-thickness model from Horvat and Tziperman (2015) to Roach et al. (2019), attempt to include a more complete description of processes that may impact the FSD, including lateral melting. Of these, Bennetts et al. (2017) and Rynders (2017) are both examples where the shape of the FSD is fully imposed. For Zhang et al. (2016) and the studies developing the prognostic floe size-thickness model, the shape is an emergent feature of the model, and a hybrid approach is used for Boutin et al. (2020). Where a power law is imposed, either within a single or split power law, values must be selected for both the minimum floe size and exponent(s). Although a range of values have been seen in observations for both the exponent and minimum floe size (Stern et al., 2018a), Bennets et al. (2017) and Boutin et al. (2020) do not explore the model sensitivity to these parameters. Rynders (2017) does incorporate a variable exponent into the FSD model but does this by expressing the exponent as a function of concentration, which the study acknowledges is not a well-tested dependency. The existing studies also do not investigate the limitations of representing processes such as lateral melting of a distribution within a model where the shape of the FSD is fixed, as highlighted in Horvat and Tziperman (2017).

Several studies, including Zhang et al. (2015) and Herman et al. (2017), have considered how the observed FSD shape might emerge out of wave break-up processes. Zhang et al. (2015), where it is assumed floes of any size are equally likely to form from wave break-up processes, finds an emergent power law in response to wave break-up. Herman et al. (2017), however, suggests that there is a preferential floe size that results from wave break-up, and therefore this process alone cannot be responsible for the observed shape of FSDs. Similarly, Montiel and Squire (2017) also found that their model of wave-sea ice interactions was incapable of producing a power

law FSD from wave-induced floe break-up events. Zhang et al. (2016) considers the role of additional processes, including lateral melting, in determining the emergent power law. This study finds a strong annual variability in the simulated FSD, driven primarily by welding processes in winter and wave break-up processes through summer. This is the first model study to identify welding as an important process in the emergent FSD, but the representation of welding is highly simplified. Roach et al. (2018a) is the first FSD model to incorporate a floe welding scheme motivated by observations. This study also considers the contribution of individual processes to the overall distribution, but the emergent distribution is best fitted by a power law with an exponent of -4 or -5, outside of the general range seen in observations of about -1.5 to -3.5. Roach et al. (2019) further develop the FSD model to enable new floes of different sizes to form depending on the local wave conditions. This study does not explicitly evaluate the emergent distribution. It is therefore an outstanding issue to determine how the FSD emerges and evolves in response to relevant processes, with the role of floe formation and growth processes particularly unclear. Zhang et al. (2016) performed limited sensitivity studies to model parameters, however, there has been no systematic effort to assess the role of individual processes in determining the mass balance impact of the emergent FSD.

More generally, there are several observed FSD processes and applications that have not yet been fully explored in the literature. Gharardi and Lagomarsino (2015) suggest that brittle fracture may be an important mechanism to explain the observed emergent power-law behaviour. Whilst several studies described in this section have developed varying models to investigate and characterise wave-induced fragmentation of the sea ice cover; other processes associated with brittle failure mechanisms such as wind stress, and shear, convergent, and divergent motions of the sea ice cover (Wilchinsky et al., 2010) have yet to be treated within the FSD modelling literature. Perovich et al. (2001) describes observations of melting and separation of floes along existing cracks and fractures. Tsamados et al. (2014) include floe size as a component of a form drag model to improve the representation of momentum exchange between the sea ice, ocean, and atmosphere in models. In this study a simple concentration-based floe size calculation is used, but FSD models may provide an improved representation of floe size in the form drag scheme.

2.4 Overview of this thesis

In chapter 1, five key objectives have been outlined for this thesis to address. Three of these are related to FSD processes and impacts, specifically how the shape of the FSD emerges and the impact the FSD has on the seasonal retreat of sea ice and the total sea ice mass balance. The second set considers whether it can be demonstrated that FSD processes are important in understanding the general seasonal retreat and evolution of the Arctic sea ice and if so, what the advantages and disadvantages are of different FSD models for use in sea ice and climate models. The use of one FSD model is not enough to address these objectives; two alternative FSD modelling approaches will therefore be used in this thesis.

The first model used is the WIPoFSD model, a power-law-derived FSD that includes a variable floe size to respond to different processes that can influence the sea ice cover, including lateral melting and wave break-up. The WIPoFSD model has been modified and adapted for use within standalone CICE from the NEMO–CICE–Waves-in-Ice (WIM) model developed at the National Oceanography Centre in the UK (Hosekova et al., 2015; NERSC, 2016), which has previously been described in Sect. 2.3. The WIPoFSD model has the advantage that by fixing the shape of the distribution to a power law, it is possible to explore the sea ice sensitivity to different exponents and other parameters reported for power-law fits to the FSD i.e. it allows an assessment of how this general FSD shape will change MIZ processes and the overall sea ice mass balance. This model will be the focus of chapters 3 – 5 to consider the impacts of the FSD on the sea ice cover.

Chapter 3 will consider the impact of the WIPoFSD model on the summer fragmentation and break-up of the Arctic sea ice cover via changes to the sea ice lateral melt. Sensitivity studies are performed both to the parameters that define the power law and the parameterisations of different processes to explore the important features of the FSD model that determine its impact on the sea ice cover. A valuable new metric to characterise the FSD, the effective floe size, is introduced in this chapter. This chapter has been formally published in The Cryosphere (Bateson et al., 2020). Chapter 4 then considers the challenges of accurately capturing the impact of individual processes using an FSD model that assumes a fixed shape. The representation of both lateral melting feedbacks and floe advection within the WIPoFSD model will be discussed and explored further as case studies of these

challenges. In chapter 5, the WIPoFSD model will be used to explore the impact of floe size on the sea ice-atmosphere-ocean momentum exchange. The form drag parameterisation of Tsamados et al. (2014) will be described and used in this chapter. This scheme accounts for the spatial features of the sea ice cover, including floe size, in calculations of surface flux exchanges.

The second FSD model used within this thesis is a prognostic model that does not assume any FSD shape, but instead allows sea ice area to transition between floe size-thickness categories in response to relevant processes. The prognostic model used in this thesis is an adapted version of the FSD model presented in Roach et al. (2018a, 2019). This second model has the advantage that the shape is an emergent feature of the FSD and is not imposed, allowing sensitivity studies to explore how individual processes can impact both the shape of the FSD and its impact on the sea ice cover. Chapter 6 will present an introduction to this model, including a description of any alterations to the original scheme of Roach et al. (2018a, 2019). The emergent FSD from the prognostic model is then compared to observations of the FSD and found to perform poorly in simulating the shape of the distribution for mid-sized floes. This motivates the addition of a new brittle fracture quasi-restoring scheme to the prognostic model in chapter 7. This scheme aims to represent the effects of in-plane fracture processes in winter and melting of the sea ice along existing cracks and fractures over the subsequent melt season on the FSD. It is demonstrated that this new scheme significantly improves the simulated FSD within the prognostic model compared to observations. The chapter then proceeds to perform a series of sensitivity studies using the updated prognostic model to explore how individual processes contribute to the overall shape of the emergent FSD and subsequently determine the impact of the FSD on the Arctic sea ice.

The WIPoFSD and prognostic FSD models represent the two broad paradigms of FSD models discussed in Sect. 2.3. The WIPoFSD model represents a class of models where the shape of the FSD in the model is actively constrained according to observations, in this case by fixing it as a power law. The prognostic model represents the model class where the shape of the distribution emerges wholly from parameterisations at the process level. They present useful case studies to consider the advantages and disadvantages of different approaches to modelling the FSD and its impacts on the Arctic sea ice. Chapter 8 presents a direct comparison of these two models. This will include results showing whether either FSD model can improve the

performance of CICE in simulating the observed sea ice behaviour. The impact of both FSD models on key sea ice and MIZ metrics will also be compared, including interannual variability and spatial differences. Finally, it will be discussed whether it is possible to capture behaviours displayed within the prognostic model using simple alterations to the WIPoFSD model. Chapter 9 will then conclude this comparison between the WIPoFSD and prognostic model using a projection to assess whether the importance of either FSD model to the sea ice mass balance or MIZ behaviour may be enhanced under future atmospheric forcing. This chapter will then proceed to review each of the thesis aims in turn to discuss how they have been addressed through this thesis and what conclusions can be reached. This will be followed by a discussion of the limitations in these conclusions and the additional research necessary to further develop understanding of the FSD and associated MIZ processes.

2.5 Summary of chapter 2

In this chapter, the CICE sea ice model has been introduced, including an overview of how sea ice melt and freeze-up is represented in the sea ice model. The mixed-layer model, a simplified 0D representation of the ocean surface layers for use within CICE to represent sea ice-mixed layer interactions, is also introduced. A description is given of the original scheme of Petty et al. (2014) and the adaptations made by Tsamados et al. (2015) for use within the Arctic. A brief critical review is given of existing research into representing the floe size distribution within sea ice models, considering both parametric and prognostic approaches to modelling the FSD. Finally, an overview of the thesis is presented, including details of the two FSD models that will be used and why they have been selected to address the key thesis objectives outlined in chapter 1.

Chapter 3 – Impact of a power-law floe size distribution on the seasonal fragmentation and melt of the Arctic sea ice

This chapter has been formally published as Bateson et al. (2020). The introduction has been truncated to avoid repetition with earlier chapters. The chapter overview that now follows is adapted from the abstract of the published work:

This chapter presents an investigation into the impact of the WIPoFSD model, introduced in chapter 2, on the evolution of the Arctic sea ice with a focus on the melting season. The WIPoFSD model represents the floe size distribution as a power law defined by an upper floe size cut-off, lower floe size cut-off, and power-law exponent. This distribution is also defined by a new tracer that varies in response to lateral melting, wave-induced break-up, freezing conditions, and advection. This distribution is implemented within a sea ice model coupled to a prognostic ocean mixed-layer model. Results are presented to show that the use of a power-law floe size distribution has a spatially and temporally dependent impact on the sea ice, in particular increasing the role of the marginal ice zone in seasonal sea ice loss. This feature is important in correcting existing biases within sea ice models. In addition, it is shown that there is a much stronger model sensitivity to floe size distribution parameters than other parameters used to calculate lateral melt, justifying the focus on floe size distribution in model development. It is also demonstrated that the attenuation rate of waves propagating under the sea ice cover modulates the impact of wave break-up on the floe size distribution. It is finally concluded that the model approach presented here is a flexible tool for assessing the importance of a floe size distribution in the evolution of sea ice and is a useful stepping-stone for future development of floe size modelling.

Author contributions

As this chapter has been published formally under multiple authors, the following is a statement to clarify the aspects of the research that I contributed to the paper and the

aspects of the research that were completed by the co-authors (my estimated percentage contribution to each task is given in brackets, where appropriate):

Lucia Hosekova (LH), with support from Yevgeny Aksenov (YA), developed the original version of the WIPoFSD model within the coupled NEMO–CICE–Waves-in-Ice (WIM) framework, described in Sect. 2.3 of this thesis. David Schröder (DS) adapted the framework into the CPOM CICE stand-alone set-up. Adam Bateson (AWB) devised and incorporated the effective floe size calculations into the WIPoFSD model. AWB completed the simulations (100%), calculations (100%), and analysis (90%) presented in this chapter under the supervision of Daniel Feltham (DLF), DS, LH, Jeff Ridley (JKR), and YA. DS provided additional technical support. AWB composed the paper with feedback from all authors.

3.1 Introduction

In this chapter, a single power law will be applied to describe the FSD within a stand-alone sea ice model coupled to a prognostic mixed-layer model, hereafter referred to as the WIPoFSD model (Waves-in-Ice module and Power-law Floe Size Distribution model). The WIPoFSD model has been selected as it is able to respond to processes that influence floe size without the computational expense of a full prognostic FSD model. The model allows an assessment of how a power-law distribution of floes will impact the sea ice cover and by what mechanisms these changes occur. Furthermore, it provides a simple framework to explore the model sensitivity to the three parameters used to define the WIPoFSD. A series of additional experiments are also possible within this framework including imposing a variable exponent, changing the parameters that define the impact of waves on sea ice, and comparing the model sensitivity of the floe size parameters to other parameters that influence the lateral melt rate. A stand-alone sea ice model has been selected over a coupled approach to limit model complexity so that the physical impacts and feedbacks of imposing the WIPoFSD model can be more easily identified and to permit more sensitivity studies. The WIPoFSD model is coupled to a prognostic mixed layer so that mixed-layer feedbacks can also be considered.

For this study results are presented to explore and understand the thermodynamic response of the sea ice to a power-law-derived FSD and the individual impacts of wave–floe size and lateral melting–floe size interactions. The focus is on the impact of

this FSD on the seasonal sea ice retreat and variability rather than on longer-term changes and trends.

This chapter will proceed as follows: Sect. 3.2 describes the sea ice model used, Sect. 3.3.1 describes standard model physics, and Sect. 3.2.2–3.2.4 outlines the new WIPoFSD model. Section 3.3 describes the modelling methodology used including the forcing data and model domain. Section 3.4 describes the results of the simulations in three sections: Sect. 3.4.1 looks at the general impacts of the FSD on the sea ice, Sect. 3.4.2 explores the model sensitivity to the different FSD parameters, and Sect. 3.4.3 looks at the model response to a series of perturbations to the model including the wave-in-ice set-up, floe shape parameter, lateral melt constants, and a variable power-law exponent. Sections 3.5 and 3.6 are the Discussion and Conclusion sections respectively.

3.2 Model description

For this study a CPOM (Centre for Polar Observation and Modelling) version of the Los Alamos Sea Ice model v5.1.2, hereafter referred to as CICE, was used (Hunke et al., 2015). This is a dynamic and thermodynamic sea ice model designed for inclusion within a climate model. CICE includes a large choice of different physical parameterisations; see Hunke et al. (2015) for details. Section 3.2.1 outlines the features pertinent to this study. Our local version also includes some state-of-the-art parameterisations not included within the general CICE distribution, also described in Sect. 3.2.1. The WIPoFSD model that we have implemented into stand-alone CICE has been modified and adapted from an implementation developed at the National Oceanography Centre of the UK within a coupled sea ice–ocean framework, called the NEMO–CICE–Waves-in-Ice (WIM) model (Hosekova et al., 2015; NERSC, 2016). An overview of this framework has previously been provided in Sect. 2.3. This approach was originally developed to understand the impact of waves on the MIZ and the upper ocean via the thermodynamic and dynamic response with applications for the operational forecasting of the MIZ and large-scale coupled sea ice–ocean global modelling, where assuming a power law is particularly practical.

The WIPoFSD model used here includes the wave attenuation and floe break-up model based on the Waves-in-Ice Model from the Nansen Environmental and Remote Sensing Center (NERSC) Norway (Williams et al., 2013a, b). An overview of this

scheme is given in Sect. 3.2.2. Floe size is assumed to follow a single power law within the WIPoFSD model. Three new global parameters and one tracer are required to define this power law. The global parameters are d_{min}, lower floe size cut-off for the distribution; d_{max}, upper floe size cut-off; and α, the power-law exponent. The introduced variable FSD tracer, l_{var}, is a function of several processes that change floe sizes: lateral melting, wave break-up of sea ice, advection, and freeze-up. We also introduce a new floe size metric l_{eff} to characterise the FSD, the effective floe size. Section 3.2.3 outlines how the imposed FSD is defined and describes amendments made to model thermodynamics to account for the change in floe size treatment. This section also provides a definition of l_{eff}. Further details about the treatment of floe size and how l_{var} evolves are given in Sect. 3.2.4.

3.2.1 Description of Standard Model Physics

Within the CICE v5.1.2 model we use the incremental remapping advection scheme (Lipscomb and Hunke, 2004), an ice thickness redistribution scheme (Lipscomb et al., 2007), along with five ice thickness categories (Hunke et al., 2015). The default elastic–viscous–plastic (EVP) rheology is used (Hunke and Dukowicz, 2002) along with an ice strength formulation (Rothrock, 1975). The frictional energy dissipation parameter is set to 12. A topographic-based melt pond scheme is used (Flocco et al., 2012) in conjunction with a delta-Eddington radiation scheme (Briegleb and Light, 2007). The atmospheric and oceanic neutral drag coefficients are assumed constant in time and space. An ocean heat flux formulation is used at the ice–ocean interface (Maykut and McPhee, 1995).

The rate of thermodynamic ice loss is calculated as follows:

$$\frac{d}{dt}(AH) = A\left[w_{top} + w_{bas} + \frac{\pi H}{\alpha_{shape} L} w_{lat}\right], \tag{3.1}$$

where A refers to the sea ice concentration, H to the ice thickness, L to the floe diameter (300 m in the default set-up), and α_{shape} a geometrical parameter to represent the deviation of floes from having a circular profile (0.66 in the default set-up). The terms w_{top}, w_{bas}, and w_{lat} refer to the melt rate at the floe upper surface (top melt), base (basal melt), and sides (lateral melt). The lateral melt rate is calculated as follows:

$$w_{lat} = m_1 \Delta T^{m_2}. \quad (3.2)$$

Here m_1 = 1.6 x 10^{-6} $m\ s^{-1}\ K^{-m_2}$ and m_2 = 1.36 (Perovich, 1983). ΔT is the elevation of the surface water temperature above freezing. The form of Eq. (3.2) was determined using laboratory observations of the vertically averaged lateral melt rate of a fresh-water ice wall melting in salt water under turbulent flow (Josberger, 1979; Josberger and Martin, 1981). The values of m_1 and m_2 were then fitted to observations taken in a single static lead near the coast of the Prince Patrick Island, part of the Canadian Arctic Archipelago (Perovich, 1983; Maykut and Perovich, 1987). The basal and top melt rates are not explicitly calculated, but instead expressed as changes in height derived from a consideration of fluxes over the top and bottom floe surfaces (Hunke et al., 2015). Both lateral and basal melting are reliant on there being sufficient heat flux from the ocean to the sea ice to produce the predicted melting. The model calculates a melting potential term, F_{frzmlt}, for the upper ocean layer:

$$F_{\mathrm{frzmlt}} = -\frac{\Delta T \rho_w c_w h_{mix}}{\Delta t}. \quad (3.3)$$

Here ρ_w is the density of seawater, c_w is the specific heat of sea water, h_{mix} is the depth of the ocean surface mixed layer, and Δt is the model timestep. F_{frzmlt} has a maximum magnitude of 1000 W m^{-2}. If $F_{\mathrm{frzmlt}} < 0$ in a grid cell where sea ice is present, lateral and basal melting will occur. If the total heat flux required to produce the calculated basal and lateral melt exceeds the value permitted by the melting potential, then both values will be reduced proportionally such that the total heat flux required equals F_{frzmlt}. Note that H stays constant with respect to lateral melt; so discarding the w_{top} and w_{bas} terms in Eq. (3.1) we have an expression for the rate of sea ice concentration loss via lateral melt,

$$\frac{1}{A}\frac{dA}{dt} = \frac{\pi}{\alpha_{shape} L} w_{lat.} \quad (3.4)$$

In these simulations, the default CICE fixed slab ocean mixed layer (ML) is not used, and instead a prognostic mixed-layer model is used wherein the temperature, salinity, and depth of the layer are all able to evolve with time (Petty et al., 2014). These variables evolve based on surface fluxes and entrainment–detrainment at the base of the ML. The ML entrainment rate is calculated based on the mechanical energy input

by wind forcing and surface buoyancy fluxes and profiles of water properties beneath the mixed layer (Kraus and Turner, 1967). This implementation also includes a minimum ML depth, set to 10 m. The prognostic mixed-layer model used here cannot capture the full extent of ocean variability; however it is sufficient to represent sea ice–mixed-layer feedbacks via the mixed-layer properties. Tsamados et al. (2015) have previously compared the performance of the prognostic ML model used here to observations (Peralta-Ferriz and Woodgate, 2015). The mixed layer was found to be generally realistic, though it shows a bias towards too shallow mixed-layer depths through the melting season.

A number of amendments are made to CICE version 5.1.2 based on recent work by Schröder et al. (2019). The maximum meltwater added to melt ponds is reduced from 100 % to 50 %. This produces a more realistic distribution of melt ponds (Rösel et al., 2012). Snow erosion, to account for a redistribution of snow based on wind fields, snow density, and surface topography, is parameterised based on Lecomte et al. (2015) with the additional assumptions described by Schröder et al. (2019). The “bubbly” conductivity formulation of Pringle et al. (2007) is also included, which results in larger thermal conductivities for cooler ice.

3.2.2 Waves-in-ice module

The full details of this module are described in Williams et al. (2013a, b), to which the reader is referred for details; here we provide an overview of the elements pertinent to our study alongside developments unique to the WIPoFSD model. The waves-in-ice module described here reproduces wave conditions near the sea ice edge within the MIZ. Local wind direction determines the direction of wave propagation with adjustments made for attenuation imposed by the sea ice cover. This is a compromise dictated by availability of forcing data, lack of observational studies, and the coarse resolution of the CICE model.

The module operates using its own internal time step defined by

$$t_{wav} = \frac{c\Delta x_{min}}{c_{g,max}}, \tag{3.5}$$

where c is the Courant–Friedrichs–Lewy (CFL) number, here set to 0.7, Δx_{min} is the size of the smallest grid cell, and $c_{g,max}$ is the highest available group velocity. This is necessary due to the high wave speeds observed in the Arctic. Over each module time step, the wave field is advected, attenuation of waves is calculated, and any ice-breaking events are identified. Note also the forcing fields within each module time step are interpolated between the prior reading and the subsequent reading to ensure smooth variations in the field (note this only applies if the grid cell remains ice-free over this period).

We construct the wave energy spectra using H_s, the significant wave height (m), and T_p the peak wave period (s). These parameters are obtained from the ERA-Interim reanalysis dataset (Dee et al., 2011). The forcings are updated at 6 h intervals, but only for locations where the sea ice is at less than 1 % coverage, i.e. grid cells where there will be negligible wave–ice interactions. The ocean surface wave spectra, S ($m^2\ s^{-1}$), are then constructed using the two-parameter Bretschneider formula,

$$S_B\left(\omega, T_p, H_s\right) = \frac{1.25}{8\pi}\frac{{T_\omega}^5}{T_p^4}H_s^2 e^{-1.25\left(\frac{T_\omega}{T_p}\right)^4}. \quad (3.6)$$

Here ω is frequency (rad s^{-1}) and T_ω the associated period (s). H_s and T_p are used rather than the full wave energy spectra for consistency with Williams et al. (2013a, b).

Once the wave field S is defined, it needs to be advected into the ice-covered regions. In the first instance this involves defining the directional space of advection. A principal direction is defined as that of the boundary surface stress component of the ocean. This is generally close to the atmospheric wind direction; however, sea ice also contributes to the boundary surface stress. The waves are advected in five directions spaced equally around the principal direction, with the total angular size of the surface wave spread equal to 90° (i.e. 45° in each direction from the principal direction). The energy is distributed amongst the bins according to $\frac{2}{\pi}(\cos\Delta\theta)^2$, where $\Delta\theta$ is the deviation from the principal wave direction. The wave energy spectra are then discretised into 25 individual frequencies from a minimum wave period of 2.5 s and a maximum of 23 s. The wave energy spectra are then advected in each of the five directions described above using an upwind advection scheme with each individual spectrum advected separately with speed according to its group velocity $c_g(\omega)$. This

advection process is necessary because the wave forcing, derived from the ERA reanalysis data, does not cover areas with a sea ice cover. Furthermore, due to differences between the modelled sea ice edge and observations, there can exist ice-free regions within the model for which no wave forcing data are available.

The decision to use the ocean surface stress to define the primary direction of wave propagation rather than the Stokes drift direction was made because the Stokes drift direction data were not available within the sea ice field at the time of model development. The use of ocean surface stress will be sensible for wind-driven seas, but not for swell-driven seas where the Stokes drift is a more appropriate choice. Stopa et al. (2016) discuss wave climate in the Arctic between 1992 and 2014 and they find that regions exposed to the North Atlantic wave climate will be strongly influenced by swells generated within the North Atlantic Ocean. Semi-enclosed and isolated seas, e.g. Laptev and Kara seas, are more event driven and have an equal mix of wind-driven and swell-driven waves. The results presented in this study should therefore be considered in the context that the direction of wave propagation is a significant approximation. Furthermore, we are only able to represent the impacts of waves generated externally to the sea ice cover within this set-up. The choice of surface wave spread is also non-trivial. Wadhams et al. (2002) showed that a wave propagating into the MIZ could experience significant wave spreading until it was essentially isotropic. However, a distinction was found between wind seas where the isotropic state could be achieved within a few kilometres and swell seas where spreading occurs much more slowly, if at all. Wave spreading has been shown to be dependent on the wavelength. Montiel et al. (2016) found that shorter wavelengths experienced spreading and longer wavelengths did not with a transition between these two regimes defined by the maximum floe size. This is consistent with the observed behaviour of wave-driven regimes and swell-driven regimes. Using a fixed surface wave spread across a limited number of categories is a significant simplification of the rather complex spreading behaviour of waves; however it represents a balance between short wave periods that quickly achieve an isotropic state and longer wave periods that propagate much further into the MIZ before they experience significant spreading.

After advection, the attenuation of waves over each wave time step is calculated. This will be calculated for each individual wave energy spectrum:

$$S_{at}(\omega) = S(\omega)e^{-\alpha_{dim}c_g(\omega)t_{wav}}, \tag{3.7}$$

where S_{at} is the wave spectrum after attenuation ($m^2 s^{-1}$), α_{dim} is the dimensional attenuation coefficient (m^{-1}), t_{wav} is the module time step (s), and other variables are as previously defined. α_{dim} can also be described as the rate of exponential attenuation per metre. It is here modelled as a sum of the linear wave scattering at floe edges in addition to a viscosity term. It is also updated discontinuously when the wave energy is large enough to cause ice breakage. α_{dim} effectively becomes a function of mean floe size, sea ice concentration, ice thickness, and wave period (see Williams et al., 2013a, for further details).

After attenuation, the wave energy spectra within each grid cell are reconstructed as a discretised function of ω by summing the advected spectra from each of the five incident directions. The final spectra, $S(\omega)$, can then be advected using the process described above for subsequent time steps. If we assume that the sea surface elevation, η, follows a Gaussian distribution, i.e. non-linear affects that can cause asymmetry are neglected, we can calculate the following properties of interest from the wave energy spectra: the mean square surface elevation of the ocean (or alternatively the variance in position of a water particle at the surface of the ocean), $\langle \eta^2 \rangle$; the mean square surface elevation of the sea ice, $\langle \eta_{ice}^2 \rangle$; the mean square strain for the sea ice (modelled as a thin elastic plate), $\langle \varepsilon^2 \rangle$; and the representative wave period, T_W. Each of these metrics requires the computation of integrals over frequency, here approximated using Simpson's rule (see Williams et al., 2013a, for further details). The significant wave height, H_s, can then be calculated as $4\sqrt{\langle \eta^2 \rangle}$ (Laing et al., 1998) i.e. the standard deviation in η is equal to one quarter of the significant wave height.

The floe fragmentation scheme used is identical to Williams et al. (2013a), which should be referred to for a detailed description of the scheme. An overview of this scheme is presented here. Defining a significant strain amplitude, E_s, as two standard deviations in strain i.e. $2\sqrt{\langle \varepsilon^2 \rangle}$, then the probability, P_E, that the maximum strain produced by a passing wave, E_W, exceeds the breaking strain, ε_c, can be calculated as:

$$P_E = e^{\frac{-2\varepsilon_c^2}{E_s^2}}. \tag{3.8}$$

P_{crit} can then be defined such that if $P_E > P_{crit}$ a breakup event occurs. Using Eq. (3.8), this criterion can be rewritten as:

$$E_s > \varepsilon_c \sqrt{-\frac{2}{\log(P_{crit})}} \tag{3.9}$$

We assume that the spectrum is narrow enough to be considered monochromatic. In this case, $E_s = \frac{1}{2}{E_W}^2$ (since E_s is defined as $2\sqrt{\langle\varepsilon^2\rangle}$), and the criterion $E_W > \varepsilon_c$ can be rewritten as $E_s > \varepsilon_c\sqrt{2}$. Comparing this expression to Eq. (3.9), P_{crit} takes the value e^{-1} under a monochromatic wave assumption. ε_c is calculated as $\frac{\sigma_c}{Y^*}$, where σ_c is the flexural strength and Y^* the effective Young's modulus for the sea ice. σ_c and Y^* are calculated using empirically derived expressions, where both are dependent on the brine volume fraction.

T_W is used to calculate the representative wavelength, λ_W, required to update the FSD after a wave fragmentation event (see Sect. 3.2.4 for details on how the FSD is changed). λ_W is calculated as $\frac{2\pi}{k_W}$, where $k_W = k_{ice}\left(\frac{2\pi}{T_W}\right)$. Here $k_{ice}(\omega)$ is the positive real root of the dispersion equation for a section of ice-covered ocean. The dispersion relation used here is that of Robinson and Palmer (1990) and is derived by adding a damping coefficient to an equation describing low-frequency, low-amplitude oscillations of a liquid under a thin elastic plate.

3.2.3 Floe size distribution model

We employ a number-weighted FSD, $N(x)$, where x is the floe diameter. $N(x)$ is fitted to a power law as shown in Fig. 3.1. It is described by the following equation:

$$N(\, x \,|d_{min} \leq x \,\leq\, l_{var}\,) = Cx^{\alpha}. \tag{3.10}$$

Here N has units of reciprocal metres, d_{min} and l_{var} have units of metres, and α is unitless. l_{var} is the variable FSD tracer, also in metres. l_{var} evolves independently in each grid cell as a function of physical processes between the upper and lower floe size cut-offs of the distribution, d_{max} and d_{min} respectively. d_{max} also has units of metres. d_{min}, d_{max}, and α can all be defined independently for each grid cell; however in this study they will be fixed across the sea ice cover within an individual simulation.

l_{var} can be considered to represent the history of a given area of sea ice in terms of physical processes that affect the FSD.

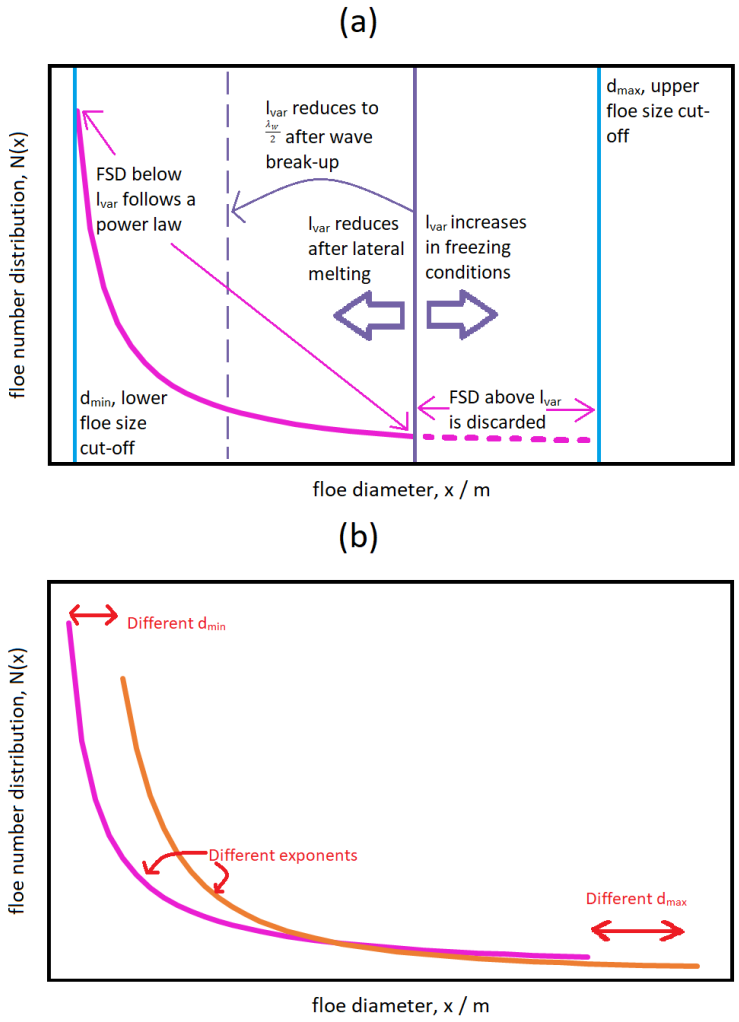

Figure 3.1: Panel **(a)** is a schematic of the imposed FSD model. This model is initiated by prescribing a power law with an exponent, α, and between the limits d_{min} and d_{max}. Within individual grid cells the variable FSD tracer, l_{var}, varies between these two limits. l_{var} evolves through lateral melting, wave break-up events, freezing, and advection. Not shown is how changes in l_{var} will also impact the floe size number distribution factor, C. Panel **(b)** shows how d_{min}, d_{max}, and α can all be varied to produce floe size number distributions. Both panels present cartoon images intended to highlight key processes and parameters within the WIPoFSD model and should not be taken as a realistic depiction of a power law distribution plotted on linear scales.

The model is initiated with l_{var} set to d_{max} in all grid cells where sea ice is present. The floe size number distribution factor, C, is determined such that the total area of individual floes, $N\alpha_{shape}x^2$, sum to equal the total sea ice area, Al^2 (where l^2 is the total grid cell area):

$$\frac{\alpha_{shape}}{Al^2}\int_{d_{min}}^{l_{var}} Nx^2\,dx = 1. \tag{3.11}$$

It should be noted this treatment of N means that in this model the sea ice cover consists only of floes between the limits of d_{min} and d_{max} in diameter. There are no floes with sizes outside these limits.

It is useful here to define an additional floe size parameter, l_{eff}, the effective floe size. l_{eff} is defined as the floe size of a distribution of identical floes that would produce the same lateral melt rate in a given instant to a distribution of non-uniform floes, when under the same conditions with the same total sea ice cover. Equation (3.4), used to calculate the lateral melt rate, can be adapted for use within the WIPoFSD model:

$$\frac{1}{A}\frac{dA}{dt} = \frac{\pi}{\alpha_{shape} l_{eff}} w_{lat}. \tag{3.12}$$

The lateral melt rate of a given area of sea ice is proportional to the total perimeter of that sea ice. It is therefore also useful to introduce a second parameter called perimeter density, ρ_P, which is the length of the ice edge per unit area of sea ice cover. l_{eff} is hence the constant floe size which produces the same ρ_P as an FSD.

First, Eqs. (3.10) and (3.11) can be used to give an expression for the total sea ice area, Al^2:

$$Al^2 = \int_{d_{min}}^{l_{var}} C\alpha_{shape} x^{2+\alpha} dx. \tag{3.13}$$

The total ice edge length, P_{fsd}, within a grid cell, can also be expressed in terms of the WIPoFSD parameters:

$$P_{fsd} = \int_{d_{min}}^{l_{var}} C\pi x^{1+\alpha} dx. \tag{3.14}$$

We can then divide the second expression by the first to give ρ_P^{fsd}, which is P_{fsd} divided by the total ice area in the grid cell, Al^2:

$$\rho_P^{fsd} = \frac{P_{fsd}}{Al^2} = \frac{\pi(3+\alpha)[l_{var}^{2+\alpha} - d_{min}^{2+\alpha}]}{\alpha_{shape}(2+\alpha)\,[l_{var}^{3+\alpha} - d_{min}^{3+\alpha}]}. \quad (3.15)$$

Whilst perimeter density has not been a standard parameter to report from observations, it can be easily calculated from available FSD data. A similar value has been reported by Perovich (2002), though this was reported per unit area of domain size (i.e. ocean plus sea ice area). We can then also define ρ_P^{con}, the perimeter density for a distribution of floes of constant size, using an analogous approach:

$$\rho_P^{con} = \frac{P_{con}}{Al^2} = \frac{\pi}{\alpha_{shape}L}; \quad (3.16)$$

L corresponds to the constant floe diameter; hence for the 300 m case we would get a perimeter density of 0.0159 m^{-1} (with α_{shape} taking the standard CICE value of 0.66). Setting the perimeter density expressions for both a constant floe size and power-law FSD to be equal, and noting that this defines $L = l_{eff}$, we obtain

$$l_{eff} = \frac{(2+\alpha)[l_{var}^{3+\alpha} - d_{min}^{3+\alpha}]}{(3+\alpha)\,[l_{var}^{2+\alpha} - d_{min}^{2+\alpha}]}. \quad (3.17)$$

Note that Eqs. (3.15) and (3.17) are not valid where $\alpha = -2$ or -3. For these cases, α is taken to be -2.001 and -3.001 to maintain code simplicity with only a negligible cost to accuracy.

3.2.4 Processes that impact l_{var}

In our model there are four ways in which the floe size distribution can be perturbed: lateral melt, break-up of floes by ocean waves, advection of floes, and restoration due to freezing. Changes in l_{var} impact the entire FSD via the floe number distribution factor, C, which is also a function of l_{var}, as defined in Eq. (3.11). Note that C is also a function of sea ice concentration and therefore, for processes such as lateral melting, changes in both l_{var} and A will contribute to changes in the floe number distribution. It should be noted here that the WIPoFSD model is not intended to represent the impact of physical processes on the details of the floe size distribution; it is indeed not possible to do so in a framework where a power law is imposed. Instead the impact of the

different processes considered here is represented via parameterisations, here expressed in terms of the model variable, l_{var}.

As lateral melt involves the loss of ice volume from the sides of floes, it can be expected to reduce floe size. To represent this in the model, we set the reduction in l_{var}^2 from lateral melting to be proportional to the reduction in A, the sea ice concentration, from lateral melting:

$$\left(\frac{l_{var,final}}{l_{var,initial}}\right)^2 = \frac{A_{final}}{A_{initial}}. \tag{3.18}$$

If we then express A_{final} in terms of $A_{initial}$ and ΔA_{lm}, the reduction in sea ice concentration from lateral melting, we obtain

$$l_{var,final} = l_{var,initial}\sqrt{1 - \frac{\Delta A_{lm}}{A}}. \tag{3.19}$$

The act of reducing l_{var} alone acts to redistribute sea ice area attributed to floes larger than l_{var} to floes smaller than l_{var}. However, the change in A also independently acts to reduce C, as described above. The combined effect is to decrease the number of floes across the whole distribution. Previous studies, such as that by Horvat and Tziperman (2017), have shown that lateral melting causes stronger deviation from the power law for smaller floes than larger floes. However lateral melting also results in floes smaller than d_{min} that will contribute to an even higher lateral melt relative to the floe size. Hence the behaviour of this lateral melt scheme compensates between these two expected changes to the distribution.

Section 3.2.2 outlines the conditions necessary to trigger the break-up of floes by waves. If these conditions are fulfilled, l_{var} is updated according to the following expression:

$$l_{var} = \max\left(d_{min}, \frac{\lambda_W}{2}\right), \tag{3.20}$$

where λ_W is the representative wavelength, as defined in Sect. 3.2.2. Here l_{var} can be considered a fragmentation length scale, defining the transition from a regime where

floes are broken up by waves to a regime where the number of floes is increasing due to this break-up of larger floes.

There are three processes thought to be the main drivers of floe formation and growth during freezing conditions: lateral growth, welding of floes, and formation of new floes (Roach et al., 2018a). The focus of this study is on the seasonal melt and fragmentation of sea ice rather than the winter evolution; hence a simple floe growth restoration scheme is used. During conditions when the model identifies frazil ice growth, l_{var} is restored to its maximum value according to the following expression:

$$l_{var,final} = \min\left(d_{max}, l_{var,initial} + \frac{d_{max}\Delta t}{T_{rel}}\right), \tag{3.21}$$

where T_{rel} is a relaxation time which relates to how quickly the ice floes would be expected to grow to cover the entire grid cell area. It is set to 10 days as standard, with 10 days selected as representative of the rapid increase in sea ice concentration during the early freeze-up season (note this parameter is subject to a sensitivity study in section 3.4.3). In grid cells that transition from being ice-free to having a sea ice cover, l_{var} is initiated with its minimum value, i.e. d_{min}. The behaviour of the full floe number distribution depends not only on l_{var} but also on A, the sea ice concentration. During periods of freezing when the sea ice concentration increases significantly, both C and l_{var} will increase in value, leading to increases in the number density across all sizes of floes. This is consistent with a scenario where lots of new floes are being formed. During periods of freezing where the sea ice concentration does not increase significantly (e.g. where the sea ice area fraction is already close to 1), then l_{var} will increase and C will decrease. This represents a shift in the distribution from smaller floes to larger floes. It corresponds physically to a scenario where floe welding is the dominant process driving changes in the FSD.

l_{var} is transported using the horizontal remapping scheme with a conservative transport equation, the standard within CICE for ice area tracers (Hunke et al., 2015), where (ice) area tracers are properties that CICE treats as area-conserved during advection. An amendment to the usual scheme involves calculating a weighted average of the l_{var} over ice thickness categories after advection and the subsequent mechanical redistribution. This is necessary as the tracer is not defined independently for each thickness category unlike other tracer fields. It is useful here to comment on

the choice of advection scheme. Firstly, properties that scale to the root of the sea ice area, such as the floe diameter, cannot be advected as an ice area tracer. Secondly, it has been shown that normalised or mean properties relating to the FSD also do not advect as an area-conserved property (Horvat and Tziperman, 2017). Here, l_{var} is a parameter assigned to areas of sea ice to represent the prior history of that sea ice area in terms of processes that can affect the FSD. l_{var} is not a parameter attributed to individual floes and it is calculated independently to the FSD and is not a diagnostic property calculated from the distribution. Hence, it is appropriate to treat l_{var} as an ice area tracer.

It is worth commenting here on the limitations of the modelling approach to floe size used in this study. The use of a power-law distribution with a fixed exponent to describe the FSD is a valuable simplification to explore the impact of floe size on the Arctic sea ice. The tracer l_{var} is an internal model tool used to enable parameterisations of how individual processes impact the FSD within this constrained framework. The parameterisations described in this section are necessarily approximations of how these processes might impact the FSD and should not be considered exact physical descriptions.

3.3 Methodology

Our modified version of CICE is run over a pan-Arctic domain with a 1° tripolar (129×104) grid. The surface forcing is derived from the 6-hourly NCEP-2 reanalysis fields (Kanamitsu et al., 2002). The mixed-layer properties are restored over a timescale of 5 days to a monthly climatology reanalysis at 10 m depth taken from the MyOcean global ocean physical reanalysis product (MYO reanalysis; Ferry et al., 2011). This restoring is needed to effectively represent advection within the mixed layer. The deep ocean post detrainment retains the mixed-layer properties; however it is restored over a timescale of 90 d to the winter climatology (herein meaning the mean of 1 January conditions from 1993 to 2010) from the MYO reanalysis.

All simulations are spun up between 1 January 1990 and 31 December 2004 using the standard set-up described in Sect. 3.2.1 with a constant floe size of 300 m (without the WIPoFSD model included). Simulations are initiated on 1 January 2005 using the output of the spin-up and evaluated for 12 years until 31 December 2016. Results are all taken from the period 2007–2016 to allow 2 years for the model to adjust to the

addition of the WIPoFSD model. A reference run is also evaluated over this period using the standard set-up and a 300 m constant floe size. Figure 3.2 shows this model setup simulates the climatological monthly sea ice extent realistically for this period over the region included in the model domain. It should be noted that parts of the Hudson Bay and Canadian Arctic Archipelago are not included within the model domain. All further simulations are evaluated over the same time period using the same initial model state, however with the WIPoFSD model imposed. Some simulations have additional modifications made to the model as described.

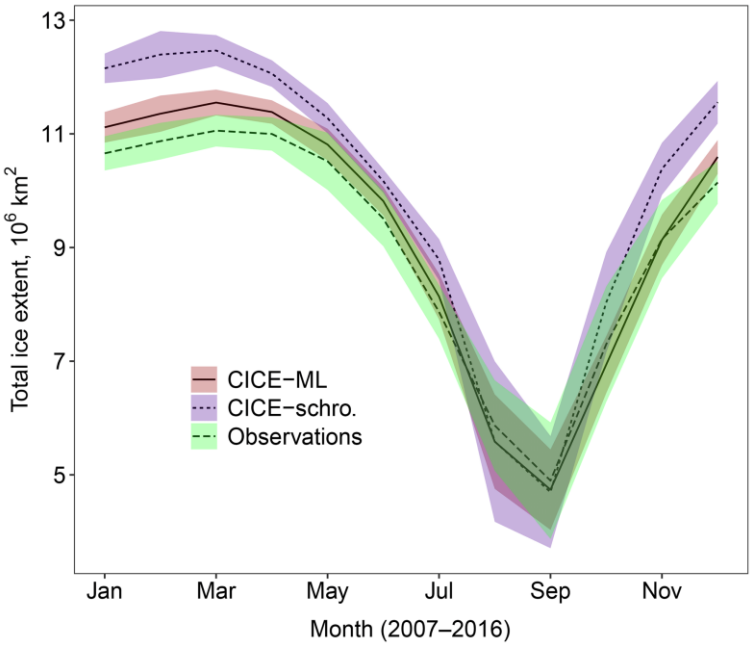

Figure 3.2: Comparison of the 2007–2016 mean cycle for the total Arctic sea ice extent within the model domain simulated in the coupled CICE–prognostic mixed-layer reference set-up (marked CICE–ML, red ribbon, solid) with the results from the standard optimised CPOM CICE model (Schröder et al., 2019, marked CICE-schro, blue ribbon, small dashes) and observed sea ice extent derived from Nimbus-7 SMMR and DMSP SSM/I–SSMIS satellites using Bootstrap algorithm version 3 (Comiso, 1999, marked Observations, green ribbon, large dashes). The ribbon shows, in each case, the region spanned by the mean value plus or minus 2 times the standard deviation for each simulation. This gives a measure of the interannual variability over the 10-year period. Results show the new model performs either comparably to or better than the previous optimum set-up throughout the year. In addition, the mean CICE–ML sea ice extent falls within the interannual variability of the observations between June and December, i.e. most of the melting season, suggesting this reference state is suitable for studies focusing on this period.

3.4 Results

Results are presented for the pan-Arctic domain with a focus on the melting season. All plots compare the mean behaviour over 10 years from 2007 to 2016 against the reference simulation, referred to as *ref*, which uses a constant floe size of 300 m. The results for 2005 and 2006 are discarded to allow 2 years for the model to adjust to the imposed FSD. In this study we are trying to understand the impact of the FSD and associated processes on the seasonal sea ice loss. The years 2007–2016 have been selected as the baseline for these simulations as they will capture the current climatology of the Arctic, including the record September minimum sea ice extent observed in 2012.

3.4.1 General impact of an imposed distribution

The WIPoFSD model introduces new parameters that can be constrained through observations. Stern et al. (2018b) were recently able to show a region of floe sizes could be described by power laws over a size range from 10 to 30 000 m. This is the largest range of floe sizes that a power law has produced a good fit to; hence these are set as the standard values for d_{min} and d_{max} in this study. Further discussion on the values of d_{min} and d_{max}, including the observational uncertainty associated with these values and physical or model limits, is presented in section 3.4.2. A collated analysis of observations (Stern et al., 2018a) shows that α can adopt values generally ranging from -1.6 to -3.5 (when the FSD is reported as a probability distribution). A standard exponent value of $\alpha = -2.5$ is adopted as an intermediate value over this range, noting in addition that this value is consistent with the ranges reported by Stern et al. (2018b). The simulation using these standard FSD parameters, $\alpha = -2.5$, $d_{min} = 10\ m$, and $d_{max} = 30{,}000\ m$, will be referred to as *stan-fsd* (see Table 3.2).

Figure 3.3 displays the percentage difference in sea ice extent and volume for *stan-fsd* compared to *ref*. In addition, it shows the spread of twice the standard deviation of these simulations as a measure of the interannual variability. The impact on the pan-Arctic scale is small, with sea ice extent and volume reductions of up to 1.2 %. The difference in sea ice area reaches a maximum in August whereas the difference in sea ice volume peaks in September. The delayed minimum in difference in volume compared to difference in extent is most likely a result of the higher sensitivity of sea ice concentration to atmospheric conditions compared to sea ice thickness. The

differences in both extent and volume evolve over an annual cycle, with minimum differences of −0.1 % and −0.2 % observed respectively between December and January for ice area and April and May for volume. The annual cycles correspond with periods of melting and freeze-up and are a product of the nature of the imposed FSD. Lateral melt rates are a function of floe size but freeze-up rates are not, and hence model differences only increase during periods of melting and not during periods of freeze-up.

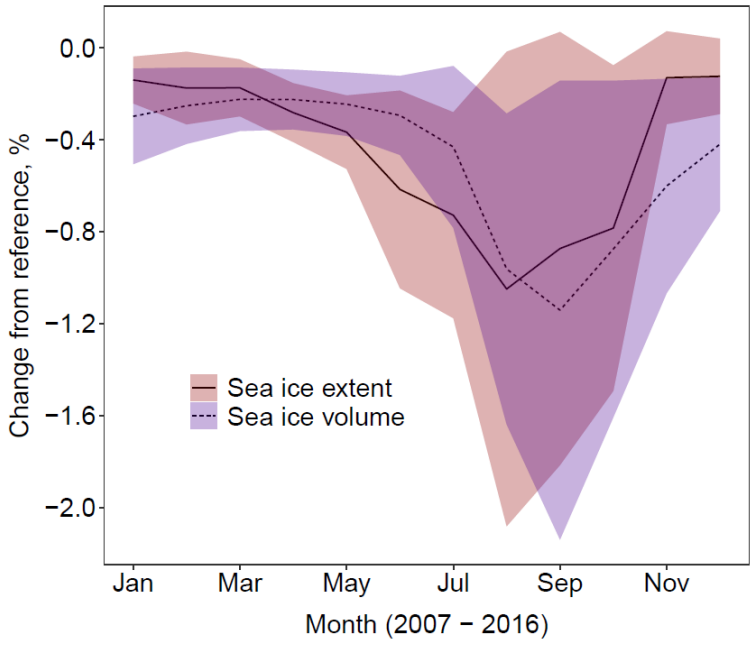

Figure 3.3: Difference in sea ice extent (solid, red ribbon) and volume (dashed, blue ribbon) between *stan-fsd* relative to *ref* (using a constant floe size) averaged over 2007–2016. The ribbon shows, in each case, the region spanned by the mean value plus or minus 2 times the standard deviation for each metric. This gives a measure of the interannual variability over the 10-year period. The mean behaviour is a reduction in the sea ice extent and volume, with losses of up to 1 % and 1.2 % respectively seen in September during the period of minimum sea ice. The interannual variability shows that the impact of the WIPoFSD model with standard parameters varies significantly between years, with some years potentially showing negligible change in extent and volume and others showing a maximum reduction of over 2 %.

The difference in sea ice extent in Fig. 3.3 decreases rapidly during the freeze-up conditions; this is a consequence of the fact this lateral freeze-up behaviour is predominantly driven by ocean surface properties, which are strongly coupled to atmospheric conditions in areas of low sea ice extent. In comparison, whilst atmospheric conditions initiate the vertical sea ice growth, this atmosphere–ocean coupling is rapidly lost due to insulation of the warmer ocean from the cooler atmosphere once sea ice extends across the ice-ocean interface. Hence a residual

difference in sea ice thickness and therefore volume propagates throughout the winter season. The interannual variability shows that the impact of the WIPoFSD model with standard parameters varies significantly depending on the year. In some years the difference between the *stan-fsd* and *ref* set-ups can be negligible, and in other years it can be up to 2 %. The span of twice the standard deviation from the mean presented in Fig. 3.3 will be a combination of both the standard variability around the mean difference and any trends in the difference between *stan-fsd and ref* over the 10-year period. The 10-year period was selected as representative of present climatology and is sufficiently short that the divergence between *stan-fsd* and *ref* over this period will be small to moderate, however results presented in chapter 8 comparing similar model setups will demonstrate that there will be a non-negligible trend in the difference over this period. The same considerations regarding trends over the period of analysis also applies to other results in this chapter where the standard deviation of some metric over the 10-year period has been calculated.

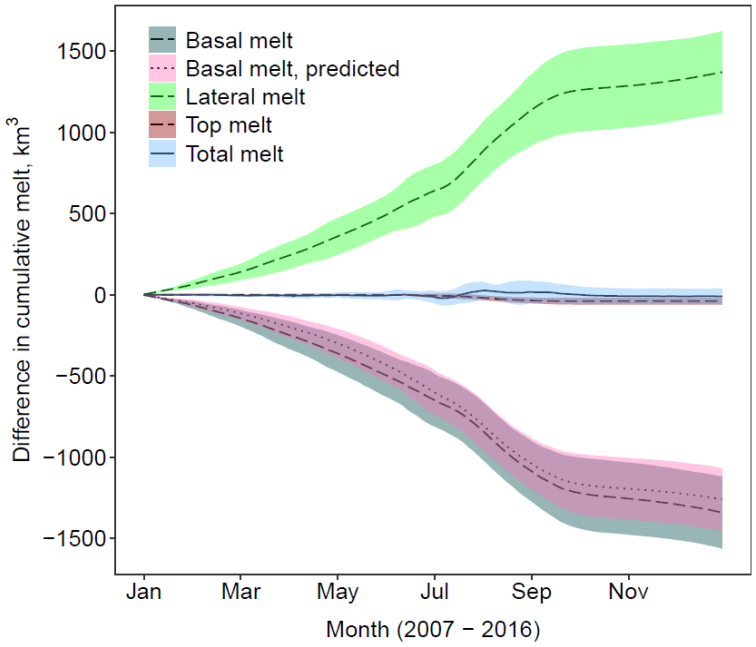

Figure 3.4: Difference in the cumulative lateral (green ribbon, dashed), basal (grey ribbon, dashed), top (red ribbon, dashed), and total (blue ribbon, solid) melts averaged over 2007–2016 between *stan-fsd* and *ref*. The ribbon shows, in each case, the region spanned by the mean value plus or minus 2 times the standard deviation for each metric. A large increase is observed in the total lateral melt; however this is mostly compensated by a reduction in the basal melt, leading to a negligible change in total melt. A small reduction in top melt can be seen. The predicted difference in basal melt is also shown on the plot (pink ribbon, dotted); this shows the expected change in basal melt accounting only for the reduction in sea ice concentration at grid cell scale from *ref* to *stan-fsd*.

Figure 3.4 shows the absolute difference in the mean cumulative annual melt components between the two simulations. The plot shows lateral, basal, top, and total melt (as defined in Sect. 3.2.1). A large increase of 107% can be seen in the lateral melt relative to *ref*; however, the change in total melt is negligible (less than a 0.1% increase relative to *ref*). This is because the lateral melt increase is largely compensated by a reduction in basal melt. The top melt also shows a negligible change. Figure 3.4 also shows the change in basal melt in *stan-fsd* only accounting for the loss of basal surface area available for melting. To explain how this is calculated, imagine for a given time step the sea ice fraction for that grid cell in the *stan-fsd* simulation is 0.81 and in the *ref* simulation it is 0.90. If this physical reduction is the only factor causing changes to the total basal melt, then the basal melt rate per unit grid cell area would also reduce by the same factor of 10 % from *ref* to *stan-fsd*. The reduction in the total basal melt volume can then be calculated for this grid cell accounting only for the reduction in sea ice fraction as the product of 0.1, the basal melt rate per unit grid cell area, and the area of the grid cell. This process can be repeated over every grid cell to obtain the total reduction in basal melt volume accounting only for reduction in sea ice concentration. The agreement (to within 1 standard deviation) between this synthetic reduction in basal melt and the actual reduction in basal melt suggests that the loss of ice area by lateral melt is sufficient to explain most of the basal melt compensation effect.

Figure 3.5 shows the spatial distribution for the predicted reduction in basal melt from *stan-fsd* to *ref*, the actual reduction in basal melt, and the difference between the actual reduction and predicted reduction in basal melt. These map plots are presented as monthly averages for March, June, and September averaged over 2007–2016. Figure 3.5 shows that the predicted basal melt can capture the regional distribution of the changes in basal melt from *ref* to *stan-fsd*, not just the area-integrated quantity.

Figure 3.6 explores the spatial distribution in the changes in ice extent and volume for 3 months over the melting season, March, June, and September. Data are shown only for regions where the sea ice cover exceeds 5 % of the total grid cell. These results show the differences increase in magnitude through the melting season. Although the pan-Arctic differences in extent and volume are marginal, Fig. 3.6 shows distinct regional variations in sea ice area and thickness metrics. Reductions in the sea ice concentration and thickness are seen both within and beyond the MIZ with reductions of up to 0.1 and 50 cm observed respectively in September. Within the pack ice,

increases in the sea ice concentration of up to 0.05 and ice thickness of up to 10 cm can be seen. In September the biggest increases in thickness are directed along the North American coast, particularly within the Beaufort Sea.

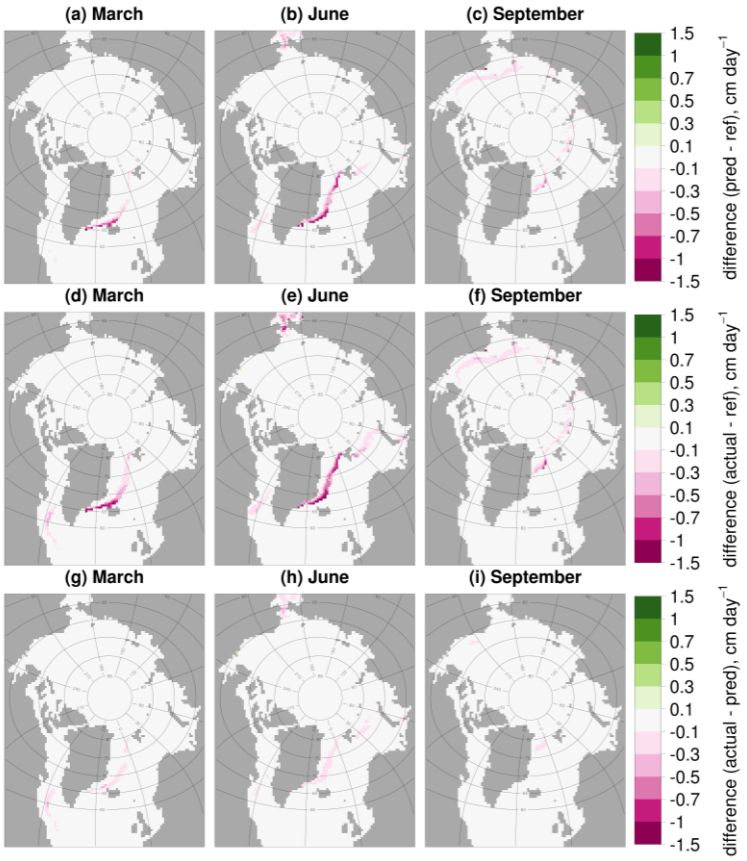

Figure 3.5: Predicted reduction in basal melt rate from *stan-fsd* to *ref* (a–c), actual reduction in basal melt rate from *stan-fsd* to *ref* (d–f), and difference between the actual reduction and predicted reduction in basal melt rate (g–i) averaged over 2007–2016. Results are presented for March (a, d, g), June (b, e, h), and September (c, f, i). Values are shown only in locations where the sea ice concentration exceeds 5 %. The predicted reduction in basal melt rate refers to the expected reduction if the change in sea ice area fraction is the only factor driving the change in basal melt rate. This is calculated by multiplying the basal melt rate for *ref* by the relative percent change in ice area fraction from *ref* to *stan-fsd* for each grid cell.

To understand the non-uniform spatial impacts of the FSD, it is useful to look at the behaviour of l_{eff}. Regions with an l_{eff} greater than 300 m will experience less lateral melt than the equivalent location in *ref* (all other things being equal), whereas locations with an l_{eff} below 300 m will experience more lateral melt. The distribution of l_{eff} is shown in Fig. 3.6 where in general we see a transition from larger floes to smaller floes moving from the pack ice into the MIZ, with the transition to an l_{eff} of a size less than 300 m observed within the MIZ. Most of the sea ice area must therefore experience

less lateral melting compared to *ref*. This result shows that the increase in lateral melt observed in Fig. 3.4 is localised to regions where the sea ice concentration is around 50 % or below. Note that where $l_{var} = d_{max} = 30\ km$, $l_{eff} \approx 550\ m$, which is why Fig. 3.6 shows that l_{eff} is generally between $500\ m$ – $600\ m$ within the pack ice.

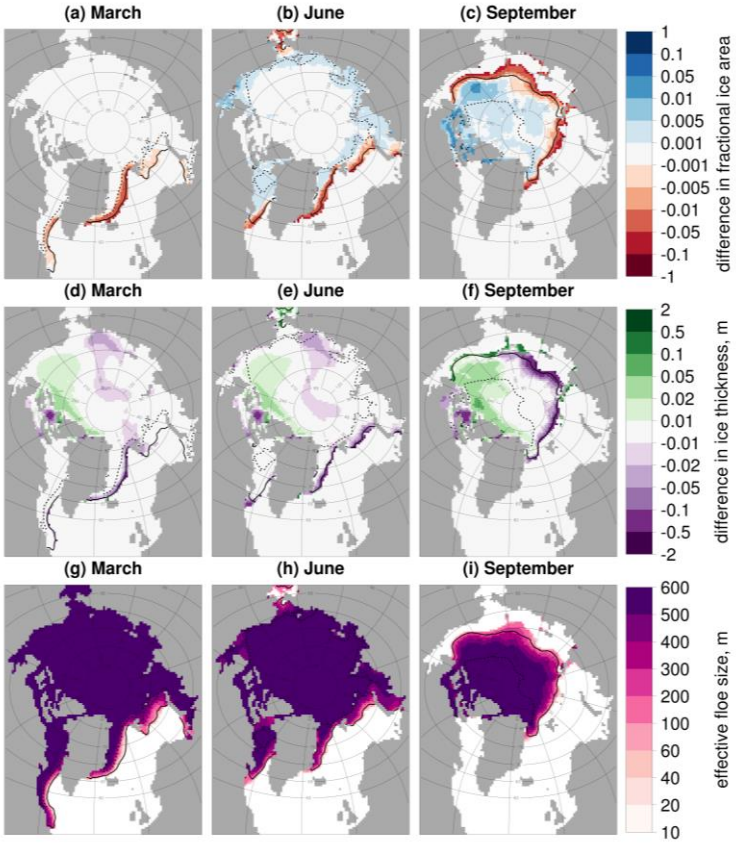

Figure 3.6: Difference in the sea ice concentration (a–c) and ice thickness (d–f) between *stan-fsd* and *ref* and l_{eff} (g–i) for *stan-fsd* averaged over 2007–2016. Results are presented for March (a, d, g), June (b, e, h), and September (c, f, i). Values are shown only in locations where the sea ice concentration exceeds 5 %. The inner (dashed black) and outer (solid black) extent of the MIZ averaged over the same period is also shown. In general, the plots show an increase in the sea ice concentration and thickness in the pack ice, but a reduction in the MIZ. This corresponds to the behaviour of the l_{eff}, with increases in regions where the l_{eff} is above 300 m and reductions where it is below 300 m.

3.4.2 Exploration of the parameter space

It has been previously discussed that the floe size parameters used within the WIPoFSD model are poorly constrained by observations. In this section experiments are performed using different permutations of these parameters to assess model sensitivity to the form of the FSD. It is valuable to consider how changes to each FSD parameter are likely to impact the distribution: increasing the magnitude of α increases

the number of small floes in the distribution and reduces the number of larger floes; increasing d_{min} removes smaller floes from the distribution entirely, increasing the number of floes across the rest of the distribution; increasing d_{max} adds larger floes to the distribution, reducing the number of floes across the rest of the distribution.

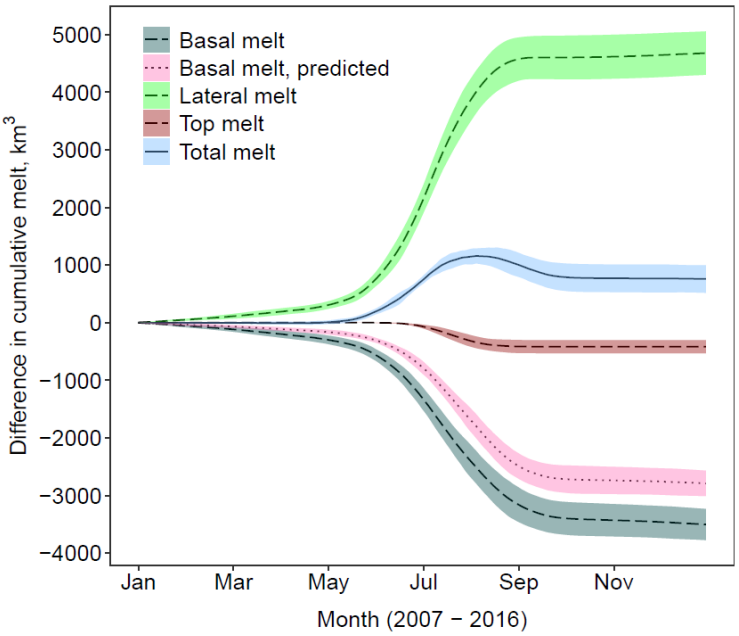

Figure 3.7: As Fig. 3.4 but the difference between (A) compared to *stan-fsd* where α is -2.5 for *stan-fsd* and -3.5 for (A) with $d_{max} = 30\ km$ and $d_{min} = 10\ m$ for both. A large increase in lateral melt is partly compensated by a reduction in basal melt; however this time a large increase is seen in the total melt.

For the first study the α is changed from -2.5 to -3.5, previously identified as the most extreme value within a reasonable observed range for the power-law exponent. This simulation will be referred to as (A). Figure 3.7 is analogous to Fig. 3.4, comparing the component and total melt evolution for an FSD with an $\alpha = -3.5$ compared to one with an $\alpha = -2.5$ (with d_{min} and d_{max} set to standard values). The plot shows an increase in the cumulative lateral melt, as seen before for *stan-fsd* compared to *ref*. Now, however, the basal melt is less effective at compensating the lateral melt, resulting in a significant increase in the total melt. There is also now a non-negligible reduction in the top melt, with the interannual variability showing the increase in total melt and reduction in top melt are consistently produced for each year of the simulations. The difference in cumulative total melt reaches a maximum in August and subsequently decreases slightly. This suggests that increasing the magnitude of α results in an earlier melting season and a correspondingly reduced melt in the late season. The predicted change in basal melt based on the reduced sea ice area is again plotted and is able to account

for 90 % of the actual reduction in basal melt. This is in contrast to Fig. 3.4, where the predicted reduction in basal melt was too high compared to the simulated reduction. The interannual variability shows that this underprediction of the reduction in basal melt is consistent throughout individual years. This implies the presence of additional mechanisms such as albedo and other mixed-layer feedbacks causing non-negligible changes in the basal melt rate; however reduction in the sea ice concentration remains the leading-order impact.

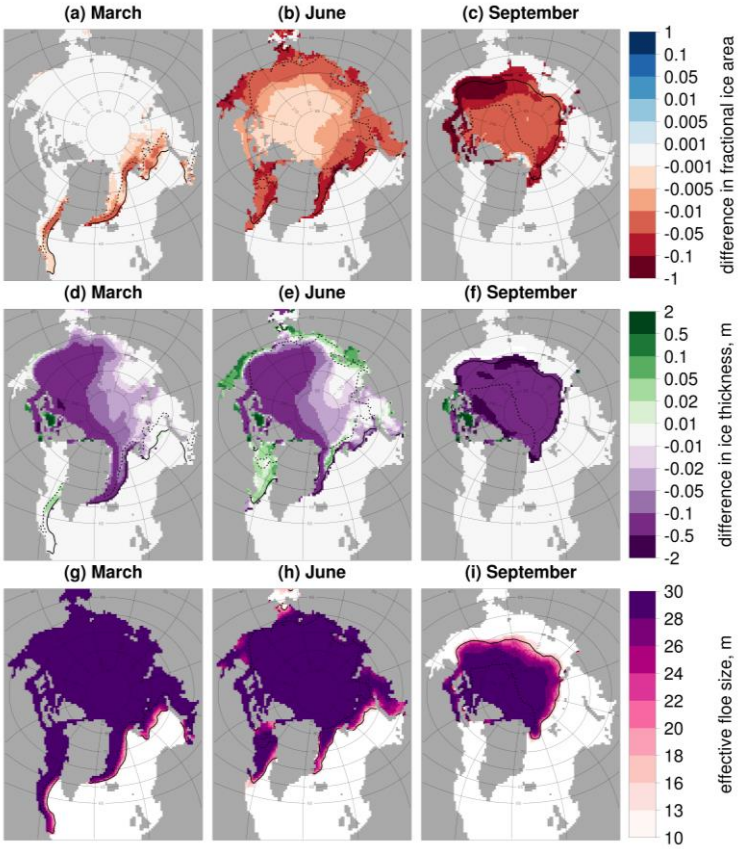

Figure 3.8: As Fig. 3.6 except now the difference between (A) compared to *stan-fsd* is given where α is -2.5 for *stan-fsd* and -3.5 for (A) with $d_{max} = 30\ km$ and $d_{min} = 10\ m$ for both. l_{eff} is reported for the simulation with the higher magnitude α. In general, the plots show a reduction in the sea ice concentration and ice thickness across the sea ice cover. This corresponds to the behaviour of the l_{eff}, with the l_{eff} 30 m or below across the sea ice cover.

Figure 3.8 shows difference map plots between the two simulations. The ice area and thickness are reduced across the sea ice cover with reductions of over 5 % and 0.5 m respectively seen in particular locations during September. However, even in March, after the freeze-up period, reductions of 0.1 m or more in sea ice thickness can be seen within the ice pack. The response of sea ice can once again be understood through the behaviour of the l_{eff}. l_{eff} is below 30 m across the entire ice cover throughout all 3

months studied, leading to increased lateral melt rates across the sea ice. The only notable exception to this overall behaviour is in the Canadian Arctic Archipelago, where the sea ice thickness for *(A)* increases compared to *stan-fsd* in some parts of this region even though the rest of the sea ice cover shows large reductions in sea ice thickness. These regions where an increase in thickness is seen are already associated with some of the thickest ice simulated by CICE, regularly exceeding 7 m in some locations even in the late melt season. Results from the *ref* simulations shows that these locations also have the highest sea ice concentrations in September when the sea ice reaches its minimum extent, and therefore it is not necessarily surprising to find a different response here compared to the rest of the sea cover. A plausible mechanism is that in these locations the non-negligible feedback of increased lateral melt in reducing the basal melt rate per unit sea ice area, as shown in Fig. 3.7 by the higher reduction in basal melt compared to the predicted reduction, has a net effect of increasing the mean ice thickness. In addition, these locations are more isolated from the rest of the sea ice cover due to their location within the Canadian Arctic Archipelago and therefore localised effects become more important compared to advection of sea ice and corresponding properties from other regions.

A further 17 sensitivity studies using different permutations of the parameters have been completed. These are formed by varying the three key defining parameters of the FSD shown in Fig. 3.1 in order to span the range of values reported in observational studies: for α values of -2, -2.5, -3, and -3.5 to span the general range of values reported in observations (Stern et al., 2018a); for d_{min} values of 1, 20, and 50 m are selected. These have been selected to reflect the different behaviours reported in studies, with some showing power-law behaviour extending to 1 m (Toyota et al., 2006) and others showing a tailing off at an order of tens of metres (Stern et al., 2018b). A further limitation for d_{min} is the smallest floe size where individual floes can be distinguished i.e. the transition from a floe regime to a brash ice regime. For the upper cut-off, d_{max}, values of 1000, 10 000, 30 000, and 50 000 m are selected, again to represent the distributions reported in different studies. The largest value is taken as 50 km for d_{max} as this serves as an upper limit to what can be resolved within an individual grid cell on a CICE 1° grid. In addition, this model does not account for processes that are expected to be important for the evolution of floes at the kilometre scale and above, such as wind stresses and melt ponds (Arntsen et al., 2015; Wilchinsky et al., 2010).

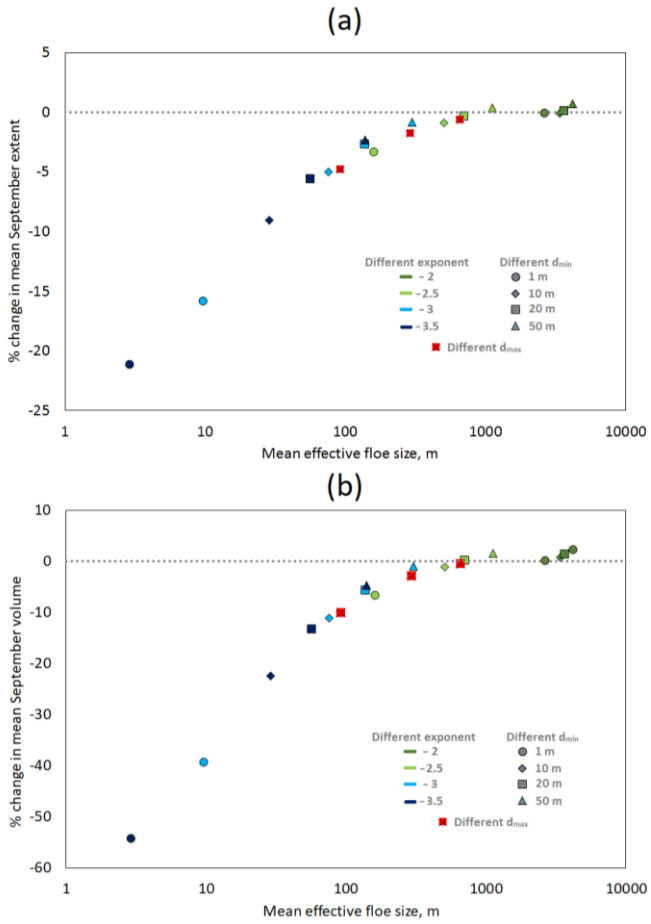

Figure 3.9: Relative change (%) in mean September sea ice extent (a) and volume (b) from 2007 to 2016 respectively, plotted against mean l_{eff} for simulations with different selections of parameters relative to *ref*. The mean l_{eff} is taken as the equally weighted average across all grid cells where the sea ice concentration exceeds 15 %. The colour of the marker indicates the value of the α, the shape indicates the value of d_{min}, and the three experiments using standard parameters but different d_{max} (1000, 10 000, and 50 000 m) are indicated by a crossed red square. The parameters are selected to be representative of a parameter space for the WIPoFSD that has been constrained by observations. Model response ranges from small increases in the sea ice extent and volume to reductions of over 20 % and 50 % respectively. The mean l_{eff} is shown to be a good predictor of the response of the sea ice extent and volume. The mean l_{eff} is calculated as equally weighted across grid cells rather than weighted by ice area because the aim here is to have a representative mean value of l_{eff} for the entire sea ice cover, whereas an area-weighted average will push the mean l_{eff} towards the behaviour in regions of high sea ice concentration i.e. the pack ice.

A total of 14 of the 17 permutations for these sensitivity studies are generated by selecting all the different α – d_{min} permutations (except the two already investigated). Each of these simulations has $d_{max} = 30{,}000\ m$. The further three simulations vary d_{max} with the α and d_{min} fixed to -2.5 and 10 m respectively. Figure 3.9 shows the change in mean September sea ice extent and volume relative to *ref* plotted against

mean annual l_{eff}, averaged over the sea ice extent. The impacts range from a small increase in extent and volume to large reductions of −22 % and −55 % respectively, even within the parameter space defined by observations. Furthermore, there is almost a one-to-one mapping between mean l_{eff} and extent and volume reduction. This suggests l_{eff} is a useful diagnostic tool to predict the impact of a given set of floe size parameters. The system varies most in response to the changes in the α, but it is also particularly sensitive to d_{min}.

It is possible to explain the relationship between the percentage change in mean September volume and l_{eff} shown in Fig. 3.9 by multiplying both sides of Eq. (3.12) by dt and evaluating the resulting integrals, assuming fixed values of l_{eff} and w_{lat}. The relative difference in sea ice area after lateral melting for a given fixed value of l_{eff} compared to the reference case can be shown to take the form $c_1 e^{-\frac{c_2}{l_{eff}}} - c_3$ where c_1, c_2, and c_3 are all functions of w_{lat} and Δt with positive values. This expression describes a similar relationship to those plotted in Fig. 3.9 between l_{eff} and the relative change in both the mean September extent and volume compared to *ref*. The assumption that l_{eff} and w_{lat} are constant will only be valid for short timescales, but nevertheless the expression described above is still able to explain the general form of the results shown in Fig. 3.9, providing a physical explanation for these results.

3.4.3 Sensitivity runs to explore specific model components and additional relevant parameters

A series of sensitivity studies have been performed to explore the behaviour of the WIPoFSD model and understand how it interacts with other model components. Table 3.1 defines the important parameters considered in this section and Table 3.2 provides a summary of the sensitivity experiments performed. It should be noted that the sensitivity studies described in this section would more formally be described as a propagation of typical uncertainty, since parameters are varied based on an estimate of their uncertainty rather than varying each by the same relative magnitude to produce a measure of relative sensitivity for each. The first two entries in Table 3.2, *stan-fsd* and *ref*, refer to a standard set-up using the standard FSD parameters described above and a constant floe size of 300 m respectively. Studies (A)–(C) are a selection of the simulations described in Sect. 3.4.2 to allow a comparison between model sensitivity to the parameters that define the FSD and model sensitivity to other relevant parameters

and components within the WIPoFSD model. In the following section a bracketed letter will follow descriptions of sensitivity studies, which correspond to the letter assigned in Table 3.2.

Table 3.3 reports key metrics for the sensitivity studies described in Table 3.2, plus a selection of the different sensitivity studies described in Sect. 3.4.2. For each experiment the September sea ice extent and volume size are reported for both the full sea ice extent and MIZ only (taken as a mean between 2007 and 2016), with the MIZ defined here as regions with between 15 % and 80 % sea ice cover. In addition, the mean cumulative lateral, basal, top, and total melts until September are reported in each case, and the September mean l_{eff} and mean sea ice perimeter per square metre of ocean area are both reported averaged over the MIZ. For each value reported (except for the l_{eff}) the difference from *stan-fsd* is also stated. Cells highlighted in italic and bold font deviate by 1 and 2 standard deviation(s) respectively from the *stan-fsd* mean (the standard deviation is calculated from the 10 annual values for each metric).

Variable	Description
d_{min}	Lower floe size cut-off within the WIPoFSD model. Standard value of 10 m.
d_{max}	Upper floe size cut-off within the WIPoFSD model. Standard value of 30000 m.
l_{var}	Variable FSD tracer. Allowed to vary between d_{min} and d_{max}.
α	Power law exponent within the WIPoFSD model. Standard value fixed at -2.5.
l_{eff}	The effective floe size is defined as the floe size of a distribution of identical floes that would produce the same lateral melt rate in a given instant to a distribution of non-uniform floes, when under the same conditions with the same total ice cover. See Eq. (3.15).
α_{dim}	The dimensional attenuation coefficient, as used in Eq. (3.6).
P_{crit}	The critical probability that must be exceeded for wave breaking events to occur, as used in Eq. (3.7).
T_{rel}	The floe restoring rate, as used in Eq. (3.19). Set to 10 as default.
α_{shape}	Floe shape parameter to account for the deviation of floes from a perfect circle. Standard value of 0.66 (Rothrock and Thorndike, 1984).
w_{lat}	Lateral melt rate, as calculated within Eq. (3.2).
m_1	Melt rate parameter, as used in Eq. (3.2) to calculate the lateral melt rate w_{lat}. Default value of 1.6 x 10^{-6} $m\,s^{-1}K^{-m_2}$ (Perovich, 1983).
m_2	Melt rate parameter, as used in Eq. (3.2) to calculate the lateral melt rate w_{lat}. Default value of 1.36 (Perovich, 1983).

Table 3.1: Definitions of the parameters relating to the sensitivity studies described in Table 3.2.

Sensitivity study	Description	Technical details
stan-fsd	CICE-ML with standard FSD	$d_{min} = 10\ m, d_{max} = 30{,}000\ m, \alpha = -2.5$
Ref	CICE-ML with constant floe size	Floe size of 300 m for all floes
(A)	Low α	$d_{min} = 10\ m, d_{max} = 30{,}000\ m, \alpha = -3.5$
(B)	Minimum l_{eff}	$d_{min} = 1\ m, d_{max} = 30{,}000\ m, \alpha = -3.5$ This is the selection of FSD parameters that produces the lowest average l_{eff}.
(C)	Maximum l_{eff}	$d_{min} = 50\ m, d_{max} = 30{,}000\ m, \alpha = -2$ This is the selection of FSD parameters that produces the highest average l_{eff}.
(D)	α evolves over a fixed annual cycle	An annual cycle, as described by Eq. (3.20), is imposed on the exponent based on the observations of Stern et al. (2018 a). The exponent does not vary spatially.
(E)	α as a function of local ice concentration	The exponent becomes a function of the local sea ice concentration (i.e. fractional sea ice area) according to Eq. (3.21).
(F)	Waves no longer break-up floes	The waves-in-ice module operates normally, however Eq. (3.18) is no longer applied after a floe break-up event is identified.
(G)	No lateral melt feedback on floe size	The model operates normally, however l_{var} is no longer reduced based on the amount of lateral melt i.e. Eq. (3.17) is removed from the model.
(H)	Big waves	The significant wave heights read into the model from ERA-interim data at ice free locations is increased by a factor of 10.
(I)	Weak ice	P_{crit} is reduced by a factor of 10.
(J)	Weaker wave attenuation	α_{dim} is reduced by a factor of 10.
(K)	Reduced floe growth rates	T_{rel} is increased from 10 to 365.
(L)	Less circular floes	α_{shape} is reduced from 0.66 to 0.44.
(M)	Perfectly circular floes	α_{shape} is increased from 0.66 to 0.79. This is the approximate value of this parameter for a perfect circle.
(N)	Reduced lateral melt rate	The parameters m_1 and m_2 are reduced by 10 % each to 1.44 x 10^{-6} $m\ s^{-1}K^{-m_2}$ and 1.22 respectively.
(O)	Increased lateral melt rate	The parameters m_1 and m_2 are increased by 10 % each to 1.76 x 10^{-6} $m\ s^{-1}K^{-m_2}$ and 1.48 respectively.
(P)	Shallow mixed layer	The minimum mixed layer depth is reduced from 10 m to 7 m.
(Q)	Deep mixed layer	The minimum mixed layer depth is increased from 10 m to 20 m.

Table 3.2: The details of the sensitivity studies to explore the behaviour of the CICE–ML–WIPoFSD model. Parameters discussed here defined in Table 3.1.

Study	Description	Metrics (reported as mean September value between 2007 – 2016, parentheses give change from reference)									
		Area metrics, 10^6 km^2		Volume, 10^3 km^3		Mean MIZ l_{eff}, m	Mean MIZ ice perimeter, m^{-1}	Annual cumulative melt by end of September, 10^3 km^3			
		Extent	MIZ	Total	MIZ			Top	Basal	Lateral	Total
stan-fsd	CICE-ML with standard FSD	4.70 (0)	2.54 (0)	7.72 (0)	2.07 (0)	453.9	0.0070	5.21 (0)	14.58 (0)	2.43 (0)	22.22 (0)
ref	CICE-ML with constant floe size	4.74 (0.04)	2.61 (0.06)	7.81 (0.09)	2.12 (0.05)	**300**	***0.0081***	5.25 (0.04)	15.79 (1.22)	1.17 (-1.26)	22.21 (-0.01)
(A)	Low α	**4.31 (-0.39)**	2.55 (0.01)	***6.06 (-1.67)***	1.75 (-0.32)	**27.7**	**0.0862**	4.79 (-0.42)	**11.19 (-3.39)**	**7.03 (4.60)**	23.01 (0.79)
(B)	Minimum l_{eff}	**3.76 (-0.96)**	2.75 (0.21)	**3.56 (-4.16)**	**1.18 (-0.90)**	**2.7**	**0.8151**	***3.60 (-1.60)***	**4.34 (-10.23)**	**16.56 (14.13)**	24.50 (2.28)
(C)	Maximum l_{eff}	4.77 (0.07)	2.58 (0.04)	7.98 (0.26)	2.14 (0.07)	**3656.3**	**0.0023**	5.27 (0.06)	15.54 (0.96)	**1.30 (-1.13)**	22.11 (-0.11)
(D)	α evolves over fixed annual cycle	4.69 (-0.01)	2.53 (-0.01)	7.70 (-0.02)	2.06 (-0.01)	**162.9**	**0.0161**	5.23 (0.02)	14.68 (0.11)	2.31 (-0.12)	22.22 (0.00)
(E)	α is a function of ice concentration	4.55 (-0.15)	2.39 (-0.15)	7.34 (-0.38)	1.85 (-0.22)	**580.6**	**0.0184**	5.13 (-0.07)	13.46 (-1.11)	**3.75 (1.32)**	22.34 (0.12)
(F)	Waves no longer break-up floes	4.78 (0.08)	2.62 (0.08)	7.93 (0.21)	2.15 (0.08)	**531.8**	**0.0045**	5.27 (0.06)	15.95 (1.37)	**0.93 (-1.50)**	22.15 (-0.07)
(G)	No lateral melt feedback on floe size	4.70 (0.01)	2.55 (0.01)	7.75 (0.03)	2.08 (0.01)	465.3	0.0068	5.21 (0.01)	14.69 (0.12)	2.30 (-0.13)	22.20 (-0.02)
(H)	Big waves	4.60 (-0.10)	2.44 (-0.10)	7.47 (-0.26)	1.94 (-0.14)	**299.8**	**0.0212**	5.16 (-0.05)	13.62 (-0.96)	**3.53 (1.10)**	22.31 (0.09)
(I)	Weak ice	4.66 (-0.04)	2.51 (-0.04)	7.65 (-0.08)	2.03 (-0.04)	***412.4***	**0.0095**	5.19 (-0.02)	14.26 (-0.32)	***2.79 (0.36)***	22.24 (0.02)
(J)	Weaker wave attenuation	4.57 (-0.17)	2.42 (-0.12)	7.40 (-0.33)	1.90 (-0.18)	**236.6**	**0.0328**	5.15 (-0.05)	13.42 (-1.16)	**3.76 (1.34)**	22.33 (0.11)
(K)	Reduced floe growth rates	4.68 (-0.02)	2.54 (0.00)	7.67 (-0.05)	2.06 (-0.01)	**372.9**	**0.0100**	5.18 (-0.03)	14.40 (-0.18)	***2.67 (0.24)***	22.25 (0.03)
(L)	Less circular floes	4.64 (-0.05)	2.50 (-0.04)	7.56 (-0.16)	2.01 (-0.06)	**442.2**	**0.0109**	5.17 (-0.03)	14.04 (-0.53)	**3.05 (0.63)**	22.26 (0.04)
(M)	Perfectly circular floes	4.72 (0.02)	2.56 (0.02)	7.79 (0.07)	2.11 (0.03)	459.1	0.0058	5.22 (0.02)	14.92 (0.34)	***2.05 (-0.38)***	22.19 (-0.03)
(N)	Reduced lateral melt rate	4.71 (0.01)	2.56 (0.01)	7.74 (0.02)	2.08 (0.01)	**456.3**	0.0069	5.22 (0.01)	14.77 (0.19)	***2.23 (-0.20)***	22.21 (-0.01)
(O)	Increased lateral melt rate	4.69 (-0.01)	2.53 (-0.01)	7.70 (-0.02)	2.06 (-0.01)	451.5	0.0071	5.20 (-0.01)	14.41 (-0.17)	2.61 (0.18)	22.22 (0.00)
(P)	Shallow mixed layer	4.70 (0.01)	2.57 (0.03)	7.84 (0.12)	2.14 (0.07)	**447.4**	0.0067	5.19 (-0.02)	14.56 (-0.01)	2.46 (0.03)	22.21 (-0.01)
(Q)	Deep mixed layer	4.64 (-0.06)	2.65 (0.10)	7.62 (-0.11)	2.34 (0.27)	**473.6**	0.0071	5.26 (0.05)	14.57 (-0.01)	2.34 (-0.08)	22.17 (-0.05)

Table 3.3: A summary of the metrics for each of the sensitivity studies described in Table 3.2. Metrics are reported for sea ice extent, MIZ extent, total sea ice volume, MIZ volume, mean l_{eff} within the MIZ, mean sea ice perimeter per square metre of ocean area within the MIZ, and cumulative melt top, basal, lateral, and total melt. All metrics are reported for September, except the cumulative melt, which is reported for all months up to and including September and given as an average between 2007 and 2016. Means for l_{eff} and ice perimeter are taken as averages over the MIZ with each grid cell equally weighted. The values within the parentheses give the change from *stan-fsd*. Cells highlighted in italic and bold font deviate by 1 and 2 standard deviation(s) respectively from the *stan-fsd* mean value (the standard deviation is calculated from the set of 10 annual values for each metric).

(i) Imposing a variable exponent on the floe size distribution

The shape of the FSD between its limiting values is defined by α. Recent evidence suggests this may not be constant in time or space (Stern et al., 2018b). We have investigated the impact of this behaviour through the use of two alternative modelling approaches. The first approach imposes a sinusoidal annual cycle on α (D):

$$\alpha = -2.35 + 0.45 \cos \frac{2\pi(d - 100)}{d_{ann}}. \quad (3.22)$$

Here d refers to the current day of the year (for example 45 would refer to 14 February) and d_{ann} is the total number of days in the year (here taken to be 365). This curve was selected as a reasonable fit to the observations of Stern et al. (2018b), though it should be noted that these observations were taken from the Beaufort and Chukchi seas so should not be assumed to be representative of the entire Arctic Ocean.

The second sensitivity experiment assumes that α is a function of sea ice concentration, A (E). This is derived from the observation that α increases in magnitude as the melting season advances and in locations of lower sea ice concentration:

$$\alpha = -4 + 2.1A. \quad (3.23)$$

The limits were selected to try and capture the variability of the exponent seen within observations.

The results in Table 3.3 show imposing the time-varying α (D) has a very small impact on the sea ice cover, whereas the spatial-varying α (E) causes a moderate reduction in September ice extent and volume of about 3 % and 5 % respectively. It is worth noting that the mean l_{eff} over the MIZ does not correlate well with the size of the response in the mean September sea ice extent and volume in these cases compared to simulations with a fixed α, with l_{eff} being much higher than expected given the size of the sea ice extent and volume reduction. The value of the sea ice perimeter averaged over the MIZ is more consistent with the observed changes in sea ice extent and volume, particularly for experiment (E). This shows that it is useful to have multiple approaches to collapsing the FSD into a representative value. Whilst map plots of l_{eff}

can be very useful for understanding the regional impacts of an FSD, as in Fig. 3.6, the mean value can be misleading.

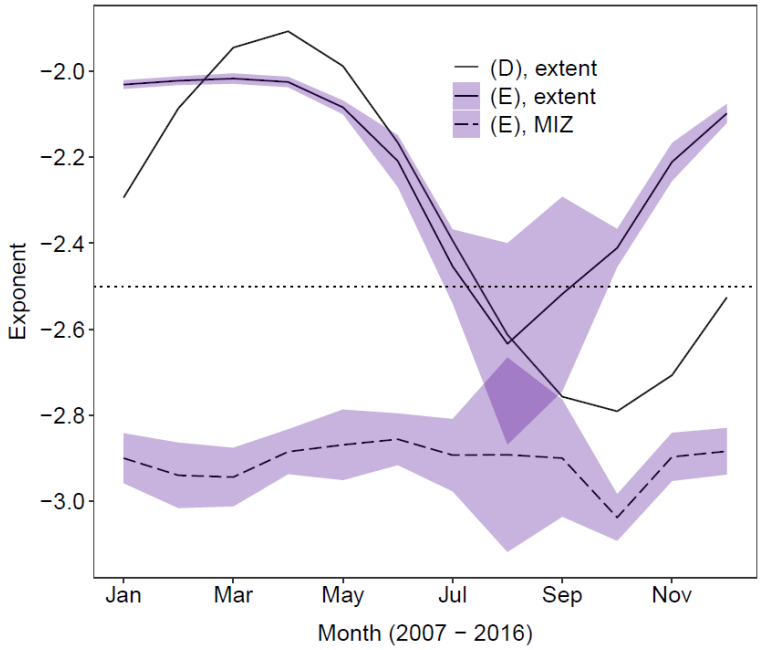

Figure 3.10: Annual variation in α averaged over 2007–2016 for two simulations with variable α. The plots show results for an α which varies depending on time through the year (D, no ribbon) or on the sea ice concentration (E, blue ribbon). Results are given as the mean α for the total sea ice extent (solid) and MIZ only (dashed). The mean α is taken as the equally weighted average across all grid cells where the sea ice concentration exceeds 5 % (total extent) or is between 15 % and 80 % (MIZ only). The imposed annual oscillation in α is identical for all grid cells for (D); hence the MIZ behaviour has not been plotted as it will be identical to the annual oscillation in α across the total sea ice extent. The ribbon shows, in each case, the region spanned by the mean value plus or minus 2 times the standard deviation. Both set-ups show an annual oscillation in the value of α averaged over the total sea ice extent. For experiment (E), no obvious annual trend in the mean value of α can be seen when averaged over the MIZ, though the interannual variation is at a maximum during the peak melting season between July and September.

Figures 3.10 and 3.11 show how α and the resultant l_{eff} respectively evolve in experiments (D) and (E) averaged over both the overall sea ice cover and the MIZ. The region spanned by twice the standard deviation of individual years within the simulation is also shown. Whilst l_{eff} in both regions behaves in corresponding ways for the simulation with a time-varying α (D), experiment (E) shows the mean α and hence l_{eff} within the MIZ are small and approximately constant throughout the year, despite the overall sea ice pack showing strong seasonal variability for these quantities. During the peak melting period between May and August the mean l_{eff} is lower for experiment (D) within the pack ice and experiment (E) within the MIZ. Given the much stronger

changes seen for experiment (E) compared to experiment (D) relative to *stan-fsd*, this supports previous findings that the impact of the WIPoFSD model is primarily dependent on the behaviour of the FSD within the MIZ. (D) shows the strongest interannual variation in l_{eff} between March and May, whereas for (E) it is strongest in the peak melting season between July and August. Figure 3.11 also includes the annual evolution of l_{eff} for the *stan-fsd* simulation. Unlike (D) and (E), *stan-fsd* shows no strong annual oscillation in the l_{eff} across the overall pack ice.

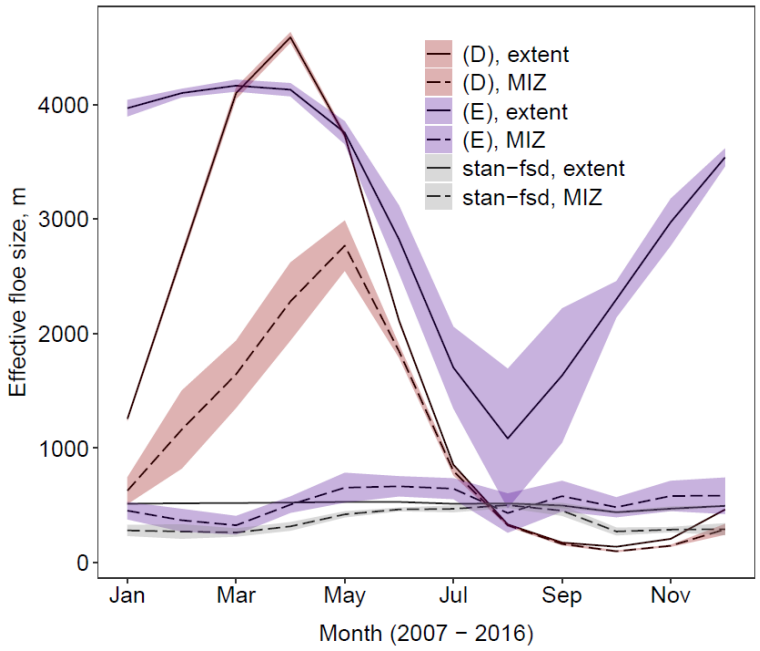

Figure 3.11: Annual variation in mean l_{eff} averaged over 2007–2016 for two simulations with variable α. The plots show the evolution of l_{eff} throughout the year for a simulation with a time-dependent α (D, red ribbon) or a sea-ice-concentration-dependent α (E, blue ribbon). Also shown is the behaviour of l_{eff} for a simulation with a fixed α of 2.5 (*stan-fsd*, grey ribbon). Results are shown for the total sea ice area (solid) and MIZ only (dashed). The mean l_{eff} is taken as the equally weighted average across all grid cells where the sea ice concentration exceeds 5 % (total extent) or is between 15 % and 80 % (MIZ only). The ribbon shows, in each case, the region spanned by the mean value plus or minus 2 times the standard deviation. The results show that introducing a variable α produces much larger intra-annual variations in l_{eff} across the overall sea ice extent than with a fixed α. (D) and (E) show an annual oscillation in the value of l_{eff} averaged over the total sea ice extent. Within the MIZ, only experiment (D) continues to show this strong variation in l_{eff}; (E) and *stan-fsd* show variations of around an order less. (D) shows the strongest interannual variation between March and May, whereas for (E) it is strongest in the peak melting season between July and August.

(ii) Other parameters affecting the floe size distribution

The two processes currently represented in the model that actively reduce l_{var} are lateral melting and wave-induced fragmentation of floes. Two simulations are undertaken where either waves are no longer able to influence l_{var} (F) or lateral melting is no longer allowed to influence l_{var} (G). An additional three simulations are performed to focus on how waves may be influencing sea ice via reductions in l_{var}: the incident significant wave height at the point of entering the sea ice cover is increased by a factor of 10 (H), the floe breaking strain is reduced by a factor of 10 (I), and the wave attenuation coefficients under the sea ice are reduced by a factor of 10 (J).

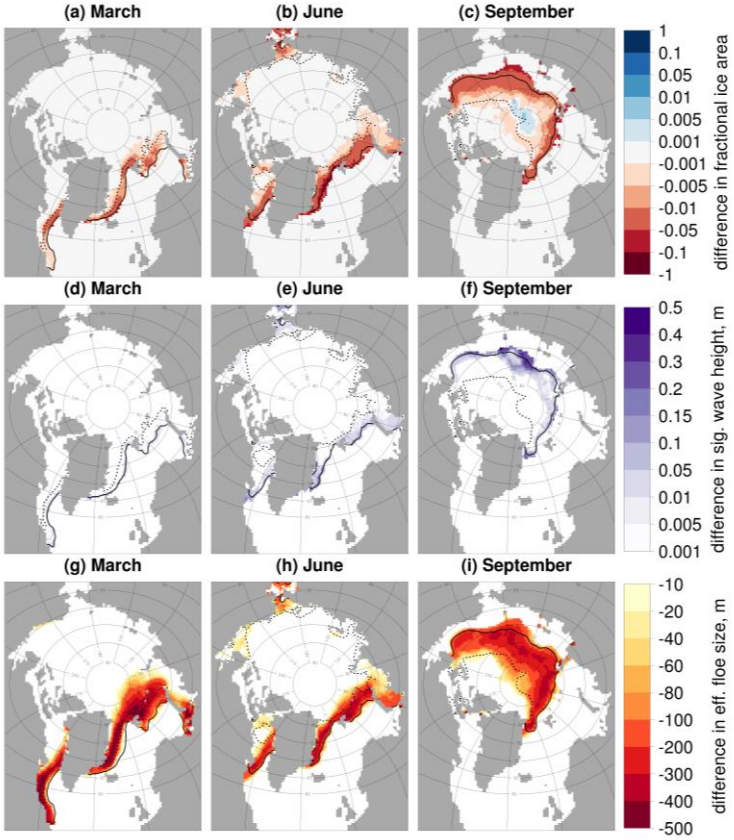

Figure 3.12: Difference in the sea ice concentration (a–c), significant wave height (d–f) and l_{eff} (g–i) for (J), with the wave attenuation rate reduced by 90 %, compared to *stan-fsd*, both using standard FSD parameters. Plots show results for March (a, d, g), June (b, e, h), and September (c, f, i) averaged over 2007–2016. Each plot shows the inner (dashed black) and outer (solid black) extent of the MIZ averaged over the same period. Values are shown only in locations where the sea ice concentration exceeds 5 %. The plots show that despite very small differences in the significant wave height, the reduced attenuation rate still drives reductions in l_{eff} and in consequence the sea ice concentration across the MIZ.

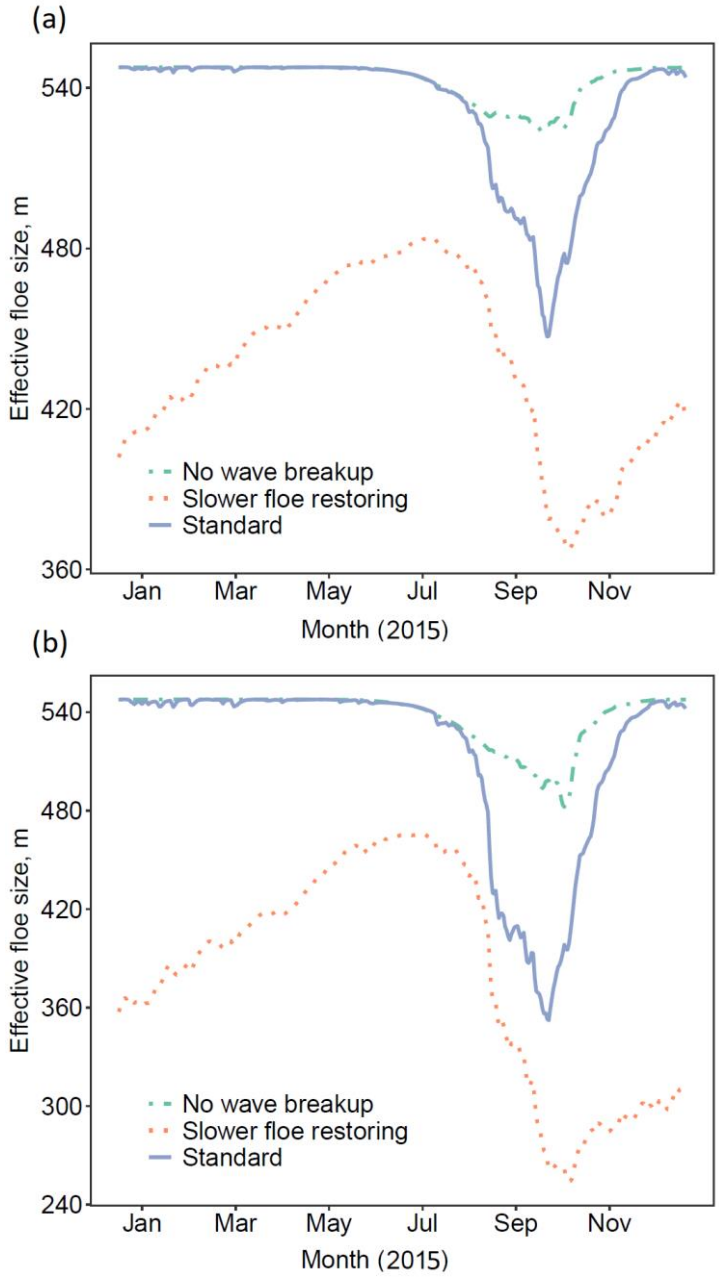

Figure 3.13: Daily variation in l_{eff} over 2015 averaged over (a) regions with between 15 % and 80 % sea ice concentration on 31 August 2015 and (b) regions with between 15 % and 30 % sea ice concentration on 31 August 2015. The three simulations demonstrate l_{eff} tendencies with respect to different processes. The plots show the evolution of l_{eff} throughout the year for the standard simulation (*stan-fsd*, blue solid), without wave break-up of floes (F, green dotted–dashed), and with a reduced floe size restoration rate in freezing conditions (K, orange dotted). Means for l_{eff} and ice perimeter are taken as averages over the selected grid cells with each grid cell equally weighted. The plots show that a strong seasonal cycle in l_{eff} can be observed, particularly in grid cells on the edge of the sea ice cover where waves are expected to have a particularly strong impact.

The results in Table 3.3 show that the wave–l_{var} interaction is more important than the lateral melt–l_{var} interaction in driving the increase in lateral melt observed by imposing the standard FSD. Study (F), where waves no longer reduce l_{var}, shows a 3 % increase in MIZ volume compared to *stan-fsd*, whereas study (G), where l_{var} does not change as a result of lateral melt, shows an increase in MIZ volume of less than 1 %. For the three simulations performed to explore the behaviour of the wave advection model, i.e. (H), (I), and (J), the strongest response is produced by reducing the wave attenuation rate of the model (J). The weakest response is produced by increasing the ice vulnerability to wave fracture (I). Figure 3.12 shows difference plots of sea ice concentration and l_{eff} between *stan-fsd* and (J), where the attenuation rate of waves under sea ice is reduced. The plots show a reduction in the sea ice concentration of around 1 % across the MIZ throughout the year for (J). This can be attributed to the reduction of l_{eff} in the same region by magnitudes of greater than 100 m.

The floe restoration rate is the parameter, T_{rel}, used in Eq. (3.21). As a standard it is set to 10 days; however this value is not well constrained. This effectively means that l_{var} is restored rapidly during freezing conditions, and hence the FSD is effectively initiated in each melting season with no memory of the previous year. There is not enough evidence available to either validate or invalidate the assumption that the FSD retains no memory of the previous melting or freeze-up season. An experiment (K) has been performed where T_{rel} is increased from 10 to 365 days to explore the impact of inter-seasonal memory retention within the FSD model. The results in Table 3.3 show that, whilst this change to the model did reduce the l_{eff} and increase the perimeter density metrics by significant amounts, it did not produce a significant change in either the melt components or sea ice extent and volume.

In Fig. 3.13 we show the evolution of simulations *stan-fsd*, (F), and (K) over 2015 averaged over selected grid cells. The year 2015 has been chosen as representative over the 2007–2016 period. There are two subplots: the first gives l_{eff} averaged over grid cells with a sea ice concentration within the MIZ on 31 August 2015, selected as the approximate date of the 2015 minimum sea ice extent in simulations. This set of grid cells is chosen to capture grid cells that are marginal for at least some of the year without also becoming ice-free, which would create an artificial seasonal cycle in l_{eff}. For the second subplot, the same set is further constrained to grid cells with between 15 % and 30 % sea ice concentration on 31 August 2015. Figure 3.6 shows that

significant reductions in l_{eff} are generally seen at the outer edge of the sea ice extent, so further restricting the maximum sea ice concentration in this way will capture this region. The significant reduction of l_{eff} by up to 140 m between (F) and *stan-fsd* in August and September shows that the wave break-up of floes is a significant component of both the floe size reduction and the subsequent reduction in sea ice concentration seen in Fig. 3.6 for these locations.

The difference between (F), i.e. the simulation without wave break-up of floes, and the maximum possible l_{eff} of just over 540 m during the melting season primarily captures the impact of lateral melting on floe size as floe restoration will not be active during this period. We see a reduction in l_{eff} of up to 60 m for (F) compared to the maximum value of l_{eff} when averaging over grid cells with 15 to 30 % sea ice concentration, so whilst not insignificant the impact is a factor of around 3–4 times lower than the wave fragmentation in these regions. This suggests that mechanical break-up of floes is a necessary precondition for the lateral melting feedback on floe size to become significant. This effect will not be as strong for other selections of FSD parameters, particular those where l_{eff} is below 50 m even when $l_{var} = d_{max}$. For these simulations we expect the much larger increase in lateral melt, as seen in Fig. 3.7, to produce a stronger lateral melt impact on the FSD. For (K), where l_{var} restoration rates during freezing conditions are reduced, l_{eff} is significantly lower throughout the year including during the melting season. l_{eff} varies between 360 and 480 m for the full MIZ grid cell selection, significantly reduced from the 450–540 m seen for the *stan-fsd* simulation. We also see a well-defined seasonal cycle, unlike with *stan-fsd*.

(iii) Lateral melt parameters

The first-order impact of introducing a variable floe size is on the lateral melt volume. Equation (3.1) shows the lateral melt volume is calculated from several parameters beyond just floe diameter, L, including lateral melt rate, w_{lat}, and floe shape, α_{shape}. α_{shape} is currently fixed to a constant value, 0.66. There has been significantly less interest in characterising how the shape of floes varies and to characterise a floe shape distribution, particularly given available evidence suggesting floe size and shape may be uncorrelated parameters (Gherardi and Lagomarsino, 2015). Two sensitivity studies are performed: one with α_{shape} reduced to 0.44 (L), corresponding to $3{:}1$ rectangular floes or similar distortions from a perfect circle, and one with α_{shape} increased to 0.79,

corresponding to approximately circular floes (M). w_{lat} is a function of two parameters, m_1 and m_2 (see Eq. 3.2). These parameters have been estimated from observations and hence are subject to uncertainty. Experiments are undertaken with either both m_1 and m_2 reduced by 10 % (N) or both increased by 10 % (O). A reduction in these parameters reduces the lateral melt rate and an increase increases it.

Table 3.3 shows that all four of these sensitivity studies did not produce a large model response in terms of the overall sea ice extent and volume. Reducing the floe shape parameter (L) produced the strongest response in the lateral melt volume, and more generally the model metrics were more sensitive to α_{shape} than the melt coefficients, m_1 and m_2. The much stronger model sensitivity to the floe size parameters justifies the focus on floe size as the main uncertainty in lateral melt volume calculation.

(iv) Minimum mixed layer depth

The minimum ocean mixed-layer depth is a constant within the prognostic mixed-layer model required to prevent the mixed-layer depths reaching unrealistically small values. As a standard it is set to 10 m. The depth of the mixed layer is important for the strength of mixed-layer feedbacks, with a deeper mixed layer acting to damp any feedbacks via mixed-layer properties. These feedbacks include the albedo feedback mechanism and the negative feedback of increased lateral and basal melts (meltwater perturbs the mixed-layer properties towards less favourable melting conditions). To understand the damping effect of increasing the depth of the mixed layer, consider a fixed input of heat energy to the mixed layer. The increase in temperature for a deeper mixed layer in response to this heat energy input will be lower than that for a shallower mixed layer, since the heat energy for the former case must be distributed across a larger mass of water (noting that the surface mixed layer is assumed to be well-mixed and therefore has uniform temperature with depth). The same analysis applies to other inputs into the mixed layer e.g. a fixed volume of freshwater. Sensitivity studies are performed with the minimum mixed-layer depth both reduced to 7 m (P) and increased to 20 m (Q).

The challenge with this set of experiments is that, unlike the other sensitivity studies presented here, it acts to influence the evolution of the sea ice both via changes in the lateral melt and via the basal melt and sea ice freeze-up rates, determined by ocean properties. Experiment (P) shows a small increase in the total sea ice extent and

volume and (Q) a small decrease; however both result in larger increases in the MIZ extent and volume. In comparison to other sensitivity studies, the changes in the lateral and basal melt are small, suggesting that mixed-layer feedbacks do not have a significant role in the impacts of the FSD found in *stan-fsd* compared to *ref*. It should be noted, however, that the evidence presented here is not enough to rule out the existence of multiple compensating feedback processes.

3.5 Discussion

We present here a series of simulations and additional sensitivity studies completed with the newly developed WIPoFSD model to explore the impacts of a variable power-law-derived floe size distribution model on the Arctic sea ice. It is useful to consider the physical mechanisms that drive the simulation results. It was previously noted that the increase in lateral melt observed when imposing the WIPoFSD model was compensated by a loss in basal melt, resulting in a more moderate increase in the total melt. Within the model there are three possible mechanisms causing the limited basal melt. Firstly, the increase in lateral melt will correspond to a reduction in available ice area for basal melting. It is shown in Figs. 3.4 and 3.7 that this mechanism is able to explain most of the reduction in basal melt, but the difference remains large enough that further mechanisms need to be considered. The second mechanism concerns F_{frzmlt}, the melting potential of the ocean. If there is a large enough increase in the lateral melt to result in insufficient melting potential, both the lateral and basal melt will be reduced proportionally, as described in Sect. 3.2.1. To explore whether this mechanism is responsible for the differences between the predicted and modelled reduction in basal melt, a simulation was performed where the step to reduce the basal melt according to F_{frzmlt} limits was omitted (though this step was retained for lateral melt). The results of this simulation (not presented) found only a small impact on the cumulative basal melt and a negligible impact on the cumulative total melt. The third mechanism concerns lateral melt feedback on the basal melt rate via the perturbation of mixed-layer properties. Higher freshwater release from the increase in lateral melt will lower the temperature and salinity of the ocean mixed layer, which will reduce the basal melt rate. However, the lateral melt increase also reduces the ice concentration, lowering the albedo of the ice–ocean system. This increases the absorption of shortwave solar radiation into the mixed layer, raising the temperature of the mixed layer; i.e. it has the opposite effect of the increased freshwater input. These two

competing feedbacks can potentially explain the overprediction of basal melt in Fig. 3.4 but underprediction of basal melt in Fig. 3.7. The increase in total melt observed in Fig. 3.7 will likely correspond to a more efficient use of the available melt potential and the aforementioned albedo-feedback mechanism. The interaction between the mixed layer and FSD is further explored through the (P) and (Q) sensitivity studies where the minimum mixed-layer depth was reduced and increased respectively. These studies provide further evidence that mixed-layer feedbacks are not a leading-order effect of the FSD, given the very small perturbations of the melt component from the *stan-fsd* simulation. Larger changes are seen for the sea ice extent and volume metrics. However, the same mixed-layer feedbacks that change the melt rates can also independently influence the freeze-up rate of sea ice; hence it is not possible to directly attribute the changes produced by varying the minimum mixed-layer depths specifically to WIPoFSD-related feedbacks. It should also be noted that the prognostic mixed-layer model used here provides a limited representation of sea ice–ocean interactions and feedbacks. The strength of these interactions may increase within a fully coupled sea ice–ocean model (Rynders, 2017).

The series of sensitivity studies to both the floe size parameters and other aspects of the WIPoFSD model are useful to understand the limitations of the model. An important result is the limited sensitivity of the model to the m_1, m_2, and α_{shape} parameters, i.e. experiments (L)–(O), with significant perturbations of these parameters reducing the sea ice extent by around 1 % or less. These are additional constants needed to calculate the lateral melt rate beyond floe size. If a strong sensitivity was found to these parameters, it would suggest that these should be considered as alternative targets rather than the FSD for future model development. Instead, these experiments support the focus on floe size as the primary uncertainty in lateral melt calculation. Experiment (K) showed very little model response to increasing the floe freeze-up timescale, T_{rel}, from 10 to 365 days. This result suggests that the use of more physically derived parameterisations of the floe growth during freezing conditions (e.g. Roach et al., 2018b) would not have a significant impact within the model framework presented here. However, Fig. 3.13 shows that the seasonal l_{eff} evolution is dependent on the floe restoration rate, and there may be specific events, such as strong winter break-up events, where accurate modelling of floe growth is important to then understand the sea ice evolution during the subsequent melting season.

The sensitivity studies also give insight into the impact of waves on the sea ice cover. In particular, the two sensitivity studies that switch off the lateral melt–l_{var} (G) and wave–l_{var} (F) feedback mechanisms respectively showed that the latter had a stronger influence on both the evolution of l_{eff} and the changes in sea ice area and extent when imposing standard parameters on WIPoFSD. This impact was enhanced through various perturbations to the wave model. The increase in significant wave height (H) and reduction in ice strength (I) are representative of future Arctic conditions when the sea ice is expected to be thinner (Aksenov et al., 2017) with storms of increasing strength and duration (Basu et al., 2018). The results presented here suggest that these changes will have only a limited impact on sea ice extent and volume via the floe size feedback mechanism. The strongest response in sea ice extent and volume was observed with a reduction in the attenuation rate (J). It is important to note that the attenuation rate is a function of floe size, with smaller floes driving stronger attenuation. This creates a feedback where the fragmentation caused by one wave changes the way subsequent waves propagate through the MIZ. It should be noted that the wave component of the WIPoFSD model is a simplified representation of waves propagating into sea ice and involves a number of approximations. In particular, the directional behaviour of the waves will be more suitable for wind waves than swell waves. As discussed in Sect. 3.2.2, swell waves have been observed to have longer wavelengths and reduced attenuation rates, suggesting they would interact differently with the FSD than wind waves. More generally, modelling the propagation and energy loss of waves as they travel under sea ice is a complex problem and an area of active research (Meylan et al., 2017), and there have been recent efforts to produce coupled wave–sea ice models (Boutin et al., 2020; Herman, 2017). However, any increase in complexity in modelling the waves will result in increased computational cost. Further observations about wave attenuation in sea ice are needed to judge the complexity of the model approach required to produce sufficient accuracy.

As stated above, the model shows a strong sensitivity to the floe size parameters with some selections of the WIPoFSD parameters showing moderate increases in the sea ice extent and volume, and other selections driving reductions of these values by over 50 % in September. The limited observational data available to constrain the selected parameters is therefore a significant challenge of this modelling approach. Furthermore, a not insignificant model response of the order of 5 % relative to *ref* has been observed to sensitivity experiment (E) performed here to explore the impacts of

the non-uniform α. Sensitivity experiments (D) and (E) were performed on the basis of evidence from Stern et al. (2018a, b) that α is not a fixed value and instead evolves spatially and temporally. Whilst it would be interesting to explore the impact of a variable d_{min}, especially considering the strong sensitivity of the model response to this parameter, we do not have an analogous set of observations focusing on how d_{min} may vary in space and time.

The WIPoFSD model used here assumes a power-law distribution with the exponent α, lower cut-off d_{min}, and upper cut-off d_{max} all fixed at constant values. Each grid cell has a locally defined variable FSD tracer, l_{var}, which evolves in response to wave break-up events, lateral melt, and freezing conditions. The use of l_{var} to represent variability within the FSD puts limits on the physical fidelity of the parameterisations of processes that change the FSD in our model. However, if l_{var} is not used to represent variability in the distribution, then within a power-law framework over a fixed floe size range the only other component of the system that can change is the exponent. The exponent in such a set-up becomes an emergent parameter rather than one determined from observations. An important component of this study is to perform sensitivity studies of the sea ice mass balance to the range of exponents seen in observations. An investigation of the evolution of the floe size distribution itself, power law or otherwise, is better approached with a prognostic model of the proximate physical processes, such as in the manner of Roach et al. (2018a). Future improved understanding of the FSD may then allow the development of improved parameterisations of floe size and related processes that do not require the assumptions made in this study regarding the shape and floe size range of the distribution. As more observational data becomes available, both from satellite and in-situ observations, these parameterisations can be developed and constrained. In particular, the MOSAiC expedition (Dethloff et al., 2016) should provide observations of the evolution and break-up of individual floes over daily to weekly timescales alongside other sea ice properties, such as melt pond fraction and strain rate. This information will allow an assessment of the relevant factors driving individual floe fragmentation events. Previous studies, particularly Hwang et al. (2017), have demonstrated that combining FSD observations with in-situ data about the sea ice, atmosphere, and ocean state can help to characterise floe evolution e.g. to demonstrate an association between high wind speeds and floe fragmentation events. The longer-term aim is the development of a floe size model for use in climate models that can reasonably capture

the physical impacts of the FSD on the complete sea ice–ocean–atmosphere system without the full complexity of the prognostic floe size–thickness distribution model. The identification of l_{eff} as a useful floe size parameter may provide a method to report useful FSD information over a larger spatial and temporal scale, as this value can be calculated from the ice perimeter length within a unit area and avoids the need to report a full distribution. This would allow an assessment of the regional, intra-annual, and inter-annual variability of the FSD and identify the FSD parameters and components that best reproduce these desired features. There have been recent efforts to develop techniques to obtain a representative floe size metric from satellite imagery over large spatial and temporal scales, though so far these techniques have only been demonstrated at low resolution (Horvat et al., 2019).

The reference simulation (*ref*) used in this study underpredicts summer sea ice concentration in the pack ice but overpredicts the concentration at the sea ice edge, consistent with other studies that use the CICE sea ice model (such as Schröder et al., 2019). An analysis of the historically forced simulations used within of the Coupled Model Intercomparison Project Phase 5 (CMIP5) found that coupled models consistently performed poorly in capturing the regional variation in sea ice concentration, showing this problem is not specific to CPOM CICE simulations (Ivanova et al., 2016). This suggests that models currently underestimate the role of the MIZ in driving the seasonal sea ice loss. The WIPoFSD model is shown here to have a non-uniform impact on the sea ice cover, with an enhancement in lateral melt and a corresponding reduction in sea ice concentration within the MIZ, as shown in Fig. 3.6. Whilst the changes are generally small, it shows that the use of an FSD model, either in the described form or otherwise, may be an important step towards improving the accuracy of sea ice models.

3.6 Conclusion

Climate model representations of sea ice currently assume that the size of floes that make up the sea ice is constant; however, observations show that floes adopt a distribution of sizes. A power law generally produces a good fit to observations of the floe size distribution (FSD), though the size range and exponent reported for this distribution can vary significantly between different studies. A power-law-derived FSD model including a waves-in-ice module (WIPoFSD) has been incorporated into the Los

Alamos sea ice model coupled to a prognostic mixed-layer model, CICE–ML. In the WIPoFSD model, the FSD is defined by a lower floe size cut-off, upper floe size cut-off, and exponent. A variable FSD tracer is also introduced, which varies in response to lateral melting, wave break-up events, and freezing conditions. The lower and upper floe size cut-offs and exponent are set to fixed values. A standard set of parameters for the WIPoFSD model is identified from observations and the results of a sea ice simulation using these parameters is compared to one with a constant floe size of 300 m. Inclusion of the WIPoFSD model within CICE–ML results in increased lateral melt compensated by reductions in basal melt, resulting in only moderate impacts on the total melt. The primary mechanism by which the increased lateral melt reduces the basal melt is shown to be the reduction in available ice area for basal melt. The impact is not spatially homogeneous, with losses in sea ice area and volume dominating in the marginal ice zone (MIZ). These impacts partially correct existing model biases in the stand-alone CICE–ML model, suggesting the inclusion of an FSD is an important step forward in ensuring that models can produce realistic simulations of the Arctic sea ice.

A series of sensitivity experiments explore the limitations of the model. The model does show a strong response to a reduction in wave attenuation rate, suggesting this is an important component in understanding wave–sea ice interactions. Different selections of parameters for the FSD show a large impact on the modelled sea ice state, with some showing a moderate increase in mean September sea ice extent and volume, with others reducing these metrics by over 20 % and 50 % respectively. A newly defined parameter, effective floe size, is found to be a good predictor of model response for simulations where the lower floe size cut-off and power-law exponent are fixed. The impact of a non-uniform exponent was also explored based on observations that these parameters evolve for a given region of sea ice. Results suggest that this parameter could further enhance the differential behaviour seen between pack ice and the MIZ in response to the imposition of an FSD. These sensitivity studies also showed that the choice of WIPoFSD parameters is a source of much larger model uncertainty than other constants used within the lateral melt parameterisation, justifying the focus on developing an FSD model as a priority for improved accuracy of sea ice modelling.

Whilst the model presented here does make a major assumption that the floe size distribution adopts a power law, this is consistent with most observations. Furthermore, it has been shown that the model can easily be modified to adapt to additional findings such as the inclusion of a non-uniform exponent. This means the WIPoFSD model is a

useful tool for assessing the importance of the FSD in the evolution of sea ice, particularly the seasonal retreat. Climate models require an important balance to be maintained between physical fidelity and computational expense. The simplicity of the WIPoFSD model makes it a useful stepping-stone for the development of new parameterisations of floe size within climate models that can reasonably capture the physical impacts of the FSD without a large computational cost. Planned observational studies such as MOSAiC should help in the development of these novel parameterisations.

Chapter 4: Further explorations of the WIPoFSD model

Chapter 3 was a self-contained manuscript that has been published as Bateson et al. (2020) and introduced the WIPoFSD model, an FSD model that assumes a fixed power-law shape but includes a floe size variable to enable parameterisations of individual processes that can change floe size. The chapter then explored how a power-law-derived FSD impacts CICE simulations of the Arctic sea ice cover, including sensitivity studies to model parameters, individual processes, and a variable exponent. The origin of the basal melt compensation effect in response to increased lateral melt is attributed to a reduction in the sea ice concentration, and the effective floe size is established as a useful metric to predict and understand the sea ice response to a given FSD. The material presented in chapter 4 aims to supplement the original manuscript, with a focus on the challenges in parameterising individual processes for an FSD model where the shape of the FSD is fixed. This chapter will revisit two of the parameterisations used within the WIPoFSD model: lateral melting, and advection of the FSD. It will be demonstrated that it is not possible to capture the exact effects of either process on the FSD, as both perturb the FSD away from a power law. A new lateral melting scheme is introduced, which is shown to correctly predict scenarios where the effective floe size increases in response to lateral melting. The new scheme is shown to have limitations in overestimating the change in effective floe size where lateral melting is high. Finally, it is demonstrated that the advection scheme used within the WIPoFSD model is a reasonable approximation.

4.1 Revisiting WIPoFSD model parameterisations

The WIPoFSD model includes several parameterisations to determine how the FSD evolves with respect to physical processes. These parameterisations often involve significant approximations to enable their use within a fixed power-law framework. Here two specific parameterisations will be reconsidered: lateral melting and the FSD advection scheme. A scheme to reconstruct l_{var} from l_{eff} will also be presented as part of an alternative lateral melt parametrisation.

4.2 Reconstructing l_{var} from l_{eff}

The WIPoFSD model uses a variable, l_{var}, to represent changes to the floe size distribution. Processes are parameterised in terms of how they impact l_{var} and useful properties such as l_{eff} can easily be calculated from l_{var}. The appeal of this approach is its simplicity. The broader impacts of a power-law distribution on the sea ice cover can be explored whilst also including spatial and temporal variability of the FSD within the model. For mechanical processes such as wave break-up, the use of l_{var} is particularly suitable. It marks a transition from a regime where floes are being broken up to a regime where the number of floes is increasing due to the break-up of larger floes. For thermodynamic processes it makes less intuitive sense. It is not possible to define two clear regimes; instead floes across the distribution reduce in diameter by the same magnitude in response to a lateral melting event. This is not to say that the standard WIPoFSD model treatment of the impacts of lateral melt on the FSD is poor, just that it is worthwhile to consider the accuracy of different approaches. A parameterisation of lateral melt in terms of l_{eff} may prove to be a more suitable approach given lateral melt is calculated as a function of l_{eff}.

In order to parameterise processes in terms of l_{eff}, a method is needed to calculate l_{var} from l_{eff}. There is no analytical solution to this problem; instead a numerical approach must be used such as Newton-Raphson iteration:

$$x_{n+1} = x_n - \frac{f(x_n)}{f'(x_n)}. \tag{4.1}$$

Here x is l_{var} and the function to solve is derived from Eq. (3.17) i.e.

$$f(l_{var}) = 0 = \frac{(2+\alpha)[l_{var}^{3+\alpha} - d_{min}^{3+\alpha}]}{(3+\alpha)\,[l_{var}^{2+\alpha} - d_{min}^{2+\alpha}]} - l_{eff}. \tag{4.2}$$

The iterative scheme can then be evaluated as:

$$l_{var,n+1} = l_{var,n} - \frac{\left(\frac{[l_{var.n}^{3+\alpha} - d_{min}^{3+\alpha}]}{(3+\alpha)} - \frac{l_{eff}[l_{var,n}^{2+\alpha} - d_{min}^{2+\alpha}]}{(2+\alpha)}\right)}{l_{var}^{1+\alpha}(l_{var.n} - f(l_{var.n}))}. \tag{4.3}$$

Note that, for simplicity, where α = -1, -2 or -3, a value of 0.001 will be taken off. Whilst an exact solution is possible for these cases, this adds additional and unnecessary complexity to a scheme that is already an approximation. This scheme is evaluated until either $l_{var,n+1}$ - $l_{var,n}$ is less than 0.01% of the change in l_{eff} over a timestep or until a maximum of 50 iterations are complete. In general, the threshold for convergence is achieved within 10 iterations, however where l_{eff} and l_{var} are close in value i.e. where l_{var} is within a few metres of d_{min}, convergence can take longer than 50 iterations. These circumstances are associated with conditions of very low sea ice concentration, where the net error in the lateral melt volume calculation associated with the failure to reach the threshold condition for convergence is negligible.

4.3 Floe size and lateral melt

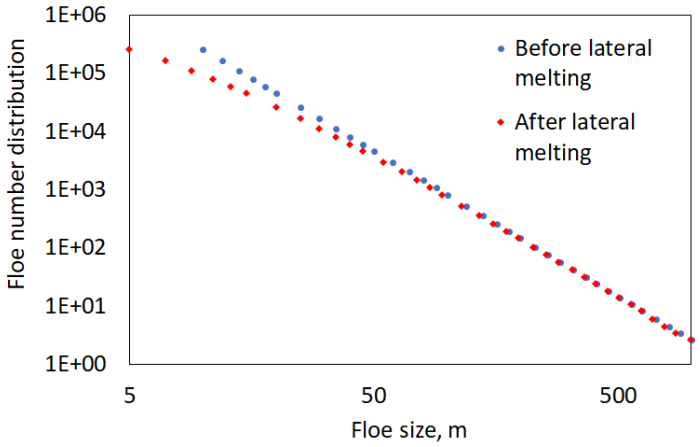

Figure 4.1: A power-law number distribution with $\alpha = -2.5, l_{min} = 10\ m, l_{var}$ = 1000 m before (blue dots) and after (red diamonds) a lateral melting event where each floe edge experiences 2.5 m of melting, reducing the total diameter of each floe by 5 m in total. The number distribution is given for a grid cell of size 56 km. This plot shows a tailing off at the lower end of the distribution after the lateral melt event i.e. lateral melting does not preserve the power-law distribution.

A leading order impact of floe size is on the lateral melt. The higher the floe perimeter per unit sea ice area, the higher the lateral melt per unit sea ice area. This process has a feedback to the original distribution. Floes decrease in size as they melt, reducing the available sea ice area but increasing the perimeter per unit sea ice area of that floe. It is not possible to represent this feedback exactly within a fixed exponent power-law distribution because lateral melting does not preserve the power law. Figure 4.1 displays a power-law distribution ($\alpha = -2.5, d_{min} = 10\ m, l_{var}$ = 1000 m) after 5 m of floe diameter is lost due to lateral melting. This shows that whilst a power law remains

a reasonable description for floes larger than 50 m, below 50 m there is a strong tailing off. Furthermore, having a fixed d_{min} means that some floes are now smaller than the lower limit of the distribution. In practice the lateral melt rate is rarely greater than 1 cm day^{-1}, occasionally reaching around 10 cm day^{-1} for some simulations. Hence, for most grid cells there will not be enough lateral melting to produce significant deviations from the power law (see also Horvat and Tziperman, 2017).

In the original WIPoFSD model set up the lateral melt feedback on floe size is parameterised assuming that l_{var}, the parameter used in the WIPoFSD model to represent changes in the FSD, reduces after lateral melting by the root of the factor that the sea ice area reduces by in response to the same lateral melting (see Eq. 3.19). Figure 3.13 shows that the lateral melt feedback on floe size has a much weaker effect on l_{eff} than the wave break-up scheme at the sea ice edge. Sensitivity study (G), where the lateral melt feedback is removed, also shows that the lateral melt feedback does not contribute significantly to WIPoFSD model impacts on pan-Arctic sea ice metrics such as the total sea ice volume and area. This suggests that this feedback is not the leading order process in determining the emergent FSD shape and is even less important for understanding the impact of the FSD on the sea ice mass balance. Here this parameterisation will be reassessed with a focus on whether it is underestimating the possible impact of the lateral melt feedback on the FSD.

Whilst it is not possible to capture cumulative changes to the FSD due to the constraints of having a power-law distribution with a lower floe size limit, it is possible to calculate exactly how the effective floe size, l_{eff}, will change over one timestep. The floe number distribution can be written explicitly according to Eq. (3.10) and Eq. (3.11):

$$N(x \,|d_{min} \leq x \leq l_{var}) = \frac{(3+\alpha)Al^2}{\alpha_{shape}} \frac{x^{\alpha}}{\left[l_{var}^{3+\alpha} - d_{min}^{3+\alpha}\right]}. \tag{4.4}$$

Equations (3.14) – (3.17) show how l_{eff} is calculated from this distribution. It is also possible to derive an expression for l_{eff} after lateral melting. If floes experience an amount Δl of lateral melting on each edge, the total diameter of each floe must decrease by $2\Delta l$. This changes the size of the floes but does not impact the shape of the number distribution i.e. floes of diameter G prior to lateral melting and floes of diameter $G - 2\Delta l$ after lateral melting have the same number density, $N(G)$, where $N(x)$ is the number distribution prior to lateral melting. This description is true provided

$d_{min} > 2\Delta l$ i.e. no floes are completely lost from the distribution due to lateral melting. The total perimeter after the lateral melting event, P_{lm}, can therefore be calculated as:

$$P_{lm} = \int_{d_{min}}^{l_{var}} \pi(x - 2\Delta l)N(x)\, dx. \tag{4.5}$$

$N(x)$ in Eq. (4.5) is the number FSD prior to lateral melting, and this equation holds provided $d_{min} > 2\Delta l$. This can then be evaluated as:

$$P_{lm} = \frac{\pi(3+\alpha)A_{old}l^2}{\alpha_{shape}\left[l_{var}^{3+\alpha} - d_{min}^{3+\alpha}\right]}\left(\frac{[l_{var}^{2+\alpha} - d_{min}^{2+\alpha}]}{(2+\alpha)} - \frac{2\Delta l[l_{var}^{1+\alpha} - d_{min}^{1+\alpha}]}{(1+\alpha)}\right). \tag{4.6}$$

The subscript for A_{old} indicates that this is the sea ice area fraction before lateral melting. An expression for the total perimeter in terms of the new effective floe size, $l_{eff,new}$, can also be written using the updated sea ice area fraction after lateral melting, A_{new}:

$$P_{leff} = \frac{A_{new}l^2\pi}{\alpha_{shape}l_{eff,new}}. \tag{4.7}$$

The two expressions for total perimeter after lateral melting can then be equated to give the updated effective floe size, $l_{eff,new}$:

$$l_{eff,new} = \frac{[l_{var}^{3+\alpha} - d_{min}^{3+\alpha}]A_{new}}{(3+\alpha)\,A_{old}}\left(\frac{[l_{var}^{2+\alpha} - d_{min}^{2+\alpha}]}{(2+\alpha)} - \frac{2\Delta l[l_{var}^{1+\alpha} - d_{min}^{1+\alpha}]}{(1+\alpha)}\right)^{-1}. \tag{4.8}$$

l_{var} can then be calculated from the updated l_{eff} using the iterative scheme described in Sect. 4.1.1. It is possible to calculate an analytical result for A_{new} as a result of lateral melting of floes across the distribution, however CICE already accounts for changes to the sea ice area fraction according to Eq. (3.12). For internal model consistency, it is this CICE A_{new} that will be used. It is nevertheless useful to calculate the analytical result for A_{new} so that both numerical methods of updating the FSD with respect to lateral melting can be compared to the analytical result. The total sea ice area after lateral melting, $A_{new}l^2$, i.e. after the diameter of each floe reduces by $2\Delta l$, is given by the following expression, using the same approach and assumptions as for estimating the perimeter density after lateral melting in Eq. (4.5):

$$A_{new} l^2 = \int_{d_{min}}^{l_{var}} \alpha_{shape} (x - 2\Delta l)^2 N(x)\, dx. \tag{4.9}$$

This can be evaluated as:

$$\frac{A_{new}}{A_{old}} = 1 + 4\Delta l^2 \frac{(3+\alpha)[l_{var}^{1+\alpha} - d_{min}^{1+\alpha}]}{(1+\alpha)[l_{var}^{3+\alpha} - d_{min}^{3+\alpha}]} - 4\Delta l \frac{(3+\alpha)\left[l_{var}^{2+\alpha} - d_{min}^{2+\alpha}\right]}{(2+\alpha)\left[l_{var}^{3+\alpha} - d_{min}^{3+\alpha}\right]}. \tag{4.10}$$

It is therefore possible to give an exact analytical result for l_{eff} after lateral melting.

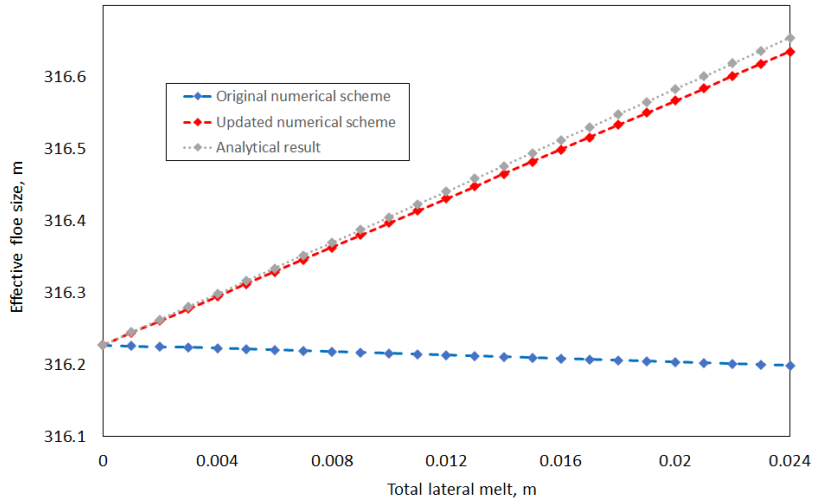

Figure 4.2: Evolution of l_{eff} over 24 iterative steps of 0.1 cm lateral melt for three scenarios: the original parameterisation where l_{var} is reduced as a function of change in the sea ice concentration (blue, long dashes); the updated scheme where l_{eff} is updated accounting for the effects of lateral melt on the full distribution but using the standard CICE scheme for changes to the sea ice concentration from lateral melting (red, short dashes); and the analytical scheme (grey dotted). The initial conditions have l_{var} = 10 km, d_{min} = 10 m and α = -2.5. The initial sea ice concentration is set to 0.9. The updated numerical scheme is a much better approximation to the actual result than the original numerical scheme, which produces the wrong sign of gradient.

In order to compare the updated numerical scheme for calculating the change in l_{eff} from lateral melting to the original numerical scheme and analytical result, the following scenario is considered. Each scheme is evaluated over 24-time steps of 1 hour each, i.e. one day in total, with Δl = 0.1 cm for each time step. This gives a total lateral melt of 2.4 cm over a day, a large but not unphysical amount. The initial sea ice concentration is set to 0.9. l_{var} is initiated as 10 km. Figure 4.2 considers this scenario with α = -2.5 and d_{min} = 10 m. Here the original numerical scheme shows a slight decrease in l_{eff} over one day of about 0.03 m, whereas the analytical results shows

l_{eff} increasing by over 0.4 m. The updated numerical scheme performs better here, underpredicting the increase shown in the analytical result by just over 0.01 m. Figure 4.3 considers the same scenario, however with α = -3.5. In this case, all three scenarios show a reduction in l_{eff}, however the original numerical scheme significantly underpredicts the change in l_{eff} compared to the analytical result and the updated scheme significantly overpredicts the change in l_{eff}. The updated numerical scheme is therefore able to capture scenarios where l_{eff} will increase, however it can perform as poorly as the original scheme for other scenarios.

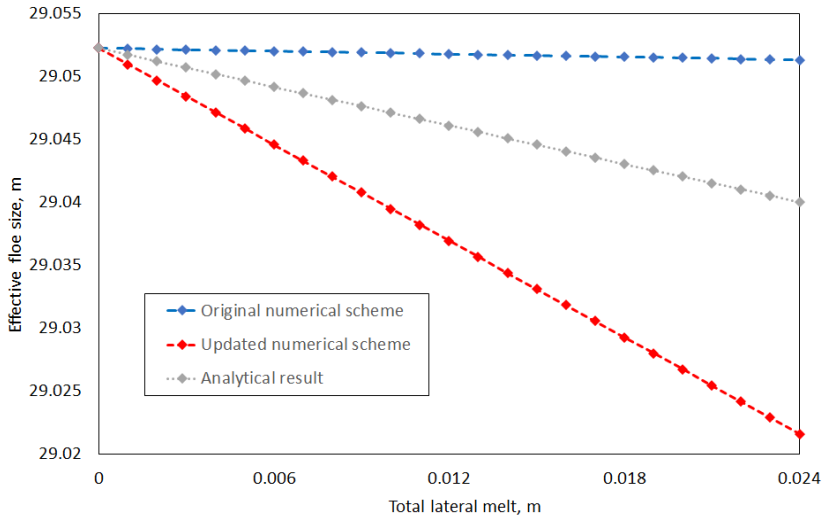

Figure 4.3: Evolution of l_{eff} over 24 iterative steps of 0.1 cm lateral melt for three scenarios: the original parameterisation where l_{var} is reduced as a function of change in the sea ice concentration (blue, long dashes); the updated scheme where l_{eff} is updated accounting for the effects of lateral melt on the full distribution but using the standard CICE scheme for changes to the sea ice concentration from lateral melting (red, short dashes); and the analytical scheme (grey dotted). The initial conditions have l_{var} = 10 km, d_{min} = 10 m and α = -3.5. The initial sea ice concentration is set to 0.9. Here the original numerical scheme significantly underestimates the change in l_{eff} from the lateral melt, but the updated numerical scheme significantly overestimates the change in l_{eff}.

It is worth considering why l_{eff} behaves as it does in these two scenarios in order to understand how differences emerge between the different schemes, particularly the counterintuitive result that l_{eff} can increase in some scenarios in response to lateral melting. Consider a distribution consisting of floes of a uniform size. l_{eff} will decrease in response to lateral melting. However, for a distribution of floes, it is not just the impact of lateral melting on the size of individual floes that matters, but also how it changes the shape of the distribution. For example, in Fig. 4.1 it is shown that lateral melting causes a perturbation of the distribution from the power law shape, where

smaller floes show a stronger perturbation from the distribution than larger floes. If both a small and a large floe experience the same absolute reduction in diameter in response to lateral melting, the relative reduction in total perimeter will be larger for the smaller floe than the larger floe. This therefore increases the weighting of larger floes in the calculation of l_{eff}, and this either moderates the expected reduction in l_{eff} or where the effect is strong enough can act to increase l_{eff}, such as demonstrated in Fig. 4.2. The first behaviour described above i.e. the impact on l_{eff} from the decrease in size of individual floes, is relevant to all FSDs whereas the second behaviour i.e. the reweighting towards larger floes in the calculation of l_{eff}, will only be significant where the distribution is not dominated by floes of uniform size. Where the exponent is more negative, i.e. where smaller floes account for most of the sea ice area, the re-weighting effect is weak and l_{eff} will decrease in response to lateral melting. Where the exponent is less negative i.e. where sea ice area is more uniformly distributed across floe sizes, the re-weighting effect is strong enough for l_{eff} to increase in response to lateral melting. The restriction of using a power law over a fixed floe size range means neither scheme can account exactly for both effects, but the updated scheme appears to perform better where the tailing off dominates changes in l_{eff} rather than the change in perimeter to area ratio.

Simulations have been completed with the new lateral melt numerical scheme to assess whether the inclusion of this scheme changes the importance of lateral melt feedback to the impact of the WIPoFSD model on the sea ice cover. These simulations use standalone CICE with an identical setup to that described in Sect. 3.3 apart from the changes to the lateral melt scheme described here, with the analysis again performed over 2007 – 2016. Here four separate simulations have been completed. For each simulation $d_{min} = 10\ m$ and $d_{max} = 30000\ m$. *lvar-2.5* and *lvar-3.5* both use the original lateral melting scheme with exponents of -2.5 and -3.5 respectively. *leff-2.5* and *leff-3.5* both use the updated l_{eff} based lateral melting scheme, again with exponents of -2.5 and -3.5 respectively. Figure 4.4 shows the percentage difference in sea ice extent and volume for *leff-2.5* relative to *lvar-2.5*; Fig. 4.5 shows the same differences but for *leff-3.5* relative to *lvar-3.5*. It is useful to compare Fig. 4.4 to Fig. 3.3, which shows the impact of the standard WIPoFSD model setup using the same FSD parameters as *lvar-2.5* relative to the reference case with a fixed floe size of 300 m. Even though the original impact of the FSD was just a reduction of up to 1% during the melting season for sea ice extent and volume, this is still over 5 times larger than the

impact of the new melting scheme on extent and volume. The interannual variability suggests the new lateral melting scheme can cause increases in extent and volume in some years, and reductions in others, spanning a maximum range of ± 0.5%. Figure 4.5 shows a very different result. Here there is a consistent reduction of the sea ice extent and volume throughout the melting season, even including the range spanned by the interannual variability, with a maximum mean reduction in sea ice extent in August of 4 % and for sea ice volume the maximum mean reduction is 6% in September. In some years this can extend to an 8 % reduction. Figure 3.9 shows that the comparable simulation (i.e. with the same WIPoFSD parameters) in the original study produced a reduction of just under 10% in sea ice extent and just over 20% in sea ice volume. The inclusion of the l_{eff} derived lateral melt scheme results in sizeable change for simulations with the more negative exponent, both absolutely and relatively.

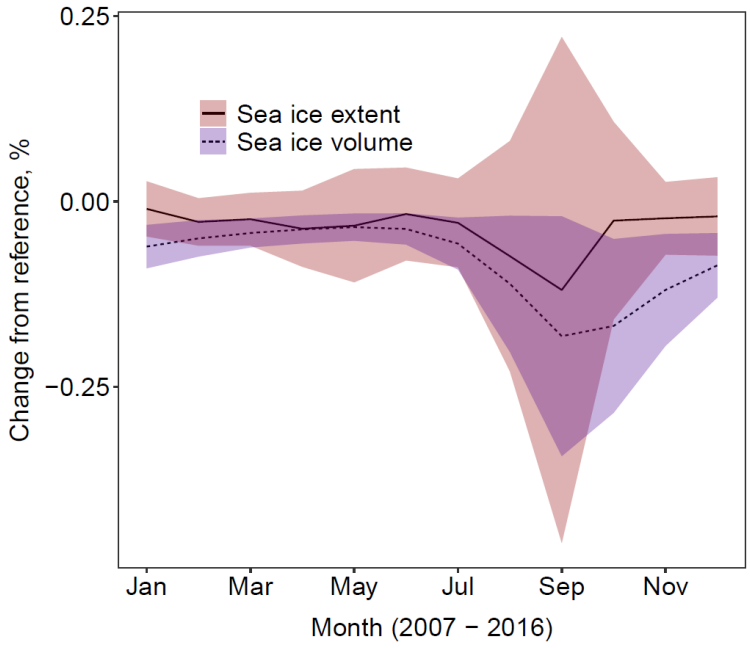

Figure 4.4: Difference in sea ice extent (solid, red ribbon) and volume (dashed, blue ribbon) of *leff-2.5* relative to *lvar-2.5* averaged over 2007 - 2016. The ribbon shows, in each case, the region spanned by the mean value plus or minus two times the standard deviation. The mean behaviour shows a negligible change, with the mean difference through the year never exceeding 0.2%. The interannual variability shows that the impact of changing the lateral melt parameterisation spans a range of +0.25% to -0.5% for extent and up to -0.35% for volume.

Figures 4.6 and 4.7 show the difference in sea ice concentration, thickness and l_{eff} for *leff-2.5* relative to *lvar-2.5* and *leff-3.5* relative to *lvar-3.5* respectively. The changes in sea ice concentration and thickness shown in Fig. 4.6 are negligible, consistent with

the results presented in Fig. 4.4. Moderate increases can be seen in l_{eff}, particularly for the MIZ in June with increases between 5 – 15 m generally seen. In certain locations within the Canadian Arctic Archipelago in September, increases in l_{eff} exceeding 25 m can be seen. This increase in l_{eff} is consistent with the predicted behaviour shown in Fig. 4.2.

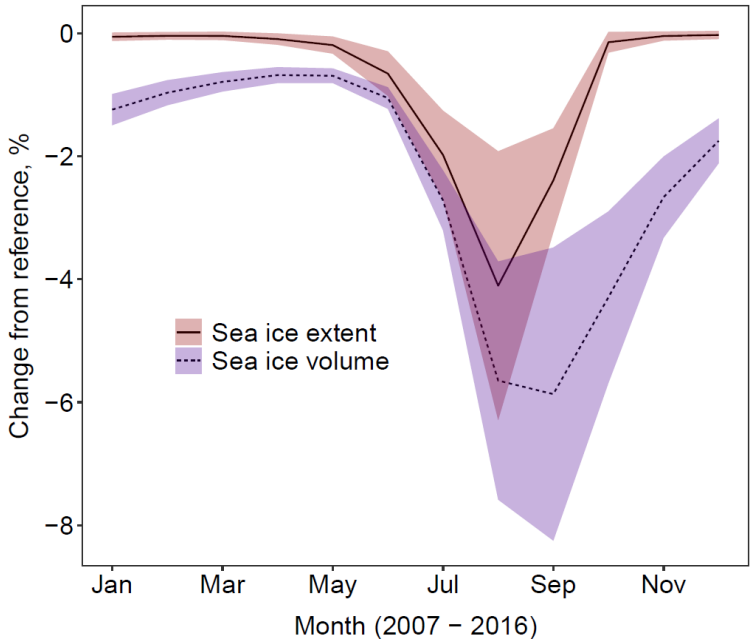

Figure 4.5: Difference in sea ice extent (solid, red ribbon) and volume (dashed, blue ribbon) of *leff-3.5* relative to *lvar-3.5* averaged over 2007 - 2016. The ribbon shows, in each case, the region spanned by the mean value plus or minus two times the standard deviation. The mean behaviour shows a significant reduction in both sea ice extent and volume during the melting season, up to a maximum of 4% and 6% respectively. The interannual variability shows that the reduction in extent and volume is consistent across each year of the simulation, as low as 2 % in some years for extent and up to 8% in some years for volume.

In Fig. 4.7 significant reductions can be seen in sea ice concentration and thickness across the MIZ through June and September, with the outer MIZ experiencing reductions in sea ice concentration fraction between 0.01 and 0.05. Similarly, reductions in the sea ice thickness of 1 cm or more can also be seen across the sea ice in September, with the strongest impact within the outer MIZ where the thickness reduces by over 10 cm in select locations. Small differences, of order 1 – 5 cm, in thickness remain through the year, particularly along the Canadian Arctic Archipelago. Reductions in l_{eff} can be seen throughout the year within the MIZ, generally between 2 – 4 m but in some locations exceeding 10 m. The maximum possible l_{eff} for this setup is just under 30 m, hence the changes in l_{eff} are significant. This indicates

significant feedback of lateral melt on l_{eff}, unlike the case shown in Fig. 3.13 for the original lateral melt scheme where this feedback was suggested to be relatively minor.

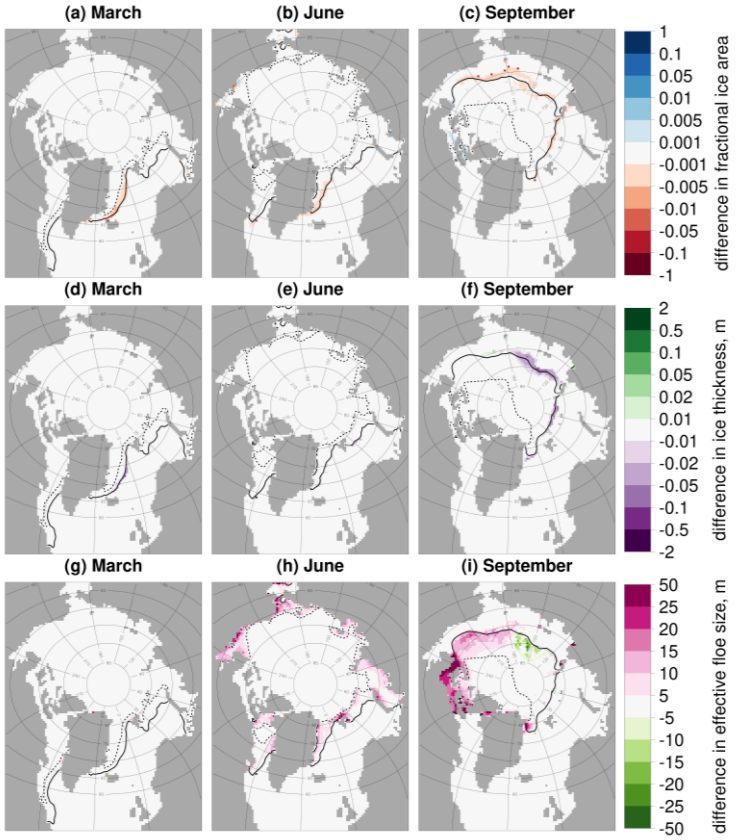

Figure 4.6: Difference in the sea ice concentration (top row, a-c), ice thickness (middle row, d-f), and l_{eff} (bottom row, g-i) between *leff-2.5* and *lvar-2.5* averaged over 2007 – 2016. Results are presented for March (left column, a, d, g), June (middle column, b, e, h) and September (right column, c, f, i). Values are shown only in locations where the sea ice concentration exceeds 5 %. The inner (dashed black) and outer (solid black) extent of the MIZ averaged over the same period is also shown. The differences in fractional sea ice area and thickness are negligible, with moderate increases seen for l_{eff} in certain locations.

Overall, the differences between the *leff-2.5* and *lvar-2.5* simulations are insignificant in the context of the thermodynamic evolution of the sea ice. Whilst the original l_{var}-derived lateral melt scheme is unable to predict the increase of l_{eff} with lateral melting shown by Fig. 4.3, this does not appear to have a large impact on the simulation. In comparison, the differences between the *leff-3.5* and *lvar-3.5* simulations have implications for the thermodynamic impacts of the WIPoFSD model, with evidence that the lateral melt-l_{eff} feedback is no longer insignificant. Fig. 4.3 indicates that the new formulation for updating l_{eff} after lateral melting is expected to significantly overestimate the expected reduction of l_{eff} by a factor of more than 2 compared to the

analytical result. Hence neither method to update l_{eff} is entirely adequate in this case. This highlights the limitations of using the fixed power-law approach to model the FSD; whilst it is possible to introduce more complex parameterisations to better represent the impact of a given physical process, the constrained shape of the distribution will always be a limiting factor in the physical fidelity of these parameterisations. *leff-2.5* and *lvar-2.5* use the standard parameter selection for the WIPoFSD model identified in chapter 3 whereas *leff-3.5* and *lvar-3.5* take a value for the exponent at the most negative limit of the range seen in observations. If the standard parameter selection holds as a generally good description of the observed FSD state, both lateral melt schemes will be adequate, albeit with a preference to the *leff-2.5* setup because it can identify scenarios where l_{eff} will increase rather than decrease in response to lateral melting.

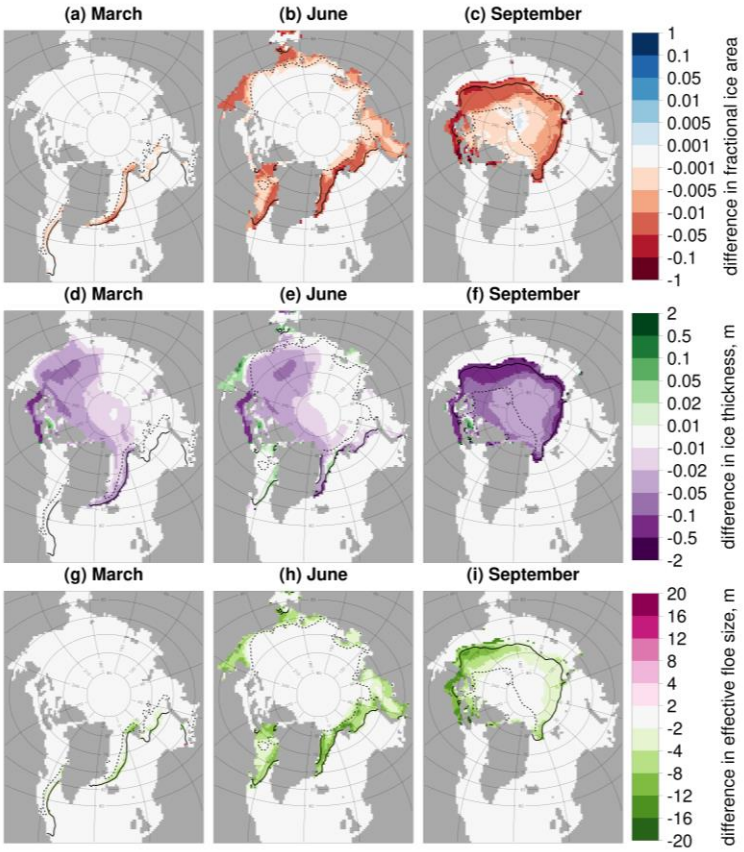

Figure 4.7: Difference in the sea ice concentration (top row, a-c), ice thickness (middle row, d-f), and l_{eff} (bottom row, g-i) between *leff-3.5* and *lvar-3.5* averaged over 2007 – 2016. Results are presented for March (left column, a, d, g), June (middle column, b, e, h) and September (right column, c, f, i). Values are shown only in locations where the sea ice concentration exceeds 5 %. Generally moderate reductions are seen for the fractional sea ice area and thickness, with a significant reduction in l_{eff}.

4.4 The advection scheme for l_{var}

In the WIPoFSD model l_{var} is treated as an area tracer and advected as an area-conserved property. This approach is justified as l_{var} is a property assigned to the sea ice area within a grid cell to represent the history of that sea ice area in terms of processes that will change the FSD, as discussed in Sect. 3.2.4. The aim of this advection scheme is not to represent the advection of the full FSD but specifically this property. It is nevertheless useful to consider how this representation of advection compares to the exact advection of the FSD.

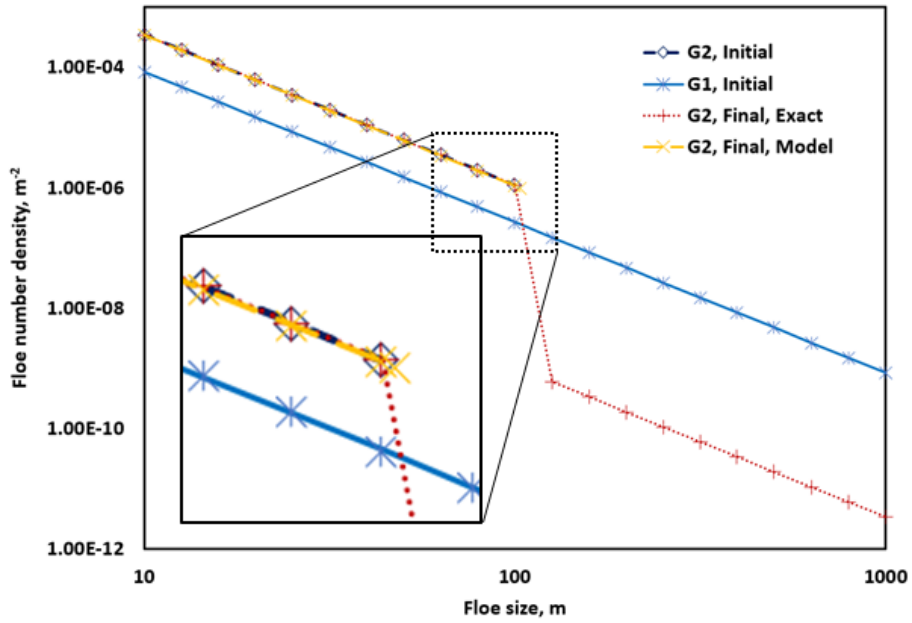

Figure 4.8: This plot considers two adjacent grid cells, $G1$ and $G2$, where $d_{min} = 10$ m and $\alpha = -2.5$ for both but $l_{var} = 1000$ m and 100 m in $G1$ and $G2$ respectively. There then follows a 1-hour advection event with sea ice drift of 5 km day^{-1} from $G1$ to $G2$, perpendicular to the boundary. The plot shows the FSDs from the four different cases: $G1$ prior to advection (dark blue, long dash, diamonds), $G2$ prior to advection (light blue, solid, stars), the analytical result in $G2$ after advection (red, dotted, vertical cross), and the modelled result where l_{var} is treated as an area tracer (yellow, medium dash, diagonal cross). Inset: Highlights difference between the FSD in $G2$ before advection and the model result for the FSD after advection, with a small but visible increase in l_{var} seen after advection. Overall, the plot shows the challenge of representing advection in an FSD model where the shape of the FSD is fixed.

As with lateral melting, it is again not possible to represent the exact details of how advection will impact the FSD within the power-law framework. This can be illustrated by considering the following scenario. In grid cell $G1$, $N_1(x\,|d_{min} \leq x \leq l_{v1}) = C_1 x^{\alpha}$. In a neighbouring grid cell, $G2$, $N_2(x\,|d_{min} \leq x \leq l_{v2}) = C_2 x^{\alpha}$. Here $l_{v1} \geq l_{v2}$. Over one

time-step the direction of advection is perpendicular to the boundary between $G1$ and $G2$, directed from $G1$ to $G2$. At the end of this timestep, $G2$ is made up of y proportion of sea ice with a distribution described by N_1 and z proportion of sea ice described by N_2, with $y + z = 1$. An updated floe size distribution can now be constructed:

$$N_{new}(x) = \begin{cases} (C_1 y + C_2 z)x^{\alpha} & d_{min} \leq x \leq l_{v2} \\ C_1 y x^{\alpha} & l_{v2} \leq x \leq l_{v1} \end{cases} . \quad (4.11)$$

N_{new} will only be a power-law distribution where $l_{v2} = l_{v1}$. Otherwise N_{new} consists of two power-law distributions with the same exponent but separated by a discontinuity at l_{v2}.

It is useful to consider a case study of advection using a realistic set of conditions, to compare the WIPoFSD model treatment of advection to the exact result. For this scenario consider the two adjacent grid cells, $G1$ and $G2$. In both grid cells, $d_{min} = 10\ \mathrm{m}$, $\alpha = -2.5$ and initially both l_{v1} and $l_{v2} = 1000\ \mathrm{m}$. Storm waves then propagate sufficiently into the sea ice cover that there is a wave break-up event in $G2$ and l_{v2} is reduced to $100\ \mathrm{m}$, however by the time these waves reach $G1$ they have attenuated sufficiently that the bending stress on the sea ice cover is not large enough for floe fracture. In the 1-hour timestep after the advection event a constant drift speed is set of 5 km day^{-1} directed from $G1$ to $G2$, perpendicular to the boundary between the two 50 km long grid boxes. The drift speed is taken as an upper estimate of likely sea ice drift speeds based on decadal averages reported in Kwok et al. (2013). It is then possible to calculate both the exact FSD that would result in $G2$ after this advection event and the FSD that would form using the treatment of FSD advection applied within the WIPoFSD model. Figure 4.8 displays four different FSDs: $G1$ immediately after the wave event; $G2$ immediately after the wave event; the exact distribution in $G2$ after 1 hour of advection; and the modelled distribution in $G2$ after 1 hour of advection where l_{var} is treated as an area tracer. This plot demonstrates the challenge of representing advection with the fixed power law. The analytical result for the FSD in $G2$ after advection includes a discrete transition at 100 m i.e. l_{v2}, which is impossible to capture within the restrictions of the WIPoFSD model. Figure 4.8 instead shows that the model treatment of FSD advection in this scenario effectively acts as a restoring. l_{var} increases by a small to moderate amount to represent the introduction of larger floes from advection into cell $G2$. An additional way to compare the two approaches is to calculate l_{eff} for the two resulting distributions, which is 31.7 m for the exact FSD and

32.2 m for the modelled FSD i.e. despite the different shapes for the modelled and analytical FSDs, they have a comparable l_{eff}.

The results presented in this section demonstrate the difficulty in representing the advection of the full FSD where a fixed power-law approach is used. However, the choice to treat l_{var} as an area tracer within the WIPoFSD model should not be taken as an attempt to represent the advection of the full FSD. Instead, l_{var} effectively acts as a property assigned to individual areas of sea ice to represent the history of the sea ice in terms of FSD processes. In this context, the treatment of l_{var} as an area tracer is appropriate.

4.5 Summary of chapter 4

The WIPoFSD model includes several parameterisations to represent the impact of processes that are expected the change the FSD via the tracer, l_{var}. These parameterisations are necessarily approximations of the processes that they represent due to the imposed power law within the WIPoFSD model. In this section I revisit two of these parameterisations, lateral melting and advection, and consider whether they are reasonable approximations to the expected physical behaviour.

For lateral melting, a new parameterisation is proposed where the expected change to l_{eff} over a single timestep is calculated based on the impact of lateral melting on the entire FSD. To facilitate this parameterisation, an iterative numerical method is outlined to describe how l_{var} can be calculated from l_{eff}. Results are presented to show that the new parameterisation can predict scenarios where l_{eff} increases with lateral melting unlike the original lateral melting parameterisation. Results also suggest that the existing parameterisation for floe size underestimates the feedback of lateral melting on l_{eff} where the power-law exponent is more negative, however the updated lateral melting scheme can overestimate this feedback. These results illustrate the physical limitations in using an FSD model where the shape of the distribution is restricted. The updated lateral melt scheme will be used in future chapters for the WIPoFSD model as it is able to capture the physical behaviour that l_{eff} can increase in response to lateral melting for certain FSD parameter choices, which the original lateral melt scheme was unable to do.

The treatment of advection of the FSD within the WIPoFSD model is also considered. It is demonstrated that the combination of two power-law distributions with different values for l_{var} will necessarily include a discontinuity in the distribution i.e. the resulting distribution will not be a power law. The model treatment of the impact of advection on the FSD is then justified as a method to conserve the history of a given area of sea ice in terms of FSD processes that have acted on that area of sea ice.

Up until now, this thesis has focused on the impact of the FSD on the Arctic sea ice via changes to the lateral melt volume. In the next chapter the impact of floe size on momentum exchange between the sea ice, atmosphere, and ocean will be explored.

Chapter 5: Floe size and form drag

In chapters 3 and 4, the WIPoFSD model impacts MIZ processes and the Arctic sea ice through changes to the lateral melt rate. This is not the only sea ice process where floe size is important. In this chapter the impact of floe size on turbulent momentum and heat exchange (also referred to as drag) between the sea ice, ocean, and atmosphere will be explored using the form drag formulation of Tsamados et al. (2014), which includes a term to account for floe size. In this chapter I will first provide an overview of the form drag scheme of Tsamados et al. (2014) with particular attention paid to the origin of the floe size dependency within the scheme. I will then then outline how this can be combined with the WIPoFSD model to explore FSD impacts on form drag. The general impact of the form drag scheme on the sea ice cover will then be reviewed. Finally, the impact of different floe size representations on the overall changes in the sea ice cover caused by the form drag scheme will then be compared, including the use of the WIPoFSD model.

5.1 Origin of floe size dependency in form drag scheme

The form drag scheme of Tsamados et al. (2014) aims to better describe the turbulent momentum and heat exchange between the sea ice, ocean, and atmosphere by accounting for the physical properties of the sea ice. This section will provide an overview of the original scheme of Tsamados et al. (2014), including an explanation of the floe size dependency within the scheme.

The scheme uses the flux aggregation method to calculate the turbulent flux over the heterogenous sea ice surface (Vihma, 1995). For this method, fluxes are calculated independently for ice-covered locations and open water and the total flux is taken as an area-weighted sum of these individual components. The turbulent momentum surface flux, τ, is calculated as follows:

$$\tau = \rho C_d(z) U(z) [cos\theta \boldsymbol{U}(z) + sin\theta \boldsymbol{k} \times \boldsymbol{U}(\boldsymbol{z})]. \quad (5.1)$$

Here $\boldsymbol{k}$ is the vertical unit vector, ρ is the fluid density (either air or water), $\boldsymbol{U}(z)$ is the difference in the fluid and sea ice velocity at a distance z from sea surface level (above for air and below for water), $U(z) = |\boldsymbol{U}(\boldsymbol{z})|$, $C_d(z)$ is the drag coefficient at a distance z

above sea surface level, and θ is the turning angle. τ is parameterised in terms of the wind speed and drag coefficient at a reference height, z. The value of z depends on the available measurements for $C_d(z)$ and $U(z)$ e.g. in CICE atmospheric forcing data generally provides the wind speed at a 10 m height. The turning angle, θ, is the angular rotation of the fluid velocity from the fluid-sea ice interface to the perpendicular distance z from the fluid-sea ice interface. In CICE the turning angle is taken to be zero (Hunke et al., 2015). The drag coefficient term, $C_d(z)$, will vary significantly depending on the stability of the fluid. This coefficient will be significantly enhanced in a turbulent boundary layer with strong turbulent mixing (Birnbaum and Lüpkes, 2002).

C is the drag coefficient for a neutral stratification of an ambient fluid. Within CICE first the neutral drag coefficient, C, is calculated before evaluating the impact of the atmospheric and oceanic stability. In the default CICE setup C is assumed to take the constants c_w and c_u in the ocean and atmosphere respectively i.e. the drag coefficients are assumed to be constant in both time and space. These constants can be considered to represent the friction associated with an effective sea ice surface roughness at both the top interface (i.e. with the atmosphere) and the basal interface (i.e. with the ocean).

In practice, the drag coefficient is composed of two distinct components, skin drag and form drag. The skin frictional or viscous drag is the drag that acts at the surface level of the sea ice and will be present even for undeformed sea ice. The form drag term accounts for the spatial shape of the sea ice; surface features such as hummocks, pressure sails, keels, and floe or melt pond edges will all impose a stress on the relevant fluid. The form drag formulation of Tsamados et al. (2014) replaces the constant drag coefficients in CICE with explicit representations of both the form drag and skin drag terms. C_u, the updated expression for the atmospheric drag coefficient can be calculated as:

$$C_u = C_u^{skin} + C_u^{f,rdg} + C_u^{f,floe} + C_u^{f,pond}. \quad (5.2)$$

C_w, the updated expression for the ocean drag coefficient can be calculated as:

$$C_w = C_w^{skin} + C_w^{f,rdg} + C_w^{f,floe}. \quad (5.3)$$

Here C^{skin} refers to the skin drag term, and $C^{f,rdg}$, $C^{f,floe}$ and $C^{f,pond}$ refer to form drag terms for ridges and keels, floe edges, and melt pond edges respectively.

Tsamados et al. (2014) first construct an expression for form drag using a generalised case, assuming a logarithmic fluid velocity profile and that the drag coefficient is measured at 10 m height from sea surface level. Here a fluid flow is obstructed by N objects that are distributed on a domain surface area, S_T, and randomly oriented. They have a height, H, and transverse length, L_y. The general formulation of a form drag coefficient can be expressed as follows:

$$C^f = \frac{NcS_c^2\gamma L_y H}{2S_T}\left[\frac{\ln\left(\frac{H}{z_0}\right)}{\ln\left(\frac{10}{z_0}\right)}\right]^2. \tag{5.4}$$

Here z_0 is the roughness parameter at the relevant sea ice surface, γ is a geometric parameter for the objects, c is the resistance coefficient of a single obstacle, and S_c is a sheltering function. A full derivation of Eq. (5.4) is given in Tsamados et al. (2014), but the general form can be understood by considering simple physical principles. The term $\gamma L_y H$ gives the total surface area of the object perpendicular to the direction of fluid flow, $\frac{N}{S_T}$ gives the object density within the domain, and cS_c^2 effectively defines the contribution per unit surface area to the total resistance of the object to a fluid flow, moderated by the effects of shielding from other adjacent objects. The shielding function, S_c, can be calculated as:

$$S_c = \left(1 - e^{-\frac{s_l D_o}{H}}\right)^{\frac{1}{2}}. \tag{5.5}$$

D_o is the distance between two obstacles and s_l is the attenuation parameter. The final logarithmic term in Eq. (5.4) emerges from two separate considerations: firstly from integrating the upstream fluid speed from the surface roughness length to the height of the object and assuming a logarithmic fluid velocity profile; it also makes the implicit assumption that the form drag term, C^f, is being measured at a 10 m perpendicular distance from the relevant interface.

$C^{f,floe}$ accounts for the drag produced by the edges of individual floes. The generalised form drag expression in Eq. (5.4) can be applied to floe edges (Hanssen-Bauer and Gjessing, 1988) in the case of surface momentum exchange over the sea ice-atmosphere interface:

$$C_u^{f,floe} = \frac{1}{2}\frac{c_{fa}}{\alpha_{shape}} S_c^2 \frac{H_f}{L} A \left[\frac{\ln\left(\frac{H_f}{z_{0w}}\right)}{\ln\left(\frac{10}{z_{0w}}\right)}\right]^2. \quad (5.6)$$

Here c_{fa} is a local form drag coefficient, taken to be constant. α_{shape} is a geometrical parameter to account for the shape of the floes. L is the average floe diameter. The sea ice concentration, A, can be expressed in terms of the object properties, $\frac{N\alpha_{shape}L^2}{S_T}$. The total length of floe edges per unit area, $\frac{NL}{S_T}$, can then be expressed as $\frac{A}{\alpha_{shape}L}$. z_{0w} is the roughness length of water upstream of the floe, given by 3.27 x 10^{-4} m (Hunke et al., 2015). H, the obstacle height parameter, is here given by H_f, the freeboard of the floe. H_f is defined as the distance between the upper surface of the floe and the sea surface. To calculate $C_w^{f,floe}$, the form drag of sea ice floes at the sea ice-ocean interface, H_f in Eq. (5.6) is replaced with D, the draft. D is defined as the distance between the lower surface of the floe and the sea surface.

S_c, the sheltering function, can be calculated as per Eq. (5.5), with $H = H_f$ and $D_o = D_{floe}$, where D_{floe} is the distance between neighbouring floes. D_{floe} can be calculated by approximating floes as square in shape and equally spaced as per Lüpkes and Birnbaum (2005). This approach divides a grid cell into individual unit cells; each unit cell has the same concentration as the overall grid cell, A, and has a square floe of length L at the centre. The perpendicular distance between the floes edges and unit cell edges is then $\frac{1}{2}D_{floe}$. A can then be written as the ratio of the floe area, L^2, and the total unit cell area, $(L + D_{floe})^2$, with the resulting expression rearranged to produce:

$$D_{floe} = \frac{L(1 - A^{\frac{1}{2}})}{A^{\frac{1}{2}}}. \quad (5.7)$$

Both $C_u^{f,floe}$ and $C_w^{f,floe}$ include a dependency on floe size, both explicitly and within the calculation of the sheltering function, S_c.

5.2 Floe contribution to form drag within CICE

Recent versions of CICE include an implementation of the form drag scheme (Hunke et al., 2015). This implementation generally follows the formulation of Tsamados et al. (2014). The values of $\frac{C_u}{A}$ and $\frac{C_w}{A}$ are capped at 0.02 and 0.06 respectively. This cap exists to prevent C_u and C_w adopting unrealistically high values, with the upper limits selected based on the observations presented in Schröder et al. (2003). The results presented in Tsamados et al. (2014) suggest that the values of C_u and C_w in general fall well within the upper limits. The ratio $\frac{c_{fa}}{\alpha_{shape}}$ takes the value 0.2. The floe diameter follows the parameterisation of Lüpkes et al. (2012), where floe diameter is expressed as a function of concentration:

$$L(A) = L_{min}\left(\frac{A_*}{A_* - A}\right)^{\beta}. \tag{5.8}$$

A_* is introduced such that the function $L(A)$ is defined for $A = 1$. It is calculated as:

$$A_* = \frac{1}{\left(1 - \left(\frac{L_{min}}{L_{max}}\right)^{\frac{1}{\beta}}\right)}. \tag{5.9}$$

Here $L_{min} = 8\,m$, $L_{max} = 300\,m$ and $\beta = 0.5$. This parameterisation for floe size is based on observations of floes taken from an aircraft over the Fram straight in Summer in 1991. CICE also uses the Lüpkes et al. (2012) approximation for S_c, which is expressed as a function of the sea ice concentration:

$$S_c = 1 - e^{-s_{lf}(1-A)}. \tag{5.10}$$

s_{lf} is the floe sheltering attenuation coefficient, with $s_{lf} = 11$ as per Lüpkes et al. (2012). In this formulation, S_c is not a function of the floe size.

5.3 Applying an FSD model to form drag

The parameterisation for floe size described in Eq. (5.8) was introduced in Tsamados et al. (2014) as a simple way to better capture variable floe size across the sea ice cover. The more complex treatment of floe size in the WIPoFSD model now provides an alternative way to determine L, the floe size parameter. For this approach L is set equal to l_{eff}, the effective floe size. The length scale of a floe is the important metric to determine the total floe drag and l_{eff} is defined to produce the same perimeter density as the given FSD i.e. the use of l_{eff} accounts for the shape of the full distribution calculated by the WIPoFSD model. The value of $C_u^{f,floe}$, calculated using Eq. (5.6), is the same whether calculated with $L = l_{eff}$ or integrated across all floes in the distribution. The approximation for S_c described in Eq. (5.10) is retained within this treatment of L, since the WIPoFSD model does not calculate the spatial distribution of floes within each grid cell.

It is helpful to comment on precisely how form drag has been implemented here to interact with the rest of CICE, since there is a difference from the implementation in Tsamados et al. (2014). In both setups, both the neutral drag coefficients and the neutral heat transfer coefficients are replaced by form drag coefficients accounting for surface features over the relevant interface. However, the calculation of the net heat flux from the sea ice to the ocean, F_{bot}, has its own heat transfer coefficient, c_h (see Eq. 2.3). In Tsamados et al. (2014), c_h is also replaced by the form drag coefficient for the ice-ocean interface. However, in this study c_h is kept at a value of 0.006, consistent with standard CICE (Hunke et al., 2015). The value of F_{bot} is still impacted by the form drag scheme since it is also a function of the friction velocity, u_*, which is calculated in terms of the turbulent momentum flux, τ, over both the ice-ocean and atmosphere-ocean interfaces.

In this chapter four simulations will be considered: the first is the standard approach to drag in CICE, without form drag (referred to as *nofd*); the second will be a simulation with form drag, using the parameterisation of Lüpkes et al. (2012) for the form drag floe size (*fd-Lüpkes*); the third will be a simulation where the form drag floe size is taken to be 300 m everywhere (*fd-cf300)*; and the final case will be a simulation using l_{eff} for the form drag floe size as determined using the WIPoFSD model (*fd-leff)*. In Sect. 5.4, *fd-Lüpkes* will be compared to *nofd*, with reference to the original study of Tsamados et

al. (2014), to review the general impacts of the form drag scheme. Then, in Sect. 5.5, the simulations applying the two different treatments of variable floe size within the form drag scheme i.e. *fd-Lüpkes* and *fd-leff*, will be compared to *fd-cf300*. This will allow an assessment of the contribution of floe size towards the total form drag impact and whether an explicit floe size model is necessary to represent that impact.

For simulations including form drag i.e. *fd-Lüpkes, fd-leff,* and *fd-cf300,* most parameters used within the form drag formulation that are not included in the discussion above will take the values described in Tsamados et al. (2014). The exceptions are the atmospheric background drag coefficient, ocean background drag coefficient, ridge impact parameter, and keel impact parameter of the form drag parameterisation, which are set to 0.001, 0.0005, 0.1 and 0.5 respectively. Schröder et al. (2019) discuss how these changes increase ice drift over level ice and reduce it over ridged ice leading to more realistic ice drift patterns compared to observations.

The simulations use a similar setup to that described in Sect. 3.3, but with some modifications. The longwave emissivity is increased from 0.95 to 0.976 in line with Schröder et al. (2019). These simulations are initiated on 1st January 1980 with the complete WIPoFSD model imposed, rather than having a period of spin-up. The model is also initiated in a sea ice free state. Simulations are evaluated until 31st December 2016. Results are then presented averaged over 2000 – 2016. Each simulation adopts the WIPoFSD model to determine the lateral melt rate using standard parameters i.e. 10 m, 30000 m and -2.5 for the lower floe size cut-off, upper floe size cut-off and exponent respectively.

5.4 General impact of form drag on the Arctic sea ice cover

In this section a direct comparison between the CICE-WIPoFSD setup with form drag (*fd-Lüpkes*) and without form drag (*nofd*) is made. Whilst the impact of the form drag scheme has already been discussed in Tsamados et al. (2014), the formulation used here includes the different parameter choices outlined in Schröder et al. (2019) and is applied to CICE including the WIPoFSD model. It is also useful to review the mechanisms leading to the observed changes in the sea ice cover in response to the form drag scheme.

Figure 5.1 shows the difference in sea ice extent and volume of *fd-Lüpkes* relative to *nofd* averaged over 2000 – 2016. The difference in extent and volume shows a large interannual variability over the 17-year period, particularly over the August to October period where the ranges spans about ±15 % for volume. The average impact is significantly smaller than the magnitude of the variability. The introduction of form drag using the original Lüpkes parameterisation to determine the size of floes within the scheme increases the sea ice volume by 1 – 2 % over July to September, with the sea ice extent showing a few percentage points increase in July and a larger reduction of about 3 % by September.

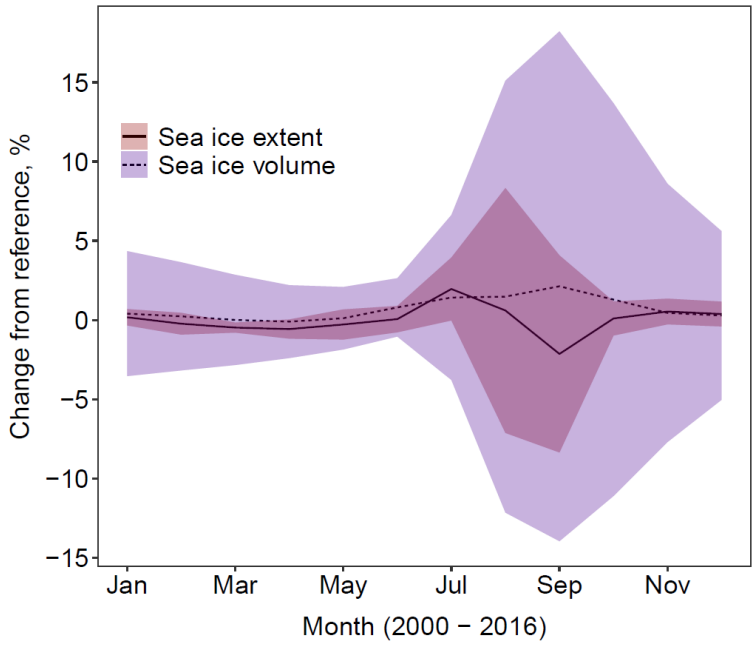

Figure 5.1: Difference in sea ice extent (solid, red ribbon) and volume (dashed, blue ribbon) of *fd-Lüpkes* relative to *nofd* averaged over 2000 - 2016. The ribbon shows the region spanned by the mean value plus or minus two times the standard deviation. Form drag has a high impact on the interannual variability but the impact on the mean values is small to moderate.

A question that emerges from Fig. 5.1 is how the high variability of the impacts from including form drag compares to the intrinsic variability of the sea ice model. In particular, is the peak of the variability in September something that is unique to the inclusion of the form drag scheme or an existing feature of the natural variability of the sea ice model under different forcing conditions? To investigate this, Fig. 5.2 compares the standard deviation calculated for timeseries of monthly averages in sea ice extent and volume for both *nofd* and the difference between *fd-Lüpkes* and *nofd*. The standard deviation here has been calculated from a detrended timeseries, to remove any contributions from trends to the standard deviation. Fig. 5.2 shows that the

standard deviation in the difference between the simulations scales with the variability of the reference simulation, *nofd*. The standard deviation in the difference is about a half and third of the value for the reference case for volume and extent respectively. CICE is a deterministic model and is not sensitive to small perturbations in initial conditions. Variability in CICE simulations is primarily driven by sensitivity to the atmosphere and ocean forcing (Hunke and Holland, 2007; Hunke, 2010). The size of the standard deviation in the difference between *fd-Lüpkes* and *nofd* being of a comparable order but smaller magnitude to the variability in *nofd* is therefore consistent with the inclusion of a new physical scheme that impacts sea ice-atmosphere interactions, given the atmospheric forcing is the main source of variability here (a fixed ocean climatology is used). This additional variability could also therefore be created through the inclusion of an ensemble of CICE simulations with perturbations to atmospheric forcing. Tsamados et al. (2014) also demonstrate strong spatial variability in the impact of sea ice drift patterns from including the form drag scheme, consistent with this overall picture.

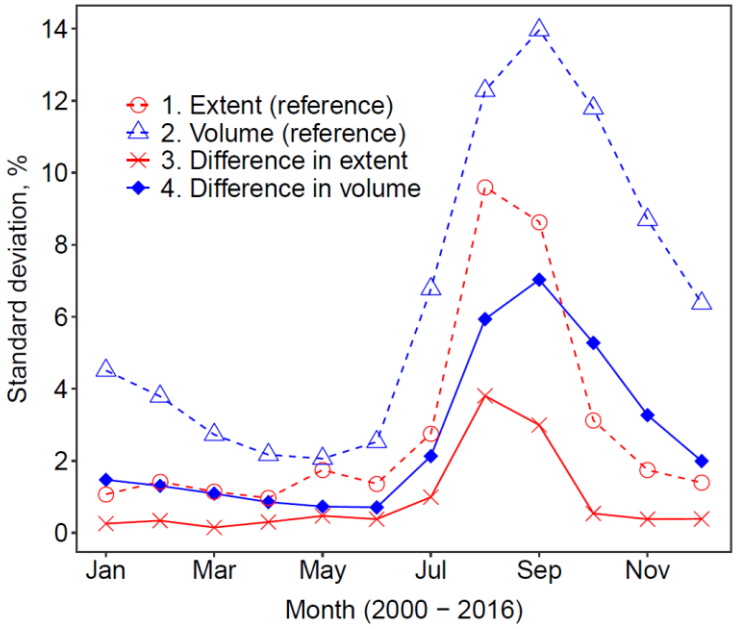

Figure 5.2: Detrended standard deviation calculated for timeseries of monthly averages in sea ice extent (red) and volume (blue) over the period 2000 – 2016. Standard deviation calculated for both the *nofd* simulation (dashed) and the difference between *fd-Lüpkes* and *nofd* (solid). The standard deviation in the difference scales at about 0.5 and 0.33 of reference values for volume and extent

The results presented in Fig. 5.1 can be understood further by considering spatial maps of differences in both extent and thickness and the 'form drag floe size'. Figure 5.3 shows spatial difference plots in both sea ice concentration and thickness for *fd-*

Lüpkes compared to *nofd*. Spatial plots to show the floe size used by the form drag scheme are also included. These are shown for three selected months: March, June and September, each averaged over 2000 – 2016. The most striking differences can be seen for thickness. The moderate increase seen in Fig. 5.1 does not reveal the significant redistribution of sea ice volume resulting from the form drag scheme. Reductions of 10 cm or higher are seen across the Beaufort and East Siberian Seas, with gains of over 10 cm over the Central Arctic Ocean. Large reductions in sea ice thickness can also be seen along the Atlantic facing sea ice edge. In Tsamados et al. (2014) a reduction in sea ice thickness across the sea ice cover is reported, though this reduction is noted to be particularly high within the Beaufort Sea and alongside the Canadian Arctic Archipelago and Greenland i.e. the locations where a reduction can be seen in Fig. 5.3. It should be noted that Tsamados et al. (2014) also report a total reduction in sea ice volume whereas here a small increase in sea ice volume is produced. This difference likely results from applying the changes to form drag parameters described in Schröder et al. (2019), hence regions where form drag caused a large reduction in sea ice thickness now see a moderate reduction and regions with a smaller reduction in sea ice thickness now see a moderate increase.

Tsamados et al. (2014) attributed the changes in sea ice thickness primarily to thermodynamic effects. As discussed in section 5.3, the form drag scheme replaces both the standard neutral drag coefficients and neutral heat transfer coefficients with terms calculated using the form drag scheme; the scheme also influences melting processes via the friction velocity. This means that where the total form drag is high, melting and freezing processes will be enhanced. Tsamados et al. (2014) concluded that the summer melt enhancement more than counters the winter sea ice growth enhancement. The regions where this effect is strongest correspond to heavily ridged regions. The results in Fig. 5.3 suggest that using the updated form drag parameters, with reduced impact factors for ridges and the ocean background drag coefficient, and higher impact factors for keels and the atmosphere background drag coefficient, changes the balance in some locations such that the increase in winter growth has a larger effect on the sea ice state than the increase in summer melting.

Whilst not identified as the dominant effect in Tsamados et al. (2014), the changes in sea ice drift are also likely to contribute to the distribution of sea ice volume. There are three key regimes that can be seen in patterns of Arctic sea ice drift averaged over 1979 – 2015 for winter seasons (defined as October to April): the Beaufort Gyre,

transpolar drift, and a motion system in the Kara Sea (Kaur et al., 2018). The clockwise (from an overhead perspective) Beaufort Gyre and transpolar drift will both act to transport sea ice to the Central Arctic. The sea ice circulation patterns also suggest a strong export of sea ice on the Atlantic facing edge, particularly through the Fram Strait. The Beaufort Gyre circulation and strong Atlantic facing export of sea ice persist through summer seasons as well as winter (Kwok et al., 2013). Tsamados et al. (2014) note that the new form drag parametrisation results in a stronger curl in oceanic drag, which would strengthen these circulation patterns, particularly the Beaufort Gyre. This would explain the broad redistribution patterns of the sea ice volume that is seen in Fig. 5.3. The reduction in thickness at the Atlantic facing edge can also be partially attributed to enhanced sea ice export in this region.

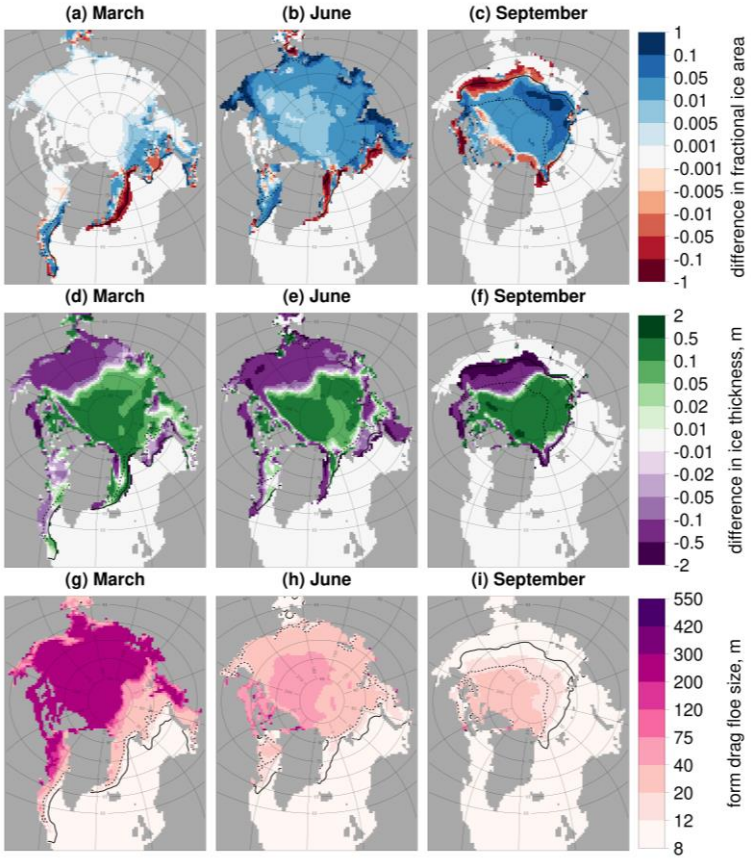

Figure 5.3: Difference in the sea ice concentration (top row, a-c) and ice thickness (middle row, d-f) between *fd-Lüpkes* and *nofd* and the form drag floe size for *fd-Lüpkes* (bottom row, g-i) averaged over 2000 – 2016. Results are presented for March (left column, a, d, g), June (middle column, b, e, h), and September (right column, c, f, i). Values are shown only in locations where the sea ice concentration exceeds 5 %. The inner (dashed black) and outer (solid black) extent of the MIZ averaged over the same period is also shown.

The difference in sea ice concentration in Fig. 5.3 generally shows a reduction in sea ice concentration for locations at the outer MIZ and an increase in the pack ice during summer months. These increases in the pack ice concentration are generally moderate with changes between 1 – 5 %. In the MIZ reductions frequently exceed 5 – 10 %. The reduction in marginal locations again is consistent with the strengthened export and enhanced melting in these locations. The increase in sea ice concentration within the pack ice suggests that the changes to the total sea ice drag increases the resilience of pack ice to the loss of sea ice cover, even in locations where there are reductions in the sea ice thickness. The high interannual variability seen in Fig. 5.1 can partly be understood by considering circulation patterns. Whilst distinct patterns can be seen in the mean behaviour over several years, the seasonal circulation pattern can vary significantly between years (Rampal et al., 2009). The impact of the form drag will depend significantly on this circulation pattern, which is a potentially significant contribution to the high interannual variability shown in Figs 5.1 and 5.2. In addition, there will be an inherent variability in the total form drag, which will also contribute to the high interannual variability shown in Fig. 5.1, particularly via the impact on sea ice thermodynamic processes.

Overall, the form drag scheme acts to enhance both sea ice melting and growth processes through changes to the heat transfer coefficient, which is directly linked within CICE to the momentum transfer coefficient, and indirectly via changes to the friction velocity. The internal redistribution of pack sea ice caused by the form drag scheme would be expected to increase the summer sea ice volume due to the increased accumulation of sea ice in regions that remain within the pack or inner MIZ throughout the year. However, this is compensated by the increased export of sea ice, particularly for Atlantic facing sea ice.

5.5 Importance of floe size to form drag impacts

In Sect. 5.4 the general impact of form drag on CICE-FSD simulations was assessed; in this section the focus will be specifically on the floe edge contribution to form drag. Tsamados et al. (2014) previously evaluated the contribution of floe edges to the total form drag, however the study did not consider any alternative schemes to the Lüpkes scheme to represent floe size, including the standard CICE assumption of a fixed floe size. The study provided some discussion of where floe size is expected to be an important contributor to the total form drag. In the pack ice, ridges and keels are

identified as the primary contributors to the total form drag. These features are expected to be particularly common in multi-year ice. The floe edge contribution is expected to be significant in locations where the sea ice concentration is lower. In particular, the contribution will be large where the sea ice cover is highly fragmented leading to a large total sea ice perimeter. Equation (5.6) shows that the contribution of floe edges to the total form drag is inversely proportional to floe size, hence where the form drag floe size is 300 m the total form drag contribution from floe edges will be small. In this section both *fd-Lüpkes* and *fd-leff* will be compared to *fd-cf300* to assess the floe edge contribution to form drag for both schemes to enable a discussion on the extent of floe size or FSD impacts on momentum exchange.

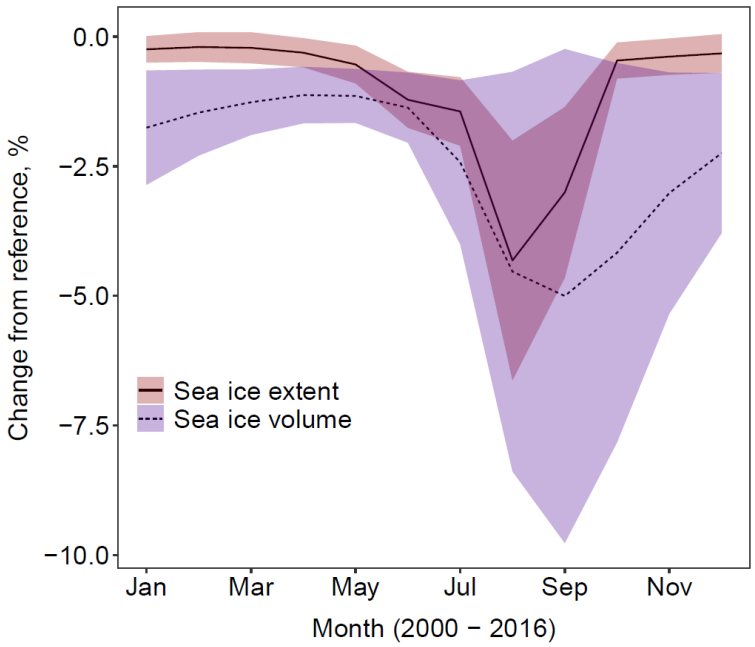

Figure 5.4: Difference in sea ice extent (solid, red ribbon) and volume (dashed, blue ribbon) of *fd-Lüpkes* relative to *fd-cf300* averaged over 2000 - 2016. The ribbon shows the region spanned by the mean value plus or minus two times the standard deviation. The use of the *Lüpkes* parameterisation for the form drag floe size causes significant reductions in the sea ice extent and volume throughout the melting season.

Figures 5.4 and 5.5 are equivalent to Figs 5.1 and 5.3 respectively, but this time comparing *fd-Lüpkes* to *fd-cf300*. Figure 5.4 shows that the sea ice extent and volume show a larger decrease over the melting season when using the Lüpkes scheme for the form drag floe size rather than constant floe size of 300 m. The difference in extent peaks in August with a reduction of just under 5 % and a variability of about 2 % around the mean. The difference in volume also increases through the melting season but instead peaks in September with a mean reduction of 5 %. This reduction persists

through the winter season with a mean reduction of at least 1 % throughout the year. The variability suggests that in some year these reductions can double, but in others the Lüpkes scheme and constant floe size give comparable results. Figure 5.5 shows a decrease in the sea ice concentration in the MIZ through the year for *fd-Lüpkes* compared to *fd-cf300* of about 1 – 5 %. Small changes in sea ice concentration can also be seen across much of the pack ice in June and September. The largest differences in sea ice thickness can be seen along the Canadian Arctic Archipelago and Greenland coast, with decreases exceeding 10 cm. Decreases of 1 to 5 cm can be seen within the Beaufort Sea. In September, large decreases in sea ice thickness can also be seen at the outer MIZ.

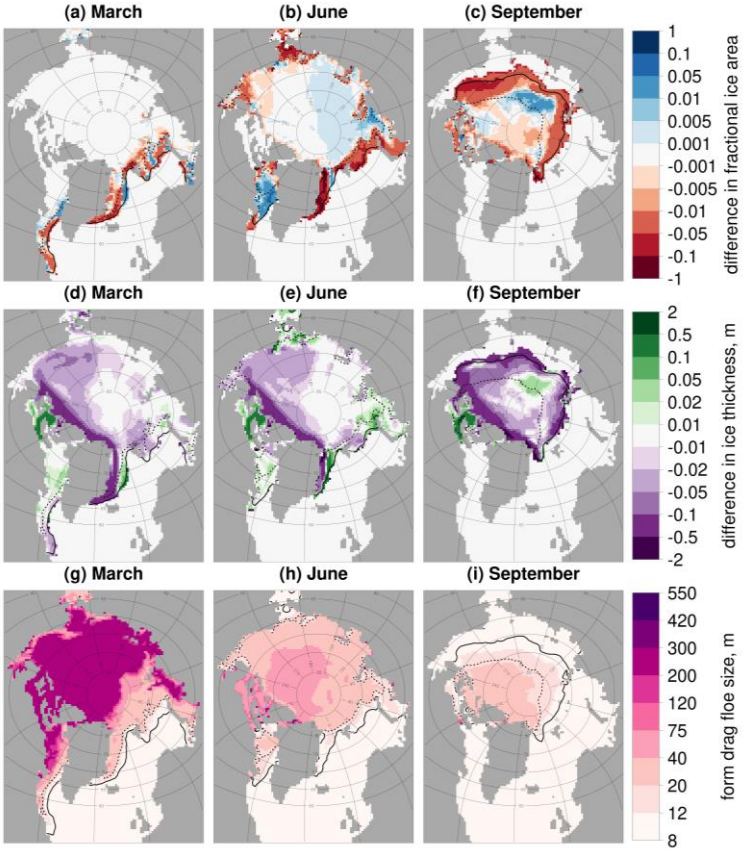

Figure 5.5: Difference in the sea ice concentration (top row, a-c) and ice thickness (middle row, d-f) between *fd-Lüpkes* and *fd-cf300* and the form drag floe size for *fd-Lüpkes* (bottom row, g-i) averaged over 2000 – 2016. Results are presented for March (left column, a, d, g), June (middle column, b, e, h), and September (right column, c, f, i). Values are shown only in locations where the sea ice concentration exceeds 5 %. The inner (dashed black) and outer (solid black) extent of the MIZ averaged over the same period is also shown.

The primary impact of the use of the Lüpkes scheme for floe size form drag rather than a fixed floe size of 300 m is the strong reduction in the summer sea ice mass balance. Figure 5.5 shows that the changes in sea ice concentration in the pack ice are generally small to negligible. This contrasts to the MIZ where the changes to the sea ice concentration are large and mostly negative. The Lüpkes-derived floe size in the pack ice ranges from 40 m up to 300m, whereas in the MIZ sizes mostly range from 8 to 20 m. Due to the inverse relationship between floe size and the floe contribution to form drag, the contribution of a 10 m floe to the total form drag will be 10 times larger than a floe of 100 m. In comparison, the contribution of a floe of 100 m in diameter will only be three times larger than the contribution of a 300 m floe. This means that the contribution of floe edges to form drag in the MIZ will be strongly enhanced relative to *fd-cf300*, whereas the changes in the pack ice are more moderate. It has also previously been noted that other factors are expected to dominate the total form drag for the pack ice, whereas floe edges are more significant in the MIZ.

The changes in sea ice thickness can persist throughout the year, but most notable is the reduction in thickness across both pack ice and the MIZ in September after the melting season. These impacts can be understood through the changes to the heat transfer coefficient and friction velocity. Where the form drag floe size is particularly small, melting and freezing rates will increase due to the higher heat transfer coefficient and friction velocity. The change in sea ice concentration is asymmetrical i.e. the loss in concentration over the melting season is more gradual than the increase in concentration during the freeze-up season. Due to the direct link between concentration and floe size within the Lüpkes scheme, the average form drag floe size is significantly lower during periods of melting than periods of freeze-up. This means that the use of the Lüpkes scheme preferentially enhances melting processes over freeze-up processes. In addition, sea ice loss can only be caused by heat flux-driven melting at ice-ocean or ice-atmosphere interfaces. In comparison, sea ice can form either through flux-driven freezing i.e. direct growth of floes, or through the formation and accumulation of frazil ice. Frazil ice forms due to the cooling of the surface mixed layer, and the primary mechanism of heat loss from the surface mixed layer in the early melt season is via longwave emission from the ocean surface and to a lesser extent heat fluxes across the atmosphere-ocean interface. These mechanisms of surface ocean cooling are not impacted by the form drag scheme. Reductions in the sea ice

thickness persist through the annual cycle and there is an overall net reduction in sea ice volume throughout the year.

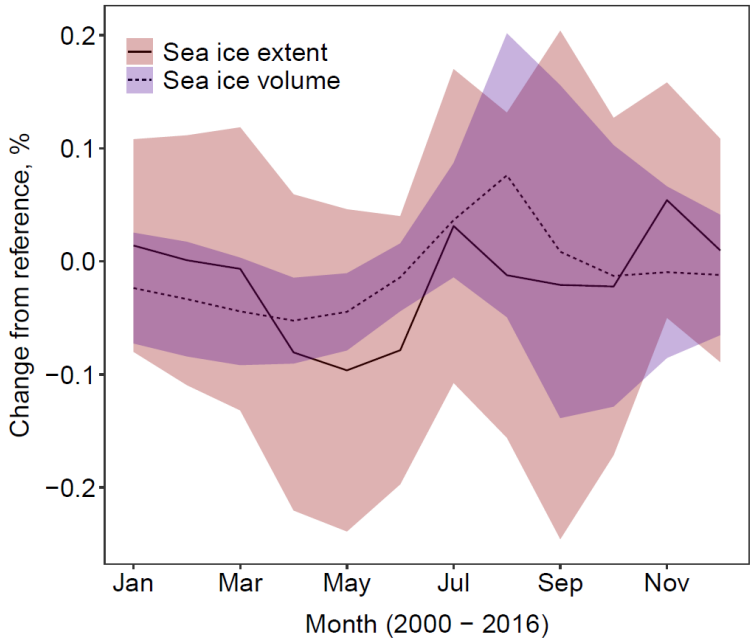

Figure 5.6: Difference in sea ice extent (solid, red ribbon) and volume (dashed, blue ribbon) of *fd-leff* relative to *fd-cf300* averaged over 2000 - 2016. The ribbon shows the region spanned by the mean value plus or minus two times the standard deviation. The two simulations are broadly comparably, with only small deviations of 0.1 – 0.2 % between them.

Figures 5.6 and 5.7 are equivalent to Figs 5.4 and 5.5 but this time comparing *fd-leff* to *fd-cf300*. Figure 5.6 shows that the mean differences in sea ice extent and volume never exceed 0.1 % in either direction. The interannual variability never extends up to about 0.2 % in either direction. Figure 5.7 shows that changes in the sea ice extent and concentration are small to negligible across almost the entire sea ice cover through March, June, and September. The Greenland Sea is the only exception to this, where a moderate reduction in sea ice concentration can be seen in March and June. The reason for such small impacts can be seen in the form drag floe size, which here is set equal to l_{eff}, determined by the WIPoFSD model. Across much of the sea ice cover it is above 300 m, with floes dropping to sizes below 40 m only in the outer MIZ. This means that for most of the sea ice cover, the floe edge contribution to form drag will either be comparable to or smaller than for *fd-cf300*. Only at the outer MIZ will there be a significant enhancement in the floe edge contribution, which is demonstrated here to be insufficient to cause large differences between the two simulations. The Greenland Sea, the only region where moderate changes in the sea ice cover can be seen, is Atlantic facing and therefore more exposed to ocean waves. The plots of the form drag

floe size show that smaller floes extend throughout the MIZ in this region, particularly in March. The Lüpkes scheme was derived from observations of the floe size from the Fram Strait, which is adjacent to the Greenland Sea, potentially explaining why the scheme predicts small floes across the MIZ. For the pack ice, the form drag floe size is about 550 m i.e. greater than the 300 m seen for *fd-cf300*. Despite this larger size, the differences in pack ice concentration and thickness shown in Fig. 5.7 are negligible. This suggests that where l_{eff} is of order 300 m or larger, the floe edge contribution to form drag is negligible.

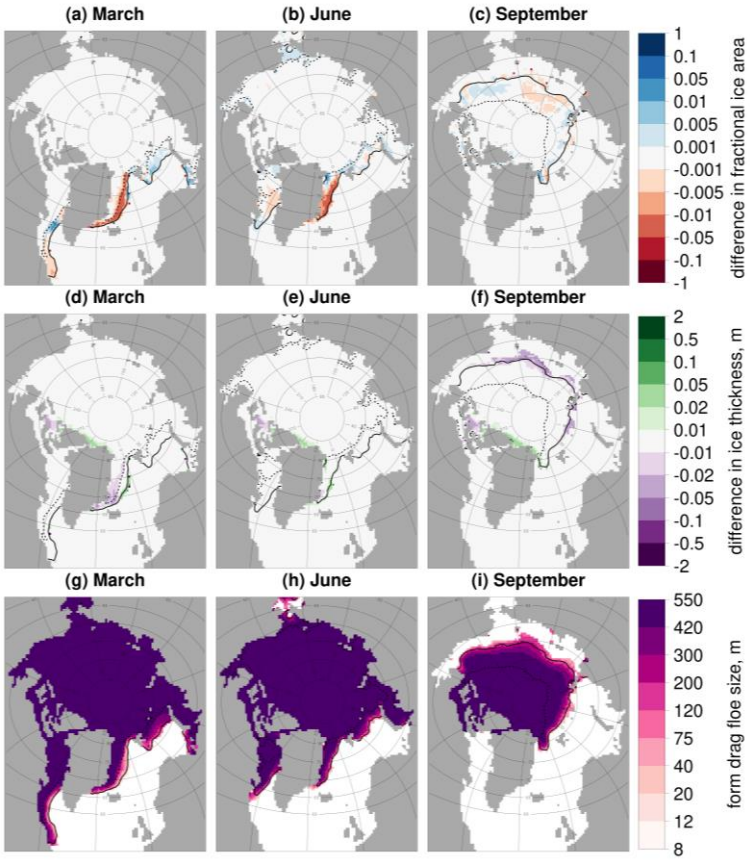

Figure 5.7: Difference in the sea ice concentration (top row, a-c) and ice thickness (middle row, d-f) between *fd-leff* and *fd-cf300* and the form drag floe size for *fd-leff* (bottom row, g-i) averaged over 2000 – 2016. Results are presented for March (left column, a, d, g), June (middle column, b, e, h), and September (right column, c, f, i). Values are shown only in locations where the sea ice concentration exceeds 5 %. The inner (dashed black) and outer (solid black) extent of the MIZ averaged over the same period is also shown.

The results presented in this section suggest that the floe edge contribution to form drag only becomes significant where l_{eff} drops below about 50 m. The distribution of l_{eff} that emerges from the WIPoFSD model setup used here suggests that this condition is generally not achieved in the current Arctic, with only locations particularly

exposed to ocean surface waves showing a moderate response in terms of the form drag impact. This scenario is different in the Antarctic, where stronger wave conditions favour the formation of smaller floes; small pancake ice floes are a frequent occurrence (Alberello et al., 2019). The Arctic is currently in a state of transition to one where waves are expected to play an increasingly important role (Thomson and Rogers, 2014); it is therefore plausible that the floe size contribution to form drag will become increasingly important.

These conclusions require that the WIPoFSD model setup with $d_{min} = 10\ m, d_{max} = 30\ km, \alpha = -2.5$ is a reasonable description of the sea ice FSD. The Lüpkes scheme is based on observations of floes from the Fram Strait in summer. This location is Atlantic Ocean facing and therefore particularly exposed to waves and not a region necessarily expected to be representative of floe behaviour across the sea ice cover. In Fig. 5.5, the average l_{eff} in September over 2000 – 2016 is approximately 20 m (l_{eff} is between 8 – 40 m at all locations). Comparing this value to Fig. 3.9, the two simulations using the WIPoFSD model with the closest average September l_{eff} had parameters $d_{min} = 10\ m, d_{max} = 30\ km, \alpha = -3.5$ and $d_{min} = 1\ m, d_{max} = 30\ km, \alpha = -3$ (this average was taken over 2007 – 2016 rather than 2000 – 2016). These parameter selections were chosen to span plausible values of α or d_{min} based on existing observations of the FSD, and therefore the large impact of the floe edge contribution to form drag produced by the Lüpkes scheme cannot be discounted based on these observations. In Chapter 6, it will be shown that the exponent that gives the best fit to novel observations of the FSD is -2.56, which does support *fd-leff* with standard model parameters as a more physically accurate description of the floe size contribution to form drag over *fd-Lüpkes* or other parameter choices for the WIPoFSD model. In addition, a recent study comparing the performance of the Tsamados et al. (2014) form drag scheme to in-situ measurements of ice-ocean form drag from autumn 2018 to autumn 2019 in the Beaufort Sea suggested that the form drag scheme appeared to be overestimating the floe size contribution to form drag by orders of magnitude (Brenner et al., 2020). A concentration-based approach to calculating floe size, such as used by Tsamados et al. (2014), would be a very simple and low computational cost approach to representing variable floe size within form drag schemes and sea ice models more generally. However, the evidence presented here suggests the Lüpkes scheme significantly underestimates the average size of floes and there is insufficient evidence to demonstrate a strong correlation between floe size and sea ice concentration.

5.6 Summary of chapter 5

In chapter 3, the impact of the FSD on sea ice thermodynamics was considered, specifically via changes to the lateral melt volume of the sea ice cover. However, this is one of several ways that floe size can impact the sea ice cover. Floe size can also impact the sea ice-atmosphere-ocean momentum exchange. The form drag formulation of Tsamados et al. (2014) replaces the standard CICE scheme for drag using constant drag coefficients with a scheme where the shape of the sea ice cover is accounted for, including the contribution from floe edges. The impact of this formulation, including adjustments to specific model parameters described in Schröder et al. (2019), on a sea ice simulation including the WIPoFSD model is explored. The changes to the sea ice cover that result from the use of the form drag scheme can be attributed to both thermodynamics (via changes to turbulent surface flux) and sea ice drift, consistent with Tsamados et al. (2014).

The specific contribution of floe edges to the overall impact of the form drag scheme is then considered through comparisons to a simulation where the form drag floe size is fixed at 300 m everywhere. Tsamados et al. (2014) calculate floe size using the scheme of Lüpkes et al. (2012), which expresses floe size as a function of the sea ice concentration. The use of the Lüpkes scheme for the floe size form drag results in a strong reduction in the sea ice extent and volume throughout the melting season compared to a fixed floe size of 300 m. This behaviour is attributed to increases in the heat transfer coefficient and friction velocity and a corresponding increase in melt within the MIZ over the melting season. The form drag floe size is then equated to l_{eff}, as calculated within the WIPoFSD model, with this setup showing only small differences to the case using a fixed 300 m form drag floe size. Moderate differences in sea ice concentration can be seen in the Greenland Sea, where ocean waves have a stronger influence on floe size. It is discussed how the Lüpkes scheme likely significantly overestimates the floe size contribution to form drag, with observations used to suggest that the much smaller impact of the floe size contribution to form drag found with the WIPoFSD model using standard parameters is a more realistic result. It is also speculated that the floe size contribution to form drag may increase in future as the Arctic sea ice retreats and waves have an increasing potential to influence the Arctic sea ice cover.

Chapter 6: A comparison of both a power-law and prognostic FSD model to observations of the FSD

In this chapter the prognostic approach to modelling the FSD is introduced, which has been adapted from the prognostic floe size-thickness distribution model of Roach et al. (2018a, 2019). This approach avoids assumptions about the shape of the distribution and instead allows the FSD to emerge from individual parameterisations derived using a combination of physical principles and process level observations. Whilst the prognostic model has the potential to better capture the impact of physical processes on the FSD, this does not necessarily mean that the emergent FSD from the prognostic model will be a better description of the observed FSD than a power-law fit. In this chapter firstly the prognostic model of Roach et al. (2018a, 2019) will be described, followed by details of amendments made to the localised version of the model used in this thesis. This is followed by a discussion of both the potential and limitations in the use of observations of the FSD to constrain FSD models. I then analyse novel observations of the FSD that have been produced by Byongjun Hwang and Yanan Wang from the University of Huddersfield. Finally, I compare the output of both the prognostic model and a power-law fit to these novel observations. It will be shown that a power-law description of the FSD is better able to represent these observations than the prognostic model in its current formulation for mid-sized floes.

6.1 The prognostic floe size-thickness distribution model

There has been significant progress recently towards the development of a prognostic floe size-thickness distribution model. This type of model makes no assumptions about the shape of the FSD, instead it distributes sea ice area between different floe size-thickness categories according to physical processes that have been observed to change the size of floes. This approach to modelling the FSD also allows the processes to be represented with higher physical fidelity than when using the WIPoFSD model. The prognostic scheme used here has been adapted from Roach et al. (2018a, 2019). A full derivation of the original prognostic floe size-thickness distribution model is presented in Horvat and Tziperman (2015) with several additional

parameterisations to this scheme described in Roach et al. (2018a, 2019). The essentials of the original prognostic floe size-thickness distribution model of Roach, Horvat, and others, that are pertinent to the present study, will be described here. The modifications made to the scheme that are unique to this study will then also be described. This modified version will hereafter be referred to as the prognostic FSD model (prognostic Floe Size-thickness Distribution model).

At the core of this model is the floe size-thickness probability distribution, $f(r,h)drdh$. This describes the fraction of a grid cell covered by floes with a radius between r and $r+dr$ and thickness between h and $h+dh$. Normalisation then requires:

$$\int_{r_{min}}^{r_{max}} \int_{0}^{h_{max}} f(r,h)drdh = 1. \tag{6.1}$$

The integral of $f(r,h)$ over the floe thickness range 0 to h_{max} gives the FSD, $F(r)$. The integral of $f(r,h)$ over the floe radius range r_{min} to r_{max} gives the ice-thickness distribution (ITD), $g(h)$. $g(h)$ is defined such that the integral from 0 to h_{max} is 1, and the integral from h_{min} to h_{max} gives the sea ice concentration. Therefore, the integral over thickness in Eq. (6.1) includes open water corresponding to $h=0$. To implement this scheme as defined would require a modification of the existing ITD scheme within CICE. It is however possible to define $L(r,h)$, the modified areal FSTD (mFSTD), such that:

$$f(r,h) = g(h)L(r,h). \tag{6.2}$$

This setup preserves the original ITD. $L(r,h)$ describes the fraction of sea ice with radius between r and $r+dr$ for a given thickness range between h and $h+dh$. The integral of $L(r,h)$ over the range r_{min} to r_{max} is 1. $L(r,h)$ is then discretised across lateral floe size space, analogous to the scheme used for the ITD (Hunke et al., 2015). In this new scheme Eq. (3.4), used to calculate the lateral melt rate, is evaluated at the mid-point of each floe size category.

6.2 Physical processes in the prognostic FSD model

$f(r,h)$ evolves in time as a result of several different processes, summarised by the following expression:

$$\frac{\partial f(r,h)}{\partial t} = -\nabla \cdot (f(r,h)\boldsymbol{v}) + \mathcal{L}_T + \mathcal{L}_M + \mathcal{L}_W. \quad (6.3)$$

$\nabla \cdot (f(r,h)\boldsymbol{v})$ represents the advection and divergence of the sea ice floe size-thickness distribution. Transport of $f(r,h)$ is achieved using the standard tracer advection scheme in CICE. $\mathcal{L}_M$ represents mechanical interactions between floes, including ridging and rafting. $\mathcal{L}_T$ represents thermodynamic changes to $f(r,h)$. $\mathcal{L}_W$ represents the fracture of sea ice floes by ocean surface waves. The standard CICE scheme for mechanical redistribution is used between ice thickness categories; this scheme does not change the mFSTD i.e. the area fractions of all floe radius categories change by the same proportion. In practice, floe size is expected to change the mechanical redistribution and advection behaviour but in this scheme these dependencies are not treated.

6.2.1 The thermodynamic term

The $\mathcal{L}_T$ term in Eq. (4.3) can be expanded as:

$$\mathcal{L}_T = -\nabla_{(r,h)} \cdot (f(r,h)\boldsymbol{G}) + \frac{2}{r} f(r,h) G_r + \mathcal{L}_{T,newfloes} + \mathcal{L}_{T,merging}. \quad (6.4)$$

$\mathcal{L}_{T,newfloes}$ and $\mathcal{L}_{T,merging}$ represent the impact from the formation of new floes and welding of existing floes respectively. **G** = (G_r, G_h), where G_r and G_h refer to the changes of floe radius or thickness in response to melt or freeze-up of existing floes respectively. For lateral melt, $G_r = \omega_{lat}$, the lateral melt rate. For lateral growth, $G_r = \frac{A_{lat} V_{new}}{\Delta t}$, where Δt is the model time step. V_{new} is the volume of new ice growth calculated within standard CICE. Note V_{new} here has units of m and is technically the increase in thickness if the new ice growth was uniformly distributed across a grid cell, used as a standard way within CICE to represent volume. A_{lat} represents the fraction of new ice growth that is taken to adhere to floe edges i.e. driving lateral growth of the floes. A derivation for A_{lat} is given in Roach et al. (2018a). Any remaining new sea ice formed in a timestep that is not attributed to lateral growth, i.e. $(1 - A_{lat})V_{new}$, is taken to form new floes. G_h is calculated through the standard CICE thermodynamic scheme for changes in sea ice thickness as a result of both top and basal growth and melt.

The first two terms on the right hand side in Eq. (6.4) represent contributions to $\mathcal{L}_T$ from lateral melt of floes, $\mathcal{L}_{T,latm}$, lateral growth of floes $\mathcal{L}_{T,latg}$, and changes in thickness from top and basal melting or basal growth, $\mathcal{L}_{T,th}$. These terms can be explicitly evaluated from Eq. (6.4):

$$\mathcal{L}_{T,latm} = -\frac{\partial}{\partial r}(\omega_{lat} f(r,h)) + \frac{2}{r}\omega_{lat} f(r,h), \tag{6.5}$$

$$\mathcal{L}_{T,latg} = -\frac{\partial}{\partial r}\left(\frac{A_{lat}V_{new}}{\Delta t} f(r,h)\right) + \frac{2}{r}\frac{A_{lat}V_{new}}{\Delta t} f(r,h), \tag{6.6}$$

$$\mathcal{L}_{T,th} = -\frac{\partial}{\partial h}(G_h f(r,h)). \tag{6.7}$$

The first term on the RHS for Eqs (6.5) - (6.7) represents the loss or gain of ice area to or from other size-thickness categories due to changes in floe size or thickness. The second term on the RHS for Eqs (6.5) and (6.6) represents change in ice area due to the physical loss or gain of ice area during lateral melting or growth. To understand the form of this term i.e. $\frac{2}{r} f(r,h) G_r$, first consider the total area of ice loss within a floe size-thickness category during a timestep. For each floe size-thickness category, this can be approximated as the product of the number of floes within the category, $\frac{f(r,h)}{\pi r^2}$, the change in floe radius from melting or growth in a single timestep, $G_h \Delta t$, and the circumference of each floe, $2\pi r$. Therefore, in the limit of small Δt, the following expression emerges: $\frac{\partial f(r,h)}{\partial t} = \frac{2}{r} f(r,h) G_h$, as expected. Note that this expression is only valid provided $G_h \Delta t \ll r$. In addition, the floe shape parameter, α_{shape}, has been neglected in this treatment. The complete derivation of the above expressions for changes in $f(r,h)$ due to melting and growth at the floe surfaces can be found within Horvat and Tziperman (2015).

The third term in Eq. (6.4) represents changes in $f(r,h)$ due to the formation of new sea ice floes:

$$\mathcal{L}_{T,newfloes} = \delta(r - r_x)\delta(h - h_{min})\dot{A}_p. \tag{6.8}$$

This function effectively means that $\mathcal{L}_{T,newfloes}$ takes the value $\dot{A}_p$ for $r = r_x$ and $h = h_{min}$ and is 0 otherwise. $\dot{A}_p$ is the rate of new floe formation and is a function of $(1 - A_{lat})V_{new}$ i.e. the available volume for new floe growth, and the thickness of the newly formed floes, h_{min}. There are alternative approaches to determine the radius of new floes that form, r_x. In Roach et al. (2018a), $r_x = r_{min}$ i.e. new floes form in the smallest floe size category. In Roach et al. (2019), a new wave dependent scheme is introduced to determine r_x. This new scheme is described in Sect. 6.2.3.

It is possible for floes to freeze together if in contact during freezing conditions (Shen and Ackley, 1991). The final term in Eq. (6.4) represents the welding together of floes:

$$\mathcal{L}_{T,merging} = \beta_{weld}. \tag{6.9}$$

β_{weld} represents gains and losses in the area distribution due to welding. Roach et al. (2018a) derive the following expression for how the number distribution of floes per unit area, N, changes with respect to welding:

$$\frac{\partial N}{\partial t} = -\frac{k}{2}A^2. \tag{6.10}$$

Here A is the sea ice area fraction, and k is the rate constant for merging. A lower bound for k has been determined from observations as 0.001 $m^{-2}s^{-1}$ (Roach et al., 2018b). Here a value of 0.01 $m^{-2}s^{-1}$ is taken for k.

6.2.2 The wave fracture term

The $\mathcal{L}_W$ term in Eq. (6.3) can be expanded as:

$$\mathcal{L}_W(r,h) = -\Omega(r,h) + \int_{r_{min}}^{r_{max}} \int_0^{h_{max}} \Omega(s,h_s)\zeta(r,h,s,h_s)dsdh_s. \tag{6.11}$$

$\Omega(r,h)drdh$ represents the fraction of a grid cell that is covered by floes of radius between r and $r + dr$ and thickness between h and $h + dh$ that is broken up by waves per unit time. $\zeta(r,h,s,h_s)drdh$ represents the fraction of a grid cell covered by floes of size between r and $r + dr$ and thickness between h and $h + dh$ that have formed from the wave break-up of floes of radius between s and $s + ds$ and thickness between $h_s +$

dh_s. The 1st term of the right-hand side in Eq. (6.11) is a sink and the 2nd term is a source of sea ice area for a given floe size-thickness category (where sinks and sources are smaller and larger floe size-thickness categories respectively).

$W(r)$ represents the histogram of floe sizes formed due to the fracture of sea ice by waves considered in 1D parallel to the direction of the wave propagation. $W(r)dr$ is equal to the number of floes of radius between r and $r + dr$ formed when waves propagate into a fully ice-covered domain of length D along the direction of wave propagation. Given the domain is completely covered by ice, the fractured floes must form a continuum i.e. the following condition must hold:

$$\int_{r_{min}}^{r_{max}} rW(r)dr = \frac{D}{2}. \tag{6.12}$$

ζ is then calculated as:

$$\zeta(r, h, s, h_s) = \frac{rW(r)}{\int_{r_{min}}^{s} rW(r)dr} \delta(h - h_s)\Theta(s - r). \tag{6.13}$$

Here $rW(r)$ is the total length of floes of size r that have formed from the breakup of floes of size s. $\int_{r_{min}}^{s} rW(r)dr$ represents the total length of floes of size s prior to break-up, calculated as the sum of the length of floes formed from this break-up and the remaining length of floes of size s that did not fragment. $\Theta(s - r)$ is a heavy-side step function i.e. it takes a value of 1 where s, the size of the original floes, is greater than r, the size of the newly formed floes. Elsewhere it is 0. This term is required since a floe of size s cannot break-up to form floes larger than size s. The $\delta(h - h_s)$ term is required since break-up of floes does not change floe thickness. To ensure Eq. (6.11) is conservative in sea ice area and volume, the integral of ζ across all floe size-thickness categories must be 1.

$\Omega(r, h)$ is calculated as the product of three terms:

$$\Omega(r, h) = f(r, h)\frac{c_g}{D}\left(\frac{2}{D}\int_{r_{min}}^{r} r'W(r')dr'\right). \tag{6.14}$$

$f(r,h)$ is the fraction of the ocean surface area covered by floes within the desired floe size-thickness category, $\frac{c_g}{D}$ gives the fraction of the domain reached by waves moving at group velocity per unit time, c_g, and $\frac{2}{D}\int_{r_{min}}^{r} r'W(r')dr'$ gives the fraction of a domain fully covered by ice that is broken up into floes smaller than the radius of interest, r.

To calculate $W(r)$, the histogram of new floe sizes, wave information is required within the sea ice cover. Observational products or hindcasts can be used to determine the ocean wave properties outside the sea ice cover. For each ice-covered grid cell, a trajectory is followed along a line of constant longitude until the nearest ice-free grid cell is reached. If this grid cell is land, then the model assumes there is no wave propagation into the present ice-covered grid cell. If the grid cell is ocean, the Bretschneider spectrum is calculated for that ocean grid cell. The wave attenuation along the trajectory from the ice-free cell to the ice-covered cell is then calculated as a quadratic function of mean sea ice thickness and wave period and is also influenced by the number of sea ice floes along the trajectory. Then, for the ice-covered grid cell, a sea surface height field can be constructed from the attenuated wave energy spectra. It is assumed that sea ice flexes with this sea surface height field, such that the distance between successive extrema will determine $W(r)$ where the imposed strain is enough to exceed a critical value. Full details of both the attenuation scheme and subsequent calculation of $W(r)$ are given in Horvat and Tziperman (2015).

To reduce the computational expense of this scheme, rather than calculating the exact $W(r)$ and c_g within each timestep, a lookup table is instead generated spanning different values of sea ice thickness, mean wave period, significant wave height and number of attenuating floes. A total of 5000 different scenarios are considered. Within each model timestep, the closest scenario is selected based on the present ocean surface wave and sea ice conditions, and the corresponding $W(r)$ and c_g selected. It should be noted that the construction of the sea surface height field to calculate $W(r)$ uses a random phase generator. This means that if a new lookup table is calculated for each new CICE simulation, the CICE model will no longer be deterministic.

6.2.3 Wave dependent growth scheme

Equation (6.8) describes changes to the floe size-thickness distribution from the formation of new sea ice floes. In Roach et al. (2018a), floes are always assumed to

form in the smallest category i.e. $r_x = r_{min}$. In such a formulation, all new floes can be considered to form as pancakes. Pancakes are common in locations with significant wave activity or high wind speeds and are particularly common in the Antarctic (Wadhams et al., 1987). However, new sea ice can also form as large sheets called nilas in calm conditions (Weeks and Ackley, 1986). Such calm conditions are significantly more likely in the Arctic where the Arctic ocean is mostly surrounded by continental land mass, constraining the fetch distance. Pancake ice is nevertheless increasing in frequency in the Arctic as wave fields become increasingly active (Thomson and Rogers, 2014).

Roach et al. (2019) introduced a new parameterisation to allow new ice to form as nilas rather than as pancake ice. This new scheme introduces a variable r_x, which is dependent on the local wave properties. A curved ocean surface will exert both a tensile and differential stress on newly forming sea ice floes (Shen et al., 2001), limiting the size of floes that can form during freezing conditions. Both laboratory (Shen et al., 2004) and field experiments (Roach et al, 2018b) suggest that during field conditions, tensile failure is the primary limit to the size of floes that can form. Based on both these observations and the work of Shen et al. (2001), Roach et al. (2019) introduce the following new parametrisation for r_x:

$$r_x = \sqrt{\frac{2C_2\lambda^2}{\pi^3 W_A g \rho_i}}. \tag{6.15}$$

Here λ is the wavelength, W_A is the wave amplitude, g is the gravitational acceleration, and ρ_i is the ice density. In this expression r_x reduces in size as the wavelength of the ocean surface waves decreases, or as the amplitude of these waves increases. This expression is derived by identifying the point of equilibrium between the tension from the differential pressure force on newly forming floes from waves in the horizontal, equal to $\frac{1}{4}\pi\rho_{ice}{r_x}^3 ghW_A\lambda^{-2}$, and a 'freezing force', equal to $C_2 r_x h$. Note waves also produce a differential shear force on the newly forming floes, but this term is neglected in Eq. (6.15) as the differential pressure force is expected to be the dominant term (Shen et al., 2004). A full derivation of Eq. (6.15) is provided in Shen et al. (2001). Roach et al. (2018b) estimate a value for C_2, the tensile stress mode parameter, of $0.167\ \mathrm{kgm^{-1}s^{-2}}$. This value is expected to be a function of temperature and salinity, however insufficient observations are available to determine a parameterisation in

terms of these variables. Equation (6.15) requires the assumption of a monochromatic wave field in its derivation. As such, λ is taken to be λ_p, the wavelength corresponding to the most energetic wave frequency. In line with Roach et al. (2018b), the wave amplitude can be calculated as follows:

$$W_A = \frac{H_{m0}}{2} = 4 \int E(f) df. \tag{6.16}$$

Here H_{m0} is the spectral height parameter and $E(f)$ is the wave energy spectrum as a function of frequency.

6.2.4 Calculation of additional wave properties within the sea ice

Alongside the new wave dependent growth scheme, Roach et al. (2019) also amend the prognostic floe size-thickness distribution model to operate with the ocean surface wave model Wavewatch III v5.16 (WAVEWATCH III Development Group, 2016). This model simulates wave attenuation in both the open ocean and within regions covered by sea ice. Wavewatch III can either be used to generate a hindcast for use as a forcing product within CICE, or actively coupled to CICE using a new floe size dependent attenuation empirical formulation (Roach et al., 2019).

The use of a full ocean surface wave model is outside the remit of this study, and as such the internal wave scheme described in Sect. 6.2.2. has been retained. This scheme has been adapted in the local version of the prognostic model to produce lookup tables for H_{m0}, the spectral wave parameter, and λ_p, the wavelength corresponding to the peak wave energy, alongside those already constructed for $W(r)$ and c_g. This information is required within sea ice-covered grid cells to evaluate Eq. (6.15).

It is worth commenting here on the different between H_{m0}, the spectral wave parameter, and H_s, the significant wave height. H_s is defined as the average size, measured from trough to peak, of the top third highest amplitude waves within a spectrum. It is considered a useful characteristic metric of waves as its value corresponds well to visually observed wave heights. H_{m0} is calculated from m_0, the total variance of a wave spectrum, as $4\sqrt{m_0}$. It is a statistical parameter of a wave spectrum that has been defined to correspond closely to the observed parameter, H_s.

These values are often used interchangeably, however H_{m0} and H_s are only equivalent for very narrow spectra that occur infrequently for real ocean waves. On average, $H_{m0} = 1.05H_s$; hence in most cases setting these values as identical is a reasonable approximation (Laing et al., 1998). It is nevertheless worth noting that the 'significant wave height' output within the sea ice field produced by both the WIPoFSD and prognostic FSD models is H_{m0} rather than H_s. The difference between these values is negligible compared to the errors in the respective wave attenuation schemes, where the errors are potentially as high as orders of magnitude due to the challenges in modelling the attenuation rate within sea ice.

6.3 Characterising the prognostic distribution

As discussed in Chapter 3, there are several metrics that can be used to characterise a floe size distribution. Roach et al. (2018) define a representative floe radius, r_a:

$$r_A = \frac{\int_{r_{min}}^{r_{max}} \int_0^{h_{max}} rf(r,h)drdh}{\int_{r_{min}}^{r_{max}} \int_0^{h_{max}} f(r,h)drdh}. \tag{6.17}$$

The area weighting of this metric makes it useful when considering the behaviour of larger floes in the distribution. It is also a useful metric to compare to observations that have a low resolution i.e. where larger floes are well characterised by the observations, but smaller floes are either under sampled or too small to be resolved e.g. Horvat et al. (2019). r_A is not useful for understanding the impact of an FSD on the sea ice mass balance because the behaviour of smaller floes in the distribution dominates the impact.

Roach et al. (2019) propose a new metric to better characterise the impact of the floe size-thickness distribution on the sea ice mass balance, the perimeter of floes per unit sea ice area, P_i. This is equivalent to the perimeter density, ρ_P^{fsd}, defined in Eq. (3.15) for the WIPoFSD model. For the WIPoFSD model, the perimeter density is used to define l_{eff}, the effective floe size, which is a single floe diameter that gives the same perimeter density per unit area of sea ice as a floe size distribution. l_{eff} and P_i are related to one another as per Eq. (3.16):

$$P_i = \frac{\pi}{\alpha_{shape} l_{eff}}. \tag{6.18}$$

Here l_{eff} will be used for consistency with chapter 3. P_i can be calculated for each ice thickness category in terms of $L(r,n)$, the modified areal FSTD defined in Eq. (6.2). For a given thickness category, n, the perimeter density per unit sea ice area can be calculated by summing the perimeter for each floe size category and dividing by the total sea ice area:

$$P_{i,n} = \frac{\pi \int_{r_{min}}^{r_{max}} r^{-1} L(r,n)\, dr}{2\alpha_{shape} \int_{r_{min}}^{r_{max}} L(r,n)\, dr}. \tag{6.19}$$

Note that $\int_{r_{min}}^{r_{max}} L(r,n)\, dr$ is equal to 1 by definition. $l_{eff,n}$ can then be evaluated for the prognostic model using Eq. (6.18) and (6.19) to give:

$$l_{eff.n} = \frac{2}{\int_{r_{min}}^{r_{max}} r^{-1} L(r,n)\, dr}. \tag{6.20}$$

A representative l_{eff} for the full FSD can then be calculated as the area-weighted average value of l_{eff} across the thickness categories.

A 2nd new characterising parameter is introduced here, a 'fitted' power-law exponent, l_{exp}. To enable a useful comparison between the prognostic FSD and WIPoFSD model, it is helpful to estimate an exponent for the floe size distribution within each grid cell, assuming a power law is a good fit to the distribution. To do this, the number distribution, $N(x)$, is expressed as $nS(x)$, where $S(x)$ is some distribution that is proportional to $N(x)$ and n is the required conversion factor. In the case of the prognostic FSD model, a valid expression for $S(x)$ is:

$$S(r_k) = \frac{a_k}{w_k \pi r_k^2}, \tag{6.21}$$

where, for a given floe size category, a_k is the total sea ice area (summed across all thickness categories), w_k is the total width of the category, and r_k is the midpoint radius

for the category. The natural log is then taken for the power-law distribution, $nS(r_k) = Cr_k{}^{\alpha}$:

$$\ln S(r_k) = \alpha \ln r_k + D. \tag{6.22}$$

Here $D = \ln C - \ln n$. Note that this expression holds whether x is the radius or diameter, as any factor combined with x can be incorporated into the constant, D. Therefore, an estimate for α can be obtained through linear regression of $\ln S(r_k)$ plotted against $\ln r_k$. Note that α is calculated such that where a distribution exists, a value can be calculated, regardless of whether the distribution follows a power law in practice.

The important information that this calculated α provides is the strength of any trend in the number distribution of floes as the size increases. It will provide useful information on where the ratio of smaller floes to larger floes is higher, and where it is lower. This provides an additional metric, alongside l_{eff}, to assess spatial and temporal variability of the FSD within the prognostic FSD model and to consider in comparisons with the WIPoFSD model. l_{exp} does not provide any indication of whether a power law is an appropriate fit to the number distribution. Whilst it would be possible to estimate confidence intervals for l_{exp}, this has not been done here because, as outlined above, l_{exp} is used as a characterising metric on the ratio of smaller to larger floes rather than to provide an estimate on the value of α for a given FSD. If the latter was the aim, it would also be necessary to assess whether a power law is a good fit to the emergent FSD.

6.4 Existing observations of the FSD

It has previously been discussed (see Sects 1.3 and 3.1) that observations of the FSD are generally fitted to a power law. Figure 6.1 is a summary of the exponents reported for the majority of FSD observation studies that use a power-law fit (or multiple power-law fit), which has been adapted from Stern et al. (2018a). There are two frequently used ways to report the distribution, either as a probability density distribution or as a cumulative distribution, where the value for a given floe size is the number of floes of that size or larger. There are two key ways these distributions differ: the exponent reported for the cumulative distribution will be one higher (i.e. less negative) than the

same distribution plotted as a probability density distribution; and if a distribution is an upper-truncated power law for the probability density distribution, then in the cumulative distribution it will not plot as an exact power law but instead will show a tailing off behaviour for larger floes. Stern et al. (2018a) suggested that the tailing off behaviour seen for larger floes in studies such as Toyota et al. (2006) can be explained by this upper-truncation effect and should not necessarily be interpreted as a physical feature of the distribution. This upper-truncation effect may also lead to a negative bias in the exponents reported for the cumulative distribution. Figure 6.1 shows a large amount of variability of the possible exponents. Even considering the studies that report an exponent for the probability density function only, the results still span a range from -1.9 to -3.5.

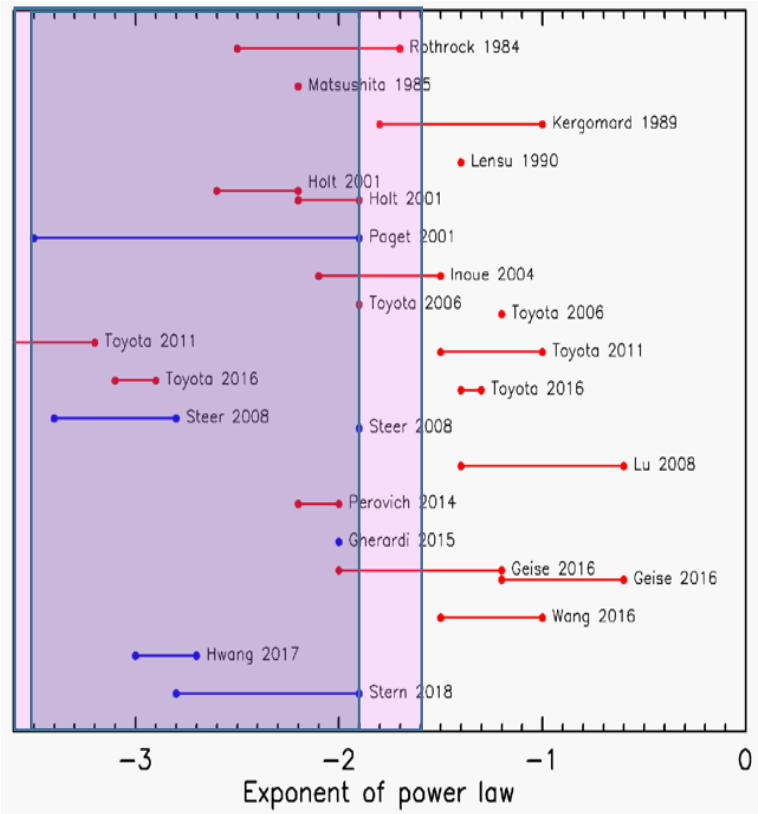

Figure 6.1: Values measured for the fitted exponent to the floe size number distribution from observational studies. Blue lines are exponents reported for the probability density distribution and the blue translucent box covers the region spanned by these values. Red lines are exponents reported for the cumulative distribution. The red translucent box covers the majority range spanned by these values but shifted down by 1 to be consistent with the values reported for the probability density distribution. Plot has been modified from Fig. 4 in Stern et al. (2018a) under CC BY 4.0 (https://creativecommons.org/licenses/by/4.0/).

There is some observational evidence of both the spatial and temporal variability of the FSD. Stern et al. (2018b) analyse MODIS (Moderate Resolution Imaging Spectroradiometer, http://modis.gsfc.nasa.gov/) satellite imagery collected over the Beaufort and Chukchi seas and report the exponent of the fitted power law in each case. The imagery has a pixel size of 250 m and the total image size of approximately 2000 km by 2000 km. The minimum floe size that can be resolved is taken to be 2 km, and the maximum size that can be sampled with reasonable frequency is taken to be 30 km. Data is collected for both 2013 and 2014, with 116 cloud free regions identified and analysed in 2013 and 140 regions in 2014. The study considers how the mean exponent changes through the melting season in both 2013 and 2014 from March to October. Both 2013 and 2014 behave in a remarkably similar way, showing approximately sinusoidal behaviour with a minimum exponent of about -2.8 in August and a maximum exponent of about -1.9 in April. These results cannot necessarily be considered representative for the full Arctic sea ice cover. The Chukchi and Beaufort Seas are expected to be more isolated from wave activity than the Atlantic facing sea ice edge, such as within the Fram Strait. This analysis also does not consider the full FSD, not accounting for any floes smaller than 2 km. Perovich and Jones (2014) also find evidence of seasonal variation in the exponent. Analysis of aerial photographic imagery was analysed from an expedition within the Beaufort Sea over the period June to September 1998 over a floe size range from 10 m to 10 km. A change in exponent from -3.0 over June and July to -3.2 in late August was associated with a high wind speed event driving fragmentation of floes under wind and ocean stress. The exponent then increased to above -3.1 by September due to freeze-up and welding.

The results from both Stern et al. (2018b) and Perovich and Jones (2014) suggest that an annual cycle in the exponent could explain some of the variability seen between observations. However, these studies also demonstrate the challenge in reaching this conclusion, since whilst the sign of gradients in the exponent over time reported for each study are consistent, the absolute values are not. There are several differences between the studies including different sampling years, different floe size ranges, and different methods of measuring the exponent (one considers a standard number density distribution, one a cumulative distribution), which may all contribute to differences in the measured exponent. This makes direct and fair comparisons between the exponents reported within these studies challenging. Perovich and Jones (2014) also noted that changes in exponent could sometimes be associated with

specific events such as high winds speeds. However, the consistency in the sign of any trend in the exponent over the period June to August and then August to September for both studies is an interesting and potentially useful observation.

There have been efforts to develop an FSD metric that can easily be produced as a product from satellite data (Horvat et al., 2019); the area weighted mean floe size, referred to as the representative radius. The minimum resolvable floe diameter for this product is taken to be 300 m and maximum size is taken to be 100 km. Spatial plots of the averaged representative radius are presented in Horvat et al. (2019) for two annual periods averaged over 2010 - 2018: October to December and February to April. The spatial distribution between these two time periods is similar, but large spatial differences in the representative radius can be seen. The smallest values can be seen in the Laptev and East Siberian Seas of order 1 km, increasing up to maximum values of 10 km in the Central Arctic. This study also considers whether the FSD data collected supports the use of a power-law fit to the FSD. It concludes that in general power law scaling is a poor description of the FSD, though in some locations a power-law fit cannot be ruled out for floes smaller than 6.5 km.

There are several challenges in understanding the shape and variability of the FSD. The remoteness of the Arctic sea ice makes in-situ studies of the FSD expensive and time consuming to carry out. Furthermore, these studies are only plausible over restricted time periods and spatial scales. Analysis of satellite imagery allows the FSD to be studied over larger spatial and temporal scales, but this can be intermittent and restricted by satellite paths. In addition, the resolution and spatial extent of the imagery produced by different satellites are limited, and generally higher resolution means a reduced spatial scale, and vice versa. For example, Stern et al. (2018b) consider two different satellite products, the MODIS imagery, which is taken to be suitable for floes between 2 km and 30 km in size; and the MEDEA imagery (Kwok and Untersteiner, 2011; http://gfl.usgs.gov/), suitable for floes of between 10 m to 5 km. In this specific study, scenarios are identified where the MODIS and MEDEA imagery is collected for similar locations and times, allowing an FSD to be constructed from 10 m to 30 km. Toyota et al. (2006) uses a similar approach, combining in-situ FSD data with satellite data to extend the range of analysis from scales of sub metre to scales of kilometres. These examples are exceptional, however, and in general floe size data is presented over a much smaller range of floe sizes. When FSD data is presented in studies, it cannot be assumed that the selected floe size range to present data over is necessarily

suitable for the limitations of the data collection and analysis. Hence, particularly for very small and large floes, it is unclear if any observed changes to the shape of the distribution are physical features or a result of the limited resolution or extent.

6.5 Novel observations of the FSD

To assess the performance of the two alternative FSD models, it is useful to consider a new observational dataset that has not been used to motivate the development of either FSD model. It is also useful to have data obtained from different sea ice locations and years, to assess whether each model can capture the necessary spatial and temporal variability. Byongjun Hwang and Yanan Wang, both of the University of Huddersfield, have produced a new set of FSD data from observations as part of the NERC funded project 'Towards a marginal Arctic sea ice cover' (NE/R000654/1). This floe size dataset has been generated from the GFL HRVI (Global Fiducials Library high-resolution visible-band image) imagery that has been declassified by the MEDEA group (Kwok and Untersteiner, 2011). This has been made available publicly as LIDPs (Literal Image Derived Products) at 1 m resolution (available at http://gfl.usgs.gov/).

The observations consist of 37 separate samples collected from three regions: the Chukchi Sea (70 N, 170 W); the East Siberian sea (82 N, 150 E); and the Fram Straight (84.9 N, 0.5 E). The observations cover three months, May – July, spanning 2000 – 2014. The raw floe size data has been retrieved using the algorithm described in Hwang et al. (2017). The total image size varies between observations, but generally has length dimensions of 10 – 20 km.

6.5.1 Analysis of floe size data

The raw floe size data consists of a list of individual floe sizes. A series of discrete floe size categories must therefore be identified to enable an analysis of the shape of the distribution. For each category, the perimeter density per unit sea ice averaged across all floes in the category is reported at the mid-point. The perimeter density is plotted rather than the number or area distribution as it is the perimeter that has been identified as most relevant to the impact of the FSD in sea ice models through lateral melt.

The floe size categories from the prognostic FSD model will be used to enable the comparison between FSD data and model output. Any floes that exceed the upper diameter cut-off of the largest category, 1892 m, will be discarded from the analysis. This step is necessary because the presence of a single particularly large floe in some images causes a large perturbation across the distribution reported for that location. Instead, only floe size categories that are small enough to consistently be populated by multiple floes across all sampled images should be considered. A lower floe size cut-off is also applied to this analysis. Figure 6.2 shows the perimeter density distribution of the same image with either a pixel size of 1 m or 2 m. The distribution shown in figure 6.2 is relatively consistent for the two scenarios above 100 m, but below 100 m a strong deviation in the distribution can be seen. This suggests that the methodology to produce the raw FSD data has a minimum resolution of around 50 times the pixel size. This ratio of pixel size to resolved floe size is high because to identify discrete floes, the separation between floes must be resolved in addition to the floes themselves. In this case the lower floe size cut-off is taken to be a diameter of 104.8 m so that only the range not sensitive to the reduction in resolution is considered. Once floes outside the range of 104.8 m to 1892 m in diameter have been discarded, the total area of remaining floes is calculated and taken to be the total sea ice area for normalising the reported perimeter density (perimeter per unit sea ice area). The perimeter density distributions presented in the remainder of this chapter use the 2 m pixel size data.

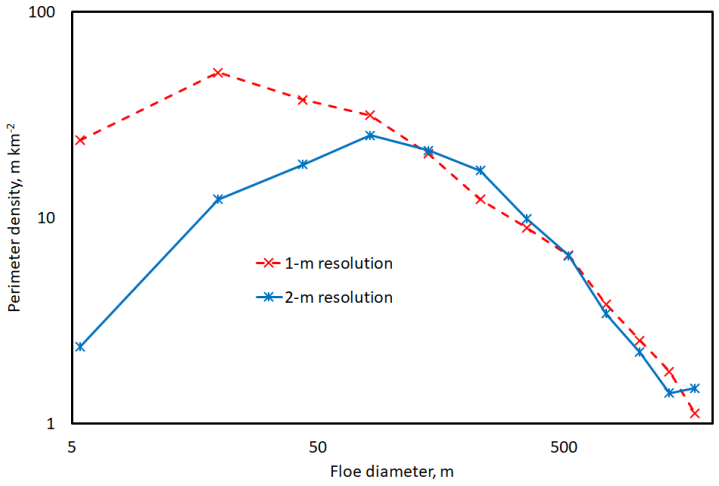

Figure 6.2: Comparison of the perimeter density distribution reported from a single LIDP satellite image for the standard pixel size of 1 m (red, dashed, crosses) and for a degraded pixel size of 2 m (blue, solid, stars). The floe size data used within this figure was produced by Byongjun Hwang using the methodology of Hwang et al. (2017). Floe sizes have been sorted into 12 bins with Gaussian spacing as per Roach et al. (2018a).

6.5.2 Summary of the FSD observations

In this section an overview of the novel observations of the FSD will be presented. The aim here is not to provide a detailed analysis of the observations, but a general overview of the spatial and temporal variability to enable a comparison to model output. Figure 6.3 provides a summary of the results for each LIDP satellite image included in the analysis. This figure shows that the perimeter density distribution in each location broadly follows a similar curve.

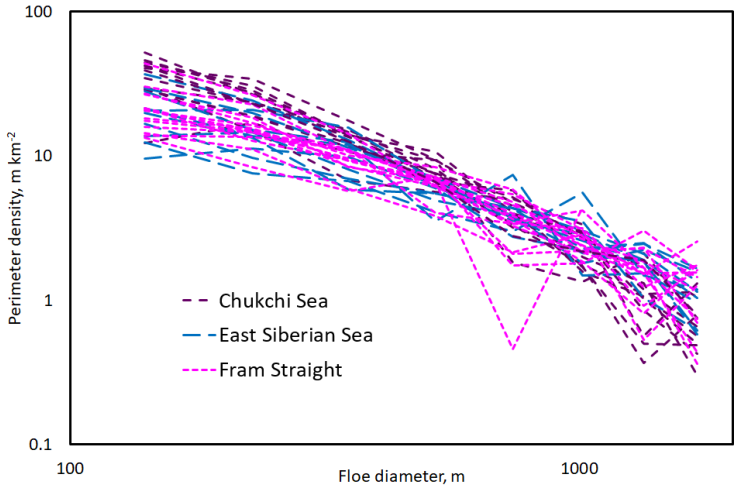

Figure 6.3: A summary of the perimeter density distribution reported from 37 different LIDP satellite images in three different locations: Chukchi sea (plum, medium dash), Fram straight (pink, short dash), and East Siberian sea (blue, long dash). The floe size data used within this figure was produced by Byongjun Hwang using the methodology of Hwang et al. (2017). In general, each perimeter density distributions follows a similar curve.

For the purpose of model comparison, it is useful to assess whether the variability seen in the observations can be attributed to spatial or temporal variation or is primarily a result of the methodology. To assess spatial variability, it is useful to perform a power-law fit to the observations at each location. Even if a power-law fit is not necessarily a good description of the general shape of the distribution, this approach should provide some insight into the balance between smaller and larger flows at each location. Yanan Wang (University of Huddersfield) has calculated the mean exponent for each location using the methodology outlined in Virkar and Clauset (2014). Note that this methodology is applied to the cumulative number distribution and considers floes of all sizes, not just the truncated set outlined in Sect. 6.5.1. This analysis produced the following values for the floe number distribution exponent, α, and associated errors: Chukchi Sea, - 2.75 ± 0.34; East Siberian Sea, - 2.46 ± 0.35; Fram Strait, - 2.46 ± 0.25 (Wang et al., 2020). The mean values for the exponent suggest that the ratio of smaller

to larger floes is similar in both the East Siberian Sea and Fram Strait, with a higher ratio indicated for the Chukchi Sea. However, these results are not enough to demonstrate spatial variability unequivocally in the FSD, due to the overlap in the error bounds. This is consistent with the results presented in Fig. 6.3, where the variability for the perimeter density distributions within each location dominates over the variability between locations.

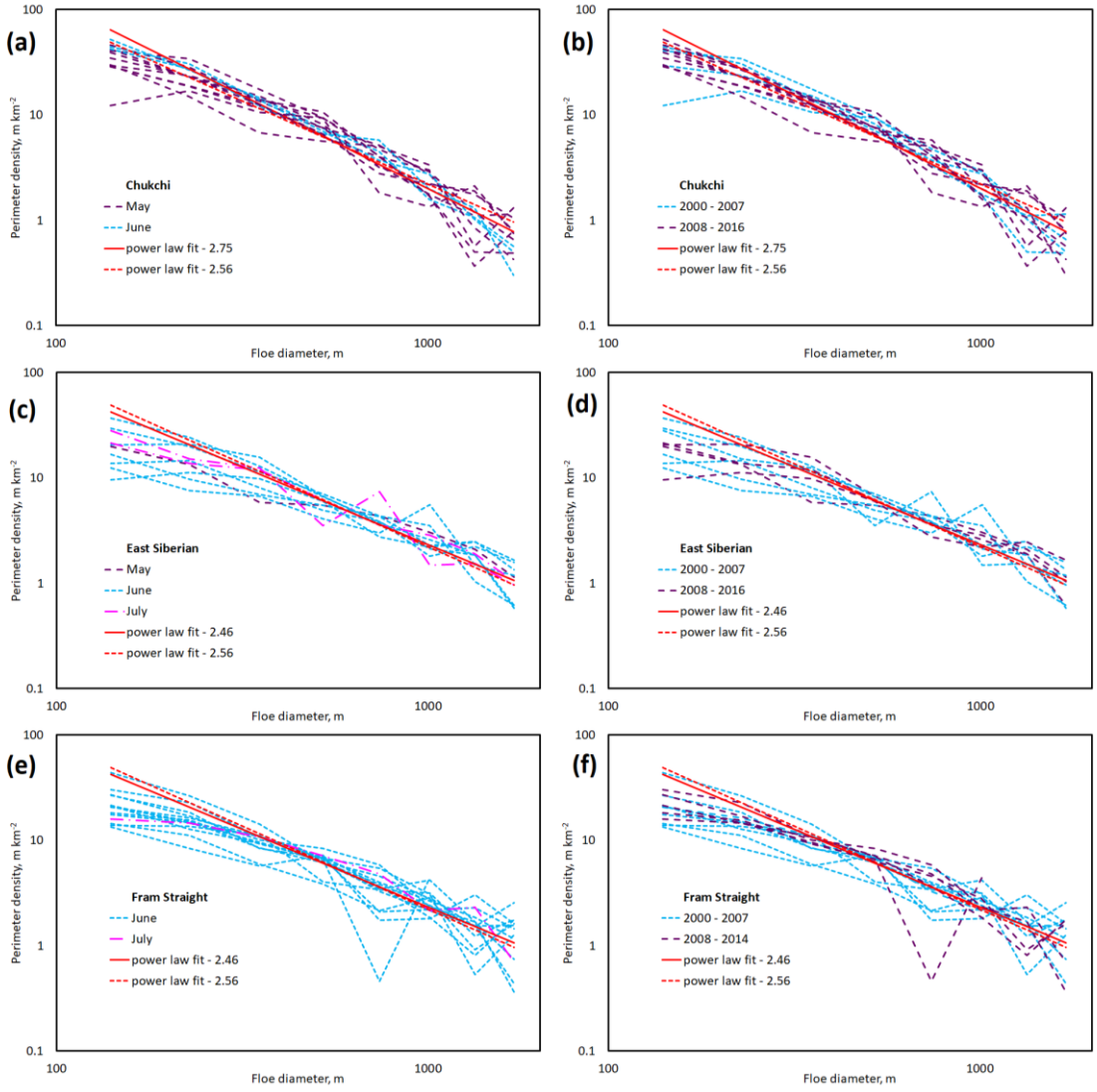

Figure 6.4: A summary of the perimeter density distributions categorised by month (a, c, e) or year (b, d, f) for the Chukchi sea (a, b), East Siberian sea (c, d) or Fram Straight (e, f). For plots a, c and e, observations are categorised as May (purple, long dash), June (blue, short dash) or July (pink, dot-dash). For plots d, b and f, observations are categorised as from either 2000 – 2007 (blue, short dash) or 2008 – 2014 (purple, long dash). A power-law fit to each location (red, solid) and averaged across all locations (red, dashed) is also shown. The floe size data used within this figure was produced by Byongjun Hwang using the methodology of Hwang et al. (2017). The exponent of the power-law fit was calculated by Yanan Wang using the methodology of Virkar and Clauset (2014).

Figure 6.4 categorises the observations at each location by either month or year to identify if there is any evidence for an annual cycle or inter-annual trends in the exponent. The figures show that there are no clear changes in FSD behaviour over the period May to July or from the 2000 – 2007 to 2008 – 2014 period. Hence the variability seen within each location appears to be dominated by random variation rather than as a result of any temporal cycles or trends. It is not possible to distinguish here the extent to which this variability is a physical feature of the FSD or a result of the finite image size to produce the distributions and other sources of error associated with the methodology.

Stern et al. (2018b) used observations of the FSD taken from the Beaufort and Chukchi Seas throughout the year to understand how the exponent changes over an annual cycle for this region. For both years considered, 2013 and 2014, the study reported a sinusoidal evolution of the exponent between limits of -1.9 and -2.8. Over the period May to June, the exponent decreased from about -2.2 to -2.8. This range is consistent with the values reported above, including for the Chukchi Sea. It is possible that if additional months were included in the analysis presented here, an annual cycle could be identified. As with the results presented here, Stern et al. (2018b) do not find any evidence for interannual trends in the FSD shape.

6.6 Comparing model output to observations

The lack of spatial or temporal variation within observations of the FSD over diameters from 100 m to 1700 m presented in Sect. 6.5 presents a useful opportunity to compare these observations with the emergent FSD from the prognostic model. If the prognostic model includes all relevant processes to determining the shape of the FSD for mid-sized floes, the observations and model output should be comparable to within the observed variability, even if the model does not replicate the precise thermodynamic and mechanical conditions of the observations.

6.6.1 Methodology for comparison

The CPOM (Centre for Polar Observation and Modelling) version of CICE, as described in Sect. 3.2, will be used. The setup used here is mostly identical to that used in Chapter 3, again using the prognostic mixed layer of Petty et al. (2014) rather than the default CICE fixed slab ocean mixed layer. The surface forcing is derived from

the 6 hourly NCEP-2 reanalysis fields (Kanamitsu et al., 2002) and wave properties are updated every 6 hours for grid cells with less than 1% sea ice cover using the ERA-interim reanalysis dataset (Dee et al., 2011). The form drag parameterisation of Tsamados et al. (2014) will also be used including the changes to form drag parameters described in Sect. 5.3, as per Schröder et al. (2019). The form drag floe size used within the scheme will be the prognostic model effective floe size as calculated in Sect. 6.3. The longwave emissivity is also increased from 0.95 to 0.976, as per Sect. 5.3.

The prognostic FSD model, as described in Sect. 6.2, will be used. The FSD model will include a total of 16 floe size categories using Gaussian spacing to determine the interval size for consistency with Roach et al. (2018a). The standard 5 ice thickness categories used within CICE are retained here for the ITD (Hunke et al., 2015). The simulation is then initiated with a sea ice free Arctic on 1st January 1980 and evaluated over a 37-year period until 31st December 2016. The standard 12 floe size categories have not been used here as the prognostic model produces an unphysical 'uptick' in the largest few categories. By using 16 floe size categories rather than 12, the largest 4 floe size categories that include this 'uptick' will fall outside the range of floe sizes included in the comparison. This 'uptick' within the FSD simulated by the prognostic model has also been reported by Roach et al. (2018a).

Figure 6.5 presents an example of the model output from this simulation with 16 floe size categories, showing the perimeter density distribution within the MIZ for April, June, and August, averaged over 2000-2016. Figure 6.5 also demonstrates how the 'uptick' is confined to the largest 3-4 floe size categories; when using 16 floe size categories this uptick falls outside the range of comparison between prognostic model output and observations. There are two plausible reasons for the formation of the 'uptick': floes that would otherwise grow to larger sizes than the upper size limit of the largest category are instead accumulating in this largest category; or the model is missing important floe fragmentation processes or misrepresenting processes already included within the model. Of these, the latter will be discussed and investigated further within this chapter and the next through the comparison of model output to observations. If the former effect is responsible i.e. the 'uptick' is simply a response to using a fixed maximum floe size, then it should not impact the physical realism of the model. Floes of size of order 1000 m will not have a significant impact on the lateral

melt volume or form drag, as both the lateral melt rate and floe edge contribution to form drag are inversely proportional to floe size.

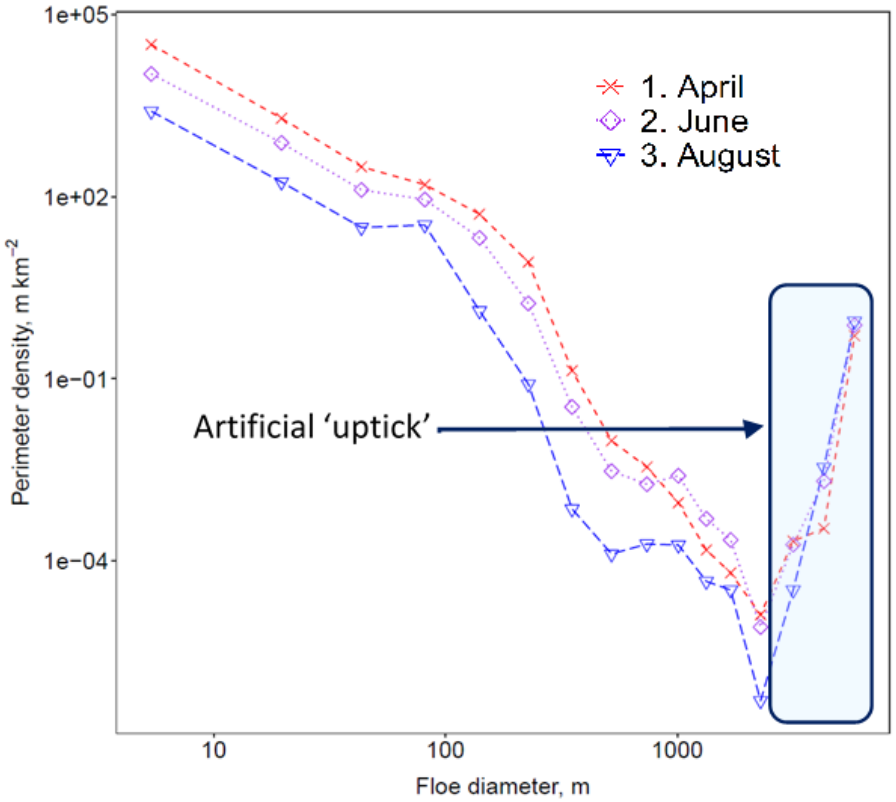

Figure 6.5: An example of prognostic model output using 16 floe size categories with Gaussian spacing. Presented in the figure is the perimeter density distribution, $m\ km^{-2}$ for the April MIZ (red, cross, dashed), June MIZ (purple, diamond, dotted), and August MIZ (blue, triangle, long-dash) averaged over 2000 – 2016. Also highlighted in the figure by a blue transparent box is an artificial 'uptick', a non-physical feature of the model also reported by Roach et al. (2018a).

6.6.2 Standard prognostic model compared to observations

To compare model output to the observations of the FSD, two sample years will be selected for each location: Chukchi Sea, May – June 2006 (4 LIDPs), May 2014 (4 LIDPs); East Siberian Sea, June 2001 (3 LIDPs), June – July 2013 (2 LIDPs); Fram Strait, June 2001 (6 LIDPs), June 2013 (2 LIDPs). These specific years have been selected as they all include at least two separate LIDPs. Perimeter density distributions from the prognostic model are reported as an average over one or two months for the relevant region. The choice of months for this average has been selected to minimise the difference between the mean day of collection for observations and median day of the model output. Figure 6.6 shows the specific areas over which the FSD is averaged. Each case study area consists of a set of 5 x 5 grid cells that includes the location

where the observations were drawn from. Figure 6.7 then shows a comparison for each selected case study between the FSD observations, a power-law fit, and the prognostic model output.

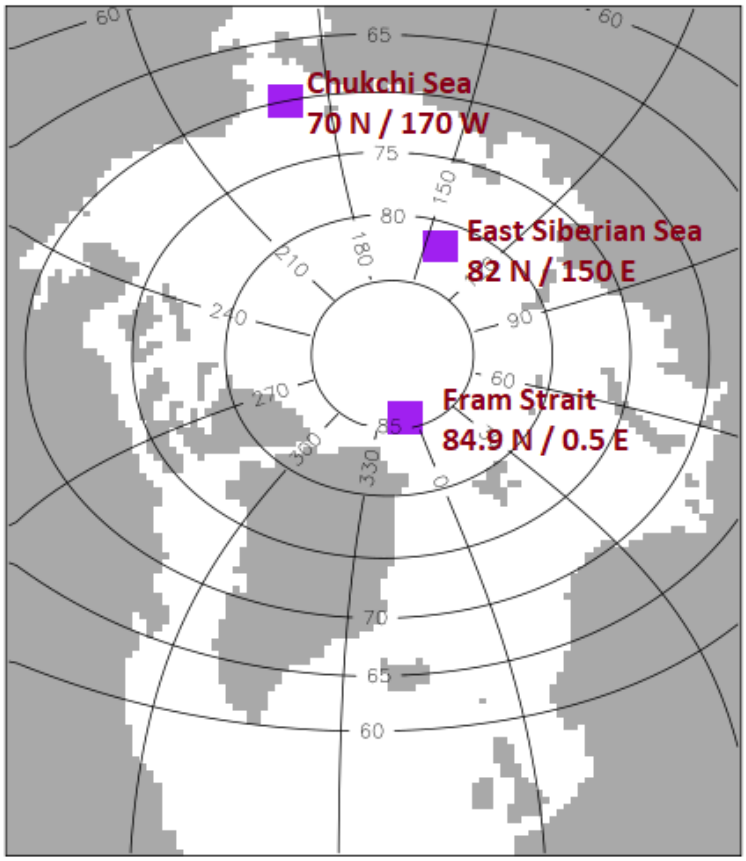

Figure 6.6: Boxes indicate the areas over which the prognostic model emergent FSD is averaged to represent the three locations included in the observational study. Each case study area spans a set of 5 x 5 grid cells that includes the site stated for collection of observations.

The results in Fig. 6.7 show that the standard prognostic model performs poorly in capturing the behaviour of the FSD for mid-sized floes in the range 100 – 2000 m. The perimeter density distribution predicted by the prognostic model for each category is in general multiple orders of magnitude from the observed value. In particular, the slope of the distribution is much steeper (more negative) for the model output than observations. The Fram Strait in June 2013 is the only location where the observations and model output are broadly comparable, and even here the gap is significant. It should be noted that whilst the prognostic model performs poorly in simulating the behaviour of mid-sized floes, this conclusion may not extend to floes outside the range

of the comparison, including floes smaller than 100 m that are particularly important for determining the impact of the FSD on the sea ice mass balance.

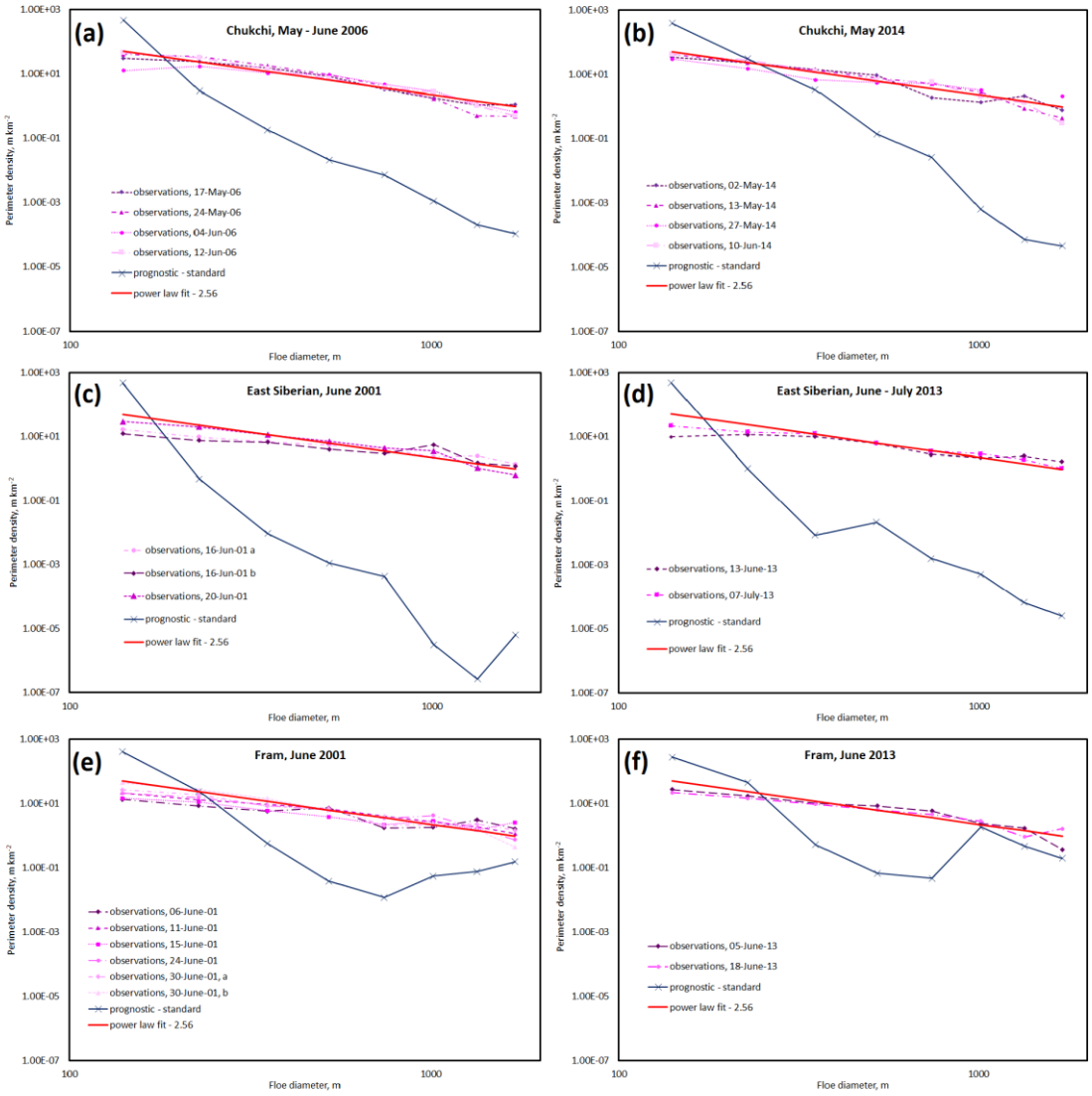

Figure 6.7: A comparison of the observations and prognostic model output for the perimeter density distributions for the Chukchi Sea in May – June 2006 (a) and May 2014 (b), the East Siberian Sea in June 2001 (c) and June – July 2013 (d), and the Fram Strait in June 2001 (e) and June 2013 (f). Observations are identified with pink or purple dashed lines. The prognostic model output (dark blue, solid, crossed) is averaged across the relevant region identified in Fig. 6.6 over the stated month(s). The average power-law fit across all locations is also shown (red, solid). The floe size data used within this figure was produced by Byongjun Hwang using the methodology of Hwang et al. (2017). The exponent of the power-law fit was calculated by Yanan Wang using the methodology of Virkar and Clauset (2014).

6.6.3 Modified prognostic model compared to observations

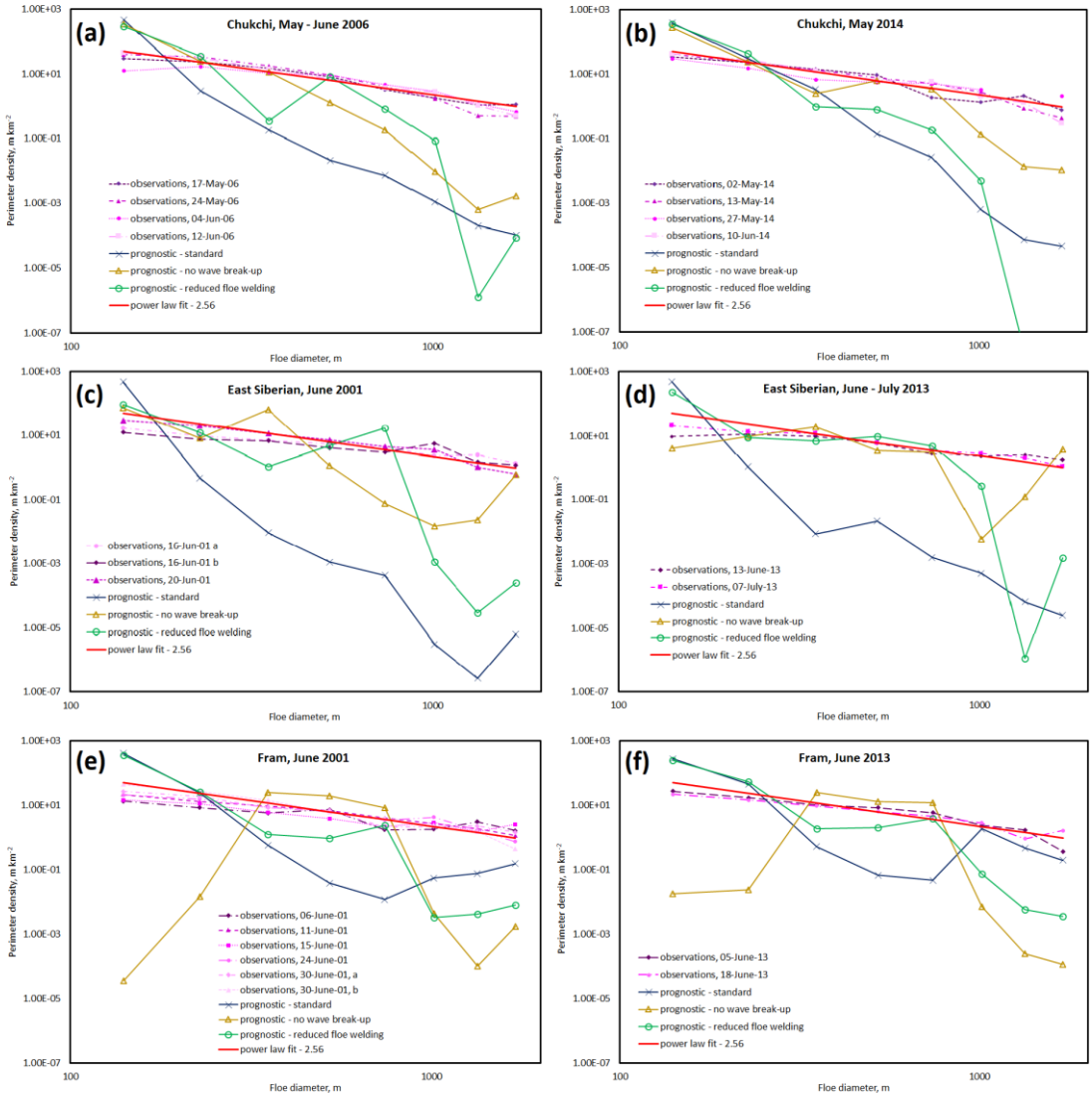

Figure 6.8: As Fig. 6.7, but the output of two additional prognostic model simulations is now included for comparison in each plot: a simulation where wave break-up impacts on the FSD are removed (gold, solid, unfilled triangles); and a simulation where the floe welding parameter is reduced significantly (green, solid, unfilled circles).

The poor performance of the prognostic FSD model compared to observations shown in Fig. 6.7 suggests that either important processes that determine the FSD are missing from the prognostic model or that the existing parameterisations and parameter values need to be modified. A series of experiments have been performed to explore whether the existing prognostic model can be modified to avoid such a steep negative gradient in the perimeter density distribution. The two most promising approaches were identified as removing wave break-up feedback on the FSD and

reducing the floe welding constant. Two additional prognostic model simulations have been completed to incorporate these changes: the first removes the wave break-up component of the model and the second reduces the floe welding constant by a factor of 10^8. Figure 6.8 compares the emergent FSDs from these additional simulations to the observations and standard prognostic model setup, as per Fig. 6.7.

Of the two approaches, the removal of the wave break-up feedback on the FSD significantly reduces the difference between the model and observations for the Chukchi and East Siberian Seas, but performs very badly in the Fram Strait, even worse than the standard prognostic model. For the reduced floe welding, in each case it appears to perform much better than the standard case for floes smaller than 1 km, but then the performance significantly drops off above 1 km. Neither suggested approach to improving the existing prognostic model appears to be adequate here. Furthermore, the removal of either wave break-up or floe welding as an important factor in determining the emergent FSD would not be justified without observational evidence that these processes are not important over the larger scale sea ice cover.

It is worth addressing the counterintuitive nature of the modifications made in this section i.e. removal of wave break-up is expected to increase the perimeter density for larger floes, whereas reduced floe welding is expected to increase the perimeter density for smaller floes. To understand this, the nature of the comparison in Fig. 6.8 needs to be considered. The prognostic model setup used to produce the simulated FSD presented in Fig. 6.8 includes 16 floe size categories. However, as explained earlier, the 4 smallest categories are excluded from the comparison as floes smaller than 100 m do not appear to be well resolved in observations with a 2 m pixel size, and the 4 largest floe size categories are excluded to avoid including the non-physical ‘uptick’ from the model output in the comparison. Hence, whilst reduced floe welding increases the ratio of smaller floes to larger floes, and removal of wave break-up of floes has the reverse effect, the impact on the shape of the distribution for the mid-sized floes considered in Fig. 6.8 is not so easily characterised. The complexity of the response is illustrated in Fig. 6.8 e.g. reduced floe welding appears to shallow the slope in the perimeter density distribution for the smaller 5 floe size categories but the response in the larger 3 is less consistent and in some cases the slope becomes much steeper such as in the Chukchi Sea in May 2014. Similarly, whilst the net effect of removal of wave break-up of floes in the Chukchi and East Siberian Seas is to shallow the perimeter density slope, in the Fram Strait, where waves are expected to have the

largest impact on the FSD, the response is best characterised as the emergence of a broad peak in the perimeter density distribution for floe sizes of around 500 m.

Evidence exists that there are processes that can influence floe size not yet included in the prognostic FSD model. For example, floes can break-up in response to moderate external forcings along existing cracks and weaknesses in the sea ice cover (Perovich et al., 2001). Winds have also been observed to produce long 'travelling' cracks in the pack ice (Hopkins et al., 2004). Chapter 7 will explore this theme further and consider whether missing floe fragmentation processes could account for the difference in the shape of the FSD for mid-sized floes between the prognostic FSD model and observations.

6.7 Summary of chapter 6

The general aim of this chapter has been to compare the emergent FSD from the prognostic floe size distribution model of Roach et al. (2018a, 2019) to observations as part of a broader assessment of both the prognostic and power-law approaches to modelling the FSD.

A summary of the prognostic FSD model has been provided, including the following amendments to the original model described in Roach et al. (2019):

- The internal wave scheme described in the Roach et al. (2018a) paper has been retained rather than using a separate wave model either as an external forcing or via coupling. The new wave dependent floe growth scheme introduced in Roach et al. (2019) has been adapted for use with the internal wave scheme.

- Two new outputs to characterise the FSD distribution have been implemented into the prognostic model: l_{eff}, the effective floe size, and l_{exp}, the 'fitted' power-law exponent. These variables can be used together to assess both the potential impact of a given distribution on the lateral melt and the ratio of smaller to larger floes for a given distribution, respectively.

I have discussed observations of the FSD, including novel observations collected from satellite imagery and subsequently analysed by Byongjun Hwang and Yanan Wang

(University of Huddersfield). This latter dataset includes 37 individual images spanning 2000 – 2014, over May to July, from either the Chukchi Sea, East Siberian Sea, or the Fram Strait. Here this new data has been presented as perimeter density distributions, the metric relevant to assessing the mass balance impact of a given FSD. Only floes spanning approximately sizes 100 m – 1900 m were included in this analysis due to limitations either from image resolution or the total image size. Whilst the mean exponent of the FSD in the Chukchi Sea was found to be more negative than the other two locations, the large variability at each location meant that this was not a conclusive indicator of spatial variability of the FSD. Likewise, no annual cycles or interannual trends could be identified in the data, with variability attributed to either natural physical local variability in the FSD or random errors from the finite sample size and methodology.

Finally, these observations have been compared to the prognostic model output for mid-sized floes in addition to a power-law fit. Whilst the power-law fit generally produced a strong fit to observations of the FSD for floes from sizes of 100 m to 1900 m, the prognostic model performed poorly in capturing the shape of the distribution for these mid-sized floes. Changes to the existing prognostic model setup, including the removal of wave break-up and weakening of welding impact on floe size, were unable to sufficiently bridge the gap between the model and observations. These results suggest that the prognostic model is missing at least one important process for determining the shape of the FSD for mid-sized floes.

Chapter 7: Exploring the emergent floe size distribution

In chapter 6, it was found that the prognostic FSD model of Roach et al. (2018a, 2019) performs poorly in comparisons to observations of mid-sized floes. In this chapter, results of a sensitivity study are presented to demonstrate that the inclusion of in-plane brittle fracture processes in the prognostic model has the potential to bridge the gap between the prognostic model output and observations. The updated prognostic FSD model is then used to investigate how different processes impact the shape of the FSD and the spatial variability of the distribution. This chapter will also assess the impact of individual FSD processes on the sea ice mass balance and discuss whether the prognostic model can explain observed FSD trends and variability.

7.1 Investigating brittle fracture as a missing FSD process

7.1.1 Brittle fracture of sea ice

The prognostic floe size distribution model (Roach et al., 2018a, 2019) discussed in chapter 6 only considers waves as a driver of floe fragmentation (as does the WIPoFSD model, at least explicitly). If the stress imposed by the external wave field becomes large enough, then the floe will fracture and break-up. Waves are not the only source of stress. External wind fields can impose a stress on the sea ice cover, as can shear, divergent, or convergent motions of the sea ice cover. Whilst most stress events would not be expected to result in fragmentation of a floe, the likelihood of break-up will be increased if the floe has existing partial cracks or weaknesses.

Perovich et al. (2001) observed that summer floe break-up of sea ice in the central Arctic in 1998 was driven by thermodynamic weakening of existing linear features in the sea ice cover during a period when the dynamic forcing and internal sea ice stress was expected to be small. During winter months, cracks and leads would form but then freeze-up again. The study outlined several reasons why this newly formed ice would be more susceptible to melting than the surrounding multi-year ice. This newly formed sea ice in the cracks and leads would be thinner, have a lower albedo due to reduced surface scattering, melt more easily, and would be lower topographically allowing

meltwater to accumulate and further lower the albedo. Kohout et al. (2016) noted that at the onset of a wave break-up event in the Antarctic in September 2012, floes broke apart along ridges and existing weaknesses in the sea ice cover. Steer et al. (2008) and Prinsenberg and Peterson (2011) also both observed the collapse of sea ice ridges into constituent parts at melt onset, enhanced by wave action in the latter case.

Satellite imagery of the Arctic sea ice cover, especially over the winter pack ice, shows linear features such as leads and fractures referred to as slip lines or linear kinematic features (Kwok, 2001; Schulson, 2001). These linear features have been found to intersect at acute angles, independent of the spatial scale, creating individual diamond shaped regions and floes over the sea ice cover (Weiss, 2001; Schulson, 2004). The similarity of these linear features to fracture patterns formed in laboratory studies of the shear rupture mechanism, where a crack forms once a large enough shear stress is imposed, has been used to argue that the shear rupture mechanism is responsible for the linear features seen in the pack ice (Weiss and Schulson, 2009). A discrete element model of the sea ice incorporating compressive, tensile, and shear rupture failure mechanisms acting under wind stress has been shown to produce distributions of fractures that are comparable to the distribution of linear features seen in the Arctic pack ice (Wilchinsky et al., 2010). These observations and model studies suggest that the pack ice behaves as a brittle material, particularly during periods of freeze-up. It is therefore likely that brittle fracture processes have an impact on the shape of the FSD within the pack ice. In addition, given the observations mentioned above of how linear cracks and features that form in winter can then determine how the sea ice cover breaks apart over the next melt season, there is also a clear mechanism of how brittle fracture processes can influence the shape of the FSD during the summer months, including in the MIZ.

Idealised models of brittle fracture can be used to predict the size distribution of fragments within a planar system acting only under brittle fracture. In a brittle fracture event, cracks can propagate and where they exceed a critical speed, the cracks become unstable and they branch. Individual branches and fractures can also merge, with the lifetime of the fracture determining the size of the subsequent fragment that forms. The branching results in a hierarchical process, with several levels of branches forming from the same central fissure (Åström et al., 2004; Kekäläinen et al., 2007). The resulting fragment size distribution adopts a power law with an exponent of -2 and

an upper cut-off determined by an exponential in the square of the fragment size (Gherardi and Lagomarsino, 2015).

7.1.2 A quasi-restoring brittle fracture model

In order to investigate the potential impact of in-plane brittle fracture processes on the FSD, the prognostic model has been modified to include a quasi-restoring brittle fracture scheme. In this scheme brittle fracture can transfer sea ice area fraction from a larger floe size category to the adjacent smaller category. This process is conservative in sea ice area i.e. the reduction in sea ice area in the larger category will be matched by an increase in sea ice area in the smaller category of equal and opposite magnitude. The net effect of this process across the full distribution will be an increase in sea ice area within the smallest category, a reduction in sea ice area in the largest category, and either a positive or negative change for the remaining intermediate categories depending on the precise balance of sources and sinks for each category. In addition, the following condition must be fulfilled:

$$\frac{\ln n_i - \ln n_{i-1}}{\ln d_i - \ln d_{i-1}} > -2. \tag{7.1}$$

Here n and d refer to the floe number density and diameter at the midpoint of category i respectively. This condition means that the restoring scheme only applies where the slope between adjacent categories in log-log space is greater (more positive) than -2. The sea ice area fraction transferred in a single timestep between two adjacent categories is Ca_i where a_i is the area fraction of the larger category. The transfer of sea ice area fraction is only allowed in one direction from larger to adjacent smaller categories since floes cannot unfracture. C, the restoring constant, is calculated as:

$$C = \frac{\tau}{\Delta t}. \tag{7.2}$$

Here τ is the restoring timescale, and Δt is the model timestep. A value for the restoring timescale, τ, needs to be determined. To do this the circumstances where brittle fracture processes are likely to be important need to be considered. As mentioned in Sect. 7.1.1, there are two mechanisms through which brittle fracture can impact the sea ice cover. Fracture events occur regularly through autumn, winter and spring within the pack ice to form linear features like leads, which subsequently freeze

up again. These linear features are then vulnerable to increased thinning and melting, increasing the likelihood of break-up along these features during late spring and summer as the sea ice retreats. It is this second mechanism that is of more relevance when considering the impacts of the FSD on the seasonal retreat of the Arctic sea ice. Whilst fracture events can occur on a timescale of seconds, the impact of brittle fracture processes relies on thermal melting timescales. The timescale for a crack or linear feature in the sea ice to fully melt through is taken to be of the order of 1 month. For simplicity, τ is here set to a fixed value of 30 days throughout the year.

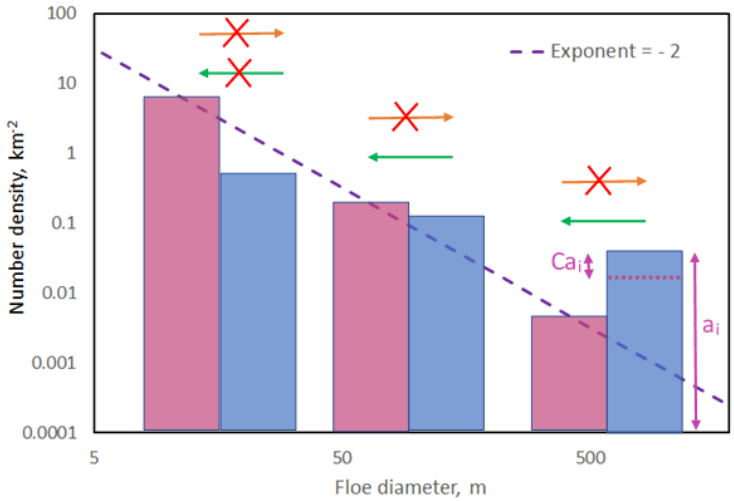

Figure 7.1: Diagram of the quasi-restoring brittle fracture scheme introduced to the prognostic FSD model. The model only transfers sea ice area fraction from a larger category to the adjacent smaller category and only where the number density gradient between adjacent categories in log-log space is larger (more positive) than – 2. The sea ice area fraction distributed is Ca_i where a_i is the total sea ice area fraction in the larger category and C is the restoring constant.

Figure 7.1 provides a visual summary of the quasi-restoring scheme. The motivation for this scheme is to impose a restoring tendency on the FSD to the predicted shape of the distribution if it were acting only under brittle fracture processes. In reality, the value of C in Eq. (7.1) is expected to be some function of several processes and parameters including sea ice strength, wind stress, pond fraction, and lateral melt rate. However, the development of a full parameterisation of both brittle fracture and thermodynamically driven fragmentation of floes requires field observations of these processes and is outside the scope of this present work.

7.1.3 Comparing the updated prognostic model to observations

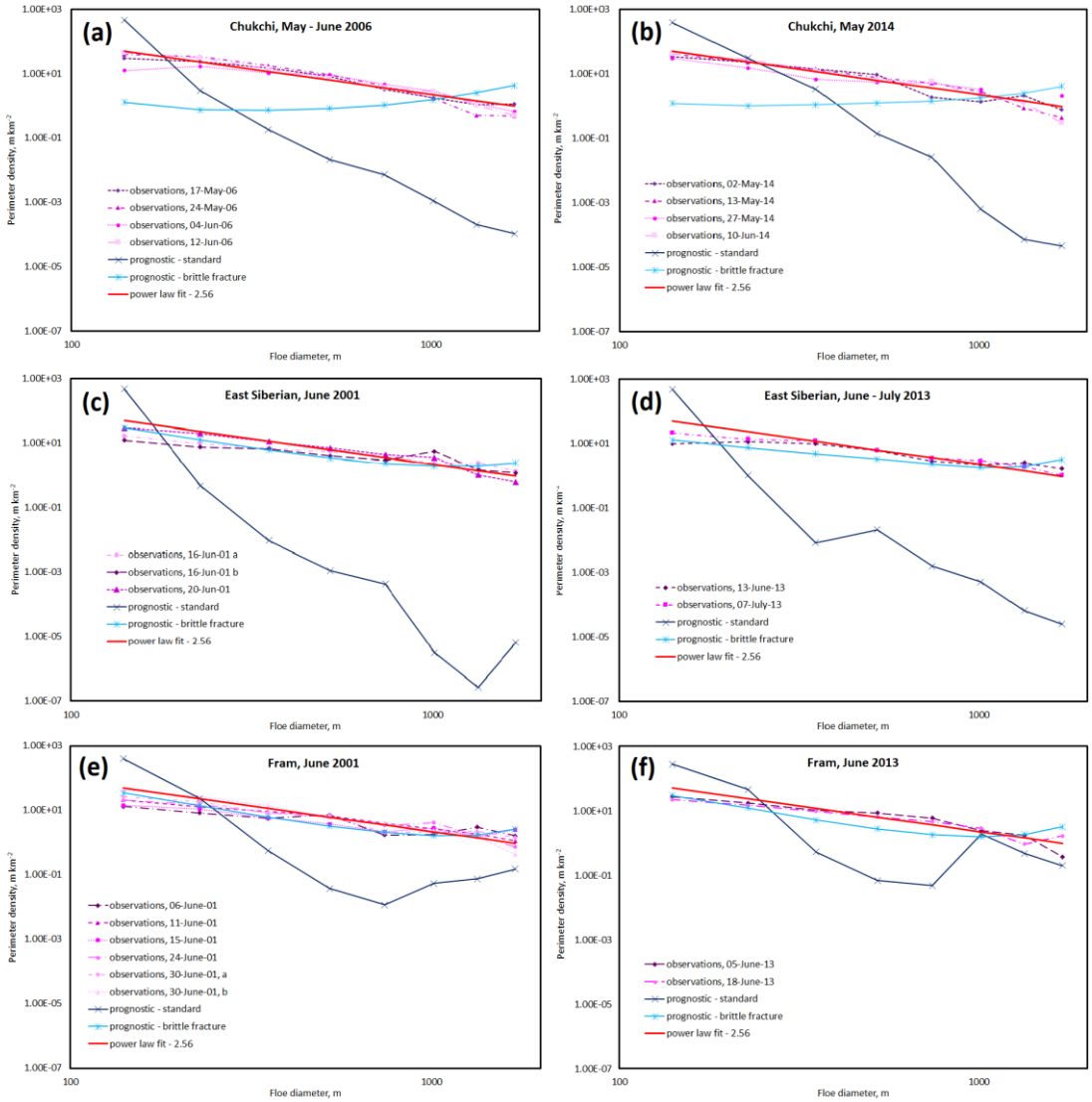

Figure 7.2: As per Fig. 6.7, but with the output of the prognostic model simulation including the quasi-restoring brittle fracture scheme also presented for comparison in each plot (light blue, stars). The prognostic model including brittle fracture performs particularly well in the Fram Strait and East Siberian Sea but less well for the Chukchi Sea. It represents a significant improvement to the standard prognostic model in all three cases.

A CICE simulation has been completed with the incorporation of the quasi-restoring brittle fracture scheme described in Sect. 7.1.2 into the prognostic FSD model. The setup, including all parameters, is otherwise identical to that outlined in Sect. 6.6.1. Figure 7.2 compares both the FSD from the original prognostic FSD scheme and updated scheme to the observations. For each case study, the prognostic model including the new brittle fracture scheme significantly improves the shape of the

emergent perimeter density distribution for mid-sized floes compared to the standard prognostic model. The updated model performs particularly well in the East Siberian Sea and Fram Strait, but less well in the Chukchi Sea.

It is worth commenting briefly on how the brittle fracture scheme can improve model performance compared to observations, given it is a counterintuitive result that increasing floe break-up would produce a shallower slope in perimeter density. Looking at the distributions presented in Fig. 7.2 for the standard prognostic model without brittle fracture, superficially it does not make sense that a redistribution of sea ice area from larger categories to smaller categories would improve the shape of the distribution compared to the observations given the gradient is already too negative. However, as discussed in Sect. 6.6.1, the largest floe size categories in the prognostic model are excluded from the comparison to observations to exclude the non-physical 'uptick' that forms (this uptick is also found in previous studies with the prognostic model e.g. Roach et al., 2018a). The inclusion of brittle fracture acts to reduce the size of the uptick and redistributes sea ice area to mid-sized floe categories, producing the results displayed in Fig. 7.2. There are two plausible factors that can produce this uptick: the truncation of the maximum possible floe size such that sea ice area accumulates in the largest category that would otherwise be distributed over several larger categories; and missing processes in the prognostic model that would act to reduce floe size e.g. brittle fracture. The results presented in this section provide evidence for the second factor, but observations of floes above the range included in the 16-category prognostic model suggest the truncation effect also contributes.

The better fit shown by the prognostic model with brittle fracture to observations in the Fram Strait and East Siberian Sea compared to the Chukchi Sea site is an illustrative example of the limitations of the brittle fracture scheme used here. To understand the difference in model performance at the different sites, consider the locations of each site shown in Fig. 6.6. The Chukchi Sea is the only one of the sites that will fully transition to an ice-free state over the melting season. Brittle fracture acts on the FSD at the two former sites throughout the year, but only for part of the year for the Chukchi Sea. τ is not a restoring timescale in the traditional sense. If the FSD was restored to a pure power law with an exponent of – 2 in just 30 days, the differences between the Chukchi Sea and other locations would not exist. τ here represents the timescale for two neighbouring categories to reach an equilibrium state, but the prognostic FSD model consists of 12 categories in total. For this setup, it would take 7.5 months for a

starting state with all sea ice area in the largest floe size category to reach equilibrium across all floe size categories, a long enough lag to explain the different prognostic model performance for the Chukchi Sea. For each perimeter density distribution presented in Fig. 7.2 from the prognostic model with brittle fracture, a positive gradient with floe size can be seen for the top few floe size categories. This feature, not consistent with observations, is a result of the interactions between the non-physical 'uptick' that emerges from the prognostic model and the brittle fracture restoring scheme. The effect of the brittle fracture restoring is to produce a less pronounced but broader 'uptick', though this would disappear if the restoring timescale, τ, was shorter.

Overall, the inclusion of the quasi-restoring brittle fracture scheme represents a demonstrable improvement in the ability of the prognostic model to capture the shape of the FSD for mid-sized floes. There are several points to address here regarding this result. It is not unexpected that the scheme is able to significantly improve the prognostic model output compared to observations, given it involves a partial restoring to a power law of exponent -2, which in itself would produce a much better fit to the observations than the existing prognostic setup. It will be demonstrated later in this chapter that whilst the brittle fracture scheme has a significant impact on the shape of the distribution, other processes in the prognostic model still have a significant and important impact on the shape of the FSD. Even in Fig. 7.2, it is clear through comparisons between the perimeter density distributions for the prognostic model with brittle fracture and the power-law fit that there is still significant variability in the prognostic FSD between different locations and more variability than is seen for the observations.

The brittle fracture scheme presented is, by design, a very simple scheme that allows an investigation into the role of brittle fracture and other break-up processes in determining the shape of the emergent FSD. Whilst the approach is simple, the distribution being restored to is that which emerges from detailed models of brittle fracture (Åström et al., 2004; Kekäläinen et al., 2007). In addition, physical considerations have motivated constraints on where and how the prognostic model is applied, for example only allowing the transfer of sea ice area fraction from larger floe size categories to smaller floe size categories. The restoring timescale of 30 days has been selected through a consideration of the details of how these brittle fracture events influence the emergent FSD, though a sensitivity study presented in section 7.2.6 will explore model sensitivity to the value of τ. This approach nevertheless has limitations.

The use of a constant restoring timescale means that the strength of the impact of brittle fracture processes is assumed to be the same everywhere and at all times. It has been previously been discussed that brittle fracture can influence the FSD through two mechanisms: pack ice fracture events and melting and break-up along existing linear features. These processes will operate over different timescales and scale with different properties. Fracture events happen almost instantaneously and scale with stress e.g. from a wind field, whereas the melt driven break-up mechanism scales with properties such as air temperature and ocean heat content and operates on a monthly timescale. An additional limitation of the brittle fracture approach is that it assumes transfer of sea ice area fraction only between adjacent categories, whereas physically a larger floe can break down into floes of any smaller size.

Despite the limitations with the quasi-restoring brittle fracture model, the results shown in Fig. 7.2 strongly suggests that brittle fracture or related fragmentation processes are required to capture the shape of the FSD for mid-sized floes, motivating the need to develop a physically derived brittle fracture parameterisation for the prognostic FSD model. The development of such a parametrisation is outside the scope of this present work. Further simulations using the prognostic model both in this and subsequent chapters will include the quasi-restoring brittle fracture scheme due to the significant improvement in the shape of the distribution for mid-sized floes compared to observations. This scheme should nevertheless not be taken as a perfect solution to the representation of brittle fracture processes in a prognostic FSD model, but instead represents a valuable intermediate step towards a fully physically derived representation of these missing fragmentation processes.

7.2 The role of individual processes in the emergent shape and impact of the FSD

The main advantage of the prognostic FSD model is that it can represent the impact of individual processes on the emergent FSD in a physically realistic manner. This is not the case for approaches that impose restrictions on the shape of the distribution such as the WIPoFSD model. In this section the prognostic model will be used to understand how different processes contribute to the emergent shape and variability of the FSD through a series of sensitivity studies where individual processes represented in the prognostic FSD model are either removed or strengthened. The impact of each

process on the sea ice mass balance will also be considered. This will contribute to an assessment of whether the full prognostic model is needed to capture the general impact of an FSD on the sea ice cover or whether a simplified FSD model such as a power-law approach could be used to similar effect.

This analysis will proceed firstly by considering the perimeter density distribution and mass balance impact of the standard prognostic model. The individual components of the evolution equation for the prognostic model, Eq. (6.3), are considered in turn. First the contribution of the wave-breaking of floes, $\mathcal{L}_W$, to the perimeter density distribution and mass balance impact is evaluated. For the thermodynamic term, $\mathcal{L}_T$, four components are considered: welding of floes, the formation of new floes, lateral melt, and lateral growth. $\mathcal{L}_M$, the term representing mechanical interactions like ridging and rafting, will be excluded from this analysis as the parameterisations used within the prognostic model do not act directly on floe size. Changes to the vertical thickness through basal or top growth or melt are also excluded for the same reason. The newly introduced brittle fracture scheme is included in this sensitivity analysis. The role of the floe size contribution within the form drag scheme to the overall mass balance impact of the prognostic model will also be considered, to allow a comparison to the results for the WIPoFSD model presented in chapter 5. These results will then be used to make an overall assessment for the important processes in determining the emergent FSD and the FSD processes that significantly affect the sea ice mass balance. Consideration will also be given to what drives the annual evolution of the sea ice FSD.

Simulations in this section will be run using the CPOM-CICE setup, as described in Sect. 3.2. Simulations are initiated with a sea ice free Arctic on 1st January 1980 and evaluated over a 37-year period until 31st December 2016. The form drag parameterisation of Tsamados et al. (2014) is used, including the modifications to parameters described in Sect. 5.3. For the reference simulation, *ref*, the floe size used for both lateral melt calculations and the form drag scheme will be set to 300 m. The standard prognostic setup, *prog-stan*, uses the standard 12 floe size categories outlined in Roach et al. (2018a) and the 5 standard CICE thickness categories (Hunke et al., 2015). The floe size used in the form drag scheme will be l_{eff}, the effective floe size, defined in Sect. 6.3. The prognostic model setup up described in Sect. 6.2 is used, now including the quasi-restoring brittle fracture scheme described in Sect. 7.1.2 with standard parameters. Additional sensitivity studies will use a modified version of the basic setup of *prog-stan*, with the modifications clearly stated.

For these experiments the perimeter density distribution will be plotted rather than the floe number or area density distributions. The perimeter density distribution is most relevant for understanding how an FSD will impact the lateral melt rate and floe size form drag contribution and therefore gives the best indication of whether a given change to the FSD model will have a significant impact on the sea ice mass balance.

7.2.1 Standard prognostic model

Before considering sensitivity studies, first plots to show the emergent FSD, spatial variability and thermodynamic impact for the standard prognostic model will be presented as a point of reference for each sensitivity study. Figure 7.3 shows the perimeter density distribution for *prog-stan* averaged over 2000 – 2016 for two different months, April and August, for both the MIZ and pack ice. Before commenting on these plots, it should be noted that they have been normalised per km^2 of sea ice area. This means that an increase in the perimeter density for a given floe size does not necessarily mean that there are more floes of that size overall, just that floes of that size account for a higher proportion of the total number of floes. There are several features of these distributions to note. Firstly, over the period April to August, the ratio of both smaller and larger floes to mid-sized floes decreases. The decrease in smaller floes is driven by the preferential lateral melt out of smaller floes (as previously discussed in chapter 4) and the vertical melt out of thin pancake floes that form in turbulent ocean conditions under the wave dependent growth scheme during the previous winter and have not yet experienced significant vertical or lateral growth. The decrease in larger floes is driven by the break-up of larger floes by either waves or brittle fracture. For both April and August, there is a higher proportion of smaller floes in the MIZ than in the pack ice, with the reverse true for the largest category. This behaviour is expected, with the more sheltered conditions of the pack ice enabling the formation and subsequent preservation of larger floes. The distribution for larger floes in August is very similar for both the MIZ and pack ice. This is driven by the new brittle fracture scheme, which acts to restore the FSD to a fixed shape. The number of larger floes in summer is only likely to change in response to break-up events. For locations where waves cannot propagate without significant attenuation, the FSD will evolve primarily under the influence of the brittle fracture scheme.

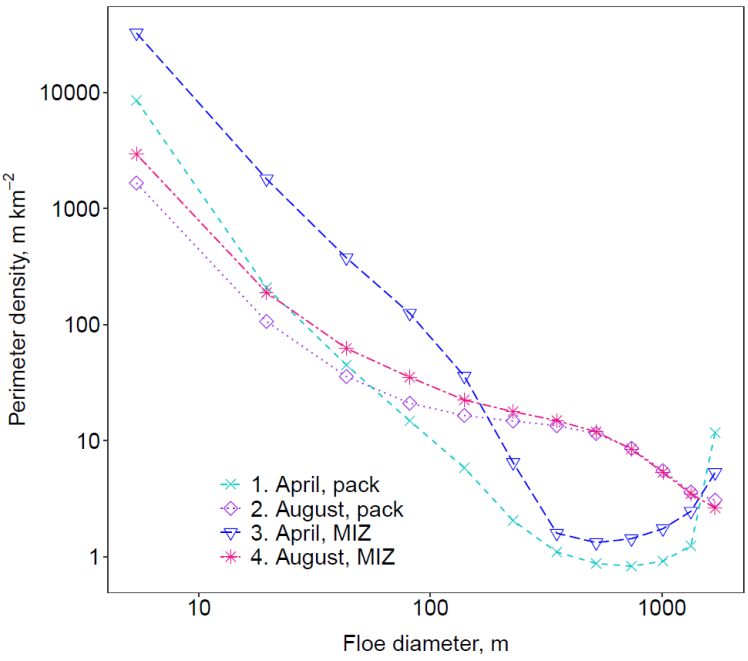

Figure 7.3: The perimeter density distribution, $m\ km^{-2}$, of sea ice area for the *prog-stan* simulation. Distributions are shown for the April pack ice (light blue, short dashed, crossed), August pack ice (purple, diamond, dotted), April MIZ (dark blue, triangle, long-dash), and August MIZ (pink, star, dot-dashed) averaged over 2000 – 2016.

Figure 7.4 shows the spatial distribution of l_{eff} and l_{exp} (defined in Sect. 6.3) averaged over 2000 – 2016 for April, June and August. Note that l_{exp} should not be interpreted as an indicator of a power-law fit but as a general metric to express the ratio of small to large floes in the distribution, with a more negative value indicating a higher ratio of smaller to larger floes. These plots show that there is significant spatial variation in both metrics across the sea ice cover. This variability is highest in April but lasts throughout the melting season. In April the largest l_{eff} can be found alongside the Canadian Archipelago and within the Kara and Laptev seas, exceeding 900 m in these locations. l_{eff} is smallest along the Atlantic facing MIZ including the Greenland Sea, dropping below values of 150 m across this region. Low values of between 80 m – 250 m can also be found in the Chukchi sea. As the melting season proceeds the values of l_{eff} drop significantly across the pack ice. By August, l_{eff} only exceeds 600 m in specific locations within the Canadian archipelago. In contrast, the mean l_{eff} within the MIZ increases over the year, with the regions where l_{eff} is less than 150 m significantly decreasing in extent from April to August. The spatial distribution for l_{exp} is not as easy to characterise. In general, values are higher for the MIZ than the pack ice. For the pack ice, values for l_{exp} are generally between – 2.5 to – 3 in April, increasing to above

– 2 in June, then decreasing down to around – 2 to – 2.5 in August. Values are usually around 0.5 more negative in the MIZ for each month. l_{exp} decreases between April and June because of melt out of smaller floes, increasing the proportion of larger floes in the distribution. The reverse is then true between June and August, with brittle fracture and wave break-up reducing the number of larger floes in the distribution. The prevalence of -2 to -2.5 in August suggests a strong influence from the brittle fracture scheme.

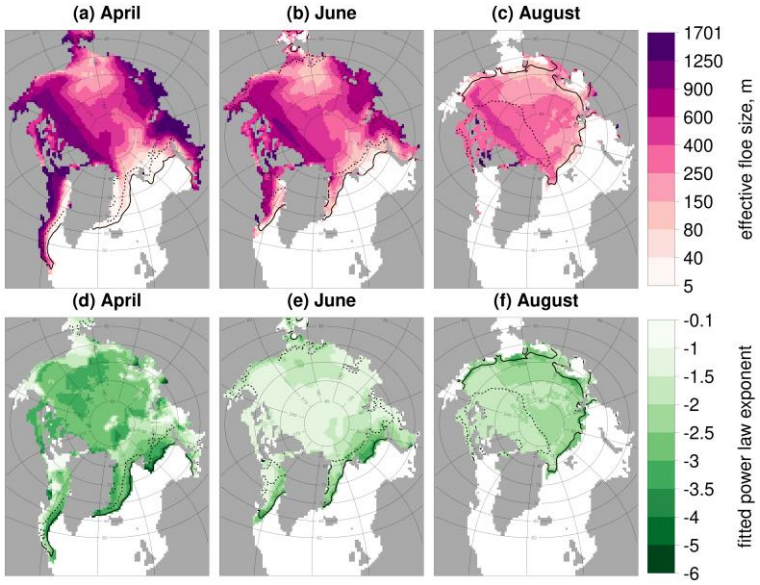

Figure 7.4: l_{eff} (top row, a-c) and fitted l_{exp} (bottom row, d-f), averaged over 2000 – 2016 for *prog-stan*. Results are presented for April (left column, a, d), June (middle column, b, e) and August (right column, c, f). Values are shown only in locations where the sea ice concentration exceeds 5 %. Note that any values for the fitted power law that are less than -6 are assigned to the most negative category. Values that exceed -0.1 are not shown.

Figure 7.5 shows the difference in sea ice extent and volume over the annual cycle for *prog-stan* compared to *ref*, i.e. the impact of the prognostic FSD scheme on the sea ice mass balance. The plot shows that the inclusion of the prognostic FSD model causes a reduction in the sea ice extent and volume throughout the year. The reduction in extent is smallest in winter months, with a mean reduction of 0.5 % in extent from November to January. The change in volume is lowest from January to June, with the reduction between 1 % and 1.5 %. The largest reduction in extent and volume are about 2 % and just under 4 % in August and September respectively. The interannual variability is highest in these months at ± 2 % for both extent and volume. The overall impact is a reduction in the sea ice volume, particularly over the melting season. There are several interesting features of this plot. In particular, the larger mean reduction in volume over

extent. Results presented in chapter 8 will show that in September regions of reduction in sea ice concentration within the MIZ are partly compensated by increases in concentration in the pack ice (where l_{eff} is, on average, larger than 300 m). In comparison large reductions in thickness in the MIZ are added to by moderate reductions in thickness across the pack ice that persist throughout the year. A second interesting feature of Fig 7.5 is that the reduction in extent shows a broad peak spread over June to August, rather than just a sharp peak in August. This can be attributed to the values of l_{eff} in the April MIZ shown in Fig. 7.4, which are below 40 m everywhere. This favours high lateral melt rates and faster sea ice retreat in the early melt season compared to *ref*. However, the melt out of smaller floes causes the average l_{eff} to increase in the MIZ over the melting season, so the enhancement of lateral melt in *prog-stan* compared to *ref* is more modest during the mid to late melting season.

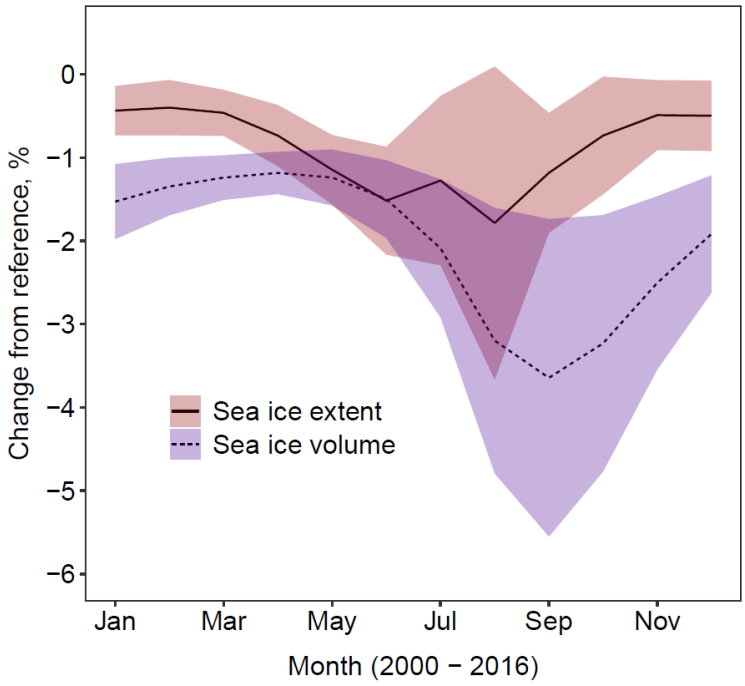

Figure 7.5: Difference in sea ice extent (solid, red ribbon) and volume (dashed, blue ribbon) of *prog-stan* relative to *ref* averaged over 2000 - 2016. The ribbon shows the region spanned by the mean value plus or minus two times the standard deviation. The inclusion of the prognostic FSD model reduces the mean extent and volume by up to 2 % and 4 % respectively.

7.2.2 Impact of wave break-up

To investigate the impact of wave break-up on the FSD and the sea ice mass balance, represented in the prognostic model through Eq. (6.11), two sensitivity studies are considered. *prog-nowb* removes the feedback of wave break-up on the FSD i.e. $\mathcal{L}_W$ is

set to 0 in Eq. (6.3), whereas *prog-morewb* reduces the attenuation rate of waves propagating into the sea ice cover by a factor of 10. This means that waves propagate further into the sea ice cover, strengthening their impact. Apart from these stated changes both simulations are identical to *prog-stan*. Note that the wave field used to calculate the size of newly formed floes is kept identical in each of *prog-nowb*, *prog-morewb* and *prog-stan*.

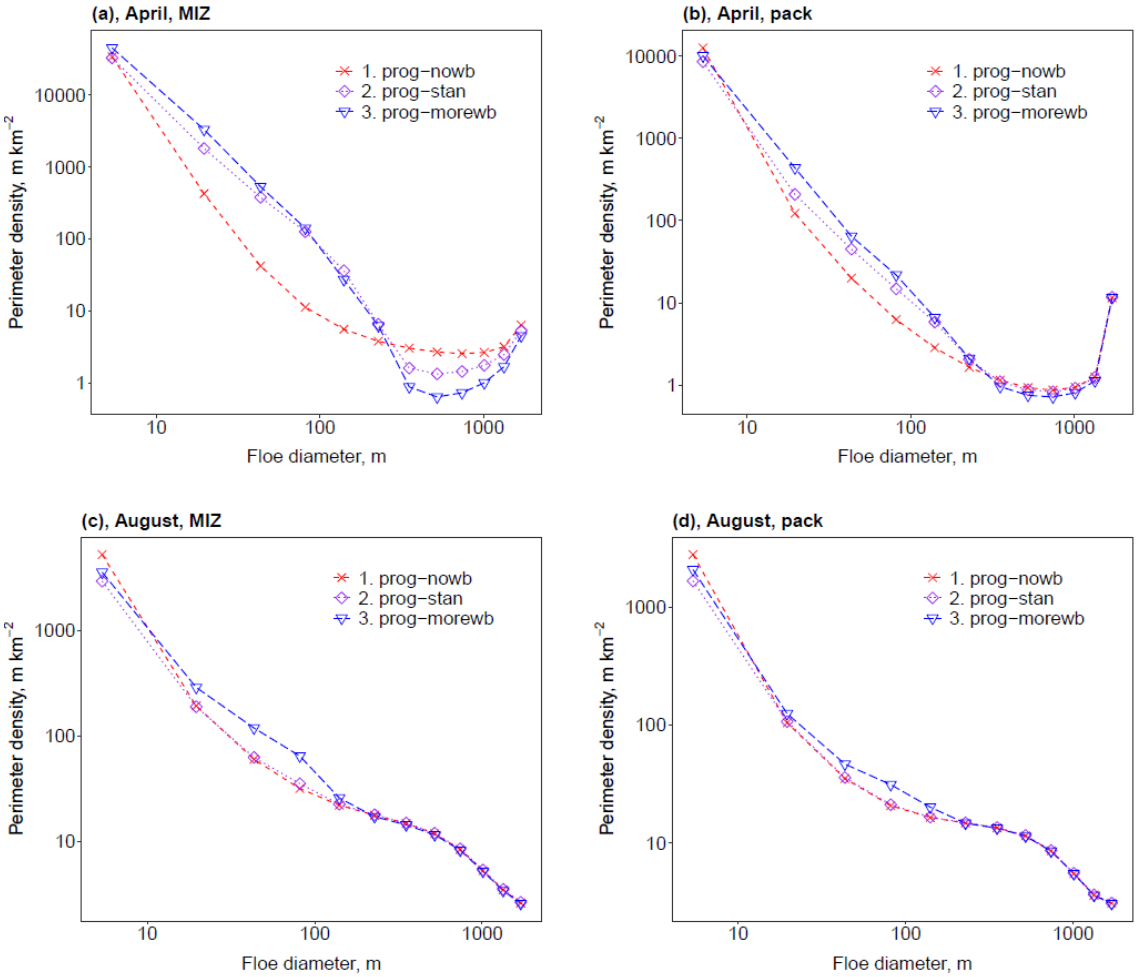

Figure 7.6: The perimeter density distribution, $m\ km^{-2}$, of sea ice area as a function of floe size for April MIZ (top left), April pack ice (top right), August MIZ (bottom left), and August pack ice (bottom right). Distributions are shown for *prog-nowb* (red, cross, dashed), *prog-stan* (purple, diamond, dotted) and *prog-morewb* (blue, triangle, long-dash), all averaged over 2000 – 2016. The plots show that wave break-up has a moderate impact on the FSD for mid-sized floes.

Figure 7.6 compares the emergent perimeter density distribution for both *prog-nowb* and *prog-morewb* in both the April and August MIZ and pack ice. In April, the results show that the inclusion of wave break-up causes a redistribution from larger floes to the smaller floes in the distribution, though the complete removal of wave break-up has a stronger effect on the shape of the distribution than the reduction in the attenuation

rate. Larger differences between *prog-nowb* and *prog-stan* can be seen within the MIZ than in the pack ice, as expected. In August the results are more complicated. In all three cases, the distributions are similar for floes larger than about 100 m. Then, below 100 m, the distribution for *prog-morewb* deviates from the other two distributions. This indicates that in summer, the lower intensity wave conditions (relative to winter) are not enough to cause significant fragmentation of the sea ice cover under the current representation of wave break-up in the model, with differences for mid-sized floes only emerging at the reduced attenuation rate. Another notable result is that the perimeter density distribution per unit sea ice area is highest in the smallest category for *prog-nowb* than *prog-stan* or *prog-morewb*. This behaviour originates from a higher perimeter density in the smallest category in the April pack ice for *prog-nowb*. This in turn can be attributed to the link between wave attenuation rate and the FSD. The prognostic model internal wave scheme calculates the wave attenuation rate as a function of several properties including the number of floes between the sea ice edge and each grid cell, since waves are scattered by interactions with floe edges (see section 6.2.2 for further details). If floes are no longer broken up by waves, waves can propagate further into the sea ice and favour the formation of small pancake floes during freeze-up conditions. Effectively the removal of one mechanism of forming small floes, wave break-up, strengthens another mechanism of forming small floes, pancake ice formation. Since these mechanisms have different profiles in terms of the size of floes formed, the net effect is an increase in perimeter density for the smallest category and a reduction in the remaining small floe size categories (about 200 m and below).

Figure 7.7 shows the spatial distribution in l_{eff} for both *prog-nowb* and *prog-morewb* for three months, April, June and August, averaged over 2000 – 2016. Whilst there are small differences in magnitude, both *prog-nowb* and *prog-morewb* produce similar distributions of l_{eff} to *prog-stan*, shown in Fig 7.4. The largest differences can be found at the ice edge, particularly the Greenland Sea. In April and June, l_{eff} in the Greenland Sea is reduced from values of 100 s of m to less than 40 m in some locations for *prog-morewb* compared to *prog-nowb*. This suggests that even though wave break-up is important in determining the shape of the emergent FSD across the sea ice cover, particularly for mid-sized floes, it is not a significant control in determining the spatial distribution of l_{eff} except at the sea ice edge.

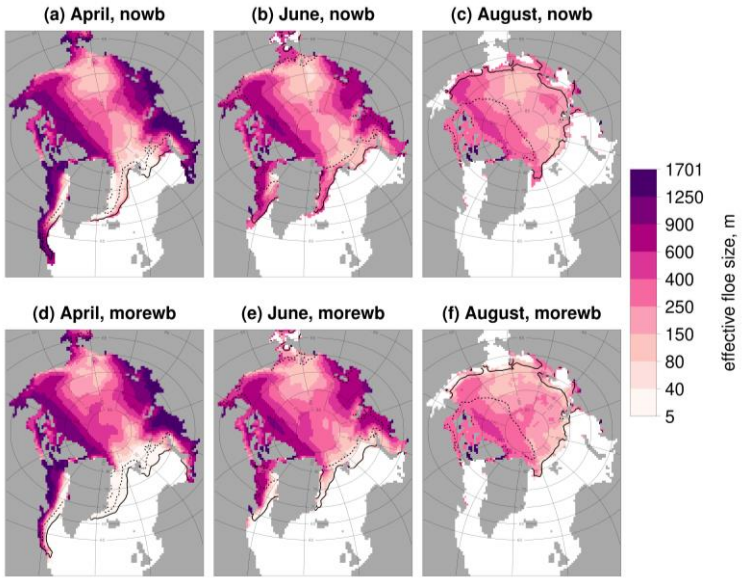

Figure 7.7: l_{eff} for *prog-nowb* (top row, a-c) and *prog-morewb* (bottom row, d-f) averaged over 2000 – 2016. Results presented for April (left column, a, d), June (middle column, b, e), and August (right column, c, f). Values are shown for locations where the sea ice concentration exceeds 5 %. The results suggest that wave break-up is not important in determining the spatial distribution in l_{eff}.

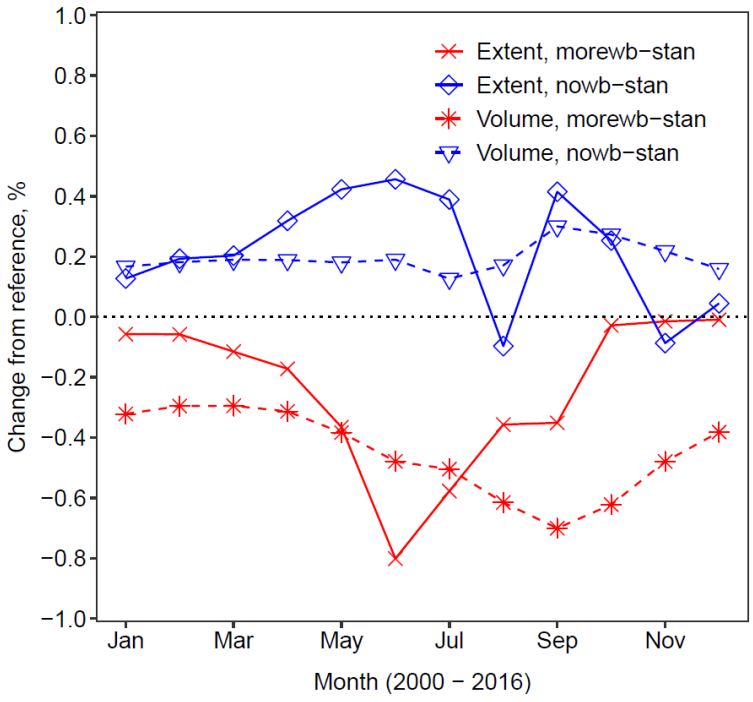

Figure 7.8: Difference in sea ice extent (solid) and volume (dashed) of *prog-nowb* (blue, diamond or triangle) and *prog-morewb* (red, cross or star) relative to *prog-stan* averaged over 2000 - 2016. The inclusion or strengthening of wave break-up results in a small to moderate reduction in the sea ice mass balance.

Figure 7.8 shows the change in the sea ice extent and volume for both *prog-nowb* and *prog-morewb* relative to *prog-stan* averaged over 2000 – 2016. Removing wave feedback on the FSD results in a small increase in the mean sea ice extent and volume, though never exceeding 0.5 %. The increase in volume is consistent through the year, usually ranging between 0.2 – 0.3 %. The small reduction for the sea ice extent in August can be linked to the increased perimeter density in the smallest category for *prog-nowb* compared to *prog*-stan in the August MIZ shown in Fig. 7.6. For *prog-morewb*, the changes have a larger magnitude and the interannual cycle is more well-defined. The reduction in extent ranges from close to 0 % in winter to about 0.8% in June. The reduction in volume ranges from 0.3 % in February to March up to 0.7 % in September. The reduction in extent peaks in June, before the sea ice minimum extent. This is a result of the changing wave field over the year, with summer associated with calmer sea conditions.

7.2.3 Impact of floe welding

The contribution of floe welding to the overall thermodynamic term, $\mathcal{L}_T$, is given by Eq. (6.9). To explore the role of floe welding in determining the emergent FSD, two sensitivity studies will be considered. This process can only occur during freezing conditions. In *prog-lowld* the floe welding constant, k, is reduced by a factor of 10 (see Sect. 6.2.1 for further discussion of k). In *prog-hiwld* k is increased by a factor of 10. Both studies are otherwise identical to *prog-stan*.

Figure 7.9 is an equivalent figure to Fig. 7.6 but this time showing the perimeter density distributions per unit sea ice area for *prog-lowld* and *prog-hiwld*. The distributions are almost identical in the April MIZ, suggesting that other processes are determining the emergent distribution for this region. However, for the pack ice moderate differences can be seen in the perimeter density for smaller floes, with higher values for *prog-lowld* and lower values for *prog-hiwld* than *prog-stan*. This is consistent with the expected behaviour, with a lower welding constant reducing the frequency of smaller floes merging to form larger floes. Eq. (6.9) shows that the welding rate is proportional to the local sea ice concentration. Floe welding causes larger differences in the April pack ice than in the MIZ due to the lower sea ice concentration in the MIZ. The differences in the April pack ice persist through to the August MIZ and pack ice, with both regions showing large variations in the perimeter density of smaller categories between the simulations. The difference in perimeter density in the smallest category between *prog-*

lowld and *prog-stan* is 10 % higher for the August MIZ compared to the April pack ice. This is a reasonable result given both the spatial variability of the FSD within the April pack ice and the continued floe welding within a significant proportion of the pack ice beyond April. This is an example of how differences in the FSD caused by winter processes persist through to the subsequent melt season.

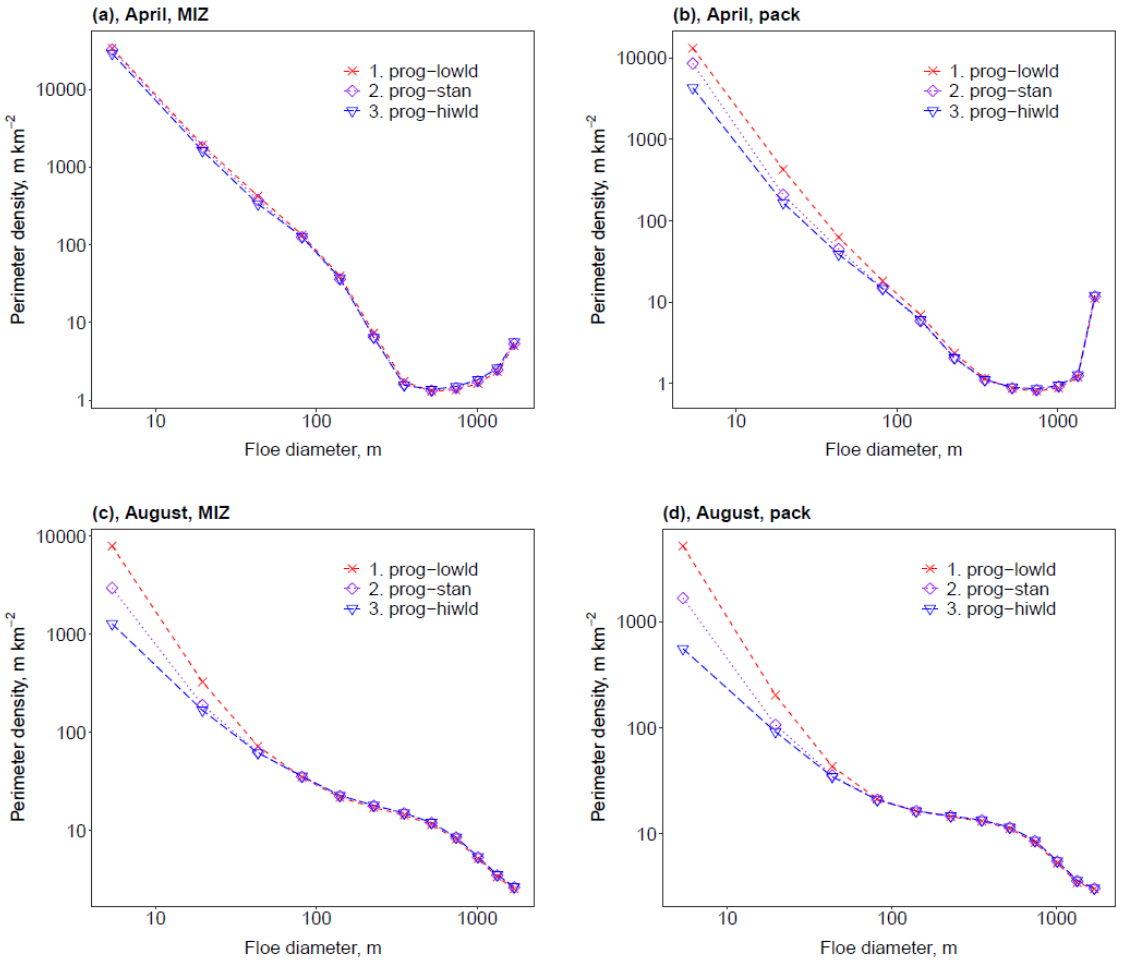

Figure 7.9: The perimeter density distribution, $m\ km^{-2}$, of sea ice area as a function of floe size for April MIZ (top left), April pack ice (top right), August MIZ (bottom left), and August pack ice (bottom right). Distributions are shown for *prog-lowld* (red, cross, dashed), *prog-stan* (purple, diamond, dotted) and *prog-hiwld* (blue, triangle, long-dash), all averaged over 2000 – 2016. The plots show that floe welding has the largest impact on the perimeter density for the smallest floe size categories.

Figure 7.10 is equivalent to Fig 7.7 but shows the spatial distribution of l_{eff} for *prog-lowld* and *prog-hiwld*. These plots show that the value floe welding constant, k, has a strong influence on the both the magnitude and spatial variability of l_{eff}. For example, for *prog-hiwld* in April the distribution looks more like Fig. 3.6 for the WIPoFSD model i.e. very high values of l_{eff} across the pack ice but then a rapid transition to smaller

floes at the ice edge. The pack ice behaviour remains somewhat homogenous through the year though with a clear reduction in l_{eff} over the melting season. For *prog-lowld*, a similar spatial distribution to *prog-stan* can be seen, though with lower values of l_{eff}. The temporal evolution of l_{eff} for the pack ice is less pronounced compared to *prog-hiwld.* For each case, there will be competing factors affecting l_{eff}. Fragmentation and lateral melting of individual floes will reduce l_{eff}. However, small floes will disproportionately melt out of a distribution, causing an increase in l_{eff}. Where the relative number density of smaller floes to larger floes in April is lower such as the pack ice for *prog-hiwld,* the behaviour of smaller floes will have a weaker effect on the evolution of l_{eff} than where the relative number density of smaller floes in April is higher, such as the *prog-lowld* pack ice. Hence l_{eff} shows a strong negative trend within the pack ice over the melting season for *prog-hiwld* but not for *prog-lowld.* The behaviour of l_{eff} over the melting season depends not only on the processes acting on the FSD during the melting season but also the shape of the initial distribution.

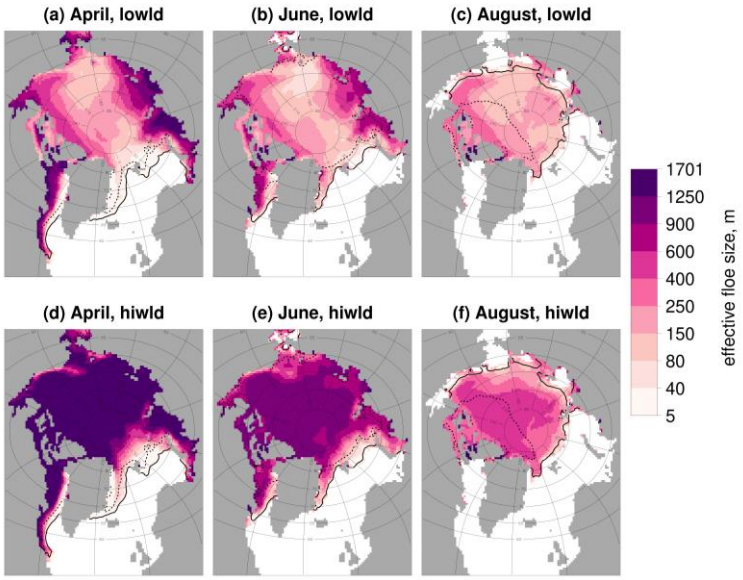

Figure 7.10: l_{eff} for *prog-lowld* (top row, a-c) and *prog-hiwld* (bottom row, d-f) averaged over 2000 – 2016. Results are presented for April (left column, a, d), June (middle column, b, e), and August (right column, c, f). Values are shown for locations where the sea ice concentration exceeds 5 %. The welding scheme is shown to have a strong impact on the variability in l_{eff}.

Figure 7.11 shows the change in the mean volume and extent for *prog-lowld* and *prog-hiwld* compared to *prog-stan*. As expected, given the perimeter density distributions, Fig. 7.11 shows a moderate positive change for *prog-hiwld* compared to *prog-stan* up to a maximum of just over 1 % in August for both extent and volume and *prog-lowld* shows a larger negative change of just over 1.5% for extent in August and 2.5 % for

volume in September. Both cases show strong seasonal cycles in both extent and volume, with effectively no difference in the extent between all three simulations through October to March. Despite floe welding being an active process only in winter freezing conditions, the choice of floe welding parameter has little impact on the winter sea ice extent but has a moderate impact on the summer sea ice extent. This is consistent with Fig. 7.9, which shows that welding primarily acts within the winter pack ice where sea ice concentration is high. These differences persist as winter pack ice regions transition to being part of the summer MIZ and therefore influence the lateral melt rate and sea ice retreat in summer.

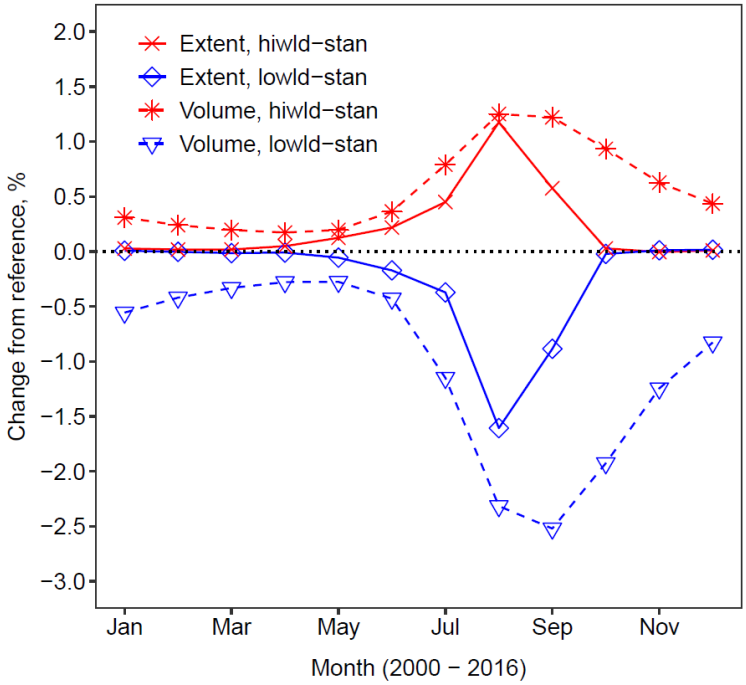

Figure 7.11: Difference in sea ice extent (solid) and volume (dashed) of *prog-lowld* (blue, diamond or triangle) and *prog-hiwld* (red, cross or star) relative to *prog-stan* averaged over 2000 - 2016. The welding scheme is shown to have a moderate impact on the sea ice extent and volume.

7.2.4 Impact of new floe formation processes

Sect. 6.2.3 described two alternative approaches to calculating the size of newly formed floes in the prognostic FSD model. The first is that all floes adopt the diameter of the midpoint of the smallest floe size category i.e. all new floes form as pancake ice. The second is that the size of new floes is determined according to the ocean surface conditions using Eq. (6.15) i.e. new floes can form as nilas or pancake ice. *prog-stan* uses the latter approach to estimate the size of new floes. In this section *prog-stan* will be compared against *prog-ni0*, where all new floes form as pancake ice and *prog-ni1*,

where all new floes form in the largest floe size category. Figure 7.12 compares the perimeter density distributions of these three simulations in April and August for the MIZ and pack ice. *prog-stan* and *prog-ni1* are broadly similar, apart from the latter showing a moderately higher perimeter density in the smallest floe size category. This behaviour is consistent across the two months and regions. In comparison, the behaviour of *prog-ni0* is very different. The perimeter density per unit sea ice area within the smallest floe size category is significantly higher for *prog-ni0*, particularly in August. The result is a reduction in the perimeter density distribution in almost all other categories for both months and regions.

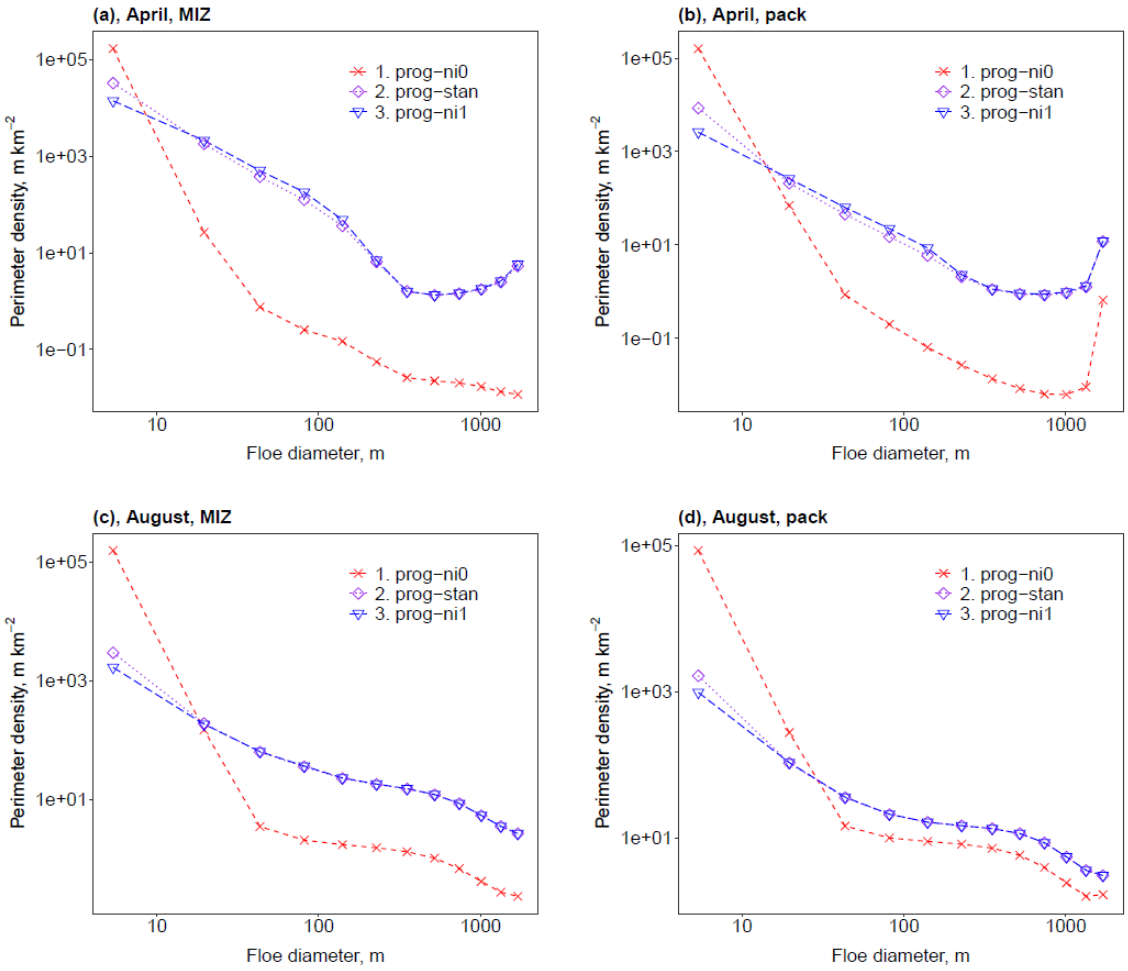

Figure 7.12: The perimeter density distribution, $m\ km^{-2}$, of sea ice area as a function of floe size for April MIZ (top left), April pack ice (top right), August MIZ (bottom left), and August pack ice (bottom right). Distributions are shown for *prog-ni0* (red, cross, dashed), *prog-stan* (purple, diamond, dotted) and *prog-ni1* (blue, triangle, long-dash), all averaged over 2000 – 2016. The plots show that the method used to determine the size of newly formed floes has a large impact on the FSD.

This raises the question as to why *prog-ni1* and *prog-stan* produce such similar probability density distributions. It turns out that Eq. (6.15), used to calculate the size of new floes, acts in a quasi-bimodal manner when applied to the prognostic model. For example, taking a value of 300 m for λ, floes are assigned to the smallest category if the significant wave height exceeds 2×10^{-3} m or the largest category if the significant wave height is smaller than 2×10^{-7} m. The rate of wave attenuation is sufficiently high that propagating waves only fall within this range for a limited distance of the order of the size of individual grid cells, and hence such conditions will only be achieved over a small proportion of the sea ice cover in any given timestep. This constrained range for the formation of mid-sized floes effectively means that floes will generally form in either the smallest or largest category. The pack ice is generally sheltered from ocean surface waves, and hence across most of the pack ice floes are expected to form in the largest floe size category, which is consistent with the similarity of the distributions for *prog-stan* and *prog-ni1* and the significant differences in the distributions between *prog-stan* and *prog-ni0* presented in Fig. 7.12. The presence of waves in locations where floes do form as pancake ice in the smallest floe size category in *prog-stan* means that floes that form in the largest category in these locations in the *prog-ni1* simulation are vulnerable to being broken up by ocean waves. This explains why the perimeter density is lower in the smallest category but higher in other small floe size categories (with a floe size less than 200 m) for *prog-ni1* compared to *prog-stan* in both the April MIZ and pack ice. Differences between *prog-ni1* and *prog-stan* are further suppressed in August compared to April; this can be attributed to the brittle fracture restoring. It is likely that the simulations presented here overestimate the similarity between *prog-ni1* and *prog-stan*, as the model does not represent any sea surface variability generated within the sea ice cover e.g. waves generated within larger leads.

Figure 7.13 shows the spatial distribution in l_{eff} for *prog-ni0* and *prog-ni1* in selected months. For *prog-ni1*, there is an increase in the magnitude of l_{eff} of the order 10^2 m in the pack ice compared to the distribution shown in *prog-stan*, but there is still significant spatial variability in l_{eff}. Moderate increases in l_{eff} can also been seen in the MIZ, with a significantly reduced proportion of the MIZ adopting values of l_{eff} below 40 m compared to *prog-stan* in all three months. For *prog-ni0* a very different distribution in l_{eff} is seen, with values below 40 m across most of sea ice cover apart from the Canadian Archipelago and a few other locations through April, June, and August. This means the high spatial variability in l_{eff} seen for *prog-stan* is no longer present. It also

means significant lateral melting will be expected across the sea ice cover throughout the melt season.

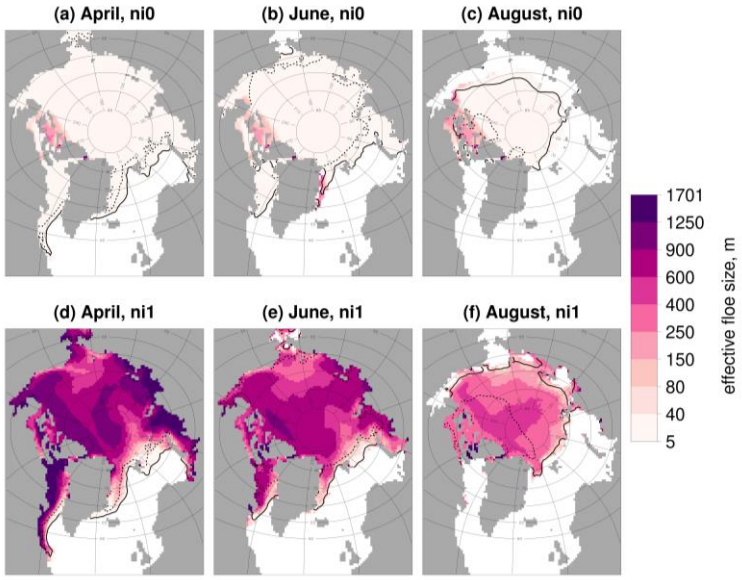

Figure 7.13: l_{eff} for *prog-ni0* (top row, a-c) and *prog-ni1* (bottom row, d-f) averaged over 2000 – 2016. Results are presented for April (left column, a, d), June (middle column, b, e), and August (right column, c, f). Values are shown for locations where the sea ice concentration exceeds 5 %. The variability in l_{eff} is strongly suppressed for the case where all floes form in the smallest category.

Figure 7.14 shows the annual mean difference in sea ice extent and volume for *prog-ni0* and *prog-ni1* relative to *prog-stan*. Small to moderate changes are seen for *prog-ni1* up to a maximum increase of up to 1 % for both the sea ice volume and extent in summer. This is consistent with the moderate increase in the values of l_{eff} seen in the MIZ in Fig. 7.13 for *prog-ni1* compared to *prog-stan*. *prog-ni0* produces very large differences compared to *prog-stan*, with a maximum reduction of about 30 % in both the extent and volume in August. The minimum difference is still significant, with a 1 % reduction in the winter sea ice extent and a minimum volume reduction of 5 % in April. The magnitude of these impacts is comparable to the more extreme parameter choices made for the WIPoFSD model in Fig. 3.9 i.e. cases where the exponent, α, is set to -3.5, or the minimum floe size, d_{min}, is set to 1 m. These results again confirm that the wave dependent growth scheme is much closer in behaviour to *prog-ni1* than *prog-ni0* in terms of impact on the sea ice cover. In addition, this is further evidence that the impact of winter processes on the FSD can persist and have a strong impact on sea ice evolution in the subsequent melt season.

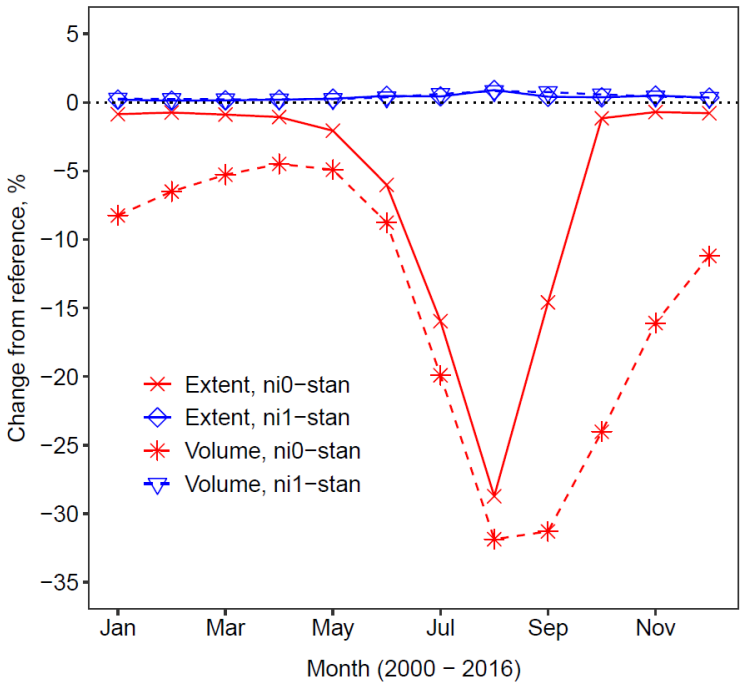

Figure 7.14: Difference in sea ice extent (solid) and volume (dashed) of *prog-ni1* (blue, diamond or triangle) and *prog-ni0* (red, cross or star) relative to *prog-stan* averaged over 2000 - 2016. The impact of the prognostic FSD on the sea ice is highly dependent on the size of newly formed floes.

It is worth commenting on how realistic both the *prog-ni0*, 'pancake' and *prog-ni1*, 'nilas' approaches to new floe size determination are. The observations of the FSD from the Chukchi and Beaufort Seas, presented in Stern et al. (2018b), indicate an approximately linear distribution in log-log space across floes of sizes from 10 m – 10 km, which is more consistent with the behaviour of *prog-stan* than *prog-ni0*. The distribution presented in Toyota et al. (2006), from the Sea of Okhotsk, is also supportive of more moderate gradients in perimeter density for smaller floes. Alberello et al. (2019) presented results from regions of the Antarctic where the sea ice consists primarily of pancake ice. The FSD obtained from these samples indicated that 50 % of the sea ice area consisted of floes with diameters between 2.3 m – 4 m, i.e. floes in the smallest category did dominate the distribution in this case. Given the strong difference in impact of *prog-ni0* compared to *prog-stan* shown in Fig. 7.14, accurately representing and discriminating between different floe formation processes appears to be an important component of any FSD model.

7.2.5 Impact of lateral growth and melt

Equations (6.5) and (6.6) in chapter 6 describe the feedback of lateral melting and growth on floe size respectively. The impact of these processes is investigated through

the following two sensitivity studies: in *prog-nolm* lateral melt feedback on floe size is removed, and in *prog-nolg* lateral growth feedback on floe size is removed. Figures 7.15 – 7.17 are equivalent to 7.6 – 7.8, displaying the perimeter density distributions, spatial distributions of l_{eff}, and sea ice extent and volume for *prog-nolm* and *prog-nolg* relative to *prog-stan* where appropriate. The three plots together show that the difference between *prog-nolg* and *prog-stan* is effectively negligible. This suggests that lateral growth is not an important process either in determining the emergent FSD or the subsequent impact of the FSD on the sea ice mass balance.

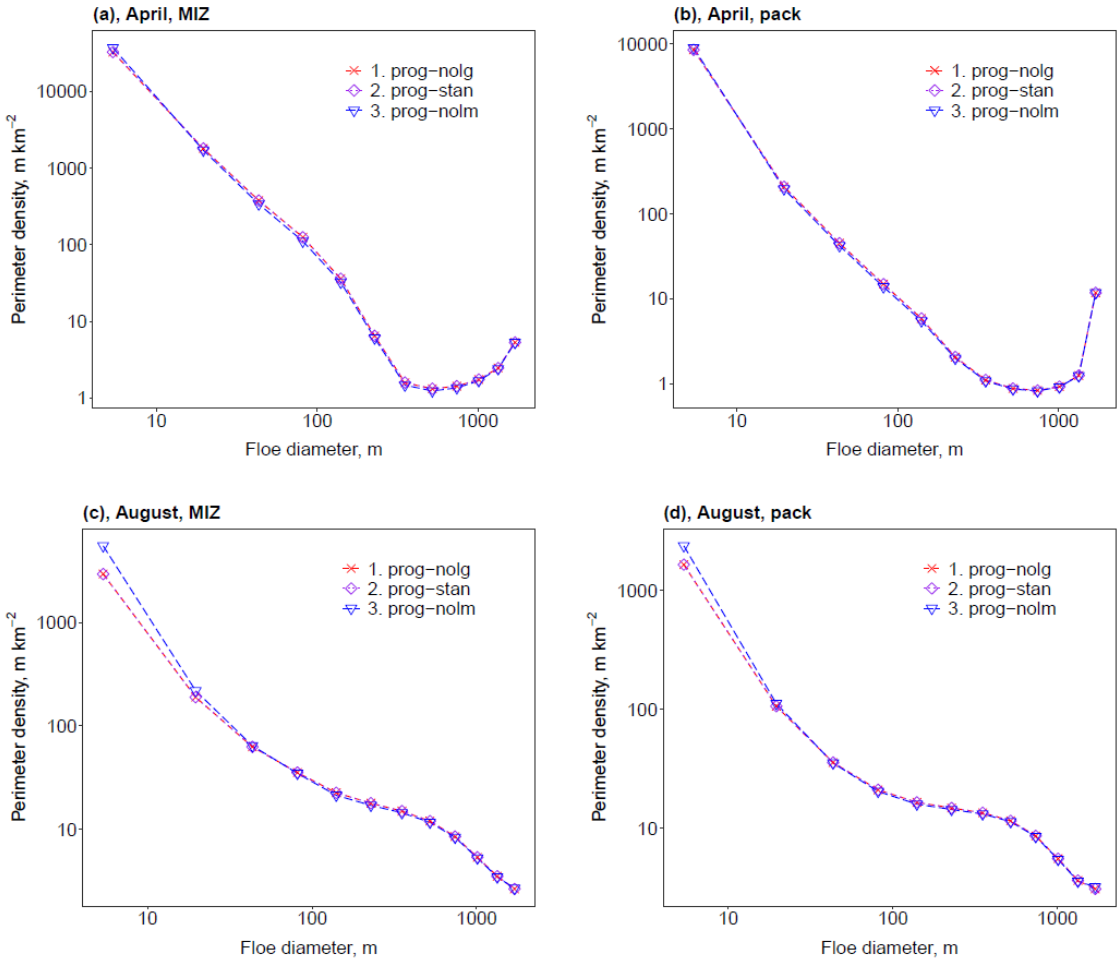

Figure 7.15: The perimeter density distribution, $m\ km^{-2}$, of sea ice area as a function of floe size for April MIZ (top left), April pack ice (top right), August MIZ (bottom left), and August pack ice (bottom right). Distributions are shown for *prog-nolg* (red, cross, dashed), *prog-stan* (purple, diamond, dotted) and *prog-nolm* (blue, triangle, long-dash), all averaged over 2000 – 2016. Small differences can be seen between *prog-nolm* and *prog-stan* in August, but *prog-nolg* and *prog-stan* are almost identical.

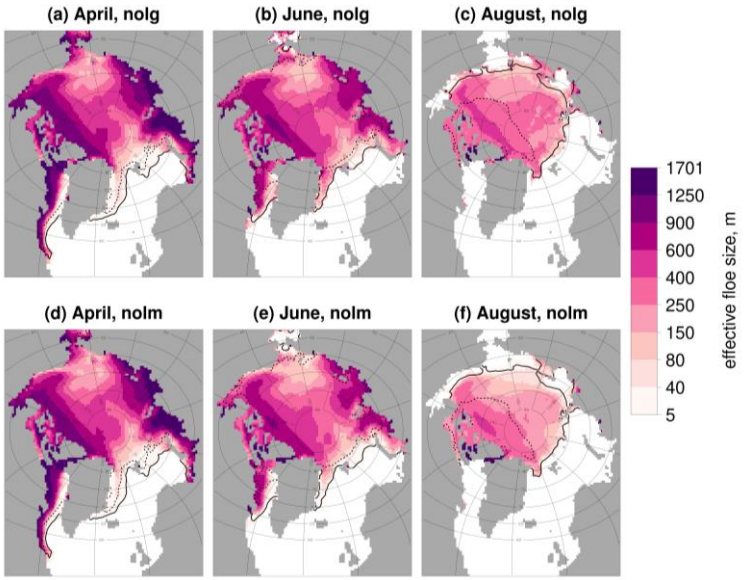

Figure 7.16: l_{eff} for *prog-nolg* (top row, a-c) and *prog-nolm* (bottom row, d-f) averaged over 2000 – 2016. Results are presented for April (left column, a, d), June (middle column, b, e), and August (right column, c, f). Values are shown for locations where the sea ice concentration exceeds 5 %. The magnitude and variability in l_{eff} are broadly similar for each case apart from for the outer MIZ.

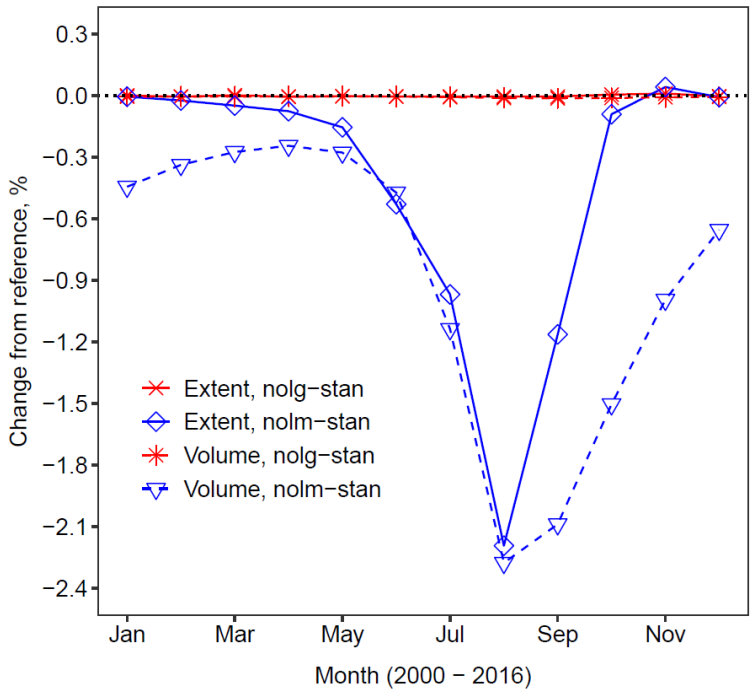

Figure 7.17: Difference in sea ice extent (solid) and volume (dashed) of *prog-nolm* (blue, diamond or triangle) and *prog-nolg* (red, cross or star) relative to *prog-stan* averaged over 2000 - 2016. *prog-nolm* produces reductions of up to 2.3 % in the sea ice extent and volume, whereas *prog-nolg* shows negligible difference to *prog-stan.*

The differences between *prog-stan* and *prog-nolm* are larger. Whilst the differences between the perimeter density distributions shown in Fig. 7.15 are small in April, by August the perimeter density per unit sea ice area in the smallest floe size category shows a moderate increase for *prog-nolm* compared to *prog-stan*, particularly in the MIZ. The magnitude and variability in l_{eff} shown in Fig. 7.16 are broadly similar between *prog-stan* and *prog-nolm*, but the exception to this is the MIZ, where a higher proportion of the sea ice cover has an l_{eff} below 80 m for *prog-nolm* in each month. The differences are particularly notable for the outer MIZ in August. Figure 7.17 shows the impact of removing lateral melt feedback on floe size is to reduce the mean extent and volume by up to 2.3% in August. This suggests that, despite the small differences in l_{eff} across most of the sea ice cover, the larger changes in the outer MIZ result in a significant difference between *prog-stan* and *prog-nolm* in terms of the sea ice mass balance.

These results for *prog-nolm* are internally consistent. The removal of lateral melt feedback increases the perimeter density per unit sea ice area for smaller floes, reducing l_{eff} in the MIZ, and therefore the total sea ice extent and volume also decrease through an increase in lateral melt. They are also counterintuitive results. As an individual floe experiences lateral melt, the floe becomes smaller and l_{eff} for that floe decreases and therefore the volume of lateral melt relative to the total sea ice surface area increases. However, as discussed in chapter 4, the behaviour of a distribution is more complicated because floes can entirely melt out from the distribution, which acting on its own will increase l_{eff}. Hence, the evolution of l_{eff} depends on the composition of the distribution, specifically the ratio of smaller to larger floes. In the case of *prog-nolm,* by excluding lateral melt feedback on the FSD, floes are not lost from the smallest category through lateral melt processes, resulting in an artificially higher overall lateral melt volume.

7.2.6 Impact of brittle fracture

In Sect. 7.1.2, the quasi-restoring brittle fracture scheme was introduced to improve the performance of the prognostic model compared to observations in simulating the perimeter density distribution for mid-sized floes. To explore the impact of this scheme on the full distribution two sensitivity studies are considered. In *prog-nobf* the brittle fracture process is removed from the model. In *prog-morebf* the restoring timescale, τ,

is reduced from 30 days to 10 days to strengthen the impact of the brittle fracture restoring on the emergent FSD.

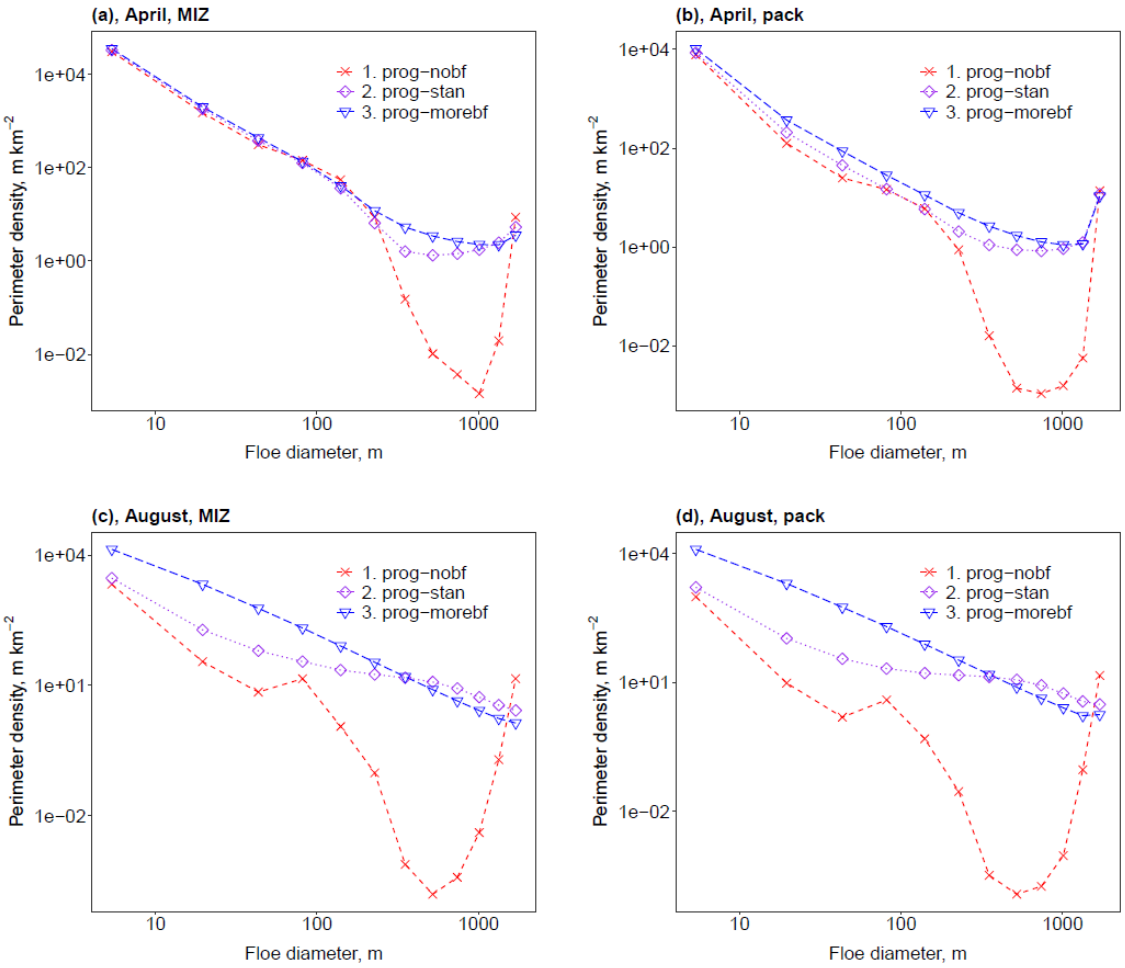

Figure 7.18: The perimeter density distribution, $m\ km^{-2}$, of sea ice area as a function of floe size for April MIZ (top left), April pack ice (top right), August MIZ (bottom left), and August pack ice (bottom right). Distributions are shown for *prog-nobf* (red, cross, dashed), *prog-stan* (purple, diamond, dotted) and *prog-morebf* (blue, triangle, long-dash), all averaged over 2000 – 2016. The inclusion of the brittle fracture scheme has a large impact on the distribution for mid-sized floes.

Figure 7.18 compares the emergent perimeter density distribution between *prog-nobf*, *prog-morebf* and *prog-stan*. In April, the distributions for floes below about 200 m in diameter are broadly similar for each simulation, particularly in the MIZ. However, for mid-sized floes and larger, differences of several orders of magnitude can be seen between *prog-nobf* and the simulations including brittle fracture. By August, the differences in the distributions span across all floe sizes. The perimeter density for *prog-nobf* is higher in the largest category but lower in all other categories, often by orders of magnitude. Larger differences can also be seen between *prog-stan* and *prog-*

morebf in August. *prog-stan* has a higher perimeter density for larger floe size categories and a lower perimeter density for smaller floe size categories, with a transition at about 300 m. The larger differences in August can be understood by considering that over winter brittle fracture competes with floe formation, welding, and wave break-up to determine the shape of the distribution, which have been demonstrated to have large impacts on the shape of the FSD in sections 7.2.2 - 7.2.4. In summer the main competing processes to brittle fracture influencing the shape of the FSD are lateral melting and wave break-up; section 7.2.5 shows the former only has a small influence on the perimeter density distribution and section 7.2.2 shows wave breakup has a larger impact on the FSD shape in winter compared to summer. The *prog-nobf* simulation shows a strong uptick in perimeter density for larger floes. Section 6.6.1 previously explained that the presence of this non-physical 'uptick' can be attributed to missing floe break-up processes such as brittle fracture and accumulation of floes in the largest category that would otherwise grow to much larger sizes without a fixed maximum. Figure 7.18 demonstrates both how the introduction of the brittle fracture scheme can significantly dampen but not entirely remove the presence of this 'uptick', even where the restoring rate is strong.

Figure 7.18 also gives an idea of the extent to which the brittle fracture restoring is dominating the overall shape of the distribution. In April in particular, the similarity between the three cases below 200 m and lack of linearity in log-log space for *prog-stan* and *prog-morebf* above 200 m suggests the brittle fracture restoring is not overly constraining the shape of the distribution. By August, at the end of the melting season, brittle fracture has had an impact on the shape of the distribution across all floe sizes, with *prog-nobf* behaving differently to *prog-stan* across the full floe size range. *prog-morebf* shows close to linear behaviour in log-log space, suggesting the brittle fracture scheme dominates the shape of the distribution. *prog-stan* shows deviation away from this linear behaviour, suggesting that, whilst the brittle fracture restoring still has a strong influence on the shape, other processes continue to influence the shape of the distribution as well. This is confirmed by the other sensitivity studies that show that the prognostic model including the brittle fracture scheme still produces a strong response to perturbations in other processes that can change floe size. *prog-morebf* produces a better fit to observations compared to *prog-stan*, as expected given the distribution being restored to, a power law with an exponent of -2, in itself compares favourably to observations compared to prognostic model output. However, the choice of a 30-day

restoring timescale has been both physically motivated, as discussed in section 7.2.2, and does not suppress the impact and role of other processes in the shape and evolution of the FSD.

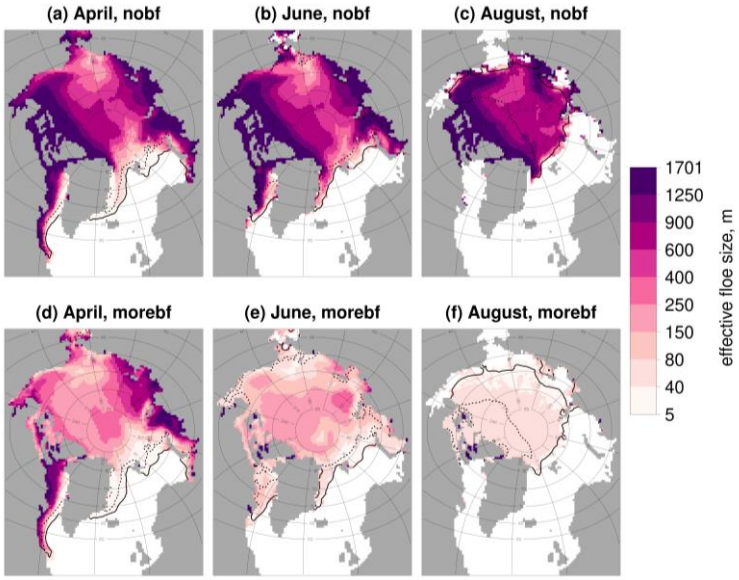

Figure 7.19: l_{eff} for *prog-nobf* (top row, a-c) and *prog-morebf* (bottom row, d-f) averaged over 2000 – 2016. Results are presented for April (left column, a, d), June (middle column, b, e), and August (right column, c, f). Values are shown for locations where the sea ice concentration exceeds 5 %. The magnitude of l_{eff} is very sensitive to the inclusion and strengthening of the brittle fracture scheme.

Figure 7.19 shows the spatial distribution in l_{eff} for *prog-nobf* and *prog-morebf* for select months. These plots show that, as expected, the removal of brittle fracture causes an increase in the mean value of l_{eff} whereas the strengthening of the restoring causes a reduction in the mean value of l_{eff} across the sea ice cover. Of the three cases the distribution of l_{eff} for *prog-stan*, presented in Fig. 7.4, appears to have both a higher spatial and temporal variability. The temporal trends of each scenario are different. For *prog-nobf*, the average l_{eff} increases as smaller floes melt out of the distribution. For *prog-morebf*, the brittle fracture scheme has a stronger influence over the evolution of l_{eff}, resulting in the negative trend in l_{eff} over the melt season shown in Fig. 7.19.

Figure 7.20 shows the difference in annual sea ice volume and extent for *prog-nobf* and *prog-morebf* compared to *prog-ref*. Removal of the brittle fracture scheme results in a small to moderate increase in the sea ice extent and volume of up to 1% in August and just over 3 % in September respectively. The reduction in the restoring timescale from 30 to 10 days reduces the extent by up to 5 % and volume by over 8 %.

Differences in the sea ice extent are only seen during the melt season, with negligible difference in the sea ice extent between November and April for all three simulations. This is consistent with the similar distributions for smaller floes in the April MIZ shown in Fig. 7.18. Figure 7.20 shows that the impact of the prognostic FSD model on the sea ice mass balance is strongly sensitive to the value of τ, particularly when it adopts values of lower than one month. Constraining the timescale over which brittle fracture processes influence the sea ice cover during the melt season is clearly important both in terms of the shape of the emergent FSD and the impact on the lateral melt volume.

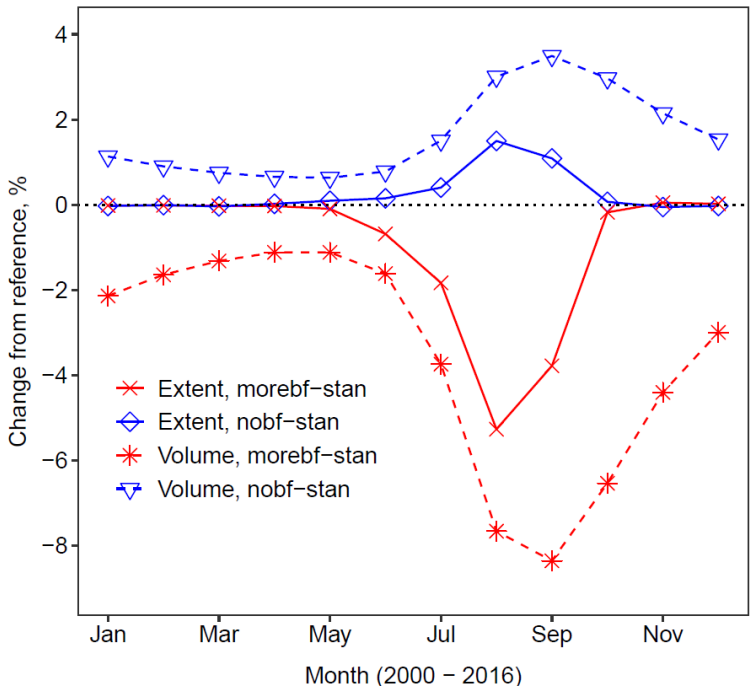

Figure 7.20: Difference in the sea ice extent (solid) and volume (dashed) of *prog-nobf* (blue, diamond or triangle) and *prog-morebf* (red, cross or star) relative to *prog-stan* averaged over 2000 - 2016. The impact of the brittle fracture scheme on the sea ice mass balance is shown to be very sensitive to the restoring timescale for brittle fracture.

7.2.7 Impact of form drag

In chapter 5, the interaction between floe size and sea ice-atmosphere-ocean momentum exchange was investigated using the form drag scheme of Tsamados et al. (2014). Both l_{eff} from the WIPoFSD model and the original Lüpkes scheme (Lüpkes et al., 2012) were compared to the use of a constant floe size as the floe size in the form drag scheme. The use of l_{eff} from the WIPoFSD model for the form drag floe size had a close to negligible impact on the sea ice mass balance relative to using a constant floe size. The large negative impact of the Lüpkes scheme on the sea ice mass

balance was found to be a result of the bias of the scheme towards producing very small floes of 50 m or less in response to small reductions in the concentration of the sea ice cover. Here, *prog-stan* will be compared to *prog-fd300*, where *prog-fd300* is a simulation using the prognostic model with a constant floe size of 300 m for the form drag floe size. In *prog-stan*, l_{eff} is taken as the form drag floe size.

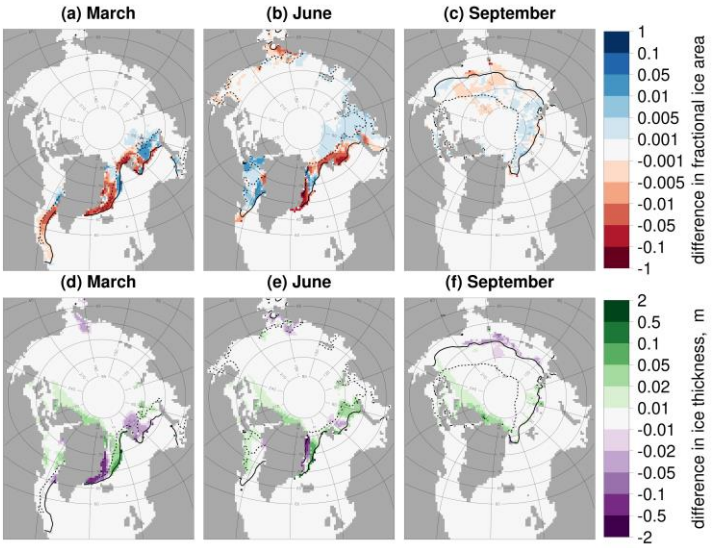

Figure 7.21: Difference in fractional sea ice area (top row, a-c) and thickness (bottom row, d-f) for *prog-stan* relative to *prog-fd300* averaged over 2000 – 2016. Results are presented for March (left column, a, d), June (middle column, b, e), and September (right column, c, f). Values are shown for locations where the sea ice concentration exceeds 5 %. The largest differences in fractional sea ice area and thickness are within the MIZ, particularly in March and June.

Figure 7.21 shows the spatial difference in the fractional sea ice area and thickness for *prog-stan* relative to *prog-fd300* over March, June, and September averaged over 2000 – 2016. The impact is not homogenous in sign, with regions of both increase and decrease in sea ice concentration and thickness across all three months. Changes in the sea ice concentration in the MIZ during March and June can exceed 0.05 in certain locations and are generally large. In September the differences are close to negligible. Similar trends apply to the sea ice thickness, with a small but persistent increase in the sea ice thickness off North Greenland and the Canadian archipelago. Comparing Fig. 7.21 to Fig. 5.6, the equivalent plot for the WIPoFSD model, both plots show similar spatial distributions for changes in the concentration and thickness over the three months, however the magnitude of the changes are much larger for the prognostic case. The larger magnitude can be attributed to the different spatial distributions in l_{eff}. In chapter 5, it is explained that within CICE the momentum and heat transfer coefficients are linked. In addition, basal melting is influenced by changes to the

momentum transfer coefficient via the friction velocity term (see Eq. 2.3). Where l_{eff} is small, thermodynamic processes will be strengthened via an increased heat transfer coefficient and friction velocity. For the WIPoFSD model, as shown in Fig. 5.6, l_{eff} only transitions to floes of smaller than 300 m at the outer edge of the sea ice cover. In comparison, Fig. 7.4 shows that for the prognostic model a much larger proportion of the sea ice has l_{eff} below 300 m over the melting season, transitioning to sizes below 40 m across most of the MIZ in March and June. The floe size contribution to form drag at sizes below 40 m becomes increasingly significant due to the inverse relationship between the form drag contribution of floe edges and floe size shown in Eq. (5.6), hence the large changes seen across the MIZ in March and June in Fig. 7.21. The region along the Canadian Archipelago that sees a small but persistent increase in sea ice thickness is shown in Fig. 7.4 to maintain an l_{eff} above 300 m throughout the melting season and exceeding 1000 m in the early melt season.

Figure 7.22 shows the difference in the annual evolution of sea ice extent and volume for *prog-stan* relative to *prog-fd300*. The plot shows a reduction in the extent between 0 % to 0.5 %, though there is no clear trend in how this evolves throughout the year. The volume displays oscillatory behaviour, up to a maximum reduction of just over 0.1 % from January to May and an increase of up to 0.2 % from June to December. The reduction in extent is a result of the low value of l_{eff} at the sea ice edge throughout the year, enhancing melting processes and driving a retreat of the sea ice edge. The oscillatory nature of the difference in volume is a response to the high values of l_{eff} within the pack ice. The heat transfer coefficient and friction velocity are reduced, resulting in less sea ice growth in winter but also less sea ice melt in summer. The corresponding plot for the WIPoFSD model, Fig. 5.5, shows that the changes in the sea ice extent and volume has limits of ± 0.1%. The larger changes for the prognostic case can be attributed to the increased spatial variability of l_{eff} compared to the WIPoFSD model. The higher proportion of sea ice cover with l_{eff} smaller than 300 m in summer amplifies melting processes during this period, whereas the much higher maximum limit of l_{eff} within the pack ice enables larger differences in the sea ice volume to form relative to the case with a fixed form drag floe size of 300 m.

It is worth noting that for both the prognostic and WIPoFSD models, the inclusion of l_{eff} to represent the form drag floe size only causes a small change to the sea ice mass balance compared to using a fixed floe size of 300 m. The large contributions of

floe edges to the total form drag predicted using the Lüpkes model are not supported in the results presented here and in chapter 5. The FSD models instead predict that floe edges will be a significant contributor to the form drag only where l_{eff} can reach particularly low values, such as in the Greenland Sea. Overall, it appears that the leading order impact of the FSD on the sea ice acts through the lateral melt rate via changes to the perimeter density, with impacts via form drag a secondary contribution.

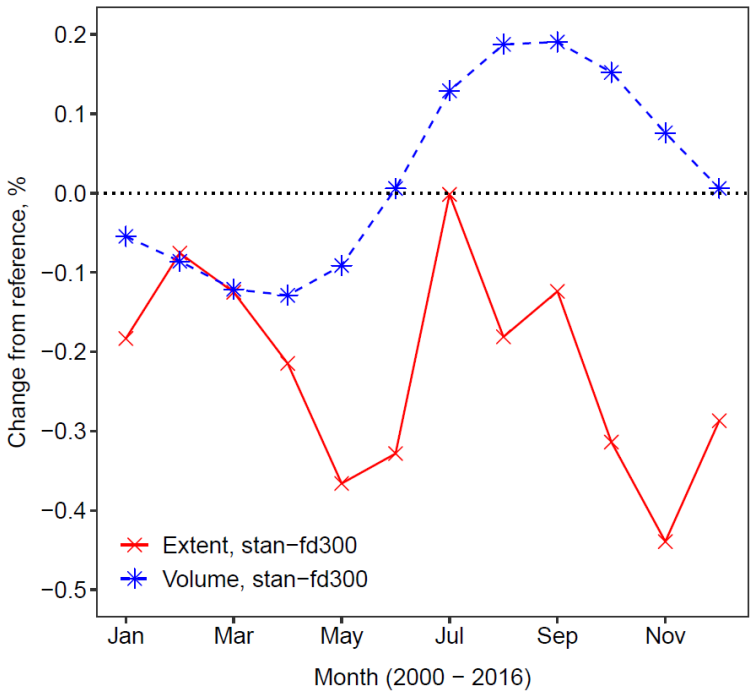

Figure 7.22: Difference in sea ice extent (solid, red, crosses) and volume (blue, dashed, stars) of *prog-stan* compared to *prog-fd300* averaged over 2000 - 2016. The form drag contribution to the change in sea ice mass balance is small in magnitude and varies in sign throughout the year.

7.2.8 The shape of the FSD and its mass balance impact

In Sect. 7.2 a series of sensitivity studies have been performed to explore how individual processes determine the emergent FSD from the prognostic model. In addition, plots have been presented to show the impact these processes have on the overall sea ice mass balance. These results can now be used to produce an overall assessment of the processes most important to the shape of emergent FSD and its impact on the sea ice cover. For the emergent FSD, the role of different processes appears to vary through the year. Here two months have been considered, April, at the start of the summer melt season, and August, at the end of the summer melt season. The FSD that emerges at the end of the winter growth season and the summer melt

season are effectively represented, but it cannot be assumed that the magnitude of the impact of each process smoothly varies between these two snapshots.

An important feature of the emergent FSD is that differences in the FSD that form over winter in response to particular processes can persist through the summer months. Furthermore, changes of scale from April to August in the perimeter density of smaller floe size categories mean that differences that have a small impact on the FSD shape in winter can have a much larger impact on the FSD shape in summer. For example, the floe welding process is only active during freezing conditions i.e. it will not be active through the summer months of April to August, however the shape of the August perimeter density distribution displays a stronger sensitivity to the welding parameters than in April. Despite floe welding not being an active process through the melting period, it still influences the shape of the distribution for smaller floes after the melting season to a greater extent than it does at the start. Similar results can also be seen in the sensitivity to the floe formation mechanism, with the perimeter density for smaller floes in summer strongly dependent on the scheme used. Though several processes that are active in summer contribute to the shape of the distribution in August, including brittle fracture, lateral melting, and wave break-up, these winter freeze-up processes have the strongest impact on the shape of the perimeter density distribution for smaller floes. The change in sea ice mass balance is consequently found to be strongly sensitive to both the welding and particularly the floe formation scheme. Given these features that form over winter persist through the melting season and have a large impact on the overall sea ice extent and volume, it supports the need for accurate physical representation of these processes in FSD models. A simple restoring approach, as used in the WIPoFSD model, may not be sufficient.

The main component of the model that impacts mid-sized and larger floes in summer is the brittle fracture scheme. Whilst the floe formation mechanism does impact the magnitude of the perimeter density of larger floes, the process does not impact the shape of the distribution overall. Given the brittle fracture scheme operates via a quasi-restoring scheme, this suggests that over this period other processes, such as wave break-up, are not strong enough to have a significant influence on the emergent shape and instead the quasi-restoring is the primarily control. This is not the case for all months, with the emergent FSD in April for mid-sized to larger floes showing a much larger response to changes in the wave break-up scheme than in August. The point here being that the strength of the restoring timescale is not so strong as to entirely

suppress the impact of other processes on the FSD. The development of the brittle fracture scheme was motivated both by observations that melting and break-up of the sea ice occurred along existing cracks and fractures in the sea ice cover and that models of brittle fracture produce fragment sizes adopting a power-law size distribution. Nevertheless, the model approach here used is a simplification and requires some significant assumptions. There is great uncertainty in the use of a single restoring timescale, τ. The value selected for this parameter, 30 days, is an estimate of the timescale melting processes require to drive the break-up of a floe along a crack or fracture. Fig. 7.20 showed that the mass balance impact of the scheme is particularly dependent on this value and hence it should be further constrained. There are good prospects that the necessary observations to constrain brittle fracture and related floe fragmentation processes can be obtained. Hwang et al. (2017) demonstrated that it was possible to produce a Lagrangian perspective of sea ice evolution and floe break-up over a time period spanning March to August through the combined use of TerraSAR-X Synthetic Aperture Radar satellite imagery and buoy clusters collecting in-situ data about the sea ice, atmosphere, and ocean state. This study was able to identify temporary floe fragmentation events coinciding with strong wind events prior to the melting season and spring breakup of floes occurring cotemporally with melting of sea ice, particularly surface melt. The MOSAiC expedition (Dethloff et al., 2016) is expected to provide high quality data tracking the evolution and breakup of individual floes on daily or weekly timescales. Similarly, further analysis of existing high-resolution satellite data such as MEDEA or TerraSAR-X imagery should also provide insights into the evolution of individual floes or clusters of floes. The combination of the techniques demonstrated in Hwang et al. (2017) with these prospective novel observations should allow a better understanding of both the conditions driving floe fragmentation events and the associated timescales. Overall, the findings here regarding the role of the brittle fracture mechanism as the primary control on the August FSD for larger floes should be taken with caution. Nevertheless, whether through the size of newly forming floes, floe welding processes, or fracture of the sea ice cover, these results indicate that processes that act on the FSD and the sea ice in winter are the primary control on the shape of the FSD throughout the melting season.

In general, the FSD in both the summer MIZ and pack ice originates from the winter pack ice; this means that the impacts of processes such as welding and floe formation on the April pack ice persist through the melting season. In contrast, the impacts of

wave break-up on the April pack ice do not persist in the same way through to the August FSD. This is primarily because wave break-up operates over a similar floe size range to the brittle fracture scheme; hence differences that form over winter from wave break-up are then suppressed by the brittle fracture quasi-restoring scheme, which operates with equal magnitude throughout the year. Whilst wave break-up can continue to act through the summer, the calmer wave conditions means the brittle fracture scheme will dominate over any changes for mid-sized and larger floes. The role of wave break-up in the evolution of the FSD and sea ice also differs from other processes in terms of the timing of the maximum impact on sea ice extent and volume. For example, Figures 7.8 and 7.11 show that the peak differences of *prog-nowb* and *prog-lowld* relative to *prog-stan* can be found in June and August, respectively. This can be understood by considering that the perimeter density distributions in April show that wave break-up is most important for shaping the FSD in the MIZ, whereas the floe welding scheme does not appear to have a significant role in the emergent FSD in the April MIZ but does for the pack ice. The impact of wave break-up on the sea ice mass balance is strongest in the earlier melt season before the sea ice retreats sufficiently to the winter pack ice, whereas the impact of welding on the sea ice mass balance is delayed to the later melt season.

Figure 7.15 indicates that lateral growth has a negligible impact on the FSD. Lateral growth could be removed from the model to no effect. Lateral melt also has a negligible impact on the FSD in April, but in August it has a larger impact, particularly in the MIZ. The main impact of lateral melt is to reduce the perimeter density distribution in the smallest floe size categories. Although lateral melt will shift larger floes into these smaller floe size categories, a greater proportion of floes are lost to the smaller category adjacent or melt out for the smallest category, resulting in this depletion of smaller floes. The feedback of lateral melt on an individual floe is to increase the perimeter to area ratio of the floe as it melts, accelerating the floe area loss as a fraction of total area. For the distribution of floes however, the lateral melt feedback on floe size has the reverse effect as it acts as a sink for smaller floes. The perimeter density per unit sea ice area therefore decreases over time. This effect is significant, preventing an additional 2 % of sea ice extent and volume loss by August. In chapter 3, the lateral melt feedback mechanism on floe size within the WIPoFSD model was found to be insignificant. Chapter 4 explored a modified approach to calculating the lateral melt feedback on the FSD in the WIPoFSD model but only found a strong

feedback for scenarios where the l_{eff} for the distribution was artificially low across the sea ice cover. The negative feedback process shown with the prognostic model i.e. lateral melt driving increases in l_{eff} through the melt out of smaller floes, cannot be represented in the WIPoFSD model due to the imposed power law and fixed minimum floe size. Even though lateral melting only appears to have a small effect on the shape of the emergent distribution compared to other processes, it can still have a complex and important role in the overall impact of the prognostic model on the sea ice mass balance.

The overall impact of the emergent FSD on the sea ice mass balance is moderate, with reductions in the mean extent and volume of up to about 2 % and 4 % respectively averaged over 2000 – 2016. Results will be presented in the next chapter to show that underlying these mean values are positive trends in the reduction in September extent and volume over the period 2000 – 2016, particularly the sea ice volume. The mean reductions are the net result of several processes that act either to reduce or increase the impact of the prognostic model. Brittle fracture and wave break-up of floes drive reductions in the sea ice extent and volume, the former by several percent. Floe welding and lateral melt feedback both act to increase the sea ice extent and volume by orders of a percent and moderate the impact of the prognostic model. The most important process, however, appears to be the mechanism to determine how new floes form. In the current formulation, where floes form according to the local surface wave properties, the system exists in a state close to one where all floes form in the largest category, maximising the role of fragmentation processes in determining the mass balance impact. For the scenario where floes all form in the smallest category, a reduction in the sea ice volume and extent of up to 35 % would be seen, dominating the impact of the prognostic model. In such circumstances, lateral melting and floe welding would have increased roles in mitigating the overall change in the sea ice mass balance. The mechanism of new floe formation effectively determines the role of each process in the subsequent evolution and mass balance impact of the FSD.

An important question to address is which of these scenarios is more likely for the Arctic; a regime where floes primarily form as pancake ice or one where they primarily form as nilas ice. The parameterisation to calculate the size of newly formed floes has been motivated by observations (Roach et al., 2018b), however it relies on accurate simulation of the wave field within the sea ice cover. The internal wave scheme used

by the prognostic model underestimates wave interactions with the sea ice compared to a full wave model coupled to the sea ice cover (Roach et al., 2019) and furthermore does not represent waves generated internally within the sea ice cover such as within large leads. A more accurate representation of waves within the sea ice cover is therefore expected to favour the formation of smaller new floes during sea ice growth compared to *prog-stan*. However, Fig. 7.12 suggest that a distribution dominated by pancake ice formation would produce distributions strongly dominated by smaller floes. As discussed in section 7.2.4, several observations of the FSD in the Antarctic are consistent with smaller floes dominating the distribution e.g. Steer et al. (2008), Toyota et al. (2011), Alberello et al. (2019). In comparison, FSDs reported for the Arctic appear to show a more consistent scaling across a large range of floe sizes (e.g. 10 m to 30 km in Stern et al., 2018b), which is more consistent with the distributions presented for *prog-ni1* and *prog-stan* in Fig. 7.12. As mentioned earlier, projects such as the MOSAiC expedition and further analysis of existing high-resolution satellite imagery e.g. MEDEA and TerraSAR-X should enable a better characterisation of FSD processes in the Arctic, including the dominant mechanisms determining the size of newly forming floes. These studies and analyses should provide information about the oceanic and atmospheric conditions during periods of sea ice formation, the size of newly formed floes, and more observations of the shape of the FSD for smaller floes.

7.2.9 Annual evolution of the FSD slope

Stern et al. (2018b) calculated the average power-law exponent from several locations in the Chukchi and Beaufort Seas from March to October for floes larger than 2 km. They found that the exponent displayed sinusoidal behaviour, ranging from a maximum of – 1.9 in April to a minimum of – 2.8 in August. This behaviour was consistent over the two years sampled, 2013 and 2014. The results in this section can be used to consider the mechanisms that are driving this change in exponent. The observations show that the exponent decreases over the melting season i.e. there is an increase in the proportion of smaller floes compared to larger floes. The results from the prognostic model suggest that fragmentation processes, whether through the brittle fracture mechanism outlined in Sect. 7.1, or through wave break-up, is most important in driving this evolution in the exponent. From August to April, the exponent increases, suggesting an increase in the proportion of larger floes over smaller floes. Note that observations are not available between October and March and trends over this period must be extrapolated. The prognostic model suggests that this increase is driven by the

formation of new floes in freezing conditions as nilas sea ice and the welding of floes. If floes were primarily forming as pancakes, a further decrease in the exponent would be expected in the early freeze-up season before the increase in sea ice concentration enhances the rate of floe welding.

There are several caveats to this comparison between the prognostic model and the observations of Stern et al. (2018b), not least that the observations were for floes of size 2 km and larger, above the range considered for the prognostic model setup used here. Though the study presented evidence that, at least for some locations, the exponent for the larger floe sizes persisted down to floes as small as 10 – 20 m. Nevertheless, it is a useful result that the prognostic model includes mechanisms that can explain the observed evolution of the FSD exponent as it suggests both that the prognostic model is performing in a broadly realistic manner and provides physical insight into the observed trends in the exponent. There does exist some evidence that comparable behaviour can be seen in observations that extend to smaller floe sizes. As discussed previously in Chapter 6, Perovich and Jones (2014) analysed observations of floes ranging from 10 m to 10 km in size and reported a change in exponent from – 3.0 over June and July to – 3.2 in late August, followed by an increase to above – 3.1 in September. These changes were associated in the study with a high wind speed event causing break-up of floes in late July and early August followed by freeze-up and welding to cause the increase in the exponent by September. These observations again support the idea that the mechanical break-up of floes over the melt season and new floe formation and welding over the freeze-up season are the key drivers of observed changes in the FSD exponent.

7.2.10 Comparison to earlier studies using the prognostic model

Several studies have been published both documenting the development of the prognostic floe size-thickness distribution (FSTD) model and using the model to improve understanding of the sea ice FSD: Horvat and Tziperman (2015, 2017), and Roach et al. (2018a, 2019). It is useful to discuss previous findings with the prognostic model and how they compare to the results presented here. Horvat and Tziperman (2015) first introduced the FSTD model to the literature. This first iteration represented the following processes: lateral and vertical melting and freezing; break-up of floes by waves; and mechanical interactions (rafting and ridging of floes during floe collisions). Simple experiments were performed in a grid cell scale domain to explore how the floe

size would respond to different thermodynamic and mechanical forcings, with the FSTD initiated as single Gaussian peaks in both floe size and thickness space.

This model was then developed into a coupled FSTD-mixed-layer model in Horvat and Tziperman (2017). In addition to the thermodynamic, mechanical, and wave break-up processes included in the 2015 study, they also represented the impact of advection. This was done by defining a pack ice FSTD state that would advect into the domain at a fixed rate alongside advection of sea ice out of the present domain into the open ocean. The FSTD was initiated as a power law both in the pack ice and the model domain, and then allowed to evolve either under one or a combination of the processes represented in the model. This study concluded that each of the processes considered perturbed the FSTD from a power law, both individually and collectively; a power law was only stable when basal melting was the primary form of sea ice volume loss rather than lateral melting. For the FSTD acting under all parameterised processes, three regimes were identified: floes from 10 – 100 m in diameter formed a shallow power law determined by advection, floe collisions, and wave break-up events; floes from 100 m – 300 m formed a steeper power law determined by the balance between floes lost from this regime in break-up events and new floes formed in this regime from floe collision events; and floes larger than 300 m followed an intermediate power law described as a "joined power law" by Horvat and Tziperman (2017).

Roach et al. (2018a) then implemented an updated FSTD prognostic model into a full sea ice-ocean coupled model. In this setup five processes were considered: lateral melt and growth, new floe formation as pancakes, welding of floes, and wave break-up. Mechanical redistribution of floes via collisions was not included in this setup. This study took the approach of evaluating the coupled model including the FSTD model with repeated 1975 atmospheric forcing for 65 years, taking the final 20 years of this simulation for analysis. These simulations were then used to evaluate the FSD in both hemispheres for both March and September, to explore how individual processes contribute to the total emergent distribution, and to consider the net impact of the FSTD model on the sea ice state. This study found that the number of floes in the smallest category was a function of the number of new pancake floes formed each freeze-up season compared to the reduction in small floes from welding and lateral melting. Wave break-up, lateral melting, and floe welding were all found to have a significant role in the evolution of the number density for the largest floe size category. The timings of the impacts of each process on the FSD were different, with wave break-up

and lateral melting driving changes primarily over the melting season, lateral growth and pancake formation driving changes primarily in Autumn, with welding then dominating over the rest of the freeze-up season. Moderate to large changes were seen in the Arctic and Antarctic sea ice concentration and volume in response to the FSTD model. The emergent FSTD had an exponent of about – 4 in March and – 5 in September in the Arctic, outside the range generally seen in observations and more negative than the exponents considered in chapter 3 with the WIPoFSD model. It is therefore unsurprising that this FSD state would drive a large reduction in the sea ice mass balance.

Roach et al. (2019) further developed the work of the 2018 paper by coupling a wave model to the sea ice – FSTD setup. They also introduced the wave dependent growth scheme, such that floes could form either as pancake ice or nilas ice depending on the local wave conditions. The study included a simulation from 2000 – 2014 using the corresponding atmospheric and oceanic forcing data for those years. In this study the full shape of the FSTD was not considered, but instead perimeter density was used to characterise the emergent FSTD as it evolved. They found that wave break-up drove significant increases in the floe perimeter density over the melt season with lateral melting having the opposite impact. Formation of new floes increased the perimeter density over the winter months.

In this chapter I have further extended the existing literature on the prognostic FSD model through the incorporation of a brittle fracture scheme. I have also systematically evaluated sensitivity studies to each process in order to consider both their role in determining the emergent FSD and how they each influence the impact of the FSD on the sea ice mass balance, something not previously considered. The results, where comparison is possible, are consistent with previous studies e.g. both this study and Roach et al. (2019) identified the floe formation mechanism as a dominant process in the winter evolution of the FSD and floe break-up processes as dominant over the summer evolution. Previous studies have also identified lateral melting as a negative feedback process due to the melt out of smaller floes. Horvat and Tziperman (2017) identified three floe regimes using the FSTD setup with 90 floe size categories, possible only due to the use of a simple domain approach and short simulations. Within CICE, the use of more than 12 – 16 floe size categories presents a prohibitive computational expense. It could be argued from Fig. 7.3 that the perimeter density distribution does undergo a transition in slope at around 100 m and then again at 300

m, particularly for the April MIZ. However, the use of a limited number of floe size categories means that it is not possible to resolve smaller floes sufficiently that any floe regimes over the 10 – 300 m range can be clearly identified.

7.3 Summary of chapter 7

Observations of linear features in the winter pack ice and the break-up of sea ice along these existing features over the subsequent melt season motivated the inclusion of a quasi-restoring brittle fracture scheme within the prognostic FSD model introduced in chapter 6. This scheme was based on explicit models of brittle fracture. The inclusion of the brittle fracture scheme significantly improved the performance of the prognostic model in simulating the shape of the perimeter density distribution of mid-sized floes compared to observations.

The updated prognostic model, including the novel brittle fracture scheme, has then been used to explore the role of individual processes in driving the emergence of the overall FSD and the subsequent impact of the FSD model on the sea ice mass balance. It was found that the shape of the perimeter density distributions of smaller floes in both the August MIZ and pack ice were primarily derived from the April pack ice with some perturbation from lateral melting. The method to determine whether floes form primarily as nilas or pancake ice has been found to strongly influence both the shape of the FSD and its impact on the sea ice mass balance. It was also noted that observations of an annually oscillating FSD exponent can be understood through processes currently included within the prognostic model. The decrease of the exponent through the melt season is consistent with the brittle fracture mechanism and wave break-up processes perturbing the distribution towards smaller floes, whereas the increase in exponent seen over the freeze-up season is consistent with the action of welding processes and new floes forming as nilas sea ice.

Chapter 8, which follows, is a comparison of the impacts on the Arctic sea ice of both the prognostic FSD and WIPoFSD models and the extent to which the relatively simple WIPoFSD model can replicate the impacts of the prognostic FSD model. The results presented in this present chapter will contribute to this comparison as they establish the important processes that determine the impact of the prognostic FSD model.

Chapter 8: Comparing the impacts of the prognostic FSD and WIPoFSD models on the Arctic sea ice cover

Previously in this thesis, two alternative approaches to modelling the sea ice floe size distribution have been investigated: the WIPoFSD model, which constrains the shape of the FSD; and the prognostic FSD model, which allows the shape of the FSD to freely evolve. In this chapter the impact of these two models on simulations of the Arctic sea ice will be directly compared with each other and against observations where available. These comparisons will address two questions: firstly, whether the inclusion of FSD processes in sea ice models can improve simulations compared to observations; and secondly, whether the key impacts of a full prognostic FSD model can be replicated using a simplified approach to modelling the FSD. This chapter will then conclude by exploring the impact of both FSD models on sea ice under future atmospheric forcing.

8.1 Overview and methodology for the FSD model comparison

8.1.1 Chapter overview

This chapter will primarily consist of a comparison between the two different FSD modelling approaches used so far within this thesis: the WIPoFSD model of Bateson et al. (2020) and the prognostic FSD model of Roach et al. (2019). This will consist of four components. The first is a comparison of both FSD models to observations to identify if the inclusion of either FSD model within CICE improves the performance of the model in simulating the observed sea ice volume and extent. The next section will consider the impact of both FSD models on the simulated mean and trends for the sea ice extent and volume to identify any differences in the impacts of the two approaches. This section concludes with a focus on four individual regions within the Arctic identified as locations that respond differently to the imposed FSD, either within or between the different FSD models. The annual evolution of several metrics will be compared between these two locations including effective floe size, sea ice concentration and thickness, and lateral and basal melt rate. The aim of this comparison is to identify how

the inclusion of the FSD drives the observed changes in each of these locations and how this differs between the FSD models. The third section will present an additional sensitivity study for the WIPoFSD model to identify if it is possible to capture the key behaviours and impacts of the prognostic model within a model where the shape of the floe size distribution is fixed. The final section will present results from partial sea ice projections using future atmospheric forcing with both FSD models to explore whether the importance of FSD processes could change in a future Arctic.

8.1.2 Aims of this chapter

In chapter 1 two sets of aims for this thesis were outlined. The first set involved using FSD models within CICE to understand how both the shape of the FSD emerges and how it impacts the MIZ and broader sea ice mass balance. Up to this point, the thesis has primarily focused on addressing these questions, particularly in chapters 3 and 7. The comparison here between the two FSD models will provide further opportunities to explore how FSD processes impact both the MIZ and pack ice evolution. The second set of questions focus specifically on whether FSD models should be incorporated into climate models and if so, whether a constrained approached such as the WIPoFSD model can be used or a full prognostic model is necessary. In this chapter these questions will be addressed through the comparison of the two FSD models both with each other and with observations, and by using an additional sensitivity study to identify if the WIPoFSD model can replicate the key impacts on the sea ice produced by the prognostic FSD model.

8.1.3 Methodology for FSD model comparison

CPOM-CICE simulations are initiated with a sea ice free Arctic on 1st January 1980 and evaluated over a 37-year period until 31st December 2016. The form drag parameterisation of Tsamados et al. (2014) will be used, including the modifications to parameters described in Sect. 5.3. Apart from these modifications, the base CICE-ML model components and parameters are identical to that described in Sects 3.2 and 3.3. For the reference simulation, *ref*, the floe size used for both lateral melt calculations and the form drag scheme will be set to 300 m. For simulations including an FSD, the form drag floe size will be set to l_{eff}. The standard prognostic setup, *prog-best*, uses the setup described in Sect. 7.2 including the brittle fracture scheme. The standard WIPoFSD model, *WIPo-best*, uses the FSD model as described in Sect. 3.2, but using

the updated lateral melt scheme described by Eq. (4.8) in Sect. 4.3. For the floe parameters, d_{max} will be set to the standard value used within chapter 3 of 30,000 m. The minimum floe size that can be resolved in *prog-best* is 5.375 m and hence d_{min} will be set to the same value. As discussed in chapter 3, it is difficult to identify whether the tailing off of the power-law shape seen for smaller floes in observations is a physical feature or a result of the finite resolution of the observations. The value selected here is within the range considered in chapter 3 of 1 m – 20 m, and it is sensible to choose the same minimum floe resolution for the models to enable a fair comparison. α is set to -2.56, the average value across the three locations represented in the novel FSD observations that are discussed in Sect. 6.5. This is close to the standard value of -2.5 used in chapter 3. This means that parameter or model choices for both *WIPo-best* and *prog-best* have been selected to produce a reasonable fit to the same set of observations.

8.2 Does the inclusion of FSD models within CICE improve model performance compared to observations?

One of the key challenges in developing sea ice models is the difficulty in obtaining pan-Arctic observations to establish the concentration and thickness of the sea ice cover at any given time. Much effort has been put into developing algorithms to retrieve sea ice concentration from passive microwave data, however accuracy can be as low as ± 20% in summer or the MIZ (Meier and Notz, 2010). The reasons for such high uncertainty include the identification of both thin ice and surface melt ponds as open ocean by algorithms (Ivanova et al., 2015). As a result, models are usually compared against the sea ice extent rather than the full sea ice concentration data, as the former only requires the identification of a single isopleth over regions where the sea ice concentration gradient is generally high. Errors in satellite measurements of the sea ice thickness using radar altimetry can be even larger. The dominant factor contributing to these errors is the surface snow depth measurements that are required to calculate the total sea ice thickness. Recent studies to estimate the sea ice thickness and volume from radar altimetry data still rely on a climatology of compiled in-situ snow depths collected from 1954 – 1991, representing a significant potential source of error (Tilling et al., 2018). Errors in the snow depth can be magnified by a factor of about 5 when calculating the sea ice thickness (Tilling et al., 2015). Due to the significant challenges in estimating sea ice thickness from radar altimetry and the very limited availability of

in-situ thickness measurements, generally model performance in simulating the total Arctic sea ice volume is assessed using PIOMAS, the Pan-Arctic Ice Ocean Modelling and Assimilation System (Zhang and Rothrock, 2003). PIOMAS is a reanalysis product and does not incorporate direct observations of the sea ice thickness. Overall, this presents a constrained opportunity to compare simulations to observations of the sea ice cover and assess whether the inclusion of FSD models improves the accuracy of sea ice simulations.

In this section the following metrics will be tested to assess the performance of the three simulations, *ref*, *prog-best*, and *WIPo-best*: their performance in capturing the annual cycle and interannual variability of the sea ice extent and volume; their performance in capturing interannual trends in the sea ice extent and volume; their performance in simulating MIZ and pack ice extent; and whether the inclusion of either FSD model reduces known model bias in sea ice concentration. Sea ice concentration data is obtained from the Nimbus-7 SMMR and DMSP SSM/I–SSMIS satellites using Bootstrap algorithm version 3 (Comiso, 1999) and NASA Team algorithm version 1 (Cavalieri et al., 1996). PIOMAS is used for the sea ice volume data. It is worth discussing why only single simulations are evaluated for each of *prog-stan*, *WIPo-stan*, and *ref* and not ensemble simulations run with perturbed initial conditions. Firstly, the models are initialised with a sea ice free Arctic to avoid assuming an initial shape for the FSD in the prognostic model. Secondly, standalone CICE is a deterministic model and is not chaotic with respect to initial conditions. The main source of interannual variability in CICE is from sensitivity to the model forcing (Hunke and Holland, 2007; Hunke, 2010). Whilst the model setup here uses a fixed ocean climatology, each year of the simulation effectively has a unique atmospheric forcing scenario. It is therefore possible to assess qualitatively how much FSD impacts vary with respect to the atmospheric forcing by comparing impacts in different years.

Figure 8.1 shows timeseries for the total Arctic sea ice extent and volume in March and September over 1990 – 2016 for *ref*, *WIPo-best, prog-best* alongside observations (for the sea ice extent) or reanalysis (for the sea ice volume) over the same period. Note that the model domain does not include sections of the Hudson Bay or Canadian Arctic Archipelago. These plots show that the inclusion of either FSD model does not improve the ability of the CICE model to simulate either the annual or interannual variability in sea ice extent and volume. *prog-best* does appear to show a small improvement in simulating the March sea ice extent, but the reverse is true for the March sea ice

volume. The differences between the simulations are significantly smaller than the difference between *ref* and the observations / reanalysis in both March and September.

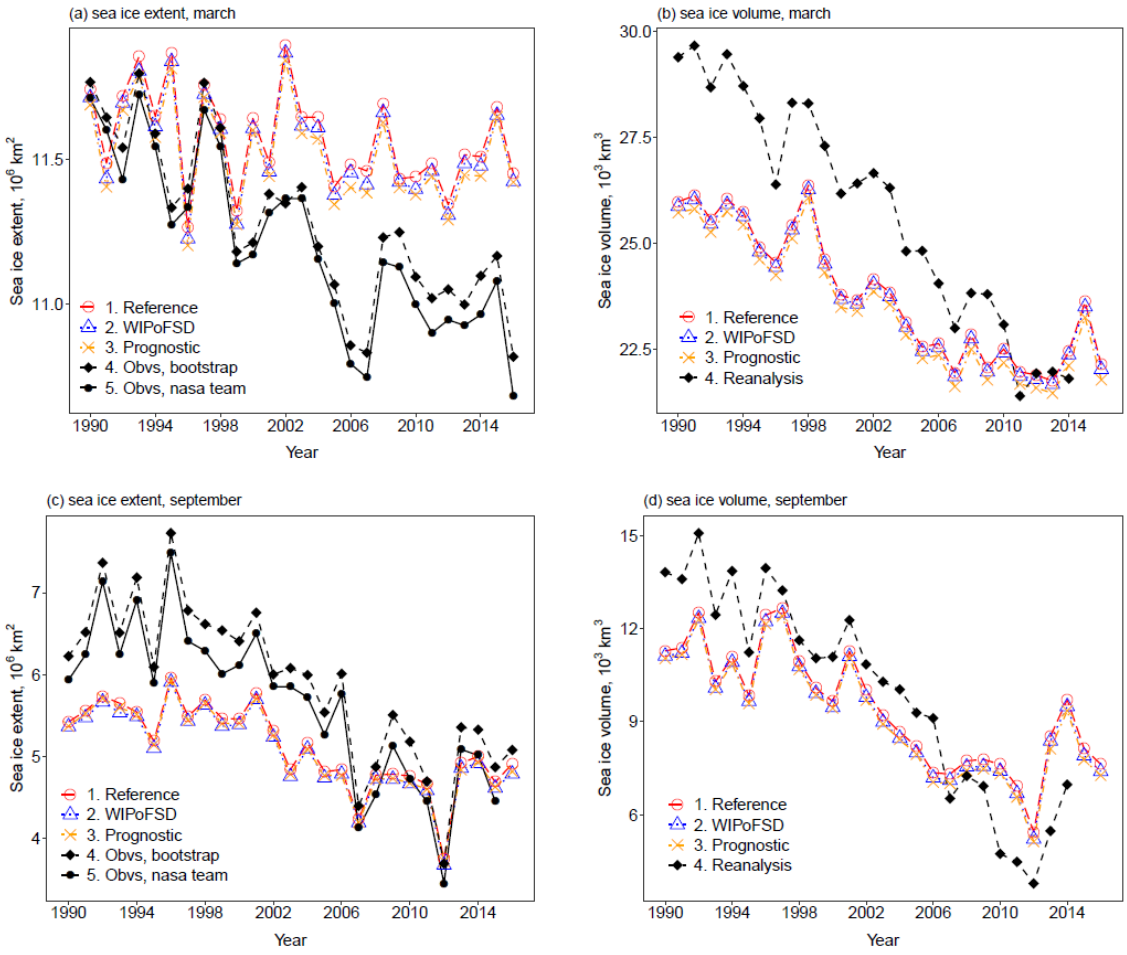

Figure 8.1: The total Arctic sea ice March extent (a, top left), March volume (b, top right), September extent (c, bottom left), and September volume (d, bottom right) within the model domain over the period 1990 – 2016 for *ref* (red, circles), *WIPo-best* (blue, triangles), *prog-best* (yellow, cross) and observations / reanalysis (black). Sea ice concentration data is obtained from satellites using the Bootstrap (filled diamond, dashed) algorithm version 3 (Comiso, 1999) and the NASA Team (filled circle, solid) algorithm version 1 (Cavalieri et al., 1996). Sea ice volume data (filled diamond, dashed) is taken from PIOMAS (Zhang and Rothrock, 2003).

An additional behaviour to consider is whether the inclusion of the FSD models can improve the ability of CICE to capture long-term trends in the sea ice cover. Figure 8.2 shows the percentage difference in the March and September sea ice extent and volume for each simulation, *ref*, *prog-best*, and *WIPo-best*, over 1990 – 2014 relative to the climatological mean for each simulation over the same period. This metric is also plotted for the observations and reanalysis. A clear negative trend in the March and September sea ice volume and September sea ice extent can be seen. In Fig. 8.2, it is again the case that the inclusion of the FSD does not improve the ability of CICE to

simulate the mass balance behaviour of the sea ice seen in observations. In this case the three CICE simulations can barely be discriminated in the plots. It should be noted that the reference CICE setup already performs well in capturing the observed trends, particularly in September, without the addition of an FSD model.

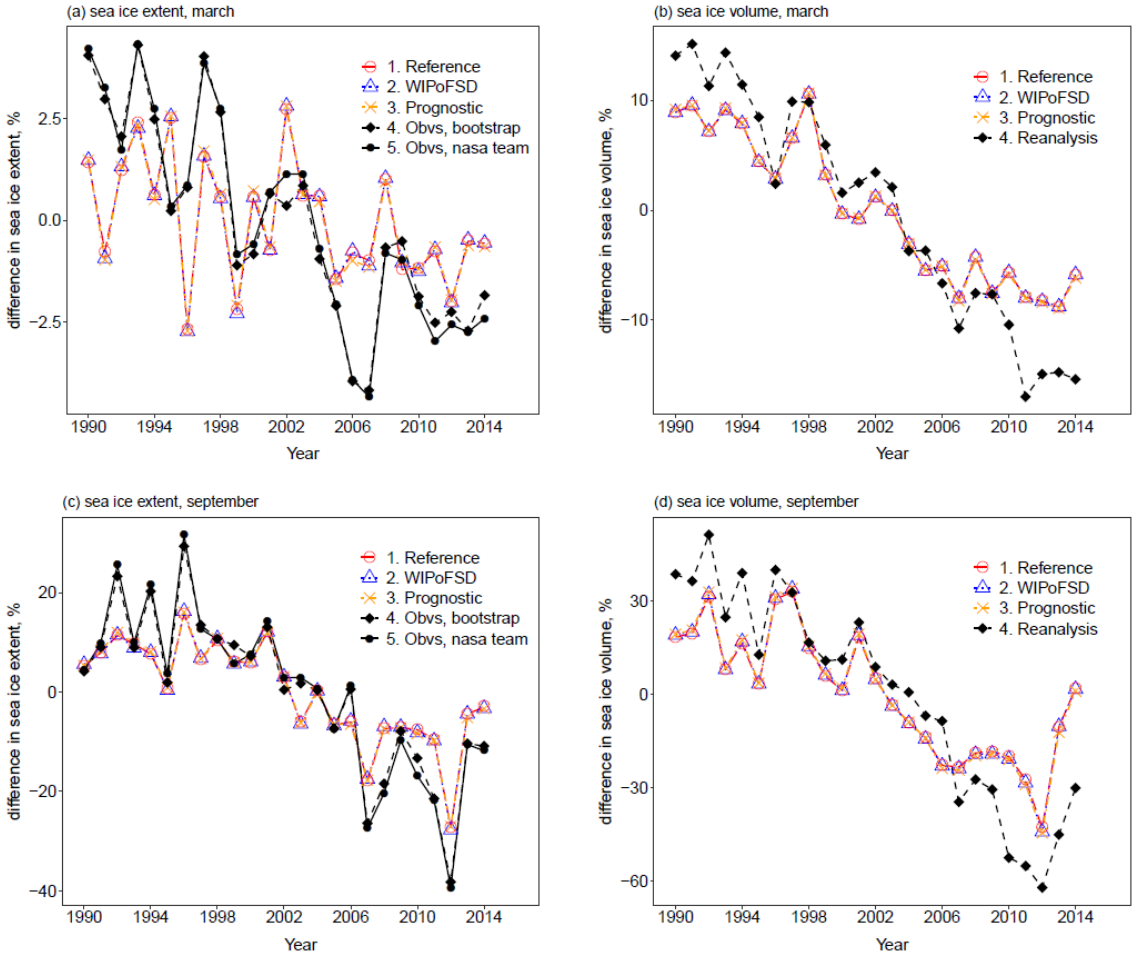

Figure 8.2: The % difference in the Arctic total sea ice March extent (a, top left), March volume (b, top right), September extent (c, bottom left), and September volume (d, bottom right) within the model domain over the period 1990 – 2014 relative to the simulated or observed climatological mean over the same period for *ref* (red, circles), *WIPo-best* (blue, triangles), *prog-best* (yellow, cross) and observations / reanalysis (black). Sea ice concentration data is obtained from satellites using the Bootstrap (filled diamond, dashed) algorithm version 3 (Comiso, 1999) and the NASA Team (filled circle, solid) algorithm version 1 (Cavalieri et al., 1996). Sea ice volume data (filled diamond, dashed) is taken from PIOMAS (Zhang and Rothrock, 2003).

Figure 8.1 presented timeseries in total sea ice extent and volume for each of *ref*, *prog-best*, and *WIPo-best*, but found only small differences between the three simulations. However, difference maps presented in chapter 3 suggest that generally the largest impacts of including an FSD model occur within the MIZ, hence more interesting results may be found considering just the pan-MIZ scale rather than the full pan-Arctic scale.

Figure 8.3 compares timeseries from 1990 – 2016 for the MIZ and pack ice extent in both March and September for each of *ref*, *prog-best*, and *WIPo-best* in addition to the Bootstrap and NASA team derived observations. Figure 8.3 shows significant disagreements between the observations in both the MIZ and pack ice extent for both March and September; the Bootstrap derived observations sometimes show a September MIZ extent exceeding twice that of the NASA team derived observations. This demonstrates the challenge in using these observational products to assess model performance beyond pan-Arctic metrics such as extent; errors in the observed concentration are sufficiently high to produce large amounts of uncertainty in the MIZ and pack extents, as demonstrated by the large differences between the two observational products shown in Fig. 8.3. For this reason, a comparison is not made here between model output and reanalysis for MIZ or pack ice volume metrics, given the uncertainty associated with the reanalysis volume will be larger than the differences between the three simulations. Similarly, the high uncertainty in sea ice concentration found in observational products prevents useful insight being gained from a direct comparison of the spatial distribution in sea ice concentration between model output and observations.

Fig. 8.3 does show that all three simulations generally simulate both the MIZ and pack ice extent within the uncertainty of the observations. The only exception to this is the March pack ice extent, where both observational products suggest a negative trend not replicated within the simulations. Focusing specifically on the differences in the MIZ extent simulated by the three simulations, *prog-best* produces a higher MIZ extent on average in March compared to *ref* but lower values for both in September. In comparison, *WIPo-best* shows a reduced MIZ extent throughout the year compared to *ref*. To understand this, it is helpful to consider l_{eff} at both the outer MIZ and inner MIZ edge. If it is close to 300 m at the inner edge but small at the outer MIZ edge, as seen for the WIPoFSD model (see Fig. 8.7 later), then the 15 % sea ice concentration contour line will retreat but not the 80 %. The net impact is to then reduce the total sea ice extent in the MIZ. Where l_{eff} is low at both contours, as seen with the prognostic model, then whilst the 15 % concentration line still retreats, so can the 80 % contour line and the MIZ extent increases or decreases depending on the exact balance between these changes. The variability of the March MIZ extent is also higher for *prog-best* than *WIPo-best* or *ref*. Considering the pack ice extent, in September all three simulations produce very similar extents, but in March there is a moderate reduction for

prog-best compared to *ref* and a small reduction for *WIPo-best* compared to *ref.* Overall, inclusion of FSD processes within CICE results in changes to extent metrics of order 1 x $10^5\,km^2$.

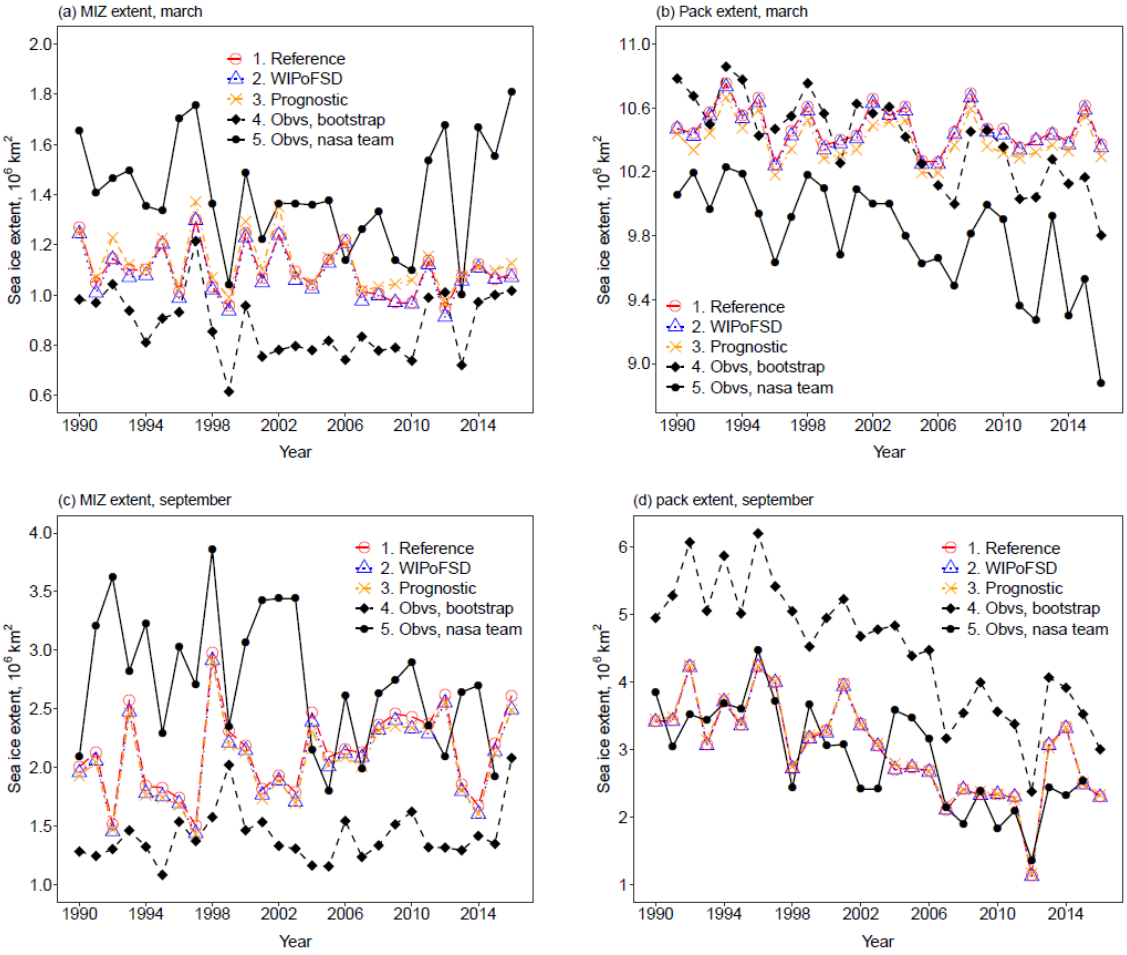

Figure 8.3: The total Arctic sea ice March MIZ extent (a, top left), March pack extent (b, top right), September MIZ extent (c, bottom left), and September pack extent (d, bottom right) over the period 1990 – 2016 for *ref* (red, circles, long dash), *WIPo-best* (blue, triangles, dotted), *prog-best* (yellow, cross, dot-dash) and observations / reanalysis (black). Sea ice concentration data is obtained from satellites using the Bootstrap (filled diamond, dashed) algorithm version 3 (Comiso, 1999) and the NASA Team (filled circle, solid) algorithm version 1 (Cavalieri et al., 1996). Sea ice volume data (filled diamond, dashed) is taken from PIOMAS (Zhang and Rothrock, 2003). The MIZ is here defined as the region with between 15% and 80% sea ice concentration. All three simulations generally lie within the range spanned by the observational products except for pack ice extent in March after 2010.

Figures 8.1-8.4 do not provide any evidence that the inclusion of an FSD model improves the performance of CICE in simulating the aggregated Arctic sea ice extent and volume behaviours and trends against observations / reanalysis. This does not preclude either FSD model from being an important improvement to sea ice models; these improvements may be at a smaller, regional scales rather than at a pan-Arctic

scale. As previously discussed, it is significant challenge to obtain high accuracy observations of the sea ice concentration and thickness, and the use of the latter to validate models requires a careful use of case studies such as demonstrated by Schröder et al. (2019). Nevertheless, significant biases have been identified in coupled climate models in simulating the sea ice concentration (Ivanova et al., 2016) and CICE, in particular, has been shown to overpredict the sea ice concentration at the sea ice edge and underpredict the concentration within the pack ice (Schröder et al., 2019). In chapter 3, the WIPoFSD model was found to provide a limited correction to this known model bias. Figure 8.7, presented in the next section, shows that the prognostic model produces a similar but stronger correction to this bias. This impact alone is not enough to demonstrate the need to include a full prognostic model or indeed an FSD model at all in sea ice simulations. Nevertheless, it does show that the inclusion of FSD models may be important to understand the Arctic sea ice evolution at the regional scale, particularly within the MIZ, even if FSD processes do not appear to be as important at a pan-Arctic scales.

A remaining question is, given the significant uncertainties remaining regarding several parameters and processes within the FSD models, could model performance against observations be improved through different choices for parameters and parametrisations. In chapters 3 and 7, a series of sensitivity studies were presented for the WIPoFSD and prognostic models respectively. In each case, some model setups produced much larger impacts than those used for *WIPo-best* and *prog-best* e.g. a more negative exponent and smaller minimum floe size for the WIPoFSD model, and the formation of all new floes as pancake floes for the prognostic model. The parametrisations and parameter choices made in *prog-best* have been derived from physical principles or determined through field observations of the relevant processes (e.g. Horvat and Tziperman, 2015; Roach et al., 2018b). The choice of the exponent for the *WIPo-best* simulation was selected to produce a strong fit to observations of the FSD; the brittle fracture restoring scheme was also introduced to the prognostic model to improve model performance against the same observations of the FSD. The observations used to produce these ‘best’ FSD model setups had significant limitations, in particular floes smaller than 100 m were not well resolved, and only selected months in the year were included. Nevertheless, this approach to determining the ‘best’ FSD model setups is preferable to model tuning with pan-Arctic extent and volume metrics, since the latter may produce a setup that does not simulate a realistic FSD and is

instead compensating for other missing processes in CICE not related to FSD processes. With a different selection of parameters, a strong pan-Arctic reduction can be produced by either FSD model, however that would not necessarily produce a better fit to observations / reanalysis of the sea ice extent and volume e.g. using an exponent of -3.5 for *WIPo-best* has a strong pan-Arctic impact, as shown in Fig. 3.8, but will also increase the reduction in sea ice extent between March and September, something that *ref* is already overestimating in Fig. 8.1. Changing *prog-best* such that all floes form as pancakes would have similar results.

8.3 Comparing the impacts on the total sea ice mass balance

8.3.1 Impacts across the Arctic sea ice cover

In this section, the *prog-best* and *WIPo-best* simulations will be compared directly, considering several metrics related to the sea ice mass balance including the total sea ice extent and volume, the extent and volume specifically for the MIZ, and spatial difference plots for concentration, thickness, and l_{eff}. The aim of this comparison is to understand the differences in the large-scale impacts of the two alternative FSD models before using regional case studies in the next section to understand how these differences might develop.

Figure 8.4 shows the percentage difference in the sea ice extent and volume for both *prog-best* and *WIPo-best* relative to *ref* averaged over 2000 to 2016. For the sea ice extent, both models show a maximum difference in August of just under 2%. For the WIPoFSD model, this is a well-defined peak, whereas for the prognostic model a similar reduction in extent can also been seen in July and August. The prognostic model also produces a reduction in extent of at least 0.5% throughout the year, whereas the WIPoFSD model shows smaller changes in the extent through the winter months and even a small increase in extent in November. A larger contrast can be seen in the volume differences. A maximum change of -2.5% in September can be seen for *WIPo-best* relative to *ref,* whereas for *prog-best* the maximum reduction is just under 4%. The minimum reduction for the prognostic model is 1.5% in the spring months, compared to just 0.5% with the WIPoFSD model. The prognostic model also shows a larger interannual variability (indicated by the width of the ribbon) compared to the WIPoFSD model, approximately 2 times larger for the volume.

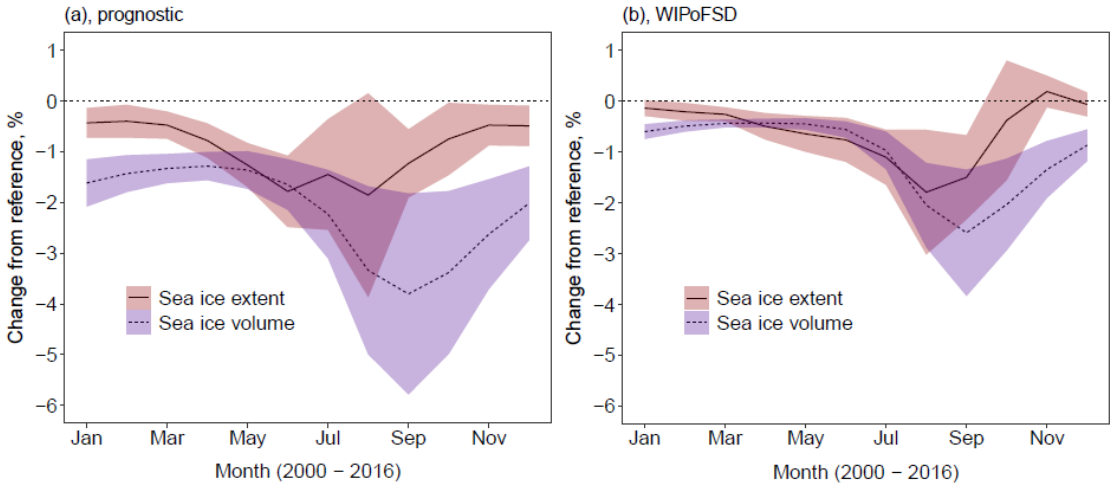

Figure 8.4: Difference in sea ice extent (solid, red ribbon) and volume (dashed, blue ribbon) of *prog-best* (a, left) and *WIPo-best* (b, right) relative to *ref* averaged over 2000 - 2016. The ribbon shows, in each case, the region spanned by the mean value plus or minus two times the standard deviation. Both *prog-best* and *WIPo-best* produce similar reductions in the August sea ice extent of just under 2 %, but the prognostic model produces a much larger reduction in the sea ice volume throughout the melting season.

Figure 8.5 shows the percentage difference in total Arctic sea ice extent and volume for both *prog-best* and *WIPo-best* compared to *ref* from 1990 – 2016 in March and September. Note that this plot is different from Fig. 8.2 in that it shows how the two simulations incorporating FSD models are diverging from *ref* over time, rather than the explicit trends in the sea ice extent and volume relative to simulation climatology. The differences are consistent with Fig. 8.4, with *prog-best* showing larger reductions than *WIPo-best* relative to *ref* except for the March sea ice extent. There appears to be a moderate positive trend for the difference in the March sea ice extent and a negative trend for the September sea ice extent for both *prog-best* and *WIPo-best* relative to *ref*, but this is inconclusive due to the high interannual variability relative to the strength of the trend. Robust trends can be seen for the difference in sea ice volume. For the September sea ice volume *prog-best* produces an average reduction of 2% compared to *ref* in the 1990s increasing to about a 5% reduction in the 2010s. A similar but weaker trend can be seen for *WIPo-best* relative to *ref*. More interesting are the results for the March sea ice volume. For *prog-best* relative to *ref*, the reduction increases from about -1.1% in the 1990s to about -1.5% in the 2010s. This is a small change in magnitude, but nevertheless larger than the interannual variability over this same period. For *WIPo-best* relative to *ref*, there is no evidence of any trend with the difference holding consistently at about -0.4%.

For the CICE setup used in the simulations considered in this chapter, floe size impacts the sea ice via two model components: the form drag scheme, and calculation of the lateral melt volume. In chapter 3 it was demonstrated that increases in the lateral melt rate when using the WIPoFSD model were compensated by a reduction in the basal melt rate, leading to only small to moderate changes in the total melt rate. It is useful to perform a similar analysis here to establish if there are differences between the two FSD models in the lateral and total melt response. Figure 8.6 shows the annual timeseries of the difference in the cumulative top, basal, lateral, and total melt for both *prog-best* and *WIPo-best* relative to *ref* averaged over 2000 – 2016 with ribbons indicating the interannual variability over this period. Also shown is the annual timeseries of the difference between *prog-best* and *WIPo-best* for the same metrics averaged over the same period.

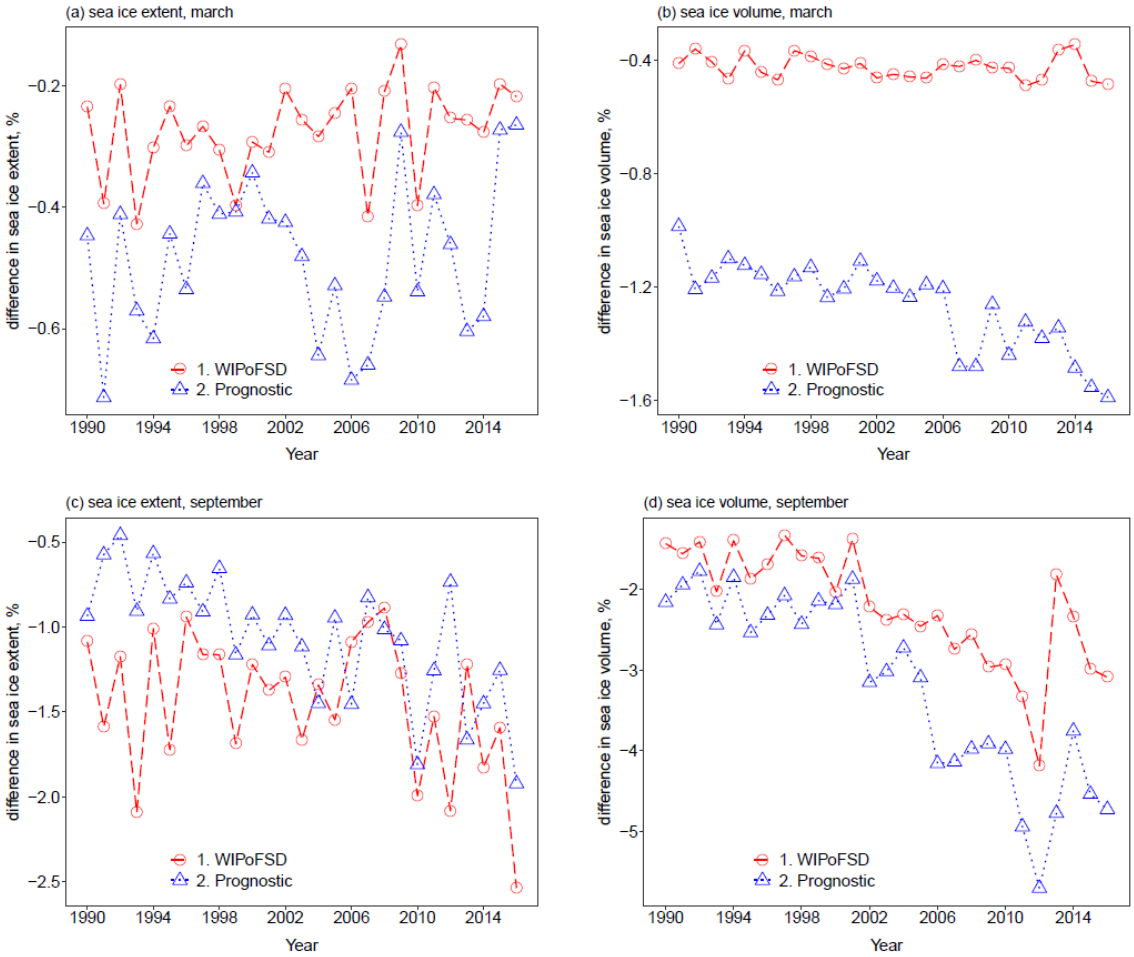

Figure 8.5: The % difference in the Arctic total sea ice March extent (a, top left), March volume (b, top right), September extent (c, bottom left), and September volume (d, bottom right) over the period 1990 – 2016 for *WIPo-best* (red, circles, dashed), and *prog-best* (blue, triangles, dotted) relative to *ref*. Trends in the extent appear to be similar for both models, but the prognostic model shows stronger trends for both the March and September sea ice volume.

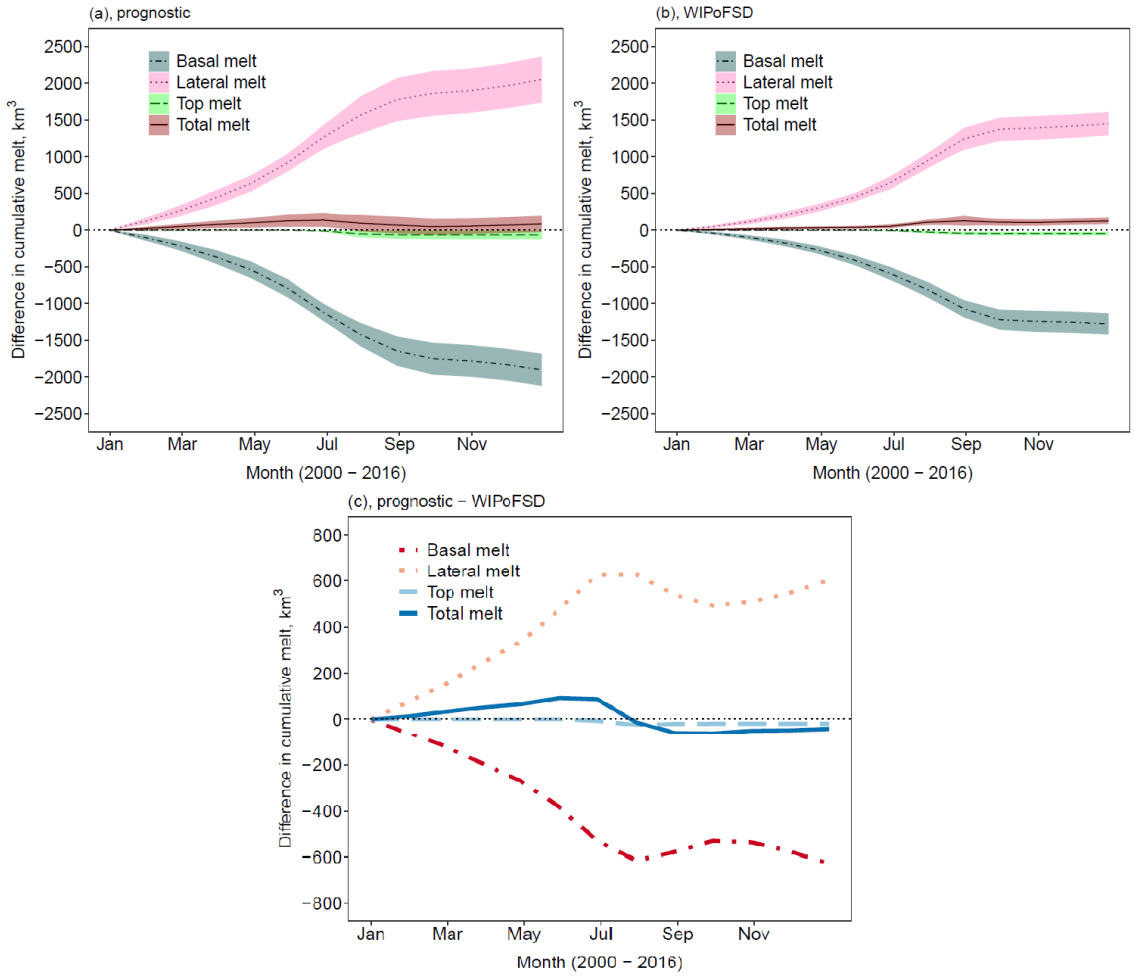

Figure 8.6: The top two plots show the difference in the cumulative lateral (pink ribbon, dotted), basal (grey ribbon, dot-dashed), top (green ribbon, dashed), and total (red ribbon, solid) melt averaged over 2000–2016 for *prog-best* (a, left) and *WIPo-best* (b, right) relative to *ref*. The ribbon shows, in each case, the region spanned by the mean value plus or minus twice the standard deviation. The bottom plot shows show the difference in the cumulative lateral (orange, dotted), basal (red, dot-dashed), top (light blue, dashed), and total (dark blue, solid) melt averaged over 2000–2016 for *prog-best* relative to *WIPo-best* (c). *prog-best* shows a larger increase in the lateral melt compared to *WIPo-best*, but the change in the total melt is small and changes sign over the year.

For both models there is a significant increase in the lateral melt compensated by a reduction in the basal melt of a similar magnitude. Due to the basal melt compensation effect, the increase in total melt is small. In Sect. 3.4.1 this compensation effect was found primarily to be a result of the physical reduction of sea ice area in locations of high basal melt. An interesting feature here is that whilst the increase in the lateral melt for *prog-best* is higher than for *WIPo-best*, both show an increase in the total melt of a small and similar magnitude. This suggests that any mixed-layer based feedbacks on the total melt, such as albedo feedback, are weak even for the *prog-best* simulation.

The similar magnitude of change in the total melt must also mean that the results seen in Figs 8.4 and 8.5, where the sea ice volume is lower in both September and March for *prog-best* compared to *WIPo-best,* is driven by the negative trends in the March sea ice volume rather than a net increase in the total melt each year. Also shown in Fig. 8.6 is the difference in melt components for *prog-best* compared to *WIPo-best*. The difference in the cumulative total melt peaks in July and then decreases and switches sign. This indicates that the differences between *prog-best* and *WIPo-best* emerge in the early melt season rather than the late melt season. This is consistent with Fig. 8.4, where *prog-best* shows a stronger reduction in sea ice extent in the early melt season compared to *WIPo-best*, but the reduction in the later melt season is comparable.

Figures 8.1 – 8.6 consider the impacts of the two FSD models on the pan-Arctic behaviour of CICE. The pan-Arctic scale is useful for assessing the broader importance of a specific process to the sea ice cover, but as shown in chapter 3, it can also disguise significant regional and local variations in impact. The spatial distribution of l_{eff} has also previously been shown to be instructive in understanding how a given FSD model changes sea ice processes. Figure 8.7 shows maps of differences in sea ice concentration, thickness, and l_{eff} for both *prog-best* and *WIPo-best* relative to *ref*. These maps are presented for three selected months: March, June, and September. For both *prog-best* and *WIPo-best*, changes in the MIZ can be seen in all three months. For differences in sea ice concentration, the spatial pattern of the reduction is similar for both FSD models, but the magnitude is generally larger for the prognostic model. Particularly strong reductions can be seen in the Greenland Sea and Barents Sea in June for *prog-best* relative to *ref*. The magnitude of reductions for *prog-best* and *WIPo-best* in the MIZ are similar in September, despite the stronger response seen for the former in earlier months. However, *prog-best* shows an increase in the sea ice concentration across much of the pack ice in September, with a particularly strong response in the central Beaufort Sea. This response is not seen with *WIPo-best*, primarily because for the WIPoFSD parameters chosen here the maximum l_{eff} is 300 m i.e. the value adopted in *ref*, whereas for *prog-best* it can be as high as 1700 m. As mentioned in Sect. 8.2, the reduction in sea ice concentration within the MIZ whilst preserving or increasing the concentration in the pack ice acts to correct known model biases in the spatial distribution of sea ice concentration. This effect is stronger for *prog-best* compared to *WIPo-best*, but in both cases the effect is too small to fully account for the known bias.

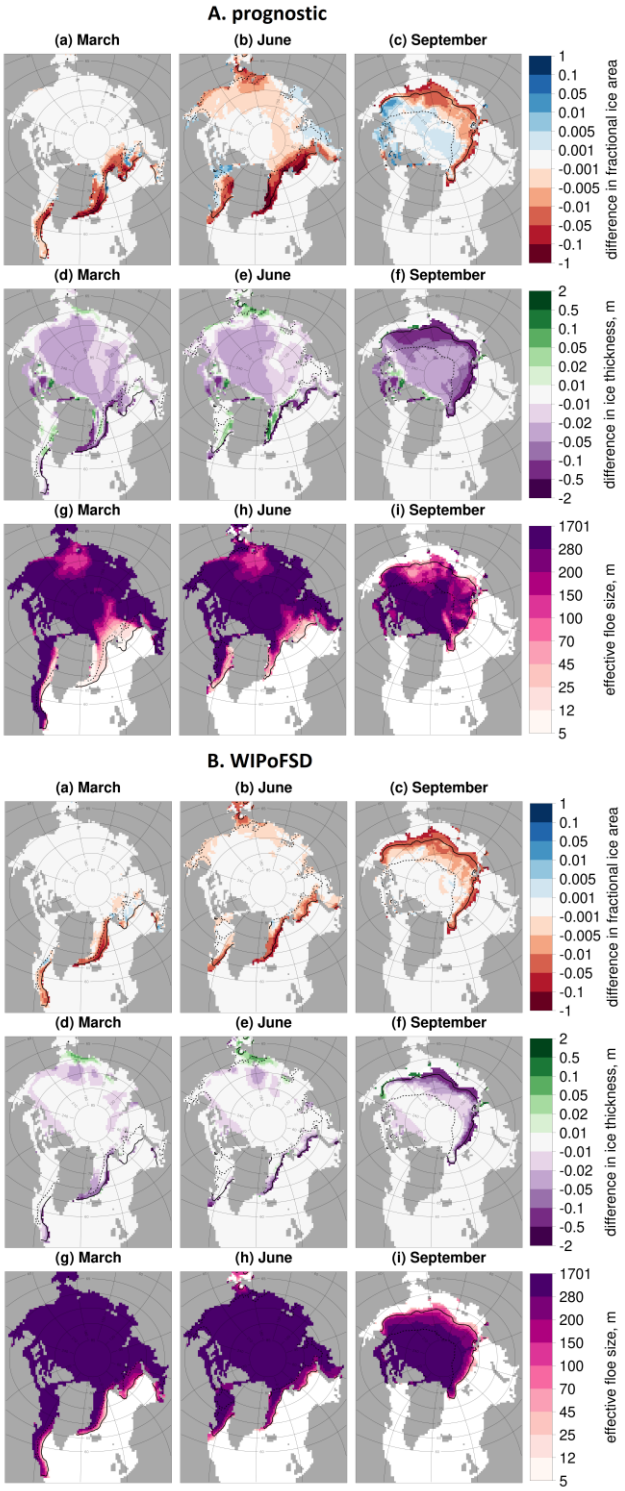

Figure 8.7: Difference in the sea ice concentration (a–c) and ice thickness (d–f) between *prog-best* (A, top) or *WIPo-best* (B, bottom) and *ref* and the absolute value of l_{eff} (g–i) for *prog-best* (A, top) or *WIPo-best* (B, bottom) averaged over 2000–2016. Results are presented for March (a, d, g), June (b, e, h), and September (c, f, i). Values are shown only in locations where the sea ice concentration exceeds 5 %. The inner (dashed black) and outer (solid black) extent of the MIZ averaged over the same period is also shown. Both *prog-best* and *WIPo-best* show a strong reduction in the MIZ concentration and thickness relative to *ref*, but the magnitude of the changes is larger for *prog-best*.

Significant differences can also be seen between the two models in the impacts on sea ice thickness. For *prog-best* relative to *ref*, reductions in thickness across the central Arctic persist through March and June, but for *WIPo-best* differences only persist in locations that become marginal for at least some of the year and along the Canadian archipelago. In September, for *prog-best* the reduction in thickness spans the full Arctic, whereas differences are mostly confined to the outer MIZ for *WIPo-best*. There are some locations within the MIZ, for example the Greenland Sea in March and June for *prog-best* relative to *ref*, where increases in the sea ice thickness can be seen. The spatial distribution in l_{eff} provides additional insight into the different impacts of the two FSD models on the sea ice cover. Firstly, the WIPoFSD model shows a narrow zone of transition from an l_{eff} of size 280 m or larger (i.e. comparable to the *ref* floe size) to a smaller l_{eff} in the MIZ. The transition is broader in September, but still confined to the MIZ. For the prognostic model, l_{eff} behaves very differently. In March and June in particular, the region of transition is much broader and the l_{eff} within the MIZ is generally well under 100 m. This will be responsible for the strong impact of the prognostic model in the early melt season. l_{eff} is particularly low in the Greenland Sea in March with the average value below 50 m. This corresponds to the region of strongest model response in the early melt season. l_{eff} is shown to increase within the MIZ over the course of the melt season from March to September. This is consistent with the results presented in Sect. 7.2.5, where lateral melting is found to increase l_{eff} because of the preferential melt out of smaller floes. This also explains the results presented in Figs. 8.4 and 8.6, which show that *prog-best* has a stronger increase in lateral melt and reduction in extent in the early melt season compared to *WIPo-best*, but the simulations are more comparable during the late melt season. The WIPoFSD model shows a certain amount of radial symmetry with respect to l_{eff}, whereas the prognostic model shows significantly higher spatial variability in l_{eff}. Chapter 7 included a series of plots to explore the sensitivity in the spatial distribution of l_{eff} to individual processes within the prognostic model. The high spatial variability indicated in Fig. 8.7 for the prognostic model could not easily be attributed to a single process but was found to be particularly sensitive to the floe formation mechanism, brittle fracture scheme, and welding, all processes not explicitly represented in the WIPoFSD model. Processes such as wave break-up of floes and lateral melt, which are included in the WIPoFSD model, were not shown to have a large impact on the spatial distribution of l_{eff} in chapter 7 within the prognostic model.

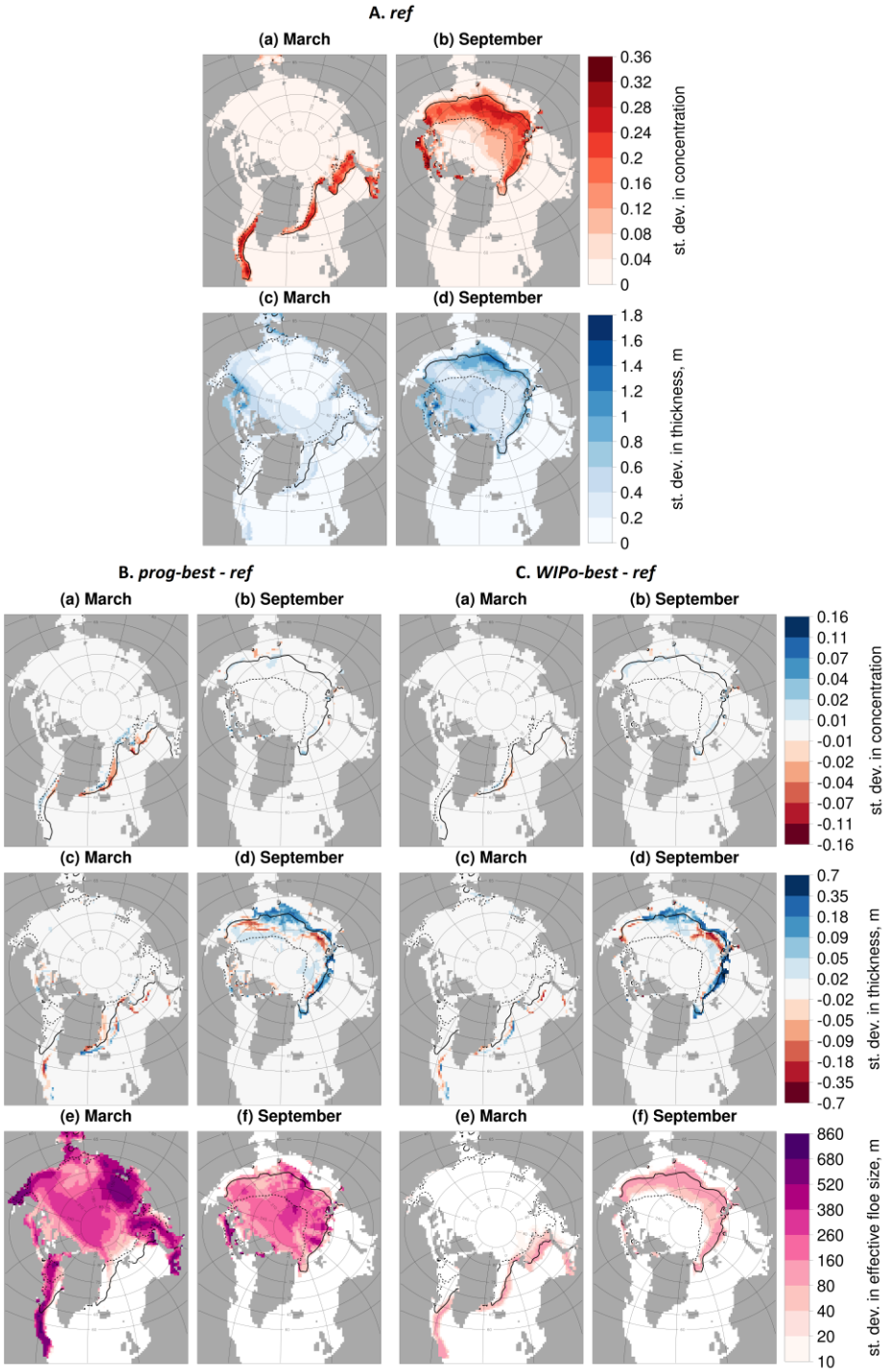

Figure 8.8: Section A (top) shows the standard deviation of the sea ice concentration (a, b) and thickness (c, d) in March (a, c) and September (b, d) for *ref*. Section B (bottom left) and C (bottom right) show difference plots in the standard deviation of the sea ice concentration (a, b) and thickness (c, d) in March (a, c) and September (b, d) for *prog-best* and *WIPo-best* relative to *ref* respectively. In B and C, the standard deviation in l_{eff} is also plotted for both March (e) and September (f). Values are shown only in locations where the sea ice concentration exceeds 5 %. The inner (dashed black) and outer (solid black) extent of the MIZ averaged over the same period is also shown. Plots show that changes to the standard deviation in the sea ice concentration and thickness are generally localised to the outer edge of the MIZ.

Figure 8.7 is useful to understand the spatial distribution of the pan-Arctic changes in sea ice state shown in Fig. 8.4, but the inclusion of an FSD model may not only act to change the mean state of the sea ice but also the interannual variability. Model variability is important to consider as it can influence how the simulated sea ice is likely to respond to future perturbations in forcings. Figure 8.8 shows the spatial distribution of the standard deviation in sea ice concentration and thickness for selected months and then shows the differences for *prog-best* and *WIPo-best* from *ref*.

Figure 8.8 also shows the standard deviation in l_{eff} for *prog-best* and *WIPo-best*. Overall, Fig. 8.8 shows that changes to the standard deviation in the sea ice concentration are mostly small. These differences have a low magnitude and are isolated rather than part of a more systematic change in behaviour. For the standard deviation of sea ice thickness, differences are again mostly small and isolated in March, but larger changes can be seen within the September MIZ of up to 10 – 20%. Generally, these changes have a positive sign, but in some locations they are negative. The spatial distribution of the differences in the thickness variability is similar for both *prog-best* and *WIPo-best* compared to *ref*, but the magnitude is larger for the latter case up to a maximum of 0.7 m. These changes in thickness variability correspond to where the largest differences in sea ice thickness can be seen in Fig. 8.7 and are consistent with the high interannual variability of the reduction in sea ice volume suggested in Fig. 8.5 for both *prog-best* and *WIPo-best* relative to *ref*. The standard deviation in l_{eff} is as expected for both *prog-best* and *WIPo-best* based on Fig. 8.7. For the latter, variability is generally only seen within the MIZ as l_{eff} remains close to the maximum value within the pack ice. For *prog-best*, the standard deviation is broadly proportional in size to the value of l_{eff} seen in Fig. 8.7. It is notable that high interannual variability can be seen across the pack ice in both March and September, suggesting that all locations experience some variability in the contributing processes to the shape of the FSD year on year. *prog-best* and *WIPo-best* are well distinguished in this metric, with the latter predicting the highest standard deviation in l_{eff} in the MIZ whereas the reverse is true for *prog-best*. The spatial distribution for the interannual variability of l_{eff} may therefore be a useful metric to measure in the Arctic as it discriminates between the different approaches to modelling the FSD.

8.3.2 Local case studies

In Sect. 8.2, it was shown that the *WIPoFSD* model and prognostic FSD model applied within CICE simulations of the Arctic sea ice do not have a significant impact on the pan-Arctic extent or volume. In Sect. 8.3.1 it has been demonstrated that despite these small impacts at the pan-Arctic scale, both FSD models still produce important and distinct impacts on the sea ice cover, particularly over localised regions of order 100 km. *prog-best* shows a stronger model response in the early melt season, higher magnitude changes in the sea ice concentration and thickness in the MIZ, and more annual and interannual variability in the MIZ extent and volume when compared to *WIPo-best*. To understand further how the differences between the impacts of the two models emerge, several case studies have been selected and studied for two specific years, 2002 and 2012. Annual timeseries over both 2002 and 2012 for different properties will be presented and compared for each of *ref*, *prog-best*, and *WIPo-best*. The properties selected for comparison are the effective floe size, sea ice concentration, thickness, and lateral and basal melt rate per unit sea ice area. These properties have been selected as they will allow an assessment of the melt partitioning at individual locations and how this drives changes in the sea ice state.

Figure 8.9 shows the locations selected for these case studies. Each site spans a range of 4 x 4 model grid cells. A total of 16 grid cells for each case study has been selected to ensure enough grid cells are included that the mean behaviour is representative of the location, whilst not including so many grid cells that any local effects, especially at the sea ice edge, are supressed within the average. These sites have been selected based on the results in Fig. 8.7 to sample regions that are part of the MIZ for at least some of the year and that also represent locations that show some notable difference or similarity between the *prog-best* impacts and *WIPo-best* impacts. Site A, in the East Siberian Sea, represents a location where the average response over 2000 - 2016 for both *prog-best* and *WIPo-best* is a comparable and moderate reduction in the sea ice concentration and thickness. Site B, in the Greenland Sea, represents a location where, for *prog-best* relative to *ref*, both increases and reductions in the sea ice thickness can be seen adjacent to each other as discussed in Sect. 8.3.1. Site C, in the Barents Sea, is a location where the average reduction in sea ice concentration and thickness shows a higher magnitude for *prog-best* than *WIPo-best*. Site D, in the Beaufort Sea, is a site where the difference between *WIPo-best* and *ref* is negligible but for *prog-best* relative to *ref*, there is a reduction in sea ice concentration

and an increase in sea ice thickness. Whilst these behaviours are an average over 17 years, and the year on year impacts will be different, they highlight these locations as good case studies to identify how similarities and differences between the models emerge.

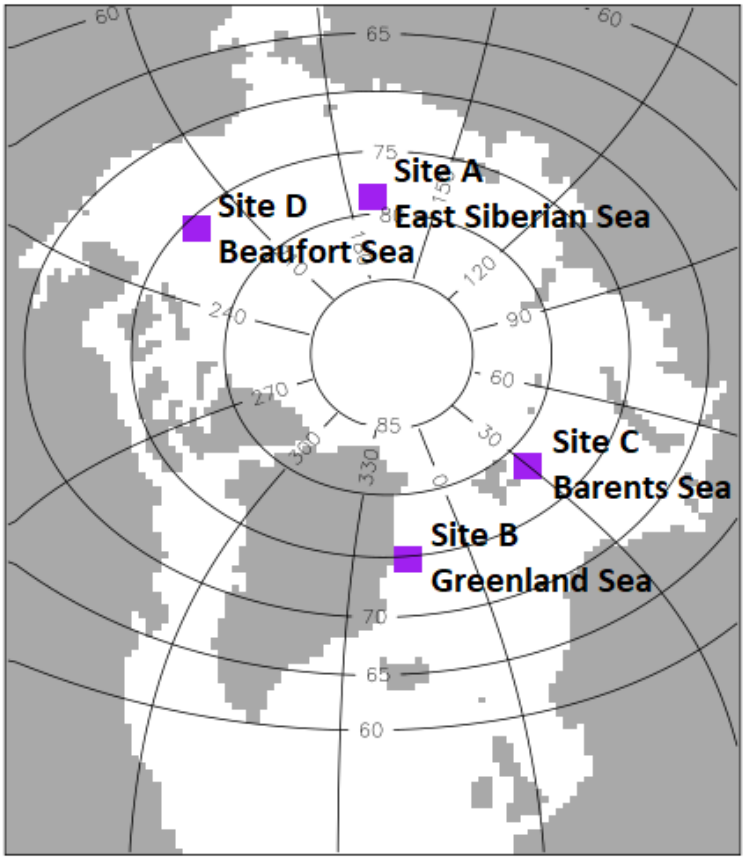

Figure 8.9: Case study regions for Sect. 8.3.2. The purple boxes indicate the grid cells selected for each case study region. Each region occupies a 4 x 4 set of grid cells. Site A is in the East Siberian Sea, Site B is in the Greenland Sea, Site C is in the Barents Sea and Site D is in the Beaufort Sea.

Figure 8.10 shows timeseries in l_{eff} for both the *WIPo-best* and *prog-best* simulations at each site in both 2002 and 2012. These plots show that l_{eff} produces distinct behaviour between the two simulations. For *WIPo-best*, a similar trajectory is followed at three of the four locations. Through the Winter months l_{eff} remains at 300 m, reducing to smaller values during the melting period before recovering rapidly to 300 m in the freeze-up season. The length of time for this interval varies at each location, from as long as 8 months in the Greenland Sea to no decrease at all in the Beaufort and East Siberian Seas in 2002. The Barents Sea is a distinct case, with l_{eff} remaining below 300 m for each month in both years. This site remains exposed to wave break-up throughout the year. The behaviour of l_{eff} in *prog-best* is significantly more

variable. In the Barents and Greenland Seas, l_{eff} adopts small values throughout winter and then increases during the melting season in response to the selective melt out of smaller floes. In the Beaufort Sea, the annual cycle follows an approximately sinusoidal shape in 2002, with l_{eff} at a maximum in April and a minimum in August. In 2012 the shape is similar until August, where l_{eff} continues to decrease through to December. This can be attributed to a different exposure to waves for this location between the two years. In 2002 floes form as nilas ice, resulting in an increase in l_{eff}, whereas in 2012 the presence of waves fragments existing floes and favours pancake ice formation, reducing l_{eff} through the freeze-up season. The East Siberian Sea appears to also follow a hybrid behaviour, with roughly sinusoidal behaviour but also displaying a spike in l_{eff} in September. Figure 8.10 therefore demonstrates several key distinctions between the FSD models. The evolution of l_{eff} is more predictable for the WIPoFSD model, showing a decrease in l_{eff} during the melting season and an increase in the freeze-up season. For the prognostic model, l_{eff} can increase or decrease throughout the year depending on the local conditions.

In order to compare the different thermodynamic evolution between the models three case studies are selected: the East Siberian Sea (region A) in 2012, the Greenland Sea (region B) in 2002, and the Barents Sea (Region C) in 2012. These case studies have been selected as they show values of l_{eff} smaller than 100 m in at least one of the simulations during the melting season. Where l_{eff} remains above 100 m throughout the melting season, the increase in the lateral melt rate will not be large enough to result in significant differences between the models. For each case study, timeseries will be presented in four key metrics: sea ice concentration, thickness, lateral melt rate per unit sea ice area, and basal melt rate per unit sea ice area. The sea ice concentration and thickness are included to show the differences in how the sea ice evolves between simulations. The lateral and basal melt rates are included to provide information on whether there is a net total local increase in the sea ice melt or just a redistribution from basal melt to lateral melt through the basal melt compensation effect, as shown in Fig. 8.6. By expressing these values per unit sea ice area, the impact of a changing sea ice concentration on the melt rates can be excluded from the comparison.

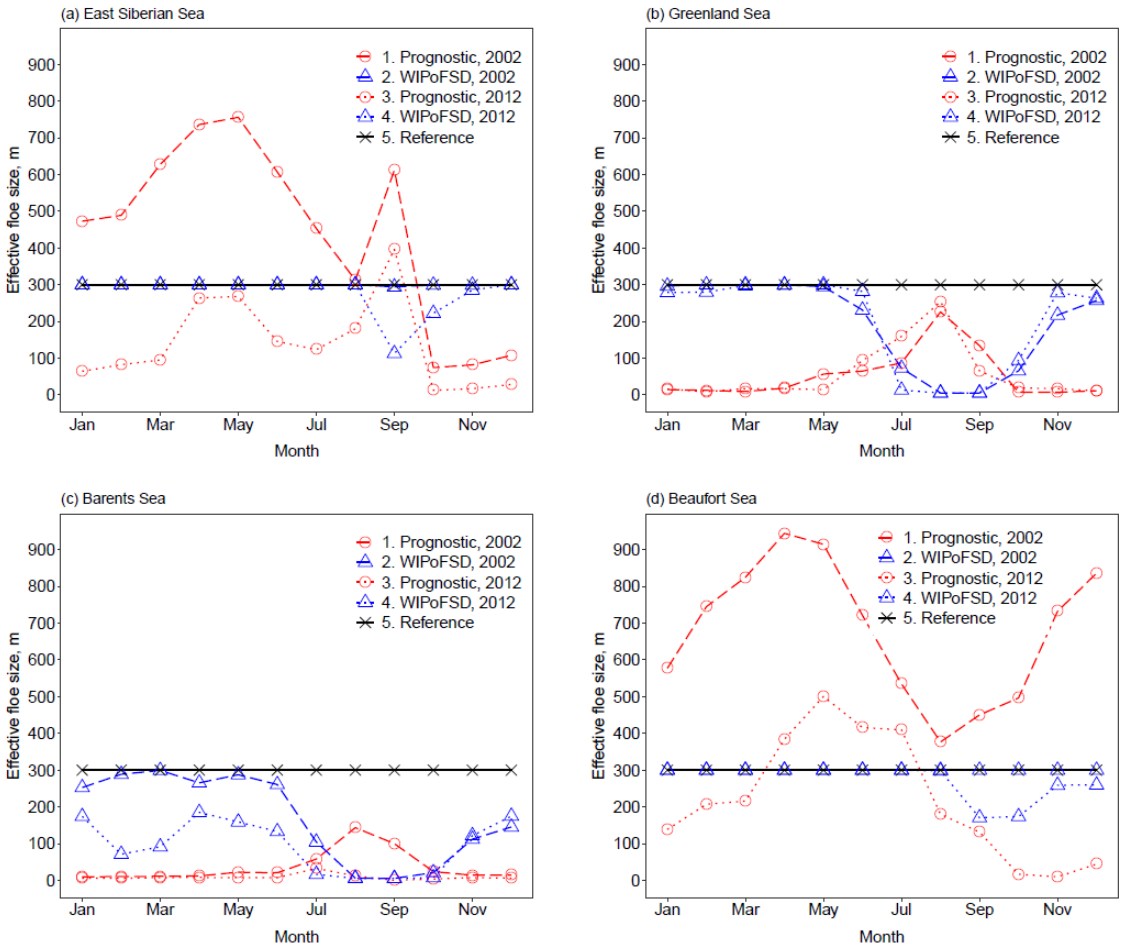

Figure 8.10: Annual timeseries in l_{eff} for the four sites described in Fig. 8.9: East Siberian Sea (a), Greenland Sea (b), Barents Sea (c), and Beaufort Sea (d). Results are presented for each of *prog-best* (red, circles), *WIPo-best* (blue, triangles), *ref* (black, crosses) in both 2002 (dashed) and 2012 (dotted). The behaviour of l_{eff} is generally consistent between sites for *WIPo-best* whereas *prog-best* shows more distinct behaviour at each location.

Figure 8.11 shows the first of these case studies, region A (East Siberian Sea) in 2012. Differences in the sea ice concentration between *ref*, *prog-best*, and *WIPo-best* are generally small, with *prog-best* showing a very small reduction in sea ice concentration compared to *ref* over the period of sea ice retreat. There are more notable differences between the mean sea ice thickness, particularly between *prog-best* and *ref*. The response in the lateral melt rate per unit sea ice area is very different between the three simulations. In *ref*, the lateral melt rate is low throughout the year, reaching a maximum of only 0.1 cm day^{-1} in September. The maximum value for the *prog-best* lateral melt rate is about 8 times higher than *ref* at 0.8 cm day^{-1} in September, with a gradual increase from June to that maximum value. For *WIPo-best*, the lateral melt rate values are comparable to *ref* in all months except September when the value reaches a

maximum of about 1.7 cm day^{-1}, nearly 20 times the value for *ref* and over double the value for *prog-best*. In comparison, the basal melt rates are broadly comparable between the three simulations, rising to a peak of just under 5 cm day^{-1} in August. There are small differences, for example in August and September *WIPo-best* and *prog-best* show a slightly increased basal melt rate compared to *ref*, but these changes are of 0.1 cm day^{-1} or less.

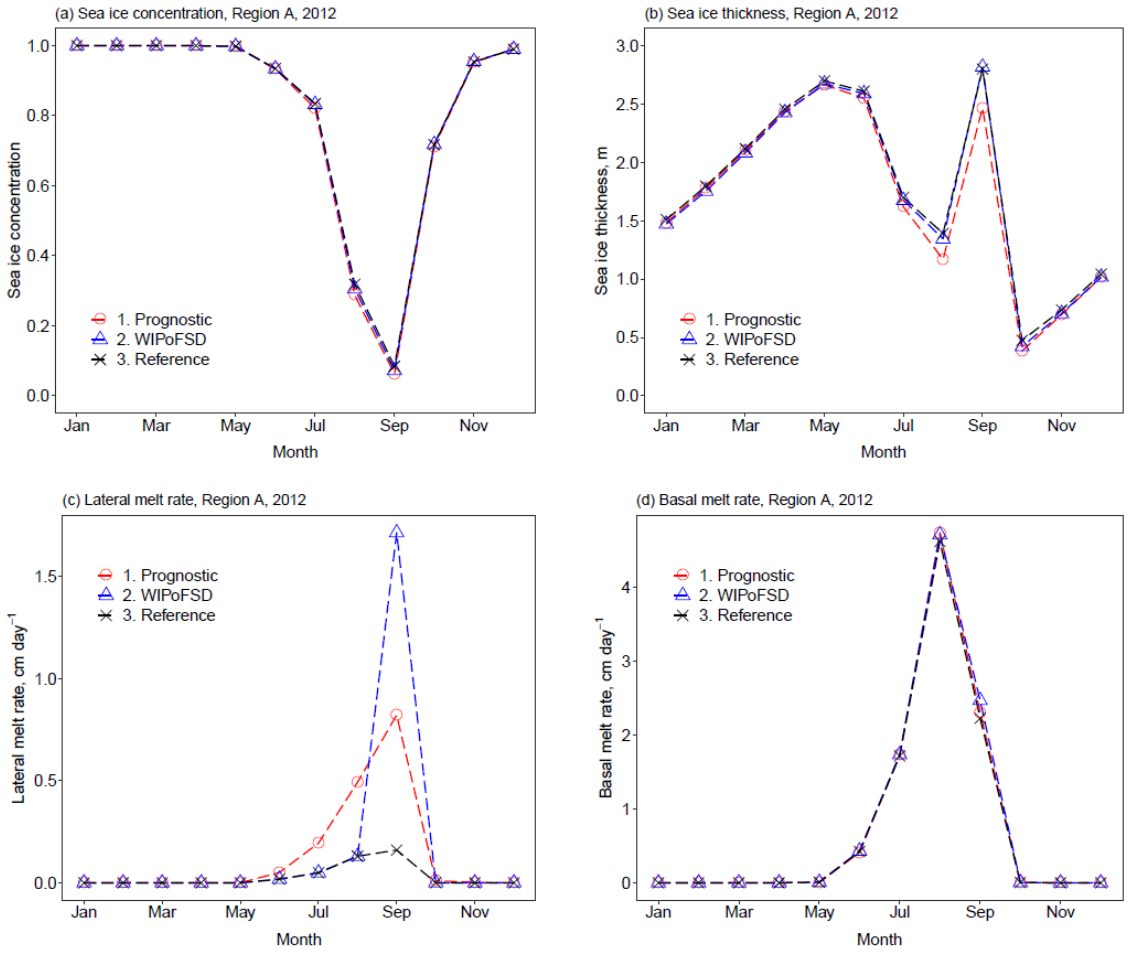

Figure 8.11: Annual timeseries presented for Region A (East Siberian Sea) in 2012 of the sea ice concentration (a, top left), sea ice thickness (b, top right), lateral melt rate per unit sea ice area (c, bottom left), and basal melt rate per unit sea ice area (d, bottom right). Results are presented for each of *prog-best* (red, circles), *WIPo-best* (blue, triangles), *ref* (black, crosses). The results show that changes are small for sea ice concentration but larger for sea ice thickness.

It is worth commenting on the general shape of the timeseries in mean sea ice thickness in Fig. 8.11. Excluding September, the general behaviour of the mean sea ice thickness is a quasi-sinusoidal evolution increasing through the freeze-up season and then decreasing through the melt season. In September, a peak in the sea ice thickness can be seen superimposed on the general sinusoidal shape of the thickness

evolution. This peak is associated with a period of very low sea ice concentration of about 0.1 fractional coverage. There are two mechanisms that can produce this peak in September. The first is the advection of thicker sea ice from pack ice locations. The second mechanism is less obvious and occurs as a result of the vertical melt out of thinner floes, increasing the contribution of thicker floes to the overall average. If the sea ice thickness distribution was evenly distributed and continuous, this effect would not be seen because the sizes of all floes would decrease. In specific circumstances, including where the distribution is either bimodal with lots of floes of smaller and larger thickness but not many of intermediate thickness, or where a discretised thickness distribution is used with thickness categories of varying size, a peak like the one shown in Fig. 8.11 can occur where the basal melt rate is high. In this case, as basal melting proceeds, the discretisation effect will drive moderate increases in the sea ice thickness. This effect is strongest as the sea ice concentration approaches zero, resulting in a peak in thickness just prior to the grid cell becoming ice free. This behaviour is important to consider when interpreting the difference between simulations as it can lead to otherwise counterintuitive differences in the sea ice thickness.

In Fig. 8.11, the large changes in the lateral melt rate for both *prog-best* and *WIPo-best* do not result in significant changes to the sea ice concentration between the simulations. In *ref*, changes to the sea ice concentration are primarily driven by vertical melt out of floes rather than horizontal melt out. Therefore, even where the lateral melt rate increases by factors of order 10, the changes to the overall sea ice concentration can remain low. In contrast, despite small changes to the basal melt rate, larger differences can be seen in the sea ice thickness, up to 0.3 m to 0.4 m in September, between *prog-best* and *ref*. As discussed, the behaviour of the mean sea ice thickness in August and September depends strongly on the shape of the sea ice thickness distribution. Differences in this thickness distribution can develop over multiple years and hence the evolution of the mean thickness cannot just be attributed to co-temporal melting. Additional factors to consider are the impacts of the form drag scheme and advection of floes from outside the region of interest. The results from Fig. 7.21 in chapter 7 show that the changes to the spatial distribution of sea ice thickness that can be attributed to form drag impacts are negligible for the region of interest. Figure 8.7 does show reduced sea ice thickness across the pack ice for *prog-best* compared to *ref*, hence the lower thickness of the pack ice advected into region A will be a contributing factor to the reduced mean sea ice thickness shown in Fig. 8.11.

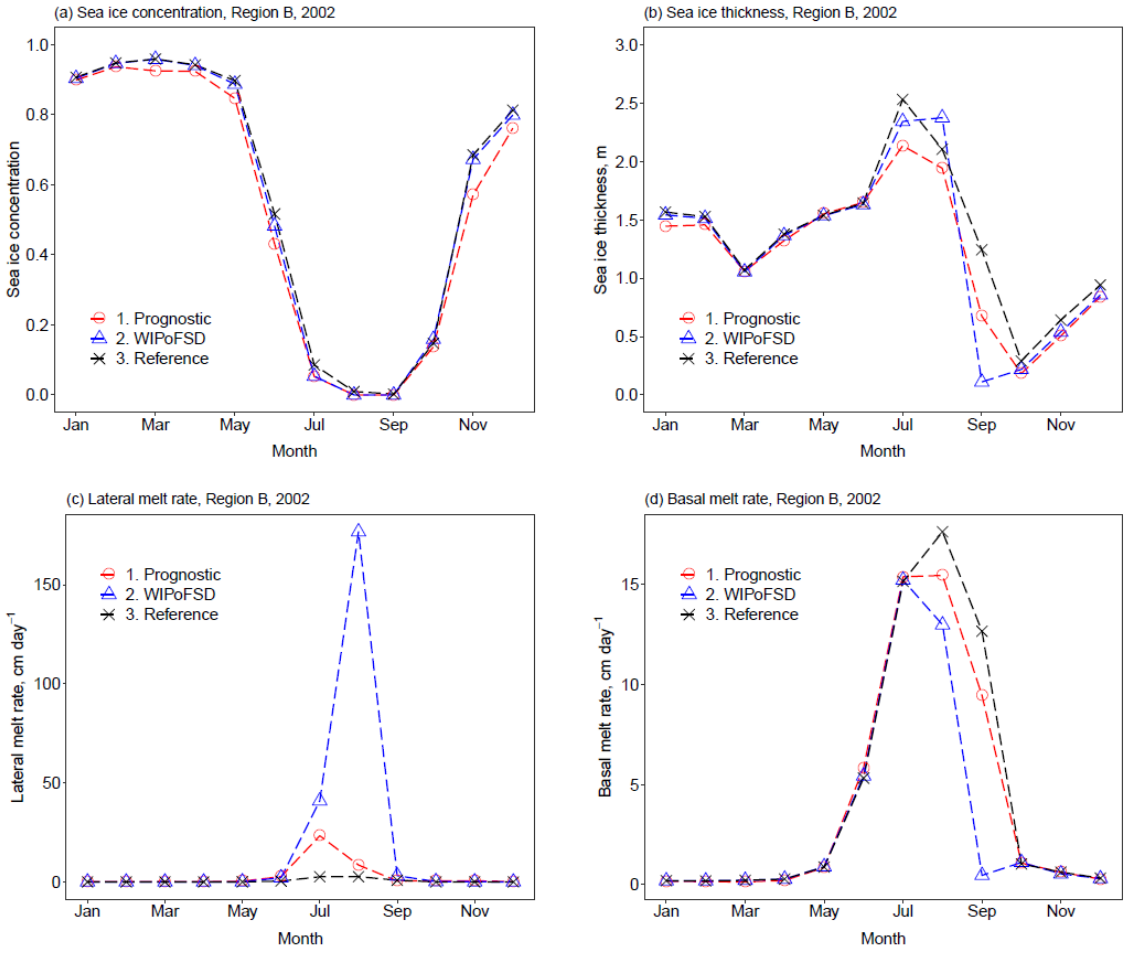

Figure 8.12: Annual timeseries presented for Region B (Greenland Sea) in 2002 of the sea ice concentration (a, top left), sea ice thickness (b, top right), lateral melt rate per unit sea ice area (c, bottom left), and basal melt rate per unit sea ice area (d, bottom right). Results are presented for each of *prog-best* (red, circles), *WIPo-best* (blue, triangles), *ref* (black, crosses). The large increase in the lateral melt rate per unit sea ice area for *WIPo-best* in July and August does not produce a large response in the sea ice concentration.

Figure 8.12 is equivalent for Fig 8.11, but this time for region B, which is sampled from the Greenland Sea in 2002. Here larger differences can be seen in the evolution of the different properties between the simulations. The sea ice concentration evolves from a maximum of about 0.95 in March to a sea ice free state over August to September. The sea ice concentration for *prog-best* is lower than *ref* throughout the rest of the year, particularly during the period of sea ice retreat in June and sea ice growth in November, with a maximum difference of about 0.1. *WIPo-best* is comparable to *ref* from September to May, with differences emerging during the period of sea ice retreat. Both *prog-best* and *WIPo-best* show a more rapid retreat in the sea ice cover compared to *ref*. The evolution of thickness is comparable to the behaviour shown in Fig. 8.11, with differences in the simulations again emerging from May to September,

but here *WIPo-best* also diverges from *ref*. Differences in the thickness over this period can be up to 1 m in magnitude. Lateral melt rates for *prog-best* are here comparable to basal melt rates, with both reaching a value of about 15 cm day^{-1} in July. For *WIPo-best* the lateral melt rate exceeds the basal melt rate, reaching values of 40 cm day^{-1} in July and nearly 200 cm day^{-1} in August. For the basal melt rate, the simulations show highly divergent behaviour in August and September, with rates much higher for *ref* than *prog-best* and *WIPo-best* in these months. These differences are partly driven by the complete melt out of sea ice in some grid cells for *prog-best* and *WIPo-best*. In addition, the increased lateral melt rate can also have a negative impact on the basal melt rate either though mixed-layer feedbacks or through the melt potential constraint described in Eq. (2.5) in chapter 2. Despite the very large values of lateral melt rate per unit sea ice area seen with *WIPo-best*, this behaviour occurs at the time of very low sea ice extent resulting in only a small impact on the sea ice concentration.

The differences in the lateral melt response in both Fig. 8.11 and 8.12 can be understood by considering the evolution of l_{eff} presented in Fig. 8.10. For region A in 2002, l_{eff} remains above 100 m for both *prog-best* and *WIPo-best* during the period of sea ice melt, resulting in a limited increase in the lateral melt rate per unit sea ice area over this period and not enough to cause large changes in the sea ice concentration. For region B in 2012, l_{eff} does decrease to values of below 50 m and as small as 10 m for *WIPo-best*, resulting in the very large values for the lateral melt rate per unit sea ice area shown in Fig. 8.12. Whilst *prog-best* produces an l_{eff} of below 10 m through most of the year in region B in 2012, during the melting season l_{eff} increases due to the selective melt out of smaller floes, and hence the increase in the mean lateral melt rate per unit sea ice area over the region is more moderate.

Fig. 8.13 displays a further case study, this time for region C in 2012 from the Barents Sea. Here, l_{eff} for both *prog-best* and *WIPo-best* remains below 10 m from July to October, and both simulations show a comparable large increase in the lateral melt rate per unit sea ice area in July. *prog-best* shows a significant reduction in the lateral melt rate per unit sea ice area from July to August, though this is associated with the earlier complete loss of the sea ice cover in *prog-best* when compared to *ref*. Fig. 8.13 presents a clear example where increases in both the lateral and basal melt rate per unit sea ice area can be seen during the melt season, specifically for *prog-best* compared to *ref* during June and July. This can be associated with a reduction in the

sea ice concentration and a subsequent increase in the mixed-layer temperature, suggesting a limited role for mixed-layer feedbacks in determining the melt response of the sea ice to the FSD model, in this case via the albedo feedback mechanism.

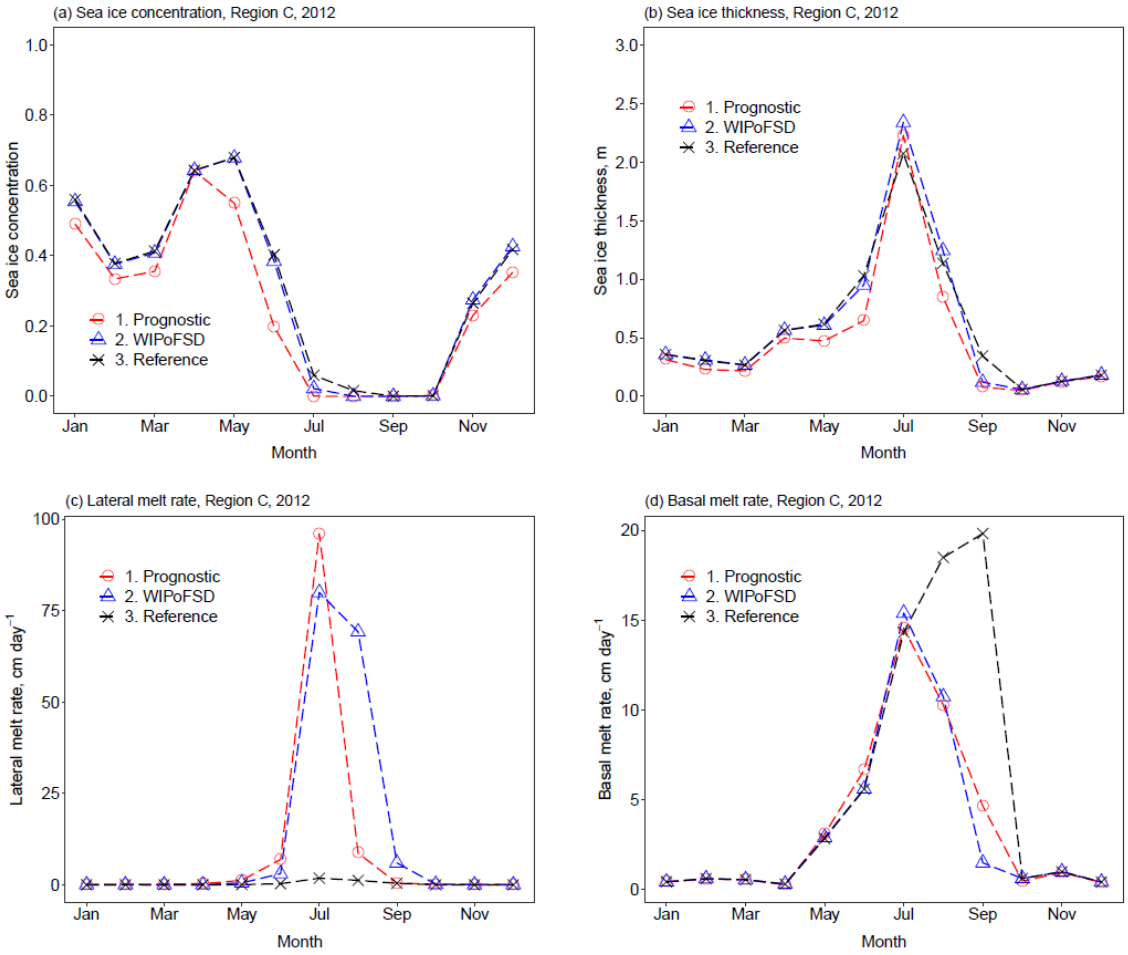

Figure 8.13: Annual timeseries presented for Region C (Barents Sea) in 2012 of the sea ice concentration (a, top left), sea ice thickness (b, top right), lateral melt rate per unit sea ice area (c, bottom left), and basal melt rate per unit sea ice area (d, bottom right). Results are presented for each of *prog-best* (red, circles), *WIPo-best* (blue, triangles), and *ref* (black, crosses). At this location there exists evidence of mixed-layer feedbacks acting for *prog-best* as there are periods where both the lateral and basal melt rates are higher for *prog-best* than for *ref*.

The figures presented in Sect. 8.3.2 lead to some important conclusions. It is possible to understand the response in the lateral melt rate per unit sea ice area to an imposed FSD by considering how l_{eff} evolves. This is consistent with the results in chapter 3 where the mean l_{eff} was found to correlate well with the mean change in the September sea ice extent in response to the inclusion of the WIPoFSD model. The change in the lateral melt rate then drives changes to the sea ice concentration. In general, these changes to the sea ice concentration are small and only reach values of

up to 0.1 to 0.2 for the more extreme cases. In comparison, larger relative changes of 0.5 m to 1 m can be seen in the response of sea ice thickness. These differences emerge despite the lack of a direct link between lateral melting and sea ice thickness, and the small to negligible changes in the basal melt rate during the early melting season between simulations. This shows that the large changes in the September sea ice thickness presented in Fig. 8.7 across much of the sea ice cover, particularly for *prog-best*, cannot be understood purely through a consideration of the local evolution of the sea ice melt and state within individual melt seasons. It has also been shown in this section how l_{eff} can be used to understand the mechanisms of how differences in the FSD model impacts emerge. Figure 8.10, showing the annual evolution of l_{eff} averaged over specific regions, demonstrates the two key systematic differences between the models. For *prog-best*, the behaviour and value of l_{eff} over winter months can vary significantly between locations. For *WIPo-best*, l_{eff} is generally rapidly restored to a maximum value during the freeze-up period and remains fixed at that value until the melting season. Secondly, during the summer melt period, selective melt out of smaller floes can drive an increase in l_{eff} during the mid to late melting season, a behaviour not seen with *WIPo-best*. These behaviours can also be seen in the map plots of l_{eff} presented in Fig. 8.7. Figures 8.11 – 8.13 then show how the response of the lateral melt rate and subsequent change in the sea ice concentration is dependent on these different behaviours in l_{eff}. A low value of l_{eff} in March to May results in a faster retreat of the sea ice in the early melt season, and the increase in or lack thereof of l_{eff} during the later melt season has a significant impact on the lateral to basal melt ratio over July to September.

8.4 A sensitivity study to better capture features of the prognostic model with the WIPoFSD model

The figures presented both in Chapter 7 and Chapter 8 identify important differences in the behaviour of the WIPoFSD model and the prognostic FSD model. Section 8.3.2 shows that differences in the impacts of these FSD models on CICE simulations can be attributed to both the model treatment of lateral melt and the representation of floe growth processes, via differences in the evolution of l_{eff}. The necessary observations required to establish whether either model produces an accurate description of the annual evolution of l_{eff} do not exist. Stern et al. (2018b) is the most useful resource in

this regard, reporting the exponent in 2013 and 2014 from March to October averaged from FSD observations sampled in the Beaufort and Chukchi Seas. This dataset is limited as only floes larger than about 2 km are included in the analysis i.e. larger than the range modelled within the prognostic model. These observations show that the exponent becomes less negative from August to October and then March to April, indicating that l_{eff} would also be expected to increase over the same time period. Panel (d) in Fig 8.10, plotting the annual l_{eff} for grid cells sampled from the Beaufort Sea, suggests that *prog-best* better simulates this gradual increase in l_{eff} over the freeze-up period, whereas l_{eff} for *WIPo-best* generally increases rapidly and then remains at the fixed maximum throughout the winter. The individual floe formation and growth processes described in the prognostic model are also motivated by observations of these processes acting on the sea ice cover (Roach et al., 2018b).

Whilst it is not possible to conclude definitively which of the two FSD models produces the better description of the real FSD, it is nevertheless useful to consider whether it is possible to capture the behaviour seen in the more complex prognostic model using a simple alteration to the WIPoFSD model. Key targets for such an alteration are the lateral melt scheme and the treatment of floe growth processes, given their important role in the different impacts of the two FSD models. Chapter 4 has previously discussed the challenges of representing lateral melt feedbacks on the FSD within the WIPoFSD model, which imposes a fixed shape on the distribution. It has already been demonstrated in chapter 4 that it is not possible to exactly represent the effects of lateral melting on the FSD within the WIPoFSD model due to the restriction of a power-law shape and fixed minimum floe size. This theme will not be revisited here. Instead the focus here will be on how floe formation and welding processes are represented in the WIPoFSD model.

The WIPoFSD model does not explicitly represent floe formation and growth processes but instead uses a simple winter restoring scheme where l_{var} increases at a fixed rate during freezing conditions. The key parameter to determine the behaviour of these winter floe processes in the WIPoFSD model is T_{rel}, the floe restoring timescale. In chapter 3 a sensitivity study was completed with the WIPoFSD model where T_{rel} was increased from 10 days to 365 days. Given the evidence from observations that the development of the FSD over the freeze-up period is gradual and not instantaneous, this sensitivity study will be repeated here, changing T_{rel} in *WIPo-best* from 10 days to

365 days. This simulation will be referred to as *WIPo-sg* (slow growth) and is identical to *WIPo-best* in all ways other than the value of T_{rel}. Figure 8.14 is comparable to Fig. 8.10, except this time comparing the evolution of mean l_{eff} over each site for *prog-best against WIPo-sg*, rather than *WIPo-best*. These plots show that the increase of T_{rel} does appear to produce a more consistent behaviour in l_{eff} between the two FSD models. For example, at site A, l_{eff} roughly follows the same evolution in both *prog-best* and *WIPo-sg* in 2012. Both models predict a very small l_{eff} throughout the year at site C, and at site D in 2012 both models show similar values in l_{eff} from September to December, once l_{eff} for *prog-best* drops below 300 m. There are still cases where the models perform differently, for example the Greenland Sea between October and May. The opposite tendency of l_{eff} in the melting season between the two models can be attributed to the fixed power-law shape in the WIPoFSD model, as discussed above. In the Greenland Sea this effect compounds with an overestimation of floe growth processes in winter for *WIPo-sg* compared to *prog-best*, with the net result being inverted annual cycles. Some differences can be attributed to model architecture, specifically there exists a maximum value of l_{eff} for both *WIPo-sg* and *prog-best* because of how the FSD is defined or simulated in each case, but this limiting value is 300 m for *WIPo-sg* but about 1700 m for *prog-best*. *WIPo-sg* is therefore not capable of simulating the large values of l_{eff} produced in the East Siberian and Beaufort Seas for *prog-best*.

Figure 8.14 demonstrates an increased similarity between the two FSD models at a localised level, but it is also useful to consider the changes for large scale metrics. Figure 8.15 compares the difference in sea ice extent and volume to *ref* for both *prog-best* and *WIPo-sg* over an annual cycle averaged from 2000-2016. The change in sea ice volume for *WIPo-sg* relative to *ref* is significantly closer to the result for *prog-best* than *WIPo-best* was shown to be in Fig. 8.4. Both *WIPo-sg* and *prog-best* show a mean reduction in the September sea ice volume of just under 4 %, compared to a 2.5 % reduction for *WIPo-best*. *WIPo-sg* also shows an increased interannual varaibility to *WIPo-best*; this remains smaller than the variability shown for *prog-best* but now about 66 – 75 % of the *prog-best* variability rather than 50 %. Improvements are less obvious for the sea ice extent, however this can be attributed to the failure to capture the negative feedback process of lateral melting on l_{eff} in the WIPoFSD model. The difference in sea ice concentration for both *WIPo-sg* and *prog-best* compared to *ref* are

comparable in July with just under 2 % reduction each, but this reduction remains under 2 % in August for *prog-best* but increases to about 2.5% for *WIPo-sg*.

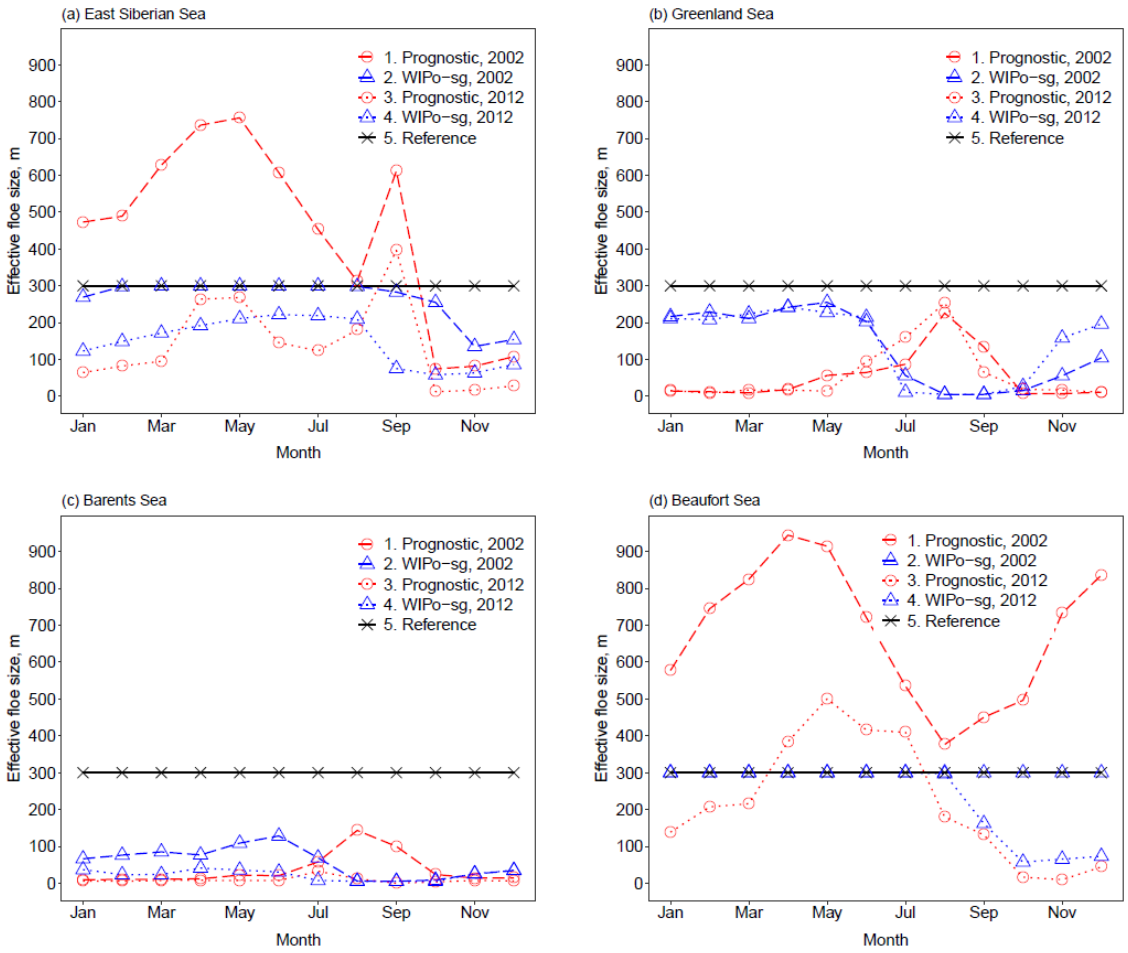

Figure 8.14: Annual timeseries in l_{eff} for the four sites described in Fig. 8.9: East Siberian Sea (a), Greenland Sea (b), Barents Sea (c), and Beaufort Sea (d). Results are presented for each of *prog-best* (red, circles), *WIPo-sg* (blue, triangles), *ref* (black, crosses) in both 2002 (dashed) and 2012 (dotted). *WIPo-sg* can capture several of the behaviours seen in l_{eff} during freeze-up for *prog-best*.

Figure 8.16 shows difference map plots in the sea ice extent and thickness for *WIPo-sg* relative to *ref* and map plots of l_{eff} for *WIPo-sg* in selected months averaged over 2000-2016. This figure is equivalent to Fig. 8.7, which presented the same spatial plots for *WIPo-best* and *stan-best*. The spatial distribution of l_{eff} within the pack ice for *WIPo-sg* is less homogenous than for *WIPo-best* and the average l_{eff} within the MIZ is reduced. However, the unique features seen for *prog-best* i.e. lack of radial symmetry and broad extent of sea ice with an l_{eff} below 25 m in the Barents and Greenland Seas, are still not replicated by the *WIPo-sg* model. For the difference plots in sea ice concentration and thickness relative to *ref*, *WIPo-sg* is able to capture features seen for

prog-best that *WIPo-best* is unable to capture. In particular, the pattern of reduction of sea ice concentration and thickness across the MIZ and pack ice are broadly comparable between *prog-best* and *WIPo-sg* in September. *WIPo-sg* also shows a larger area of pack sea ice where the reduction in thickness persists throughout the year. There are still spatial features that only *prog-best* produces, such as the strong model response in the Greenland Sea during the earlier melt season.

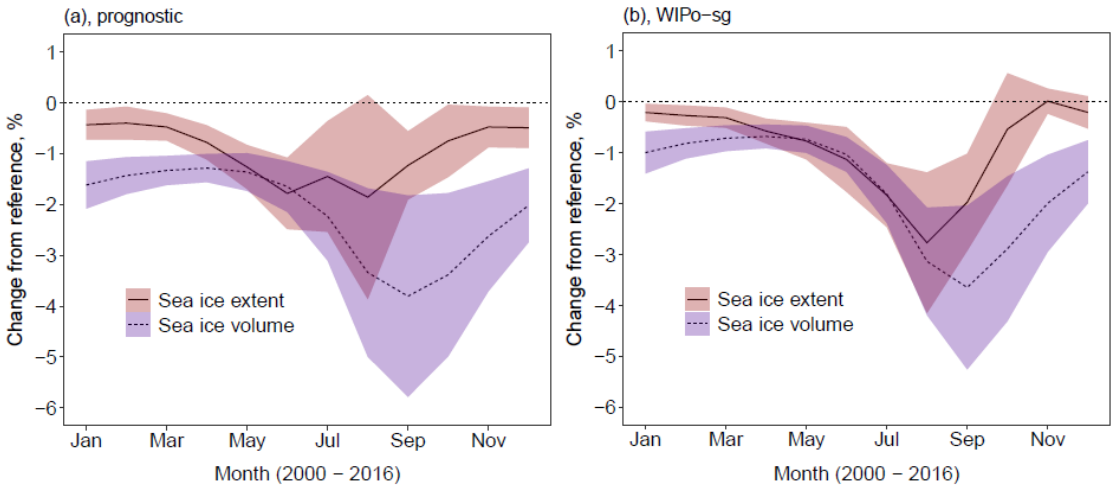

Figure 8.15: Difference in sea ice extent (solid, red ribbon) and volume (dashed, blue ribbon) of *prog-best* (a, left) and *WIPo-sg* (b, right) relative to *ref* averaged over 2000 - 2016. The ribbon shows, in each case, the region spanned by the mean value plus or minus two times the standard deviation. Both models show a comparable reduction in sea ice volume over the melt season but produce a different response in the sea ice extent.

In summary, through a simple tuning of the WIPoFSD model by increasing the floe restoring timescale, several of the features and impacts shown by the prognostic model can be replicated. This is despite the models using very different approaches to representing the FSD within CICE. Differences remain, particularly resulting from the inability of the WIPoFSD model to capture the precise effects of lateral melting on the shape of the FSD. Nevertheless, the WIPoFSD model appears capable of broadly capturing the impacts on CICE found with the prognostic model. Therefore, the WIPoFSD model appears to be a reasonable alternative approach to representing the FSD compared to the prognostic model for the 2000 – 2016 sea ice climatology, assuming careful tuning of the model parameters. The question then follows; will the tuning of the WIPoFSD model for the present-day climatology hold for the Arctic sea ice under future atmospheric forcing? In chapter 7 it is shown that the impact of the prognostic model on the sea ice mass balance is strongly determined by whether sea ice primarily forms as pancake floes or nilas ice, with the latter formation mechanism

found to dominate for present day climatology. However, pancake floes are becoming increasingly important in the Arctic as the sea ice retreats and the waves become a more important component of the Arctic system (Jones, 2009; Thomson and Rogers, 2014). Whilst the WIPoFSD model appears to be capable of capturing moderate perturbations to the FSD within the current climatology, it is less clear that this will continue to hold under future forcings where the processes relevant to the evolution of the FSD may change.

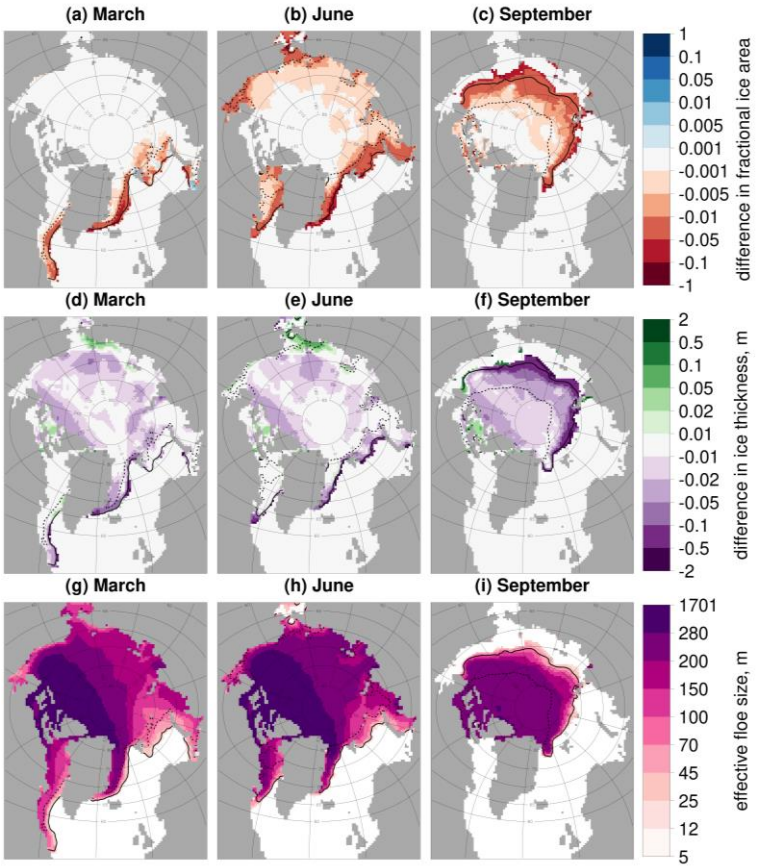

Figure 8.16: Difference in the sea ice concentration (a–c) and thickness (d–f) for *WIPo-sg* relative to *ref* and l_{eff} (g–i) for *WIPo-sg* averaged over 2000–2016. Results are presented for March (a, d, g), June (b, e, h), and September (c, f, i). Values are shown only in locations where the sea ice concentration exceeds 5 %. The inner (dashed black) and outer (solid black) extent of the MIZ averaged over the same period is also shown. In the pack ice the spatial distribution of l_{eff} is no longer homogenous and reductions in the sea ice thickness persist throughout the year.

8.5 Projections of the sea ice incorporating an FSD model

Previously in this chapter, a direct comparison of the impact on the sea ice state of incorporating both the prognostic FSD and WIPoFSD models within CICE found only a small to moderate change in the sea ice extent and volume under the present

climatology. However, these differences may increase under a future climatology if the relevant FSD processes change e.g. if pancake ice becomes a more dominant mechanism of floe formation. In this section results from CICE simulations using atmospheric forcing data over the period 2017 to 2060 are presented to explore if there are indications for such a transition in the FSD behaviour.

The main purpose of these projections is to explore if the diverging behaviour between simulations with and without an FSD model over time, as shown in Fig. 8.5, will persist as the sea ice continues to retreat under future atmospheric forcing. It is not the intention here to produce an accurate simulation of the future sea ice state but simply a representative simulation that will allow an exploration of the importance of the FSD as the Arctic transitions to a sea ice cover that is seasonal with limited to no regions of permanent sea ice cover.

8.5.1. Methodology for the projections

Previously in this chapter, three simulations have been considered: *ref*, where CICE was evaluated with the standard fixed floe size of 300 m; *prog-best*, where CICE was evaluated with the prognostic FSD model including the brittle fracture scheme described in chapter 7; and *WIPo-best* where CICE was evaluated with the WIPoFSD model and the associated power-law exponent selected to produce the best fit to observations. For this study, the methodology will be almost identical to that described in Sect. 8.1.3 for *ref*, *prog-best* and *WIPo-best* except for some important differences that will be described here. The simulation will use the output of the original *ref* / *prog-best* / *WIPo-best* simulation, restarting on 1st January 2017 and evaluated until 31st December 2060, adding an additional 44 years to the original 37-year simulations. The atmospheric forcing data is taken from the RCP8.5 pathway for the HadGEM2-ES implementation of the CMIP5 centennial simulations (Jones et al., 2011). Given the change in atmospheric forcing data product between 2016 and 2017, the model output from 2017 – 2019 should be considered as a period of adjustment to the new forcing data. The ocean state will be restored to the 1993 – 2010 climatology from the MyOcean global ocean physical reanalysis product (Ferry et al., 2011), as per the hindcast simulations performed in this chapter. For the wave forcing data, the ERA-Interim reanalysis dataset (Dee et al., 2011) over the period 2012-2016 will be used, repeating over 5-year cycles. In total, three simulations have been completed for this section, using the forcing setup described above. *ref-proj* uses the output of *ref* with a

fixed floe size of 300 m, *prog-proj* uses the output of *prog-best* with an identical prognostic FSD model setup, and *WIPo-proj* uses the output of *WIPo-best* with an identical WIPoFSD model setup.

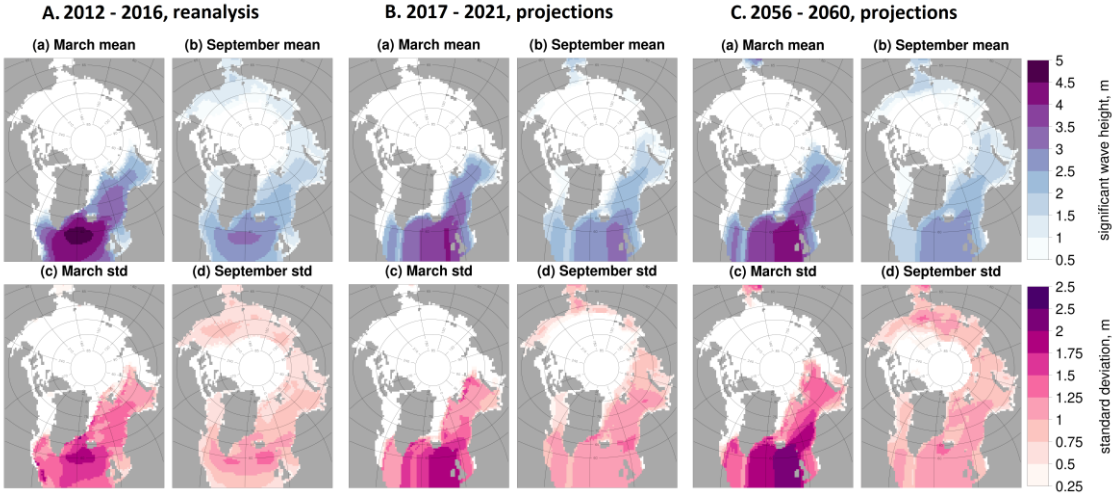

Figure 8.17: Plots show the mean (a, b) and standard deviation (c, d) of the significant wave height taken over the 5-year named period for March (a, c) and September (b, d). Section A (left) shows the reanalysis values for 2012 – 2016. Section B (middle) shows the projected values for 2017 – 2021. Section C (right) shows the projected values for 2056 – 2060. The reanalysis is taken from the ERA-Interim reanalysis dataset (Dee et al., 2011). Projections were prepared by Lucy M. Bricheno of the National Oceanography Centre, Liverpool from a global RCP 8.5 wave projection (Bricheno and Wolf, 2018). For the projections, data is only available at latitudes above 60° N. These plots demonstrate that the 2012 – 2016 wave climatology in the reanalysis holds as a reasonable description of the wave climatology shown for both the 2017 – 2021 and the 2056 – 2060 periods in the projections.

It is worth commenting on why this methodology has been selected for these projections. The RCP8.5 pathway, selected for the atmospheric projection, represents a worse-case scenario where no meaningful climate action is taken through the 21st century or positive climate feedbacks turn out to be larger than expected. Given the aim of these projections is to understand the potential importance of the FSD and FSD processes in a future Arctic that is trending towards no permanent sea ice cover, the RCP8.5 pathway presents a useful forcing scenario to explore this state, even if it does not represent the most realistic emissions trajectory based on current understanding (Hausfather and Peters, 2020). The use of the 1993 – 2010 climatology for the ocean forcing is reasonable here because the simulations that produced the trends shown in Fig. 8.5, which shows a divergence of the sea ice state between *ref*, *WIPo-best*, and *prog-best*, were evaluated using the same climatology for the ocean state i.e. the trends in Fig. 8.5 was not driven by changes in the ocean state. It is, of course,

possible that changes in the ocean state may also change the role of the FSD and FSD processes in the evolution of the Arctic sea ice, and this is a limitation of the results presented in this section. However, this question would be best addressed using a coupled sea ice-ocean framework where both changes to the ocean state and sea ice-ocean interactions can be considered. It has already been demonstrated that the inclusion of an FSD model can perturb the ocean state under present climatology (Rynders, 2017).

Another choice made for the projections is the use of the 2012-2016 wave forcing data over 5-year cycles. This decision has been made due to technical limitations in the use of the projected wave data. Given the importance of wave processes to the evolution of the FSD, both through the break-up of floes and determining the size of newly formed floes, it is important that any projection to explore the potential future role of the FSD and FSD processes includes a realistic ocean surface wave climatology. Figure 8.17 compares the spatial distribution in both the magnitude and interannual variability of the significant wave height for this 5-year period to projections of the significant wave height over the period 2017 – 2021 and 2056 – 2060 in both March and September. The wave projections were prepared by Lucy M. Bricheno of the National Oceanography Centre, Liverpool, from a global RCP 8.5 wave projection (Bricheno and Wolf, 2018) using the WaveWatch III^{TM} spectral wave model version 3.14 (Tolman, 2009) and forced with EC-EARTH model (Hazeleger et al., 2012) atmosphere and sea ice concentration. The EC-EARTH setup simulates the sea ice concentration using a NEMO Version 2 ocean model setup (Madec, 2008), which includes the Louvain-la-Neuve Ice Model version 2 (LIM2) as the sea ice model component. The wave projections of Bricheno and Wolf (2018) cannot be used directly in projections with the FSD models as the peak wave period associated with the significant wave height is unavailable. Figure 8.17 demonstrates that the 2012 - 2016 reanalysis in general produces a reasonable climatology over the full time-range of the projections, with each 5-year period showing values of comparable magnitude for the mean and standard deviation of the significant wave height. The spatial distributions in these metrics are also comparable. There is some evidence of a positive trend in the March mean and standard deviation in significant wave height from 2017 – 2021 to 2056 – 2060 of about 0.5 m and 0.25 m respectively, but these changes are not large enough to represent a step change in the surface ocean wave forcing. Whilst the use of the 2012-2016 wave forcing is a limitation of the methodology for these projections, the 2012-2016

reanalysis climatology is sufficiently close to the projected 2056-2060 climatology for the purpose of these projections in producing a representative simulation.

8.5.2. Results of projections

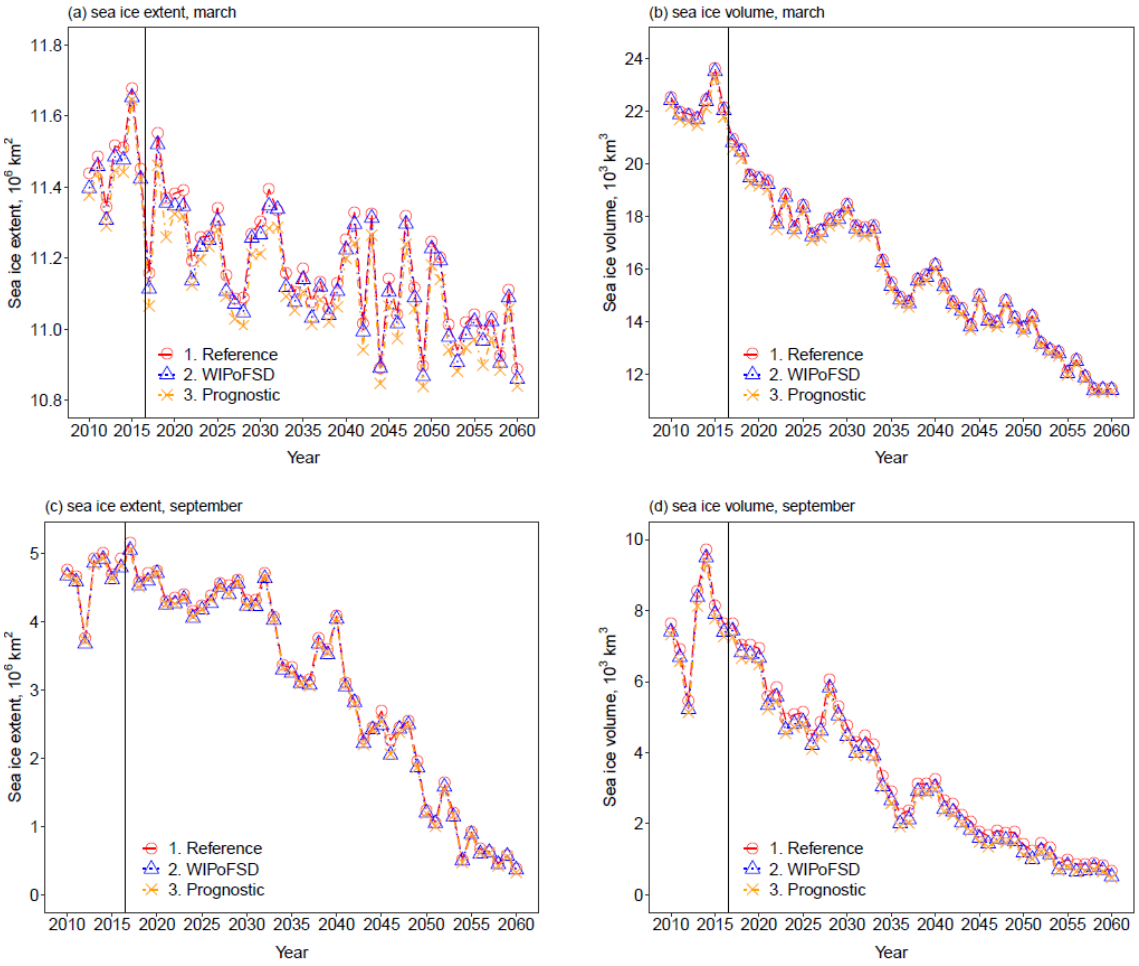

Figure 8.18: The total Arctic sea ice March extent (a, top left), March volume (b, top right), September extent (c, bottom left) and September volume (d, bottom right) within the model domain over the period 2010 - 2060 for *ref-proj* (red, circles), *WIPo-proj* (blue, triangles) and *prog-proj* (orange, crosses). The solid vertical black line separates the hindcast region over 2010 – 2016, using data from *ref*, *prog-best*, and *WIPo-best*, and the projection from 2017 – 2060. Whilst the sea ice mass balance is generally lower for *prog-proj* and *WIPo-proj* compared to *ref-proj*, especially in September, these differences are generally lower than the interannual variability and long-term sea ice trends.

Figure 8.18 shows the March and September sea ice extent and volume from 2010 to 2060 (using the hindcast simulation results from 2010 – 2016) for *prog-proj*, *WIPo-proj*, and *ref-proj*. This figure shows that *prog-proj* and to a lesser extent *WIPo-proj* produce a lower sea ice extent and particularly volume compared to *ref-proj*. Nevertheless, the impact of including the FSD is still less than the interannual variability and is also small

in comparison to the long term FSD trends. It is possible that the switch from an atmospheric reanalysis product to atmospheric projections between 2016 and 2017 results in a period of readjustment in the simulations. Fig. 8.18 does not show any behaviour from 2017 – 2019 that is necessarily inconsistent with adjacent years within the general variability shown. The only behaviour of note is a significant reduction in the sea ice extent in March in 2017 compared to 2016 that is larger than the year-on-year differences usually seen. Overall, there is no strong evidence of any significant discontinuities in the atmospheric forcing data between 2016 and 2017 based on the behaviour of the sea ice extent and volume, though 2017 – 2019 should nevertheless still be treated as a period of adjustment to the new forcing data and results over this period taken with caution.

Figure 8.19 shows timeseries in the percentage difference in the total Arctic extent and volume for *prog-proj* and *WIPo-proj* relative to *ref-proj* in both March and September over the period 2010 – 2060 (*prog-best* or *WIPo-best* relative to *ref* for 2010 – 2016). The largest differences can be seen in the September sea ice volume. For *prog-proj* relative to *ref-proj* the September volume changes from an average reduction of about 5 % between 2010 and 2016 to a mean reduction of over 20 % by the 2050s. In comparison the magnitude of the reduction for the March sea ice volume peaks in the later 2010s and the 2020s at about 1.8 %, but then reduces to less than 1 % by the mid-2050s. The March sea ice extent maintains a mean reduction of about 0.6 % over the time period, whereas the September sea ice extent maintains a mean reduction of 1 – 2 % until the early 2040s where the difference increases in size to a mean value of about 6 % through the 2050 s. In 2060 the reduction in September sea ice extent is 12 %. For *WIPo-proj* relative to *ref-proj* the trends are broadly similar, with some important similarities and differences. The September sea ice volume changes from a mean reduction of about 3 % over 2010 – 2016 to a mean reduction of about 20 % in the 2050s, with the strength of the trend away from *ref-proj* very similar for both *WIPo-proj* and *prog-proj*. For the September sea ice extent, both *prog-proj* and *WIPo-proj* relative to *ref-proj* behave in a similar way up to the early 2040s, but then the negative trend seen for *prog-proj* is not so well defined for *WIPo-proj*. In both cases a transition can be seen in the early 2040s to a state of significantly higher interannual variability in the percentage difference, and this makes long term trends difficult to identify over the time range considered. This transition to higher interannual variability is associated with the period where the September sea ice extent consistently falls below 3×10^6 km^2; further

analysis shows that the September pack ice extent is close to negligible for most years from 2045 onwards i.e. the MIZ effectively covers the entire September sea ice cover.

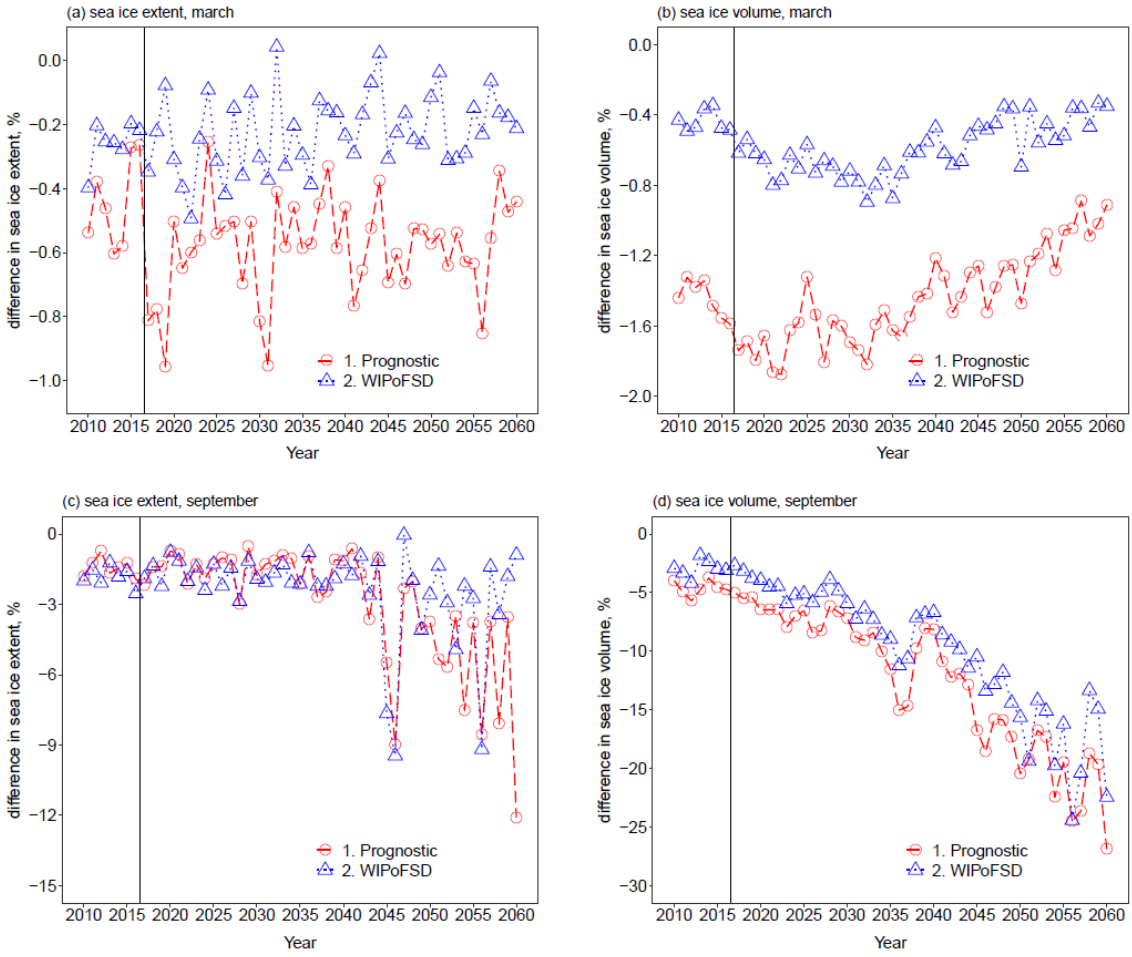

Figure 8.19: The % difference in the total Arctic sea ice March extent (a, top left), March volume (b, top right), September extent (c, bottom left), and September volume (d, bottom right) over the period 2010 – 2060 for *WIPo-proj* (blue, dotted, triangles) and *prog-proj* (red, dashed, circles) relative to *ref-proj*. The solid vertical black line separates the hindcast region over 2010 – 2016, using data for *WIPo-best* / *prog-best* relative to *ref*, and the projection from 2017 – 2060. These plots show that whilst the % difference trends back to zero in both cases for the March sea ice volume over the 2040s and 2050s, both *WIPo-proj* and *prog-proj* continue to separate from *ref-proj* for the September sea ice volume, to reductions consistently exceeding 20 % in the 2050s.

Overall, Fig. 8.18 indicates that the FSD does not appear to be that important in determining the long-term sea ice trends and when events such as an ice-free summer will occur. However, Fig. 8.19 here shows that the FSD is important for predicting the sea ice climatology in the mid-21st century. In addition, both *prog-proj* and *WIPo-proj* identify similar trends for the percentage reduction in September sea ice volume compared to *ref-proj*. This suggests that this trend is a general feature expected from

the enhanced lateral melt when incorporating an FSD model and is not something unique to the prognostic model.

Figure 8.20 shows maps of the difference in sea ice concentration and thickness for both *prog-proj* and *WIPo*-proj relative to *ref-proj* averaged over 2050 – 2060 for March, June, and September. The plot also shows the average l_{eff} in *prog-proj* and *WIPo-proj* over 2050 – 2060 for these same months. For *prog-proj* relative to *ref-proj* in March and June, reductions in sea ice concentration and thickness are strongest within the MIZ though there are regions of small increases and decreases within the pack ice. In September the MIZ covers the entire sea ice cover. Small to moderate reductions can be seen in the sea ice concentration, and reductions in the sea ice thickness of 10 – 50 cm can be seen across the sea ice cover. This is consistent with Fig. 8.19, which showed that by the 2050s the sea ice climatology is significantly more sensitive to the inclusion of the prognostic FSD model. The behaviour of l_{eff} is similar to the 2000 – 2016 climatology shown in Fig. 8.7. Here there is less variability across the pack ice cover, with l_{eff} larger than 280 m for most of the pack ice except Atlantic facing regions. In September, l_{eff} is greater than 100 m across most of the sea ice cover, despite the MIZ comprising the entire sea ice cover. This is again a result of the negative feedback of lateral melt on l_{eff}.

For *WIPo-proj* relative to *ref-proj* a similar pattern of reduction in concentration and thickness can be seen in September compared to the *prog-proj* case at the sea ice edge. However, within and along the Canadian archipelago and north Greenland coast, the magnitude of the changes is either much smaller or negligible. For l_{eff} in September, a higher proportion of the sea ice cover has an l_{eff} smaller than 280m for *WIPo-proj* compared to *prog-proj*, but a smaller proportion of the sea ice cover has l_{eff} smaller than 45 m. Again, the standard WIPoFSD model shows more homogenous behaviour in l_{eff} compared to the prognostic model. In Fig. 8.19 it was shown that both simulations produced a similar reduction of about 20 % in September sea ice volume compared to *ref-proj*. Figure 8.20 shows that this reduction is more evenly distributed across the sea ice for *prog-proj* but concentrated at the sea ice edge for *WIPo-proj.*

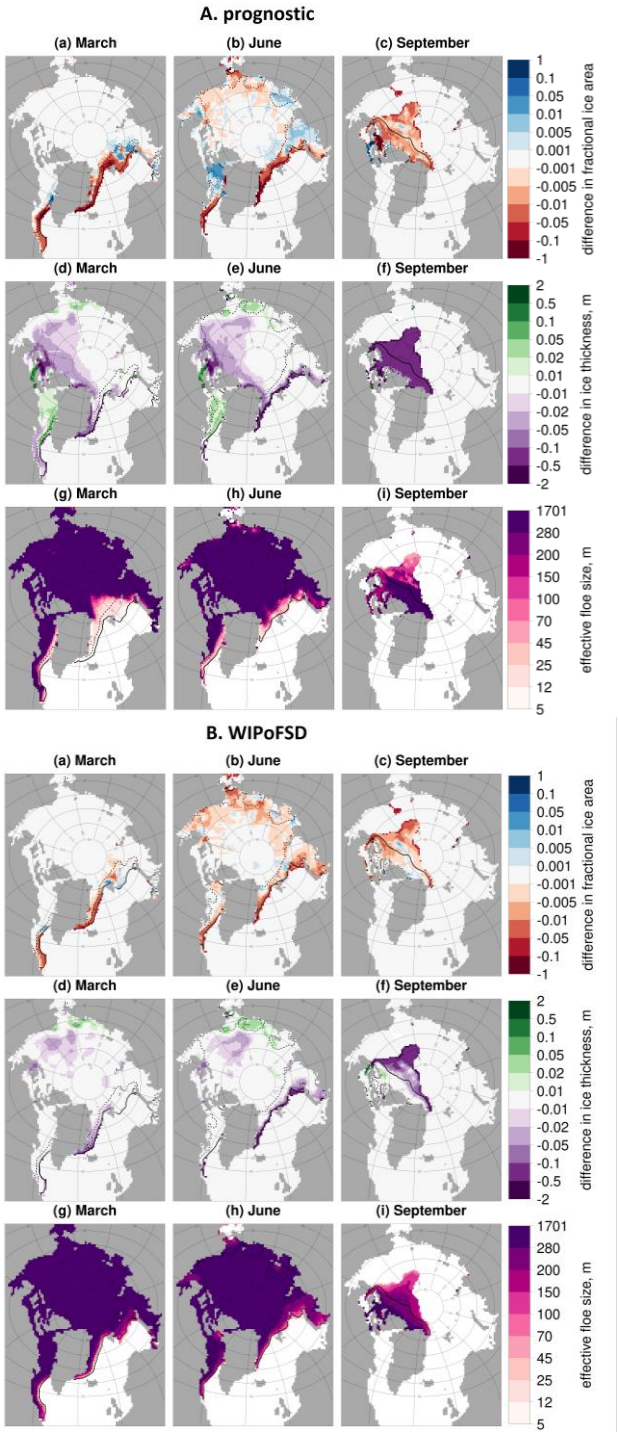

Figure 8.20: Difference in the sea ice concentration (a–c) and thickness (d–f) between *prog-proj* and *ref-proj* (A, top) or *WIPo-proj* and *ref-proj* (B, bottom) and l_{eff} (g–i) for *prog-proj* (A, top) or *WIPo-proj* (B, bottom) averaged over 2050–2060. Results are presented for March (a, d, g), June (b, e, h), and September (c, f, i). Values are shown in locations where the sea ice concentration exceeds 5 %. The inner (dashed black) and outer (solid black) extent of the MIZ averaged over the same period is also shown. In September, large reductions in sea ice thickness can be seen across the extent alongside moderate reductions in concentration for *prog-proj* compared to *ref-proj*. Similar reductions can be seen for *WIPo-proj* compared to *ref-proj* but less extensive across the sea ice.

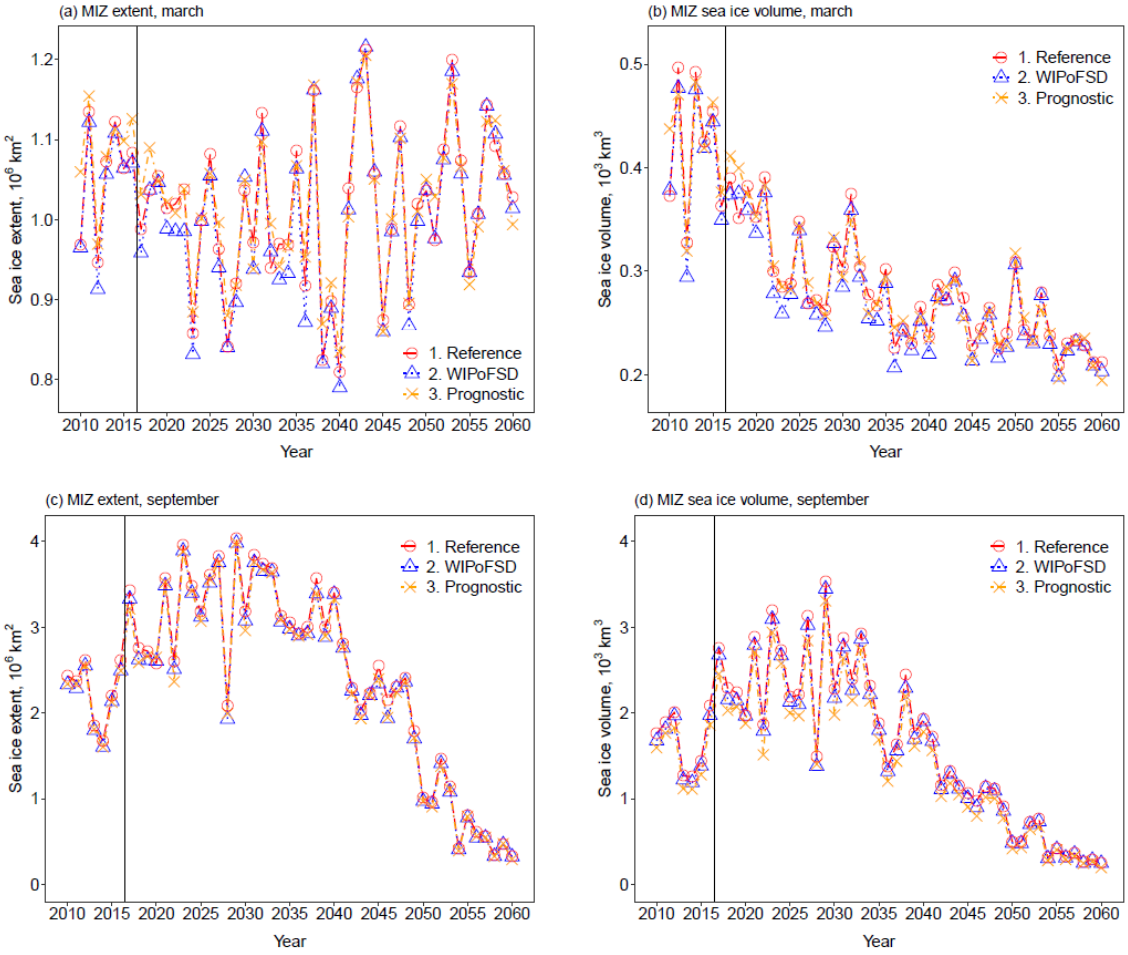

Figure 8.21: The total Arctic MIZ March extent (a, top left), March volume (b, top right), September extent (c, bottom left), and September volume (d, bottom right) over the period 2010 – 2060 for *ref-proj* (red, circles, long dash), *WIPo-proj* (blue, triangles, dotted), and *prog-proj* (yellow, cross, dot-dash). The solid vertical black line separates the hindcast region over 2010 – 2016, using data for *ref*, *WIPo-best*, and *prog-best* respectively, and the projection from 2017 – 2060. The MIZ is here defined as the region with between 15% and 80% sea ice concentration. Differences between the simulations are significantly smaller than the interannual variability in the MIZ extent and volume shown in *ref-proj.*

Figure 8.21 compares the September and March sea ice extent and volume for the MIZ only for each of *ref-proj*, *prog-proj*, and *WIPo-proj* over 2010 – 2060 (using hindcast results from 2010 – 2016). These plots show a very similar trajectory for the MIZ mass balance until 2060, with no clear separation in MIZ evolution between the simulations. There are nevertheless some interesting features e.g. *WIPo-proj* consistently shows the lowest MIZ extent and volume in March until about 2050 where *prog-proj* produces a slightly lower MIZ extent and volume. As an aside, the MIZ September extent and volume both show interesting trends across all three simulations. For all three simulations in September, there is an increase in the MIZ extent from about 2 x 10^6 km^2

over 2010 – 2016 to a maximum of 4 x 10^6 km^2 in 2030. This is followed by a moderate period of decline from 2030 to 2040 and a faster decline from 2040 to a minimum below 0.5 x 10^6 km^2 by 2060. The September MIZ volume shows similar trends with the same timings. Rolph et al. (2020) previously found no evidence in the satellite record from 1979 – 2017 of trends in the September MIZ extent, whereas the simulations here suggest that this lack of trend will not hold under future atmospheric forcing.

The projections performed in this section do have significant caveats, including the use of a fixed ocean climatology. Projected forcing data is also not used for the wave component of the FSD models, though it has been demonstrated here that the cycled use of the 2012 – 2016 reanalysis dataset for wave information is a reasonable approximation. Nevertheless, these results provide valuable information about the changing role of the FSD under a future atmospheric forcing scenario. It has been shown that whilst the inclusion of an FSD model within CICE does not appear to have a significant impact on the long-term trajectory of the Arctic sea ice, the FSD and related processes have been shown to have an increasingly important role in determining the sea ice climatology over the early to mid-21st century. For example, Fig. 8.19 shows that the inclusion of FSD processes reduces the September sea ice volume by an average of about 20 % in the 2050s compared to 5 % in the 2010s.

8.6 Summary of chapter 8

Chapter 8 has presented a series of comparisons between the two FSD models considered within this thesis, the WIPoFSD model and prognostic FSD model. The purpose of this comparison has been to assess if either FSD model improves the ability of CICE to simulate the observed sea ice mass balance. In addition, the comparison allows an assessment of the differences between the two modelling approaches, and whether the features produced by the prognostic model can be replicated using the more constrained WIPoFSD model.

It was not possible to demonstrate unequivocally an improvement to CICE in simulating the observed sea ice extent and volume using either FSD model, though changes to the spatial distribution in sea ice concentration were consistent with known model biases, particularly for the prognostic model. Clear differences were nevertheless found between the models, particularly in terms of the timing of the melt season and long-term trends in the sea ice volume for both March and September. The spatial

distribution of the interannual variability in effective floe size showed a very distinct behaviour between the two models and was suggested as a useful future observational product to assess and discriminate between different FSD models. Regional case studies were used to improve understanding of the difference in the impacts of the two models on CICE, and changes to the lateral melt rate and subsequently the sea ice concentration could be explained by considering the annual evolution of the effective floe size. In the penultimate section, it was shown that simple tuning can reduce the difference in behaviour and impacts of the WIPoFSD and prognostic models, though with the caveat that this may only hold for the present climatology.

Finally, partial projections of the sea ice cover using future atmospheric forcing were performed with the reference run and both FSD models, to explore whether the role of the FSD and specific FSD processes in the evolution of the sea ice cover may change in future. Timeseries of the September and March extent and volume suggested that the simulated general trajectory of sea ice decline over the period 2020 – 2060 was not impacted significantly by the inclusion of either FSD model. However, the projections did suggest that the inclusion of FSD processes will be important for sea ice climatology in the 2050s e.g. the sea ice volume is on average about 20% lower with an FSD model than without. The impact of both the WIPoFSD model and prognostic model on the projected sea ice cover over 2020 – 2060 was comparable, albeit with a generally larger magnitude for the prognostic model. This result does not suggest a significant transition in the relevant processes determining the FSD in the prognostic model under future atmospheric forcing such as an increase in pancake ice formation over nilas ice. These findings all carry the significant caveat that these projections were completed using a standalone sea ice model with future atmospheric forcing data only; projections with a fully coupled atmosphere-sea ice-ocean-surface wave model will be required to validate these findings or otherwise.

The next and final chapter will present a summary of key findings presented in this thesis, alongside a review of the questions posed in chapter 1 to outline how they have been addressed. The chapter will conclude with a discussion of future work to further develop the key themes developed in this thesis.

Chapter 9 – Discussion and conclusions

This thesis has explored the impact of the sea ice floe size distribution on the Arctic sea ice mass balance, with a view to the potential inclusion of FSD models within the sea ice component of fully coupled climate models. In this final chapter, a summary of research findings will be presented before reviewing each of the key questions posed in the introduction to this thesis. These questions will be discussed in turn to describe how they have been addressed and what conclusions can be reached. The final section will consider the research required to develop further understanding of FSD processes and impacts and how best to represent floe size within sea ice and climate models.

9.1. Summary of research findings

The purpose of this thesis has been to discuss the representation of the sea ice floe size distribution, or FSD, within sea ice models. This has included considering both modelling of the FSD and the role of floe size and related processes in influencing the evolution of the Arctic sea ice cover, particularly melting and break-up. Two FSD models have been explored: the WIPoFSD model that assumes the FSD follows a power law, or the prognostic model that allows that shape of the FSD to emerge at process level. Here follows a summary of the key results presented in this thesis.

Setups of both the prognostic model and the WIPoFSD model where parameter choices were selected or new parameterisations introduced to produce the best fit to observations only resulted in small impacts on pan-Arctic metrics such as the sea ice extent and volume, however impacts were more significant on regional or local scales. In addition, the inclusion of FSD processes preferentially reduced sea ice concentration in the MIZ over the pack ice, partially correcting known model biases. Both FSD models demonstrated high sensitivity to parameters within observational constraints. This highlights the need for further observations of both the FSD and related processes, including wave propagation into the sea ice cover, to improve parameterisations, constrain model parameters, and validate FSD model output. The effective floe size, defined as the single floe size with the same floe perimeter density per unit sea area as a given FSD, was introduced as a metric to characterise FSD

model output. It has been demonstrated throughout this thesis that both the spatial distribution and spatial averages of the effective floe size can be very useful to characterise and understand the impacts of both FSD models on the sea ice state.

It has been demonstrated using case studies the challenges of using a model where the shape of the FSD is assumed in some way e.g. assuming the FSD follows a power law. It was shown that the WIPoFSD model can only approximate the impact of advection and lateral melting on the FSD, processes that would otherwise perturb the FSD shape from a power law. It was also demonstrated that the lateral melting parameterisation can be improved by ensuring it accurately calculates the change in the effective floe size from lateral melting. The updated parameterisation was able to capture scenarios where the analytical result showed that the effective floe size would increase in response to lateral melting, which the original parameterisation was unable to do. The new parameterisation remained unable to capture the effects of smaller floes melting out of the distribution because of the use of a fixed minimum floe size cut-off. This demonstrates the challenges in using FSD models that restrict the FSD shape and highlights the need for parameterisations that conserve or accurately calculate the change in key properties such as floe perimeter density.

The contribution of floe edges to sea ice-ocean-atmosphere momentum exchange was investigated using the form drag scheme of Tsamados et al. (2014) that accounts for the shape of the sea ice cover when calculating drag coefficients. The WIPoFSD model was compared to the original Lüpkes scheme as a way to calculate the floe edge contribution to form drag. The Lüpkes scheme produced a significantly larger floe edge contribution to form drag. For the WIPoFSD model the impacts of floe edge contributions to form drag were small to negligible across the sea ice apart from the Greenland Sea, where larger impacts were seen; this region was noted to be particularly exposed to waves. It was suggested that the WIPoFSD case was closer to the truth than the Lüpkes case, since the Lüpkes parameterisation was based on observations of floes taken from locations of high wave activity and a recent observational study found that the Lüpkes scheme significantly overestimated the floe edge contribution to form drag (Brenner et al., 2020).

Brittle fracture impacts on the FSD, both from winter fracture events and summer fragmentation of floes along existing weaknesses, were discussed as a potentially important process in determining the shape of the emergent FSD. It was demonstrated

that including a restoring process in the prognostic model towards the expected fragment distribution of an system acting under brittle fracture was able to significantly improve the performance of the prognostic FSD model in simulating the shape of the distribution for mid-sized floes compared to observations. High sensitivity was demonstrated to the restoring constant in this scheme, highlighting the need for in-situ observations of brittle fracture processes to develop a full physical parameterisation.

A series of sensitivity studies were evaluated using the prognostic model to provide insight into the spatial and temporal variability of the FSD, in particular whether the prognostic model could be used to understand the observed annual cycle in exponent found by Stern et al. (2018b). The sensitivity studies suggested that the observed trend towards a more negative exponent over the melt season was driven by floe break-up processes rather than lateral melt. Similarly, the prognostic model was used to suggest an observed increase in exponent over the freeze-up season can be explained by floes forming in larger floe size categories as nilas ice and the welding of existing smaller floes. A case study was presented of how the prognostic model can be used to constrain WIPoFSD model parameters. In the example considered, it was shown how the use of weaker floe growth restoring within the WIPoFSD model improved the rate of effective floe size increase in winter, taking the prognostic model as a base line. Whilst it is not possible to determine if this prognostic base line is representative of the true behaviour of the FSD without further observations to validate FSD model output, it does demonstrate the potential of the prognostic model to enable the development of low cost but accurate floe size representation in sea ice and climate models.

9.2. Reviewing the research aims

9.2.1. How does the observed sea ice floe size distribution emerge from the constituent processes that affect the FSD?

In chapter 6 the prognostic model of Roach et al. (2018a, 2019) was introduced. This model is a floe size-thickness distribution model that aims to represent each process that can influence floe size in a physically realistic manner such that the shape of the distribution emerges from the model and is not imposed. Processes represented in the prognostic model include floe formation and welding motivated by observations described in Roach et al. (2018b). It was shown that the prognostic setup performed poorly in simulating the shape of the distribution for floes between 100 m – 2 km. In

chapter 7, it was then suggested that the discrepancy between the model and observations could be bridged through the representation of brittle fracture processes. During winter, brittle fracture events can occur frequently in response to both external and internal stresses of the sea ice. Floes can then subsequently weld and freeze back together, but it has been observed that floes can break apart along these existing linear features during the subsequent melt season (Perovich et al., 2001). Idealised brittle fracture models have been found to produce fragment sizes that follow a power-law number distribution with an exponent of -2. This motivated the quasi-restoring brittle fracture scheme introduced in chapter 7, which was shown to significantly improve the shape of the FSD for mid-sized floes.

To understand how power-law behaviour can emerge from the individual processes, a series of sensitivity studies were then completed where each process was either weakened / removed entirely or strengthened. Using these studies, I was able to identify the processes that were important for driving changes in the FSD within the model over different periods of the year for the Arctic environment. Large floes form in winter through the welding together of existing floes and the formation of new floes as nilas sea ice where the ocean surface conditions are calm. Throughout the year, these large floes are broken up either in response to mechanical stress or through melting along existing floe cracks and linear features that are often created by winter brittle fracture events. The power-law behaviour of the FSD is then attributed to these brittle fracture derived behaviours of the sea ice. The precise exponent is determined by the balance of processes, with a higher or less negative exponent representing a shallower negative slope in the floe number distribution with increasing floe size, and a lower or more negative exponent representing a steeper negative slope. A less negative exponent during winter and early spring is driven by welding together of floes and new floes forming as nilas ice, and a more negative exponent in summer is driven by break-up of larger floes by waves and melting apart, with the latter represented in the prognostic model using the brittle fracture scheme. Lateral melting, whilst seemingly not important for the overall power law like behaviour seen in observations, acts to selectively melt out smaller floes both causing a perturbation from power-law behaviour for these smaller floes, and causing an increase in the power-law exponent, where a power law can still be reasonably fitted.

This broad framework is generally consistent with several different observations of the spatial and temporal variability in the FSD power-law exponent. Kergomard (1989) for

the Fram Strait in June and Inoue et al. (2004) for the Sea of Okhotsk in February both find that the exponent becomes more negative as the sea ice edge is approached, indicating that the ratio of smaller to larger floes is increasing. This is consistent with the increased influence of wave break-up of floes at edge locations. Both Stern et al. (2018b) for the Beaufort and Chukchi Seas, and Perovich and Jones (2014) for the Beaufort Sea report a transition to a more negative exponent over the melting season from June to August. The former only considers floes larger than 2 km, but Perovich and Jones (2014) report this behaviour for floes from 10 m to 10 km. This is again consistent with a regime where the main control on the exponent is the break-up and fracture of floes rather than where lateral melting dominates and preferentially melts out smaller floes, which would drive a positive trend in the exponent over the melt season. Some studies report a change to a more negative exponent from smaller to larger floes e.g. Toyota et al. (2006) in the Sea of Okhotsk and Geise et al. (2016) in the East Siberian Sea, though Stern et al. (2018a) points out this effect may at least be partly an artefact of plotting the FSD as a cumulative distribution.

In chapter 7, Fig. 7.12 suggests that where floes primarily form as pancake ice, the FSD is dominated by small floes with floes of all other sizes contributing very little to the total perimeter density. Figure 7.14 then shows that if pancake ice dominates the FSD there are significant implications for the sea ice mass balance, with the August sea ice volume dropping over 30 %. There is some evidence of this kind of regime existing within the Antarctic, for example Toyota et al. (2011) report an FSD exponent for the Weddell Sea in September and October of about -2 to -2.5 for floes smaller than 40 m but -4.2 to -8.6 for floes larger than 40 m, i.e. the FSD is dominated by smaller floes. Steer et al. (2008) find a similar result with an FSD exponent of -1.9 for floes below 20 m and -2.8 to -3.4 for floes above 20 m. Alberello et al. (2019) report a particularly pronounced example, with 50 % of the sea ice area attributed to floes of between 2.3 m and 4 m. The FSD observations for this study were ship-based observations collected within the Antarctic in 2017.

The prognostic FSD model still requires further development and validation using observations, particularly in terms of the representation of brittle fracture and other floe break-up processes. Nevertheless, the current model framework can explain key observed behaviours in the spatial and temporal variation of the FSD. This provides some confidence that the model description of how a power-law or power-law-like FSD shape emerges from individual processes also holds for real systems.

9.2.2. How does the FSD change the seasonal retreat of the Arctic sea ice cover?

One of the more notable impacts of the FSD on the sea ice cover is the changes to the sea ice melt partitioning. The increase in lateral melt from the inclusion of an FSD model results in a compensating reduction in the basal melt, which has been shown through Figs 3.4 and 3.5 to be mostly caused by a reduction in the available sea ice basal surface area for basal melt. The same compensation effect can be demonstrated using different model parameters e.g. with a more negative exponent, as shown in Fig. 3.7, and is also found with the prognostic model in Fig. 8.6. Figure 3.4 also shows, however, that the total increase in melt is small. This means that whilst the total reduction in sea ice volume over the melt season is similar for simulations with and without the FSD model, an increased proportion is associated with a reduction in the sea ice concentration rather than the sea ice thickness. The basal melt volume for a given area of sea ice is relatively independent of thickness (the conduction flux is proportional to the inverse of the thickness), provided the total length of vertical melt is less than the total thickness of the sea ice. In comparison, the lateral melt volume for a particular area of sea ice is proportional to vertical thickness i.e. a higher lateral melt rate increases the relative contribution of thicker floes to the total melt. Basal melt primarily drives the loss of thin sea ice area whereas lateral melt reduces the area of thinner and thicker sea ice equally, assuming the shape of the FSD does not vary significantly for different floe thicknesses. Therefore, an increase in the total lateral melt and reduction in the total basal melt has the effect of preserving thinner sea ice within the thickness distribution at the expense of thicker ice. This means that the mean sea ice thickness decreases both over the course of a melting season and with effects lasting over several melt seasons. This leads to the reductions in the MIZ mean sea ice thickness shown in Figs 3.6 and 8.7 in response to the inclusion of an FSD model. These figures also show that for both the prognostic model and the WIPoFSD model, reductions in the sea ice volume are generally seen within the MIZ, particularly along the 30% sea ice concentration isopleth, with smaller reductions or even increases in total volume seen within the pack ice. Therefore, another impact of including FSD processes in sea ice models appears to be a further reduced role for pack sea ice in contributing to the total volume loss during a melt season, with melt rates preferentially enhanced within the MIZ.

Another change is the magnitude of the retreat in the sea ice cover during the early melt season. In chapter 8 it was found that including the prognostic model within CICE produced a strong response in the earlier melt season due to the presence of many small floes in the distribution. As these floes melted out of the distribution l_{eff} increased, reducing the lateral melt rate per unit sea ice area. l_{eff} for the WIPoFSD model either decreased or remained low throughout the melt season due to the restrictions in using a fixed shape distribution. This leads to the behaviours seen in Figs 8.4 and 8.7 that show a faster retreat in the sea ice extent during the earlier melt season for the prognostic model compared to the WIPoFSD model, but by the late melt season both simulations had a similar net reduction in the sea ice extent. In the prognostic model, fragmentation and break-up of floes over winter effectively conditions the sea ice cover to retreat more rapidly during the early melt season but this effect then is not sustained throughout the melt season. A possible consequence of both the faster initial retreat in sea ice extent and the general overall reduction in MIZ sea ice concentration is a stronger aggregated albedo feedback effect, but the limited increase in the total sea ice melt shown in Fig. 8.6 does not indicate the presence of a strengthened albedo feedback. It is possible that the short temperature restoring timescale of 5 days used for the mixed-layer model significantly limits the impact of the albedo feedback mechanism, since any temperature changes in the surface mixed layer associated with the increased input of shortwave solar radiation will be opposed by a strong restoring back to climatology.

In chapter 5 the interaction between floes and the momentum and heat exchange between the sea ice, atmosphere, and ocean was investigated using the form drag scheme of Tsamados et al. (2014) with the WIPoFSD model. Here it was found that the overall impact of using l_{eff} within the form drag scheme rather than a fixed size of 300 m on the total sea ice volume and extent was small, but there were larger localised impacts within the Greenland Sea during March and June. A similar experiment using the prognostic model produced larger differences in the March and June sea ice concentration and thickness within the MIZ, but the signs of these differences alternated across small spatial scales. In addition, the differences in September were close to negligible. This again indicates that whilst form drag and the FSD might interact to redistribute sea ice volume within the MIZ during the early melt season, the results presented here do not suggest that these interactions have a significant role in the seasonal retreat of the sea ice.

As mentioned above, a significant caveat to the above conclusions is the use of a standalone sea ice model rather than a fully coupled sea ice-ocean-atmosphere setup. As discussed above, whilst the mixed-layer ocean model allows an investigation into feedbacks between floe size and the surface mixed layer that operate over shorter time scales, feedback processes that operate over long timescales e.g. higher ocean heat content by the late melting season due to the faster initial retreat of sea ice, cannot be represented. There are also potentially important feedbacks with the atmosphere that might enhance or diminish the impacts of the floe size distribution. For example, cloud radiative feedbacks can occur due to changes in cloud formation processes associated with the increased surface heat and moisture fluxes and perturbed radiative balance at the surface. However, recent research suggests that whilst global cloud feedbacks have a significant impact on radiative forcing at the surface, Arctic cloud feedbacks have a negligible impact (Middlemas et al., 2020). Similarly, increases in moisture concentration in the lower troposphere associated with the increased ocean to atmosphere moisture flux from lower sea ice concentration can enhance surface warming via the water vapour and lapse rate feedbacks (Boisvert et al., 2015; Goosse et al., 2018). Fully coupled simulations will be required to properly evaluate the strength of each of these sea ice-atmosphere feedbacks associated with the inclusion of an FSD model into CICE.

9.2.3. How does inclusion of the FSD impact the overall Arctic sea ice mass balance?

Chapter 8 compared the impact of both the WIPoFSD and prognostic FSD models using setups optimised against observations of the FSD. The impact of each model was a moderate reduction in the sea ice mass balance of up to 4 % in September compared to the reference state with a fixed floe size of 300 m. The size of this impact is strongly dependent on the setups used for each model and varies over the annual cycle, with differences generally peaking over August to September with small to negligible changes over the winter to early spring period of November to March. The source of this reduction in the sea ice mass balance is different between the two FSD models. Fig. 8.4 shows that the reduction in sea ice extent can explain a greater proportion of the volume loss for the WIPoFSD model than the prognostic model; for the latter case a larger proportion of the volume loss can be attributed to a reduction in the sea ice thickness.

In chapter 3, a series of sensitivity studies were evaluated using different choices for the lower and upper floe size cut-offs and the exponent of the fitted power-law FSD. The set of values selected for each parameter were within the ranges seen for observations of the FSD, and yet the impacts spanned a huge range from a 2 % increase to over a 50 % reduction in the mean September sea ice volume. It was demonstrated in chapter 3 that the mean l_{eff} showed a strong correlation to the percentage reduction in volume for a given simulation, demonstrating the potential value of this characterising metric for estimating the likely impact of an observed FSD on the sea ice mass balance. Two sensitivity studies were also explored to investigate the possible impact of a variable exponent, one that evolves on a fixed annual cycle and one that is determined from the local sea ice concentration. Both approaches used values constrained from the observations of Stern et al. (2018b). The study using an annual cycle to vary the exponent produced very little change in the sea ice mass balance, but the case using the local sea ice concentration to determine the exponent produced a 5 % reduction in the mean September sea ice extent. Here l_{eff} was found to be less accurate as a predictor of the total change in the sea ice mass balance compared to cases with a fixed exponent.

In chapter 7, sensitivity studies were performed to establish the importance of individual processes represented in the prognostic model on the total sea ice mass balance. These studies show a similar result to chapter 3 i.e. that whilst in its current formulation the prognostic model produces a moderate reduction in the sea ice volume of up to 4 %, there are formulations where these differences are either much smaller e.g. without the brittle fracture scheme, and formulations where the reduction in the sea ice volume can exceed 30 % e.g. where all new floes form as pancakes. In each case, the impacts of each change to the prognostic model can generally be understood through changes to the spatial distribution in l_{eff}, again demonstrating the value of this metric in understanding how the FSD is likely to impact the sea ice mass balance. The impact of the FSD on sea ice volume also shows reasonable sensitivity to wave break-up, welding, and lateral melt, but the largest sensitivities are found with the new floe formation and brittle fracture schemes. Both schemes are associated with significant uncertainties. The determination of the size of newly forming floes relies on accurate representation of wave propagation into the sea ice cover, whereas the wave treatment used in chapter 7 for the prognostic model adopts an approach of projecting wave properties from outside the sea ice cover rather than using an explicit wave advection

model. In addition, the treatment of waves that are generated internally within the sea ice cover e.g. within leads, is entirely neglected. A significant limitation of the treatment of waves within both FSD models considered in this thesis is the assumption that linear wave theory applies. Observations of storm-induced wave events suggest this assumption may significantly underestimate the distance of wave propagation into the sea ice cover (Kohout et al., 2014). The brittle fracture scheme is currently a quasi-restoring approach towards the fragment shape distribution expected for a system acting purely under brittle fracture. The strength of the restoring has been determined based on physical considerations, but nevertheless it represents a complex set of processes with different mechanisms in winter (through direct brittle fracture events) and summer (break-up of floes along existing linear features from prior fracture events).

9.2.4. Does the inclusion of an FSD model improve the simulated sea ice mass balance compared to observations?

This question was the key focus of Sect. 8.2 in chapter 8, where it was not possible to demonstrate unequivocally that the inclusion of an FSD model in simulations of the Arctic sea ice was able to correct existing model biases. This assessment included simulating both the absolute values, long term trends, and the interannual variability in the sea ice extent and volume. In addition, model output was also compared against observations of the MIZ and pack ice extent in both March and September, however large discrepancies between the two observational products prevented a useful assessment being made of the performance of the different simulations. It was suggested based on qualitative evidence that the inclusion of the prognostic FSD model or, to a lesser extent, the WIPoFSD model in CICE simulations does partially correct known model biases where the sea ice concentration is underestimated in the pack ice and overestimated in the MIZ. A more complete quantitative comparison was not performed here due to the significant uncertainties associated with the satellite derived sea ice concentration data.

Even if the inclusion of an FSD does not produce a marked improvement in simulating the sea ice mass balance, this does not necessarily mean FSD processes should be excluded from Arctic sea ice or climate models. Firstly, as discussed in Sect. 8.5, relevant sea ice processes over the current climatology do not necessarily remain relevant for a future climatology and vice versa. If the Arctic sea ice transitions to a

state where pancake ice becomes a more dominant form of newly formed sea ice over nilas ice, a representation of the FSD in the sea ice model will be required to capture the transition between these different states. In addition, this thesis has only explored FSD processes in respect to the impact on lateral melting and momentum and heat exchange between the sea ice, ocean, and atmosphere. There are further FSD-sea ice interactions that have not been considered here that may be more important for the large-scale evolution of sea ice e.g. the interaction between floe size and sea ice rheology (Rynders, 2017) or the impact of a heterogenous sea ice-ocean surface on the atmospheric boundary layer (Wenta and Herman, 2019). Finally, whilst it has not been successfully shown that the FSD is relevant to the sea ice climate, it has been shown to be relevant to the sea ice weather. Short-term projections of the sea ice are used by shipping companies to estimate navigable shipping routes in the subsequent few days or weeks. As shown in Fig. 8.7, the inclusion of the FSD can cause reductions in the sea ice thickness of orders of 10s of cm within the MIZ, which could impact whether a given ship can safely traverse this region. Similarly, Figs 8.19 and 8.20 suggest that FSD processes will have a significant impact on the sea ice climatology in the mid-21st century and their inclusion within models may therefore be important for predicting the future viability of shipping routes through the central Arctic.

9.2.5. What are the advantages and disadvantages of different approaches to representing the FSD in sea ice models? Is there an 'optimal' approach to modelling the sea ice floe size distribution?

In chapter 2, an overview was presented of the different approaches in the literature to modelling the FSD. These were subdivided into two broad categories: one where the shape of the FSD was imposed or restricted in some way; and one where the shape of the FSD emerges from parameterisations at the process level. The two FSD models investigated in this thesis, the WIPoFSD model and the prognostic FSD model, were selected as representatives of these two paradigms. Whilst this thesis has demonstrated that neither of these models should be taken as complete, with important processes missing from the prognostic model and significant uncertainties remaining in the WIPoFSD model parameters, they are still good representatives to consider the advantages and disadvantages of each modelling paradigm.

For the WIPoFSD model, one of the key advantages is that it is simple. It is significantly easier to identify and constrain the mechanisms that cause an observed impact on the

sea ice state. In chapter 6 it was found that a power law was able to produce a strong fit to observations of floes over a mid-sized (100 m – 2 km) range. The prognostic model was unable to produce as strong a fit to these observations, even when incorporating the brittle fracture scheme introduced in chapter 7. In addition, the simplicity of the WIPoFSD model limits the computational expense of the inclusion of FSD processes. The inclusion of the WIPoFSD model within CICE currently changes the model run time by a factor of 1.3, but the wave advection and attenuation scheme is the most intensive component of the WIPoFSD model. Sea ice model setups with a pre-existing wave advection and attenuation component included would avoid this additional expense (see Roach et al., 2019). Alternatively, it may be possible to approximate the ocean surface state based on local variables such as wind speed, sea ice concentration, and the distance to the sea ice edge, using a similar method to Zhang et al. (2016). There are several key disadvantages to the WIPoFSD model, however. There is growing evidence that the power law may not hold across all floe sizes (Horvat et al., 2019). In addition, as discussed in chapters 4 and 8, it is not possible to properly represent the impact of processes such as lateral melting that perturb the distribution away from a power-law state. It has been shown in chapter 8 that through a simple change to a model tuning parameter, the floe size restoring rate in freezing conditions, the WIPoFSD model can better capture the features and impacts of the prognostic model. There is also good evidence from multiple studies that the exponent changes significantly over an annual cycle (Stern et al., 2018b). In chapter 3, it was found that imposing the annual cycle reported by Stern et al. (2018b) on the exponent only had a small impact on the sea ice state. The annual cycle investigated in chapter 3 was taken as the mean value of exponents reported only from the Chukchi and Beaufort Seas, so it is not sufficient evidence to conclude that a fixed exponent is a reasonable assumption. Finally, the WIPoFSD model effectively operates by tuning the model parameters to best capture observations of the FSD, however this assumes that this tuning will hold over the timescale of a simulation. It has previously been discussed that the processes that determine the FSD in the Arctic may change significantly in the future e.g. a transition to increased pancake ice formation rather than nilas ice, and the WIPoFSD model is not well suited to represent such a transition. It should be noted that the prognostic model can represent both pancake and nilas ice growth (see section 6.2.3 for further details) and is therefore capable of capturing such a transition provided waves within the sea ice cover are accurately simulated. However, the projections completed in Sect. 9.1 show no evidence of this transition, with both the

prognostic and WIPoFSD models showing comparable trends in the September sea ice volume relative to the reference case with a fixed floe size.

The prognostic FSD model addresses several of the limitations of the WIPoFSD model in terms of necessary model assumptions. As the shape of the FSD is an emergent feature of the model rather than imposed, it does not require any assumptions about the variability in the exponent. Physical processes can be represented through their impact on floe size at the floe scale rather than a parametrisation to calculate the collective impact on the whole distribution. This means the prognostic model can be used to understand the role of individual processes in determining the emergent FSD, as shown in chapter 7, and can respond to future changes in the behaviour or strength of these processes. Whilst this aspect has not been considered in much detail in this thesis, the prognostic model incorporates both a floe size and thickness distribution and can also represent interactions between these two distributions e.g. the differential impact of a wave break-up event on floes of different thicknesses. The prognostic approach has several disadvantages, however. In particular, the model comes with significant computational expense and is data intensive. The use of 12 floe size categories with the standard 5 thickness categories introduces a total of 60 floe size-thickness outputs to the model and simulation times increase by a factor of 2.1. Extending this to 16 floe size categories leads to a total of 80 categories and further increases to the simulation run time. The number of floe size-thickness categories can also make it difficult to diagnose and understand how changes to the sea ice state emerge in response to prognostic model processes. These problems scale up moving from a standalone sea ice model to a fully coupled climate model, where model efficiency in both time and data is particularly important. In addition, as the shape of the distribution is not imposed, the prognostic model can only produce a physically realistic distribution if all relevant processes are included in the model. Each process requires either observations or lab-based studies to identify the mechanism that changes the size of floes and then determine the necessary parameterisation and associated parameters to describe the physical process in the model.

The ‘optimal’ approach to representing the sea ice floe size distribution inevitably depends on the application. Efforts to develop high resolution short-term forecasts of sea ice will need a very different level of detail to climate models aiming to understand what the climate will look like by 2100. A good starting point here is to address the needs of the UK Met Office, mentioned in the introduction. The Met Office operates

using its Unified Model (UM), which in practice means using the same dynamical core and parameterisations where possible across different spatial and temporal scales. This includes the HadGEM3 family of models, operating over global spatial scales and decadal to centennial timescales. These models are already very bulky, and simulations can take several weeks to complete. Efficiency in both computational power and data is therefore very important. It needs to be demonstrated that any new physical process produces a significant improvement in model performance with respect to observations or at the very least can be shown to be a potentially important component in the evolution of the future climate. Based on the results presented in chapter 8, neither the prognostic FSD model nor the WIPoFSD model have demonstrated that they meet either of these criteria to a sufficient degree. The impact of either FSD model on the present sea ice state is much smaller than the difference between the reference CICE state and observations. The inclusion of either FSD model in projections of the Arctic sea ice does not either extend or shorten the time period before an ice-free summer Arctic is reached. At best, a simple model where l_{eff} is parametrised from other local sea ice properties e.g. sea ice concentration, would be justified. This approach would be able to represent the observations of a more fragmented sea ice cover towards the sea ice edge, resulting in a higher lateral to basal melt ratio in these regions at small computational cost.

There are limits to this conclusion. Firstly, there are several limitations with the model setups used within this thesis, for example both FSD models use a simplified representation of waves, the mixed-layer model uses a high restoring rate for temperature and salinity, and the projections only consider sea ice response to the future atmospheric forcing. In addition, whilst the Antarctic has not been a focus of this thesis, it is worth noting that there is evidence that the inclusion of FSD processes may be significantly more important for the evolution and seasonal cycle in Antarctic sea ice cover. Several observational studies have been mentioned e.g. Alberello et al. (2019), that show the presence of FSDs dominated by pancake ice floes smaller than 10 m. As shown in several sensitivity studies, both in chapter 3 and chapter 7, distributions dominated by such small floes can dramatically reduce the sea ice mass balance. Hence, whilst FSD processes appear to be a minor component to the evolution of the Arctic sea ice, for the Antarctic sea ice this conclusion does not necessarily hold. Roach et al. (2019) apply a version of the prognostic model to both the Arctic and Antarctic (including a coupled wave model but not the brittle fracture scheme) and

demonstrate a pan-Antarctic reduction in sea ice volume whereas in the Arctic there are regions of volume increase and decrease, with the latter found primarily in the MIZ.

In addition, whilst the inclusion of an FSD model for the Arctic sea ice may not be suitable within global, decadal climate simulations, there are many other applications of sea ice models where it may have more importance. For example, the ECMWF (European Centre for Medium-Range Weather Forecasts) have found that their forecasts of sea ice concentration are used for operational use e.g. by shipping companies (Johnson et al., 2019). For such users knowing the local and regional state of the sea ice, including the thickness and how fractured it is, can determine whether a route can be safely traversed. It is expected that as a higher proportion of the sea ice cover becomes marginal in the next decades, the sea ice 'fragmentation' state i.e. the floe size distribution, will become a prevailing factor in Arctic navigation (Aksenov et al., 2017). For this application the prognostic FSD model would be a suitable choice to include in forecast models for operational purposes in order to provide detailed information about the size and thickness of floes. Sea ice thickness is also a metric of interest to Arctic ecologists because thinning sea ice and an increase in melt ponds has been observed to produce algal blooms (Arrigo et al., 2012). It has been previously demonstrated that sea ice models can be used to understand and predict transmission of solar radiation to the ocean surface layer in order to better understand the formation of these blooms (Horvat et al., 2017). The sea ice concentration and thickness are both important factors in determining the solar radiation that reaches the ocean surface layers. Both FSD models have been shown to cause significant changes to the spatial distribution of these metrics both under the current climatology (Fig. 8.7) and future atmospheric forcing (Fig. 8.20).

9.2.6. Limitations in the conclusions reached

Whilst there has been some discussion in the limitations of the conclusions reached in this chapter due to constraints in the model setup and observational uncertainty, it is useful to provide a more complete overview and discussion of these limitations and what their implications are for the findings presented here.

A significant source of uncertainty is associated with high sensitivity to poorly resolved parameters. Whilst the parameters selected for the standard setup of the WIPoFSD model considered in chapters 3 - 5 and 8 were motivated as a best fit to observations,

chapter 3 demonstrates high sensitivity in the model response within the observational uncertainty of these parameters, particularly the exponent and lower floe size limit of the power law. The choice of a fixed exponent that does not evolve spatially or temporally is also a significant assumption, with particularly strong evidence available of an annual cycle in the exponent (Stern et al., 2018b). For the prognostic model, the uncertainties are primarily associated with potentially important processes currently missing in the model. The parameterisations of processes currently represented in the prognostic model have been developed either from basic physical principles e.g. lateral melting and growth (Horvat et al., 2015) or derived from observations e.g. floe welding (Roach et al., 2018b).

The quasi-restoring brittle fracture scheme introduced in chapter 7 is also motivated by both observations and an idealised model of a system acting under brittle fracture, however the scheme remains a very simplified representation of the processes it aims to describe, in particular using a fixed restoring rate throughout the year. The scheme represents both winter brittle fracture events, which occur over much shorter timescales than the CICE model timestep, and the separation of floes along existing cracks and fractures as a result of melt-induced weakening and thinning along these cracks, which occurs over timescales of weeks. Given the prognostic model aims to represent the FSD with high physical fidelity, the model should be able to treat these brittle fracture processes independently, with fracture rates calculated as a function of relevant parameters including local strain rate, melt pond fraction, and melt rates. In addition, a fracture distribution should be calculated from these floe breakup events, rather than assuming that floes adopt the size of the adjacent smaller category after breakup. As with previous parameterisations introduced into the prognostic model, the combination of physical theory with in-situ observations of floes will enable the improved representation of the brittle fracture model within CICE. Observations tracking the evolution of clusters of floes, as previously demonstrated by Hwang et al. (2017), would be particularly helpful in the development of such parameterisations, as they should allow the observation of individual floe break-up events and the state of the sea ice, ocean, and atmosphere prior to these events. The continued production of satellite-derived FSD snapshots (e.g. Stern et al., 2018b) in addition to the application of novel ways of characterising floe size on a pan-Arctic scale demonstrated in Horvat et al. (2019) to higher resolution satellite data should enable a more complete validation of prognostic model output. The combination of these further observations, in

addition to insight gained from the prognostic model, will then enable better constraining of parameters for the WIPoFSD model, including whether a fixed exponent is a sensible assumption.

Another significant uncertainty is associated with the representation of waves in the model setups used. Roach et al. (2019) demonstrated that using a full wave model coupled to CICE rather than the internal wave scheme approximately doubled the total lateral melt, though this was compensated by a reduction in basal melt of comparable magnitude. Another caveat with the approach used for wave modelling in both the FSD models considered here is potential feedbacks between sea ice extent and wave climatology cannot be captured, for example the positive feedback mechanism of wave action reducing the sea ice extent, therefore increasing the potential fetch distance for subsequent waves.

The use of a standalone sea ice model prevents the full representation of sea ice-ocean or sea ice-atmosphere feedbacks, whether positive or negative. Whilst the use of a mixed-layer model allows the representation of short-term feedbacks between the sea ice and ocean, the high restoring rate for temperature and salinity prohibits any feedbacks that operate over long timescales e.g. delayed ocean freeze-up due to an increase in the ocean heat content. Referring again to Roach et al. (2019), a coupled CICE-NEMO setup showed the increase in lateral melt in the Arctic from including their prognostic FSD model setup was about 3-4 times higher than the reduction in basal melt, resulting in an approximately 20% increase in the total lateral and basal melt, whereas standalone CICE simulations considered both in this thesis and Roach et al. (2019) generally show the vast majority of the increase in lateral melt is compensated by a reduction in basal melt. This result suggests the presence of important FSD-ocean feedbacks that enhance the total sea ice melt in the coupled CICE-NEMO setup that are not present in standalone CICE with a prognostic mixed layer model, though the precise mechanism of this feedback cannot be determined from the results presented in Roach et al. (2019).

The standalone CICE setup used here is similarly unable to represent fully any atmosphere-sea ice feedback processes that may be influence by the inclusion of an FSD model. It was discussed in Sect. 9.2.2 how increases in the heat and moisture flux across the ocean-atmosphere interface due to reductions in sea ice concentration can perturb several feedback processes such as the lapse rate, cloud, and moisture

feedbacks, though simulations completed using a fully coupled sea ice-ocean-atmosphere will be required in order to properly assess how much the inclusion of an FSD model perturbs any feedbacks with the atmosphere. In addition to these large-scale feedbacks, the spatial distribution, size, and separation of floes can also influence convective structures in the ABL, or atmospheric boundary layer (Wenta and Herman, 2019). This presents an additional FSD influence on sea ice-atmosphere feedbacks, and also suggests the FSD can have a direct impact on ABL structure and stability. Current coupled sea ice-atmosphere model setups are unable to represent the impact of the surface distribution of ice on ABL structure, though a parameterisation is in development (Wenta and Herman, 2019). It has yet to be demonstrated that the size of any FSD impact on the atmosphere or sea ice-atmosphere feedbacks is significant relative to the intrinsic chaos of the atmosphere. Given the small direct impact of either FSD model with standard parameters on the sea ice extent and volume, as shown in Fig. 8.4, it seems unlikely that any changes to surface fluxes will be sufficiently large to significantly perturb any feedback processes, but larger impacts could result from the more extreme parameter choices. In addition, Wenta and Herman (2019) suggest that including the impact of the surface distribution of floes and open ocean on ABL structure will have a significant effect on area-averaged fluxes over the sea ice-ocean-atmosphere interface with a high potential to correct known inaccuracies in regional and global weather and climate models.

9.3. Future research directions

A leading uncertainty, already highlighted in Sect. 9.2, are interactions between the ocean and FSD processes. The simulations in this thesis use an ocean climatology from 1993 – 2010 and high salinity and temperature restoring within the mixed-layer model. This setup is not well designed to fully capture any ocean feedbacks with the FSD, especially over longer timescales. Hence an obvious next step is to perform either coupled sea ice-ocean simulations or fully coupled climate simulations including the two FSD models, to identify whether FSD-ocean interactions change the conclusions regarding the importance of the FSD in understanding the present and future state of the Arctic sea ice. An important part of such simulations will be the inclusion of known additional sea ice-ocean or sea ice-atmosphere processes that floes can influence or be influenced by, either directly or indirectly, that have not been explicitly considered in this thesis: lateral melt driven eddies within the surface mixed

layer, which may significantly change the relationship between lateral melt volume and floe size (Horvat et al., 2016); the inclusion of wave mixing impacts on the surface ocean (Rynders, 2017); wave generation within leads and polynyas (Jardon et al., 2011); and fully coupled atmosphere-waves-ocean-sea ice momentum and heat exchange (Johnson et al., 2019) mediated by floes (Tsamados et al., 2014).

In chapter 7 the quasi-restoring brittle fracture scheme was introduced to the prognostic FSD model. This scheme aimed to represent two related processes: brittle fracture of the sea ice mostly in winter months; and melting and break-up along existing fractures and weaknesses in the sea ice mostly in the summer months. The scheme involves a partial restoring to a power law with an exponent of -2, the shape of the fragment distribution predicted by idealised models of brittle fracture (Gherardi and Lagomarsino, 2015). In the context of this thesis, this was a simple approach to improve the prognostic model performance compared to observations of the FSD for mid-sized floes. The potential importance of brittle fracture in simulating a realistic FSD shape and the high sensitivity of the sea ice state to the restoring rate, as indicated in Fig. 7.20, highlights the need to develop a physical representation of brittle fracture and associated processes within the prognostic model to replace the simple quasi-restoring scheme used here.

In Sect. 9.2.5, several additional applications of FSD models were mentioned, including the use of an FSD model for short term forecasts of the sea ice and to better predict impacts of sea ice on biogeochemistry. These ideas can be developed further by exploring whether the FSD can drive changes to the sea ice state over short timescales within high resolution sea ice models. This approach will allow an assessment of whether the inclusion of FSD processes in forecasting models will provide additional value to operational users of these products. Furthermore, information regarding the state of the FSD in itself can be useful to operational users of sea ice forecasts. Sea ice charts, which use observations of the sea ice to produce a best estimate of the current sea ice state, present information about the sea ice using a standardised ‘egg code’ (Dedrick et al., 2001). This egg code includes information about the sea ice concentration, thickness, and representative floe size to provide detailed information regarding the state of the sea ice in an easy to interpret format. It would be valuable for operational users to produce sea ice forecasts that incorporate these egg codes, but in order to do so some form of floe size treatment in the sea ice model is required (Rynders, 2017). The sea ice projections outlined in section 8.5 can also be developed

and used to identify if the thinning produced by the inclusion of FSD models would change the magnitude and frequency of future algal blooms.

In this thesis, interactions between the FSD and sea ice were considered in two ways, lateral melting and form drag. There are additional interactions that have not been considered here including the impact of floe size on sea ice rheology. Feltham (2005) developed and solved a series of equations to describe the role of floe collisions on sea ice rheology using techniques from granular fluid dynamics. Feltham found that ice jets, observed rapid flows of ice parallel to the ice edge, are an emergent process from this mathematical description. One important parameter in determining the extent of granular behaviour in the sea ice is floe size. Feltham's scheme was subsequently implemented into a coupled NEMO-CICE setup by Rynders (2017) as a combined collisional-EVP rheology to apply across the sea ice cover. In this work, the floe size was represented as the mean floe size calculated using a precursor version of the WIPoFSD model (a description of the FSD model used by Rynders is included in Sect. 2.3). This work could be extended by comparing the impacts of this composite rheology when using either the prognostic or WIPoFSD model to calculate the floe size metric used to evaluate both the collisional component of the rheology and the granular temperature (the variable that enables the use of both EVP and collisional rheology without requiring discontinuous boundaries in the sea ice cover between where the different schemes apply). Rynders (2017) also noted that the composite rheology assumes that all floes have an equal size, but it has been demonstrated using a binary distribution of small and large floes that the granular temperature used within the scheme is strongly sensitive to the shape of the FSD (Lu et al., 1989). The adaptation of the composite collisional-EVP rheology to consider a full FSD rather than an average floe size metric may also prove to be an important step forward in understanding the role of the FSD in the evolution of the Arctic sea ice.

Finally, this thesis highlights the need to collect further observations of the sea ice floe size distribution. l_{eff} has been shown to be a useful metric to characterise the FSD and its impact on the sea ice mass balance. Horvat et al. (2019) have demonstrated that it is possible to estimate the area-weighted floe size from satellite imagery, hence it seems plausible that l_{eff} could be reported alongside this metric to provide additional information about the state of the FSD. It would also be possible to estimate l_{eff} for a given distribution by calculating the total perimeter and area of the constituent sea ice

floes, providing a simple way to report l_{eff} for high resolution imagery where individual floes can be distinguished. The ability to measure l_{eff} from satellite imagery would present a way to establish the spatial and temporal variability of the FSD. These observations can then provide further constraints for FSD models e.g. Fig. 8.8 has already demonstrated that the interannual variability of l_{eff} can be used to discriminate between different FSD models.

Hwang et al. (2017) demonstrated how the combined use of satellite observations of floes and data collected in-situ using buoys can produce insights about floe evolution. The extension of this methodology to more floe clusters over longer periods of time offers significant potential to characterise floe evolution and break-up. The production of high-resolution aerial photography over weekly intervals would enable the tracking of individual floes with high temporal resolution. Buoys can also be used to collect data about the atmosphere, ocean, and sea ice state including weather conditions, the sea ice mass balance, and temperature profiles through the sea ice and surface ocean. For example, GNSS/INS (Global Navigation Satellite System Inertial Navigation System) buoys provide high resolution and accuracy data about floe location, strain rate, and acceleration. Whilst it is non-trivial to collect multiple datasets for the same floe or floe clusters, each dataset can be used alongside satellite observations of the same floes to enable the characterisation of conditions precluding or associated with break-up events such as wind speeds or melt rates. In addition, it may be possible to estimate timescales and breaking strain associated with floe break-up events through the use of strain rate and acceleration data. The MOSAiC expedition (Multidisciplinary drifting Observatory for the Study of Arctic; Dethloff et al., 2016) should be a source of several of the datasets described here, and therefore there are high short-term prospects for new and useful in-situ observations of floe evolution and break-up. These new observations should enable the development of either one or several physical parameterisations of brittle fracture processes to include within the prognostic model.

The combination of additional in-situ or satellite derived FSD observations, alongside the extraction of pan-Arctic FSD metrics from remote sensing as per Horvat et al. (2019), will present new datasets to assess the prognostic and WIPoFSD model performance. In the latter case, these datasets also offer significant potential to tune the WIPoFSD model to best fit observations, particularly if further evidence emerges that a fixed power-law exponent is a poor assumption.

Data Availability Statement

Model output used in this paper is publicly available via the University of Reading Research Data Archive. Model output used within chapter 3 is accessible at https://doi.org/10.17864/1947.223 (Bateson, 2019). Model output used within the remaining results chapters (4-8) is accessible at https://doi.org/10.17864/1947.300 (Bateson, 2021). Please contact the thesis author to discuss access to model code.

Bibliography

Aksenov, Y., Popova, E. E., Yool, A., Nurser, A. J. G., Williams, T. D., Bertino, L., and Bergh, J.: On the future navigability of Arctic sea routes: High-resolution projections of the Arctic Ocean and sea ice, Mar. Policy, 75, 300–317, https://doi.org/10.1016/j.marpol.2015.12.027, 2017.

Alberello, A., Onorato, M., Bennetts, L., Vichi, M., Eayrs, C., MacHutchon, K., and Toffoli, A.: Brief communication: Pancake ice floe size distribution during the winter expansion of the Antarctic marginal ice zone, The Cryosphere, 13, 41–48, https://doi.org/10.5194/tc-13-41-2019, 2019.

Aporta, C.: Life on the ice: Understanding the codes of a changing environment, Polar Rec. (Gr. Brit)., 38, 341–354, doi:10.1017/S0032247400018039, 2002.

Aporta, C.: Shifting perspectives on shifting ice: Documenting and representing Inuit use of the sea ice, Can. Geogr., 55, 6–19, doi:10.1111/j.1541-0064.2010.00340.x, 2011.

Arntsen, A. E., Song, A. J., Perovich, D. K., and Richter-Menge, J. A.: Observations of the summer breakup of an Arctic sea ice cover, Geophys. Res. Lett., 42, 8057–8063, https://doi.org/10.1002/2015GL065224, 2015.

Arrigo, K. R., van Dijken, G. and Pabi, S.: Impact of a shrinking Arctic ice cover on marine primary production, Geophys. Res. Lett., 35(19), 1–6, doi:10.1029/2008GL035028, 2008.

Arrigo, K. R., Perovich, D. K., Pickart, R. S., Brown, Z. W., Van Dijken, G. L., Lowry, K. E., Mills, M. M., Palmer, M. A., Balch, W. M., Bahr, F. and Bates, N. R.: Massive phytoplankton blooms under Arctic sea ice, Science, 336, 1408-1408, doi:10.1126/science.1215065, 2012.

Åstrom, J. A., Ouchterlony, F., Linna, R. P. and Timonen, J.: Universal dynamic fragmentation in D dimensions, Phys. Rev. Lett., 92, 1–4, doi:10.1103/PhysRevLett.92.245506, 2004.

Basu, S., Zhang, X., and Wang, Z.: Eurasian Winter Storm Activity at the End of the Century: A CMIP5 Multi-model Ensemble Projection, Earth's Future, 6, 61–70, https://doi.org/10.1002/2017EF000670, 2018.

Bateson, A. W.: Simulations with the sea ice model CICE investigating the impact of sea ice floe size distribution on seasonal Arctic sea ice retreat, University of Reading [data set], doi:10.17864/1947.223, 2019.

Bateson, A. W., Feltham, D. L., Schröder, D., Hosekova, L., Ridley, J. K. and Aksenov, Y.: Impact of sea ice floe size distribution on seasonal fragmentation and melt of Arctic sea ice, Cryosphere, 14, 403–428, doi:10.5194/tc-14-403-2020, 2020.

Bateson, A. W.: Simulations of the Arctic sea ice comparing different approaches to modelling the floe size distribution and their respective impacts on the sea ice cover, University of Reading [data set], doi:10.17864/1947.300, 2021.

Bennetts, L. G., O'Farrell, S., and Uotila, P.: Brief communication: Impacts of ocean-wave-induced breakup of Antarctic sea ice via thermodynamics in a stand-alone version of the CICE sea-ice model, The Cryosphere, 11, 1035–1040, https://doi.org/10.5194/tc-11-1035-2017, 2017.

Birnbaum, G. and Lüpkes, C.: A new parameterization of surface drag in the marginal sea ice zone, Tellus, Ser. A Dyn. Meteorol. Oceanogr., 54, 107–123, doi:10.1034/j.1600-0870.2002.00243.x, 2002.

Blackport, R., Screen, J. A., van der Wiel, K. and Bintanja, R.: Minimal influence of reduced Arctic sea ice on coincident cold winters in mid-latitudes, Nat. Clim. Chang., 9(9), 697–704, doi:10.1038/s41558-019-0551-4, 2019.

Boisvert, L. N., Wu, D. L. and Shie, C. L.: Increasing evaporation amounts seen in the Arctic between 2003 and 2013 from AIRS data, J. Geophys. Res., 120, 6865–6881, doi:10.1002/2015JD023258, 2015.

Boutin, G., Ardhuin, F., Dumont, D., Sévigny, C., Girard-Ardhuin, F., and Accensi, M.: Floe Size Effect on Wave-Ice Interactions: Possible Effects, Implementation in Wave Model, and Evaluation, J. Geophys. Res.-Oceans, 123, 4779–4805, https://doi.org/10.1029/2017JC013622, 2018.

Boutin, G., Lique, C., Ardhuin, F., Rousset, C., Talandier, C., Accensi, M., and Girard-Ardhuin, F.: Towards a coupled model to investigate wave–sea ice interactions in the Arctic marginal ice zone, The Cryosphere, 14, 709–735, https://doi.org/10.5194/tc-14-709-2020, 2020.

Brenner, S. D., Rainville, L., Thomson, J., Cole, S. T., & Lee, C. M.: Comparing observations and parameterizations of ice-ocean drag through an annual cycle across the Beaufort Sea, J. Geophys. Res.-Oceans, https://doi.org/10.1002/essoar.10504759.1, 2020.

Bricheno, L. M. and Wolf, J.: Future Wave Conditions of Europe, in Response to High-End Climate Change Scenarios, J. Geophys. Res. Ocean., 123, 8762–8791, doi:10.1029/2018JC013866, 2018.

Briegleb, B. P. and Light, B.: A Delta-Eddington Multiple Scattering Parameterization For Solar Radiation In The Sea Ice Component Of The Community Climate System Model, NCAR Tech. Note, https://doi.org/10.5065/D6B27S71, 2007.

Budyko, M. I.: The effect of solar radiation variations on the climate of the earth, Tellus, 21, 611–619, 1969.

Casas-Prat, M., Wang, X. L., and Swart, N.: CMIP5-based global wave climate projections including the entire Arctic Ocean, Ocean Model., 123, 66–85, https://doi.org/10.1016/j.ocemod.2017.12.003, 2018.

Casas-Prat, M. and Wang, X.: Projections of extreme ocean waves in the Arctic and potential implications for coastal inundation and erosion, J. Geophys. Res. Ocean., 125(8), doi:10.1029/2019JC015745, 2020.

Cavalieri, D. J., C. L. Parkinson, P. Gloersen, and H. J. Zwally.: Sea Ice Concentrations from Nimbus-7 SMMR and DMSP SSM/I-SSMIS Passive Microwave Data, Version 1, Natl. Snow and Ice Data Cent., Boulder, CO, available at: http://nsidc.org/ data/NSIDC-0051/versions/1.html (last access: 31 December 2016), 1996 (updated 2016).

Cohen, J., Screen, J. A., Furtado, J. C., Barlow, M., Whittleston, D., Coumou, D., Francis, J., Dethloff, K., Entekhabi, D., Overland, J. and Jones, J.: Recent Arctic amplification and extreme mid-latitude weather, Nat. Geosci., 7(9), 627–637, doi:10.1038/ngeo2234, 2014.

Cohen, J., Zhang, X., Francis, J., Jung, T., Kwok, R., Overland, J., Ballinger, T. J., Bhatt, U. S., Chen, H. W., Coumou, D., Feldstein, S., Gu, H., Handorf, D., Henderson, G., Ionita, M., Kretschmer, M., Laliberte, F., Lee, S., Linderholm, H. W., Maslowski, W., Peings, Y., Pfeiffer, K., Rigor, I., Semmler, T., Stroeve, J., Taylor, P. C., Vavrus, S., Vihma, T., Wang, S., Wendisch, M., Wu, Y. and Yoon, J.: Divergent consensuses on Arctic amplification influence on midlatitude severe winter weather, Nat. Clim. Chang., 10(1), 20–29, doi:10.1038/s41558-019-0662-y, 2020.

Comiso, J.: Bootstrap Sea Ice Concentrations From NIMBUS-7 SMMR and DMSP SSM/I, Natl. Snow and Ice Data Cent., Boulder, CO, available at: http://nsidc.org/data/nsidc-0079.html (last access: 31 December 2017), 1999 (updated 2017).

Condron, A., Joyce, A. J. and Bradley, R. S.: Arctic sea ice export as a driver of deglacial climate, Geology, 48(4), 395–399, doi:10.1130/G47016.1, 2020.

Curry, J. A., Schramm, J. L., and Ebert, E. E.: Sea ice-albedo climate feedback mechanism, J. Climate, 8, 240–247, https://doi.org/10.1175/1520-0442(1995)008<0240:SIACFM>2.0.CO;2, 1995.

Day, J. J. and Hodges, K. I.: Growing Land-Sea Temperature Contrast and the Intensification of Arctic Cyclones, Geophys. Res. Lett., 45, 3673–3681, https://doi.org/10.1029/2018GL077587, 2018.

Dedrick, K. R., Partington, K., Woert, M. Van, Bertoia, C. A. and Benner, D.: U.S. National/naval ice center digital sea ice data and climatology, Can. J. Remote Sens., 27(5), 457–475, doi:10.1080/07038992.2001.10854887, 2001.

Dee, D. P., Uppala, S. M., Simmons, A. J., Berrisford, P., Poli, P., Kobayashi, S., Andrae, U., Balmaseda, M. A., Balsamo, G., Bauer, P., Bechtold, P., Beljaars, A. C. M., van de Berg, L., Bidlot, J., Bormann, N., Delsol, C., Dragani, R., Fuentes, M., Geer, A. J., Haimberger, L., Healy, S. B., Hersbach, H., Hólm, E. V., Isaksen, L., Kållberg, P., Köhler, M., Matricardi, M., Mcnally, A. P., Monge-Sanz, B. M., Morcrette, J. J., Park, B. K., Peubey, C., de Rosnay, P., Tavolato, C., Thépaut, J. N., and Vitart, F.: The ERA-Interim reanalysis: Configuration and performance of the data assimilation system, Q. J. Roy. Meteor. Soc., 137, 553–597, https://doi.org/10.1002/qj.828, 2011.

Dethloff, K., Rex, M., and Shupe, M.: Multidisciplinary Drifting Observatory for the Study of Arctic Climate (MOSAiC), in: EGU General Assembly Conference Abstracts, 17–22 April 2016, Vienna, Austria, vol. 18, 2016.

Dickinson, R. E., Meehl, G. A., and Washington, W. M.: Ice-albedo feedback in a CO2-doubling simulation, Climatic Change, 10, 241–248, https://doi.org/10.1007/BF00143904, 1987.

Dumont, D., Kohout, A. and Bertino, L.: A wave-based model for the marginal ice zone including a floe breaking parameterization, J. Geophys. Res. Ocean., 116, 1–12, doi:10.1029/2010JC006682, 2011.

Durkalec, A., Furgal, C., Skinner, M. W. and Sheldon, T.: Climate change influences on environment as a determinant of Indigenous health: Relationships to place, sea ice, and health in anInuit community, Soc. Sci. Med., 136–137, 17–26, doi:10.1016/j.socscimed.2015.04.026, 2015.

Durner, G. M., Whiteman, J. P., Harlow, H. J., Amstrup, S. C., Regehr, E. V. and Ben-David, M.: Consequences of long-distance swimming and travel over deep-water pack ice for a female polar bear during a year of extreme sea ice retreat, Polar Biol., 34, 975–984, doi:10.1007/s00300-010-0953-2, 2011.

Ferry, N., Masina, S., Storto, A., Haines, K., Valdivieso, M., Barnier, B., and Molines, J.-M.: Product user manual global-reanalysis-phys-001-004-a and b, MyOcean, Eur. Comm., Brussels, Belgium, 2011.

Feltham, D. L.: Granular flow in the marginal ice zone, Philos. T. R. Soc. Lond, 363, 1677–1700, https://doi.org/10.1098/rsta.2005.1601, 2005.

Feltham, D. L., Untersteiner, N., Wettlaufer, J. S. and Worster, M. G.: Sea ice is a mushy layer, Geophys. Res. Lett., 33, 4–7, doi:10.1029/2006GL026290, 2006.

Fleischer, D., Schaber, M. and Piepenburg, D.: Atlantic snake pipefish (Entelurus aequoreus) extends its northward distribution range to Svalbard (Arctic Ocean), Polar Biol., 30(10), 1359–1362, doi:10.1007/s00300-007-0322-y, 2007.

Flocco, D., Schroeder, D., Feltham, D. L., and Hunke, E. C.: Impact of melt ponds on Arctic sea ice simulations from 1990 to 2007, J. Geophys. Res.-Oceans, 117, 1–17, https://doi.org/10.1029/2012JC008195, 2012.

Francis, O. P., Panteleev, G. G. and Atkinson, D. E.: Ocean wave conditions in the Chukchi Sea from satellite and in situ observations, Geophys. Res. Lett., 38, 1–5, doi:10.1029/2011GL049839, 2011.

Francis, J. A., Vavrus, S. J. and Cohen, J.: Amplified Arctic warming and mid-latitude weather: new perspectives on emerging connections, Wiley Interdiscip. Rev. Clim. Chang., 8(5), 1–11, doi:10.1002/wcc.474, 2017.

Fuglestvedt, J. S., Dalsøren, S. B., Samset, B. H., Berntsen, T., Myhre, G., Hodnebrog, Ø., Eide, M. S. and Bergh, T. F.: Climate penalty for shifting shipping to the Arctic, Environ. Sci. Technol., 48, 13273–13279, doi:10.1021/es502379d, 2014.

Geise, G. R., Barton, C. C. and Tebbens, S. F.: Power Scaling and Seasonal Changes of Floe Areas in the Arctic East Siberian Sea, Pure Appl. Geophys., 174, 387–396, doi:10.1007/s00024-016-1364-2, 2016.

Gherardi, M. and Lagomarsino, M. C.: Characterizing the size and shape of sea ice floes, Sci. Rep., 5, 1–11, https://doi.org/10.1038/srep10226, 2015.

Gilchrist, H. G. and Robertson, G. J.: Observations of Marine Birds and Mammals Wintering at Polynyas and Ice Edges in the in the Belcher Islands, Nunavut, Canada, Arctic, 53(1), 61–68, doi:10.14430/arctic835, 2016.

Goosse, H., Kay, J. E., Armour, K. C., Bodas-Salcedo, A., Chepfer, H., Docquier, D., Jonko, A., Kushner, P. J., Lecomte, O., Massonnet, F., Park, H. S., Pithan, F., Svensson, G. and Vancoppenolle, M.: Quantifying climate feedbacks in polar regions, Nat. Commun., 9, doi:10.1038/s41467-018-04173-0, 2018.

Guest, P. S., and K. L. Davidson.: The effect of observed ice conditions on the drag coefficient in the summer East Greenland Sea marginal ice zone, J. Geophys. Res.-Oceans, 92, 6943-6954, https://doi.org/10.1029/JC092iC07p06943, 1987.

Häkkinen, S.: A coupled dynamic-thermodynamic model of an ice-ocean system in the marginal ice zone, J. Geophys. Res. Ocean., 92, 9469–9478, doi:10.1029/JC092iC09p09469, 1987.

Hanssen-Bauer, I. and Gjessing, Y. T.: Observations and model calculations of aerodynamic drag on sea ice in the Fram Strait, Tellus A, 40A, 151–161, doi:10.1111/j.1600-0870.1988.tb00413.x, 1988.

Hauser, D. D. W., Laidre, K. L., Stafford, K. M., Stern, H. L., Suydam, R. S., and Richard, P. R.: Decadal shifts in autumn migration timing by Pacific Arctic beluga whales are related to delayed annual sea ice formation, Glob. Change Biol., 23, 2206–2217, https://doi.org/10.1111/gcb.13564, 2017.

Hausfather, Z. and Peters, G. P.: Emissions – the ‘business as usual’ story is misleading, Nature, 577, 618-620, doi:10.1038/d41586-020-00177-3, 2020.

Hazeleger, W., Wang, X., Severijns, C., Ştefănescu, S., Bintanja, R., Sterl, A., Wyser, K., Semmler, T., Yang, S., Noije, T. Van, Linden, E. Van Der and Wiel, K. Van Der: EC-Earth V2.2: description and validation of a new seamless earth system prediction model, 39, 2611–2629, doi:10.1007/s00382-011-1228-5, 2012.

Heinemann, G.: The polar regions: A natural laboratory for boundary layer meteorology - A review, Meteorol. Zeitschrift, 17, 589–601, doi:10.1127/0941-2948/2008/0327, 2008.

Herman, A.: Sea-ice floe-size distribution in the context of spontaneous scaling emergence in stochastic systems, Phys. Rev. E, 81, 1–5, https://doi.org/10.1103/PhysRevE.81.066123, 2010.

Herman, A.: Influence of ice concentration and floe-size distribution on cluster formation in sea-ice floes, Cent. Eur. J. Phys., 10, 715–722, doi:10.2478/s11534-012-0071-6, 2012.

Herman, A.: Wave-induced stress and breaking of sea ice in a coupled hydrodynamic discrete-element wave–ice model, The Cryosphere, 11, 2711–2725, https://doi.org/10.5194/tc-11-2711-2017, 2017.

Herman, A.: Wave-Induced Surge Motion and Collisions of Sea Ice Floes: Finite-Floe-Size Effects, J. Geophys. Res.-Oceans, 123, 7472–7494, https://doi.org/10.1029/2018JC014500, 2018.

Herman, A., Evers, K.-U., and Reimer, N.: Floe-size distributions in laboratory ice broken by waves, The Cryosphere, 12, 685–699, https://doi.org/10.5194/tc-12-685-2018, 2018.

Ho, J.: The implications of Arctic sea ice decline on shipping, Mar. Policy, 34, 713–715, https://doi.org/10.1016/j.marpol.2009.10.009, 2010.

Hopkins, M. A., Frankenstein, S. and Thorndike, A. S.: Formation of an aggregate scale in Arctic sea ice, J. Geophys. Res. C Ocean., 109, 1–10, doi:10.1029/2003jc001855, 2004.

Horvat, C. and Tziperman, E.: A prognostic model of the sea-ice floe size and thickness distribution, The Cryosphere, 9, 2119–2134, https://doi.org/10.5194/tc-9-2119-2015, 2015.

Horvat, C., Tziperman, E. and Campin, J. M.: Interaction of sea ice floe size, ocean eddies, and sea ice melting, Geophys. Res. Lett., 43, 8083–8090, doi:10.1002/2016GL069742, 2016.

Horvat, C., Jones, D. R., Iams, S., Schroeder, D., Flocco, D. and Feltham, D.: The frequency and extent of sub-ice phytoplankton blooms in the Arctic Ocean, Sci. Adv., 3, 1–8, doi:10.1126/sciadv.1601191, 2017.

Horvat, C. and Tziperman, E.: The evolution of scaling laws in the sea ice floe size distribution, J. Geophys. Res.-Oceans, 122, 7630–7650, https://doi.org/10.1002/2016JC012573, 2017.

Horvat, C. and Tziperman, E.: Understanding Melting due to Ocean Eddy Heat Fluxes at the Edge of Sea-Ice Floes, Geophys. Res. Lett., 45, 9721–9730, https://doi.org/10.1029/2018GL079363, 2018.

Horvat, C., Roach, L. A., Tilling, R., Bitz, C. M., Fox-Kemper, B., Guider, C., Hill, K., Ridout, A., and Shepherd, A.: Estimating the sea ice floe size distribution using satellite altimetry: theory, climatology, and model comparison, The Cryosphere, 13, 2869–2885, https://doi.org/10.5194/tc-13-2869-2019, 2019.

Horvat, C., Blanchard-Wrigglesworth, E. and Petty, A.: Observing Waves in Sea Ice With ICESat-2, Geophys. Res. Lett., 47(10), 1–10, doi:10.1029/2020GL087629, 2020.

Hosekova, L., Aksenov, Y., Coward, A., Williams, T., Bertino, L., and Nurser, A. J. G.: Modelling Sea Ice and Surface Wave Interactions in Polar Regions, in: AGU Fall Meeting Abstracts, 15–18 December 2015, San Francisco, USA, GC34A-06, 2015.

Hunke, E. C. and Dukowicz, J. K.: An elastic-viscous-plastic model for sea ice dynamics, J. Phys. Oceanogr., 27(9), 1849-1867, doi:10.1175/1520-0485(1997)027<1849:AEVPMF>2.0.CO;2, 1997.

Hunke, E. and Dukowicz, J.: The elastic-viscous-plastic sea ice dynamics model in general orthogonal curvilinear coordinates on a sphere-incorporation of metric terms, Mon. Weather Rev., 130, 1848–1865, https://doi.org/10.1175/1520-0493(2002)130<1848:TEVPSI>2.0.CO;2, 2002.

Hunke, E. C. and Holland, M. M.: Global atmospheric forcing data for Arctic ice-ocean modeling, J. Geophys. Res. Ocean., 112(4), 1–13, doi:10.1029/2006JC003640, 2007.

Hunke, E. C.: Thickness sensitivities in the CICE sea ice model, Ocean Model., 34(3–4), 137–149, doi:10.1016/j.ocemod.2010.05.004, 2010.

Hunke, E. C., Lipscomb, W. H., Turner, A. K., Jeffery, N., and Elliott, S.: CICE: The Los Alamos Sea ice Model Documentation and Software User's Manual Version 5, Los Alamos National Laboratory, Los Alamos, New Mexico, USA, Tech. Rep. LA-CC-06–012, 115 pp., 2015.

Hwang, B., Wilkinson, J., Maksym, E., Graber, H. C., Schweiger, A., Horvat, C., Perovich, D. K., Arntsen, A. E., Stanton, T. P., Ren, J., and Wadhams, P.: Winter-to-summer transition of Arctic sea ice breakup and floe size distribution in the Beaufort Sea, Elem. Sci. Anth., 5, p. 40, https://doi.org/10.1525/elementa.232, 2017.

Inoue, J., Wakatsuchi, M. and Fujiyoshi, Y.: Ice floe distribution in the Sea of Okhotsk in the period when sea-ice extent is advancing, Geophys. Res. Lett., 31, 2–5, doi:10.1029/2004GL020809, 2004.

Ivanova, N., Pedersen, L. T., Tonboe, R. T., Kern, S., Heygster, G., Lavergne, T., Sørensen, A., Saldo, R., Dybkjær, G., Brucker, L., and Shokr, M.: Inter-comparison and evaluation of sea ice algorithms: towards further identification of challenges and optimal approach using passive microwave observations, The Cryosphere, 9, 1797–1817, https://doi.org/10.5194/tc-9-1797-2015, 2015.

Ivanova, D. P., Gleckler, P. J., Taylor, K. E., Durack, P. J., and Marvel, K. D.: Moving beyond the total sea ice extent in gauging model biases, J. Climate, 29, 8965–8987, https://doi.org/10.1175/JCLI-D-16-0026.1, 2016.

Jardon, F. P., Bouruet-Aubertot, P., Cuypers, Y., Vivier, F. and Loureno, A.: Internal waves and vertical mixing in the Storfjorden Polynya, Svalbard, J. Geophys. Res. Ocean., 116(12), 1–19, doi:10.1029/2010JC006918, 2011.

Johnson, S. J., Stockdale, T. N., Ferranti, L., Balmaseda, M. A., Molteni, F., Magnusson, L., Tietsche, S., Decremer, D., Weisheimer, A., Balsamo, G., Keeley, S. P. E., Mogensen, K., Zuo, H. and Monge-Sanz, B. M.: SEAS5: The new ECMWF seasonal forecast system, Geosci. Model Dev., 12(3), 1087–1117, doi:10.5194/gmd-12-1087-2019, 2019.

Jones, C. D., Hughes, J. K., Bellouin, N., Hardiman, S. C., Jones, G. S., Knight, J., Liddicoat, S., O'Connor, F. M., Andres, R. J., Bell, C., Boo, K. O., Bozzo, A., Butchart, N., Cadule, P., Corbin, K. D., Doutriaux-Boucher, M., Friedlingstein, P., Gornall, J., Gray, L., Halloran, P. R., Hurtt, G., Ingram, W. J., Lamarque, J. F., Law, R. M., Meinshausen, M., Osprey, S., Palin, E. J., Parsons Chini, L., Raddatz, T., Sanderson, M. G., Sellar, A. A., Schurer, A., Valdes, P., Wood, N., Woodward, S., Yoshioka, M. and Zerroukat, M.: The HadGEM2-ES implementation of CMIP5 centennial simulations, Geosci. Model Dev., 4, 543–570, doi:10.5194/gmd-4-543-2011, 2011.

Josberger, E. G.: Laminar and turbulent boundary layers adjacent to melting vertical ice walls in salt water, Ph.D. thesis, University of Washington, Seattle, Washington, USA, 1979.

Josberger, E. G. and Martin, S.: A laboratory and theoretical study of the boundary layer adjacent to a vertical melting ice wall in salt water, J. Fluid Mech., 111, 439–473, doi:10.1017/S0022112081002450, 1981.

Kanamitsu, M., Ebisuzaki, W., Woollen, J., Yang, S. K., Hnilo, J. J., Fiorino, M., and Potter, G. L.: NCEP-DOE AMIP-II reanalysis (R-2), B. Am. Meteorol. Soc., 83, 1631–1644, https://doi.org/10.1175/BAMS-83-11-1631(2002)083<1631:NAR>2.3.CO;2, 2002.

Kaur, S., Ehn, J. K. and Barber, D. G.: Pan-arctic winter drift speeds and changing patterns of sea ice motion: 1979-2015, Polar Rec. (Gr. Brit)., 54, 303–311, doi:10.1017/S0032247418000566, 2018.

Kekäläinen, P., Aström, J. A. and Timonen, J.: Solution for the fragment-size distribution in a crack-branching model of fragmentation, Phys. Rev. E - Stat. Nonlinear, Soft Matter Phys., 76, 1–7, doi:10.1103/PhysRevE.76.026112, 2007.

Kergomard, C.: Analyse morphométrique de la zone marginale de la banquise polaire au nordouest du spitsberg à partir de l'imagerie SPOT panchromatique, Bulletin-Société française de photogrammétrie et de télédétection, 115, 17–20, 1989.

Khon, V. C., Mokhov, I. I., Pogarskiy, F. A., Babanin, A., Dethloff, K., Rinke, A. and Matthes, H.: Wave heights in the 21st century Arctic Ocean simulated with a regional

climate model, Geophys. Res. Lett., 41, 2956–2961, doi:10.1002/2014GL059847, 2014.

Kohout, A. L., Williams, M. J. M., Dean, S. M. and Meylan, M. H.: Storm-induced sea-ice breakup and the implications for ice extent, Nature, 509, 604–607, doi:10.1038/nature13262, 2014.

Kohout, A. L., Williams, M. J. M., Toyota, T., Lieser, J. and Hutchings, J.: In situ observations of wave-induced sea ice breakup, Deep. Res. Part II Top. Stud. Oceanogr., 131, 22–27, doi:10.1016/j.dsr2.2015.06.010, 2016.

Kraus, E. B. and Turner, J. S.: A one-dimensional model of the seasonal thermocline II. The general theory and its consequences, Tellus, 19, 98–106, https://doi.org/10.3402/tellusa.v19i1.9753, 1967.

Kwok, R.: Deformation of the Arctic ocean sea ice cover between November 1996 and April 1997: a qualitative survey, IUTAM symposium on scaling laws in ice mechanics and ice dynamics, Springer, Dordrecht, 315–322, 2001.

Kwok, R. and Untersteiner, N.: New high-resolution images of summer arctic Sea ice, Eos (Washington. DC)., 92, 53–54, doi:10.1029/2011EO070002, 2011.

Kwok, R., Spreen, G. and Pang, S.: Arctic sea ice circulation and drift speed: Decadal trends and ocean currents, J. Geophys. Res. Ocean., 118, 2408–2425, doi:10.1002/jgrc.20191, 2013.

Kwok, R.: Arctic sea ice thickness, volume, and multiyear ice coverage: Losses and coupled variability (1958–2018), Environ. Res. Lett., 13, 105005, https://doi.org/10.1088/1748-9326/aae3ec, 2018.

Laidler, G. J., Ford, J. D., Gough, W. A., Ikummaq, T., Gagnon, A. S., Kowal, S., Qrunnut, K., and Irngaut, C.: Travelling and hunting in a changing Arctic: Assessing Inuit vulnerability to sea ice change in Igloolik, Nunavut, Climatic Change, 94, 363–397, https://doi.org/10.1007/s10584-008-9512-z, 2009.

Laing, A., Gemmill, W., Magnusson, A., Burroughs, L., Reistad, M., Khandekar, M., Holthuijsen, L., Ewing, J., and Carter, D.: Guide to wave analysis, Second edn., World Meteorological Organization, Geneva, Switzerland, 159 pp., 1998.

Lecomte, O., Fichefet, T., Flocco, D., Schroeder, D., and Vancoppenolle, M.: Interactions between wind-blown snow redistribution and melt ponds in a coupled ocean-sea ice model, Ocean Model., 87, 67–80, https://doi.org/10.1016/j.ocemod.2014.12.003, 2015.

Lee, C. M., Cole, S., Doble, M., Freitag, L., Hwang, P., Jayne, S., Jeffries, M., Krishfield, R., Maksym, T., Maslowski, W., Owens, B., Posey, P., Rainville, L., Roberts, A., Shaw, B., Stanton, T., Thomson, J., Timmermans, M., Toole, J., Wadhams, P., Wilkinson, J., and Zhang, J.: Marginal Ice Zone (MIZ) Program: Science and Experiment Plan, Washington University Seattle Applied Physics Lab, Washington, Seattle, USA, APL-UW 1201 October 2012, 2012.

Lipscomb, W. H. and Hunke, E. C.: Modeling Sea Ice Transport Using Incremental Remapping, Mon. Weather Rev., 132, 1341–1354, https://doi.org/10.1175/1520-0493(2004)132<1341:MSITUI>2.0.CO;2, 2004.

Lipscomb, W. H., Hunke, E. C., Maslowski, W., and Jakacki, J.: Ridging, strength, and stability in high-resolution sea ice models, J. Geophys. Res.-Oceans, 112, C03S91, https://doi.org/10.1029/2005JC003355, 2007.

Liu, A. K., Vachon, P. W., Peng, C. Y., and Bhogal, A. S.: Wave attenuation in the marginal ice zone during limex, Atmos.-Ocean, 30, 192–206, https://doi.org/10.1080/07055900.1992.9649437, 1992.

Livina, V. N. and Lenton, T. M.: A recent tipping point in the Arctic sea-ice cover: Abrupt and persistent increase in the seasonal cycle since 2007, Cryosphere, 7, 275–286, doi:10.5194/tc-7-275-2013, 2013.

Lu, Q., Larsen, J. and Tryde, P.: On the role of ice interaction due to floe collisions in marginal ice zone dynamics, J. Geophys. Res., 94(C10), 14525-14537, doi:10.1029/jc094ic10p14525, 1989.

Lüpkes, C. and Birnbaum, G.: Surface drag in the Arctic marginal sea-ice zone: A comparison of different parameterisation concepts, Boundary-Layer Meteorol., 117, 179–211, doi:10.1007/s10546-005-1445-8, 2005.

Lüpkes, C., Gryanik, V. M., Hartmann, J., and Andreas, E. L.: A parametrization, based on sea ice morphology, of the neutral atmospheric drag coefficients for weather prediction and climate models, J. Geophys. Res.-Atmos., 117, 1–18, https://doi.org/10.1029/2012JD017630, 2012.

Marchenko, N..: Russian Arctic Seas: navigational conditions and accidents. Springer-Verlag, Berlin Heidelberg, https://doi.org/10.1007/978-3-642-22125-5, 2012.

Maslanik, J. A., Fowler, C., Stroeve, J., Drobot, S., Zwally, J., Yi, D., and Emery, W.: A younger, thinner Arctic ice cover: Increased potential for rapid, extensive sea-ice loss, Geophys. Res. Lett., 34, L24501, https://doi.org/10.1029/2007GL032043, 2007.

Maykut, G. A. and McPhee, M. G.: Solar heating of the Arctic mixed layer, J. Geophys. Res., 100, 24691–24703, https://doi.org/10.1029/95JC02554, 1995.

Maykut, G. A. and Perovich, D. K.: The role of shortwave radiation in the summer decay of a sea ice cover, J. Geophys. Res. Ocean., 92(C7), 7032–7044, doi:10.1029/JC092iC07p07032, 1987.

McPhee, M. G., Maykut, G. A., and Morison, J. H.: Dynamics and thermodynamics of the ice/upper ocean system in the marginal ice zone of the Greenland Sea, J. Geophys. Res.-Oceans, 92, 7017–7031, https://doi.org/10.1029/JC092iC07p07017, 1987.

Mecklenburg, C. W., Stein, D. L., Sheiko, B. A., Chernova, N. V, Mecklenburg, T. A. and Holladay, B. A.: Russian-American Long-Term Census of the Arctic : Benthic Fishes Trawled in the Chukchi Sea and Bering Strait, August 2004, Northwestern Naturalist, 88(3), doi:10.1898/1051-1733(2007)88[168:RLCOTA]2.0.CO;2, 168–187, 2020.

Meier, W. and Notz, D.: A note on the accuracy and reliability of satellite-derived passive microwave estimates of sea-ice extent, Climate and Cryosphere Sea Ice Working Group Consensus Document, World Climate Research Program,

http://www.arcus.org/files/page/documents/1707/GCW_CliC_Sea_ice_Reliability.pdf, 2010.

Meneghello, G., Marshall, J., Campin, J. M., Doddridge, E. and Timmermans, M. L.: The Ice-Ocean Governor: Ice-Ocean Stress Feedback Limits Beaufort Gyre Spin-Up, Geophys. Res. Lett., 45(20), 11,293-11,299, doi:10.1029/2018GL080171, 2018.

Meylan, M. and Squire, V. A.: The response of ice floes to ocean waves, J. Geophys. Res., 99, 891–900, https://doi.org/10.1029/93JC02695, 1994.

Meylan, M. H., Bennetts, L. G. and Kohout, A. L.: In situ measurements and analysis of ocean waves in the Antarctic marginal ice zone, Geophys. Res. Lett., 41, 5046–5051, doi:10.1002/2014GL060809, 2014.

Meylan, M. H., Bennetts, L. G., and Peter, M. A.: Water-wave scattering and energy dissipation by a floating porous elastic plate in three dimensions, Wave Motion, 70, 240–250, https://doi.org/10.1016/j.wavemoti.2016.06.014, 2017.

Middlemas, E. A., Kay, J. E., Medeiros, B. M. and Maroon, E. A.: Quantifying the Influence of Cloud Radiative Feedbacks on Arctic Surface Warming Using Cloud Locking in an Earth System Model, Geophys. Res. Lett., 47, 1–9, doi:10.1029/2020GL089207, 2020.

Montiel, F., Squire, V. A., and Bennetts, L. G.: Attenuation and directional spreading of ocean wave spectra in the marginal ice zone, J. Fluid Mech., 790, 492–522, https://doi.org/10.1017/jfm.2016.21, 2016.

Montiel, F. and Squire, V. A.: Modelling wave-induced sea ice break-up in the marginal ice zone, Proc. R. Soc. A Math. Phys. Eng. Sci., 473, 1–32, doi:10.1098/rspa.2017.0258, 2017.

Mori, M., Kosaka, Y., Watanabe, M., Nakamura, H. and Kimoto, M.: A reconciled estimate of the influence of Arctic sea-ice loss on recent Eurasian cooling, Nat. Clim. Chang., 9, 123-129, doi:10.1038/s41558-018-0379-3, 2019.

Naumann, A. K., Notz, D., Håvik, L., and Sirevaag, A.: Laboratory study of initial sea-ice growth: properties of grease ice and nilas, The Cryosphere, 6, 729–741, https://doi.org/10.5194/tc-6-729-2012, 2012.

NERSC: Ships and Waves Reaching Polar Regions D5.1 Validation Reports, Bergen, available at: https://swarp.nersc.no/system/files/Deliverable/SWARP_D5.1.pdf (last access: 29 January 2020), 2016.

Niiler, P. and Kraus, E. B.: One-dimensional models of the upper ocean, Modeling and prediction of the upper layers of the ocean, Pergamon Press, New York, 143–172, 1977.

Notz, D. and Stroeve, J.: The Trajectory Towards a Seasonally Ice-Free Arctic Ocean, Curr. Clim. Chang. Reports, 4, 407–416, https://doi.org/10.1007/s40641-018-0113-2, 2018.

Overland, J. E. and Stabeno, P. J.: Is the climate of the Bering Sea warming and affecting the ecosystem?, Eos (Washington. DC)., 85(33), 1997–2003, doi:10.1029/2004EO330001, 2004.

Pabi, S., van Dijken, G. L. and Arrigo, K. R.: Primary production in the Arctic Ocean, 1998-2006, J. Geophys. Res. Ocean., 113(8), 1998–2006, doi:10.1029/2007JC004578, 2008.

Parkinson, C. L. and Cavalieri, D. J.: Antarctic sea ice variability and trends, 1979–2010, The Cryosphere, 6, 871–880, https://doi.org/10.5194/tc-6-871-2012, 2012.

Peralta-Ferriz, C. and Woodgate, R. A.: Seasonal and interannual variability of pan-Arctic surface mixed layer properties from 1979 to 2012 from hydrographic data, and the dominance of stratification for multiyear mixed layer depth shoaling, Prog. Oceanogr., 134, 19–53, https://doi.org/10.1016/j.pocean.2014.12.005, 2015.

Perovich, D. K.: On the summer decay of a sea ice cover, Ph.D. thesis, University of Washington, Seattle, Washington, USA, 1983.

Perovich, D. K., Richter-Menge, J. A. and Tucker, W. B.: Seasonal changes in Arctic sea-ice morphology, Ann. Glaciol., 33, 171–176, doi:10.3189/172756401781818716, 2001.

Perovich, D. K.: Aerial observations of the evolution of ice surface conditions during summer, J. Geophys. Res., 107, SHE-24, https://doi.org/10.1029/2000JC000449, 2002.

Perovich, D. K. and Jones, K. F.: The seasonal evolution of sea ice floe size distribution, J. Geophys. Res.-Ocean., 119, 8767–8777, https://doi.org/10.1002/2014JC010136, 2014.

Petty, A. A., Holland, P. R., and Feltham, D. L.: Sea ice and the ocean mixed layer over the Antarctic shelf seas, The Cryosphere, 8, 761–783, https://doi.org/10.5194/tc-8-761-2014, 2014.

Pilfold, N. W., Derocher, A. E., Stirling, I. and Richardson, E.: Multi-temporal factors influence predation for polar bears in a changing climate, Oikos, 124, 1098–1107, doi:10.1111/oik.02000, 2015.

Pilfold, N. W., McCall, A., Derocher, A. E., Lunn, N. J. and Richardson, E.: Migratory response of polar bears to sea ice loss: to swim or not to swim, Ecography (Cop.)., 40, 189–199, doi:10.1111/ecog.02109, 2017.

Porter, D. F., Cassano, J. J. and Serreze, M. C.: Local and large-scale atmospheric responses to reduced Arctic sea ice and ocean warming in the WRF model, J. Geophys. Res. Atmos., 117(11), 1–21, doi:10.1029/2011JD016969, 2012.

Post, E., Forchhammer, M. C., Bret-Harte, M. S., Callaghan, T. V., Christensen, T. R., Elberling, B., Fox, A. D., Gilg, O., Hik, D. S., Høye, T. T., Ims, R. A., Jeppesen, E., Klein, D. R., Madsen, J., McGuire, A. D., Rysgaard, S., Schindler, D. E., Stirling, I., Tamstorf, M. P., Tyler, N. J. C., Van Der Wal, R., Welker, J., Wookey, P. A., Schmidt, N. M., and Aastrup, P.: Ecological dynamics across the arctic associated with recent climate change, Science, 325, 1355–1358, https://doi.org/10.1126/science.1173113, 2009.

Pringle, D. J., Eicken, H., Trodahl, H. J., and Backstrom, L. G. E.: Thermal conductivity of landfast Antarctic and Arctic sea ice, J. Geophys. Res.-Oceans, 112, C04017, https://doi.org/10.1029/2006JC003641, 2007.

Prinsenberg, S. J., & Peterson, I. K. .: Observing regional-scale pack-ice decay processes with helicopter-borne sensors and moored upward-looking sonars, Annals of Glaciology, 52, 35-42, https://doi.org/10.3189/172756411795931688, 2011.

Rampal, P., Weiss, J., Marsan, D. and Bourgoin, M.: Arctic sea ice velocity field: General circulation and turbulent-like fluctuations, J. Geophys. Res. Ocean., 114, 1–17, doi:10.1029/2008JC005227, 2009.

Regehr, E. V., Hunter, C. M., Caswell, H., Amstrup, S. C., and Stirling, I.: Survival and breeding of polar bears in the southern Beaufort Sea in relation to sea ice, J. Anim. Ecol., 79, 117–127, https://doi.org/10.1111/j.1365-2656.2009.01603.x, 2010.

Regehr, E. V., Laidre, K. L., Resit Akcakaya, H., Amstrup, S. C., Atwood, T. C., Lunn, N. J., Obbard, M., Stern, H., Thiemann, G. W. and Wiig, Ø.: Conservation status of polar bears (Ursus maritimus) in relation to projected sea-ice declines, Biol. Lett., 12, doi:10.1098/rsbl.2016.0556, 2016.

Rinke, A., Maslowski, W., Dethloff, K. and Clement, J.: Influence of sea ice on the atmosphere: A study with an Arctic atmospheric regional climate model, J. Geophys. Res. Atmos., 111(16), 1–14, doi:10.1029/2005JD006957, 2006.

Rinke, A., Dethloff, K., Dorn, W., Handorf, D. and Moore, J. C.: Simulated Arctic atmospheric feedbacks associated with late summer sea ice anomalies, J. Geophys. Res. Atmos., 118(14), 7698–7714, doi:10.1002/jgrd.50584, 2013.

Roach, L. A., Horvat, C., Dean, S. M., and Bitz, C. M.: An Emergent Sea Ice Floe Size Distribution in a Global Coupled Ocean-Sea Ice Model, J. Geophys. Res.-Oceans, 123, 4322–4337, https://doi.org/10.1029/2017JC013692, 2018a.

Roach, L. A., Smith, M. M., and Dean, S. M.: Quantifying Growth of Pancake Sea Ice Floes Using Images From Drifting Buoys, J. Geophys. Res.-Oceans, 123, 2851–2866, https://doi.org/10.1002/2017JC013693, 2018b.

Roach, L. A., Bitz, C. M., Horvat, C. and Dean, S. M.: Advances in Modeling Interactions Between Sea Ice and Ocean Surface Waves, J. Adv. Model. Earth Syst., 11, 4167–4181, doi:10.1029/2019MS001836, 2019.

Robinson, N. J. and Palmer, S. C.: A Modal Analysis of a Rectangular Plate Floating on an Incompressible Fluid, J. Sound Vib., 142, 453–460, doi:10.1016/0022-460X(90)90661-I, 1990.

Rolph, R. J., Feltham, D. L., and Schröder, D.: Changes of the Arctic marginal ice zone during the satellite era, The Cryosphere, 14, 1971–1984, https://doi.org/10.5194/tc-14-1971-2020, 2020.

Rösel, A., Kaleschke, L., and Birnbaum, G.: Melt ponds on Arctic sea ice determined from MODIS satellite data using an artificial neural network, The Cryosphere, 6, 431–446, https://doi.org/10.5194/tc-6-431-2012, 2012.

Rothrock, D. A.: The energetics of the plastic deformation of pack ice by ridging, J. Geophys. Res., 80, 4514–4519, https://doi.org/10.1029/JC080i033p04514, 1975.

Rothrock, D. A. and Thorndike, A. S.: Measuring the sea ice floe size distribution, J. Geophys. Res., 89, 6477–6486, https://doi.org/10.1029/JC089iC04p06477, 1984.

Rynders, S.: Impact of surface waves on sea ice and ocean in the polar regions, University of Southampton, Southampton, UK, 2017.

Schröder, D., Vihma, T., Kerber, A. and Brümmer, B.: On the parameterization of turbulent surface fluxes over heterogeneous sea ice surfaces, J. Geophys. Res. C Ocean., 108, 3195, doi:10.1029/2002jc001385, 2003.

Schröder, D., Feltham, D. L., Tsamados, M., Ridout, A., and Tilling, R.: New insight from CryoSat-2 sea ice thickness for sea ice modelling, The Cryosphere, 13, 125–139, https://doi.org/10.5194/tc-13-125-2019, 2019.

Screen, J. A., Simmonds, I., Deser, C., and Tomas, R.: The atmospheric response to three decades of observed arctic sea ice loss, J. Climate, 26, 1230–1248, https://doi.org/10.1175/JCLI-D-12-00063.1, 2013.

Screen, J. A., Deser, C., Smith, D. M., Zhang, X., Blackport, R., Kushner, P. J., Oudar, T., McCusker, K. E. and Sun, L.: Consistency and discrepancy in the atmospheric response to Arctic sea-ice loss across climate models, Nat. Geosci., 11(3), 155–163, doi:10.1038/s41561-018-0059-y, 2018.

Schulson, E. M.: Brittle failure of ice, Eng. Fract. Mech., 68, 1839-1887, doi:10.1016/S0013-7944(01)00037-6, 2001.

Schulson, E. M.: Compressive shear faults within arctic sea ice: Fracture on scales large and small, J. Geophys. Res. C Ocean., 109, doi:10.1029/2003JC002108, 2004.

Serreze, M. C. and Barry, R. G.: Processes and impacts of Arctic amplification: A research synthesis, Glob. Planet. Change, 77, 85–96, doi:10.1016/j.gloplacha.2011.03.004, 2011.

Sévellec, F., Fedorov, A. V. and Liu, W.: Arctic sea-ice decline weakens the Atlantic Meridional Overturning Circulation, Nat. Clim. Chang., 7(8), 604–610, doi:10.1038/NCLIMATE3353, 2017.

Shen, H. H., Hibler, W. D. and Leppäranta, M.: On applying granular flow theory to a deforming broken ice field, Acta Mech., 63(1-4), 143-160, doi:10.1007/BF01182545, 1986.

Shen, H. H., Hibler, W. D. and Lepparanta, M.: The role of floe collisions in sea ice rheology, J. Geophys. Res., 92(C7), 7085–7096, doi:10.1029/JC092iC07p07085, 1987.

Shen, H. H. and Ackley, S. F.: A one-dimensional model for wave-induced ice-floe collisions. Ann. of Glaciol., 15, 87-95, https://doi.org/10.3189/1991AoG15-1-87-95, 1991.

Shen, H. H., Ackley, S. F. and Hopkins, M. A.: A conceptual model for pancake-ice formation in a wave field, Ann. Glaciol., 33, 361-367, https://doi.org/10.3189/172756401781818239, 2001.

Shen, H. H., Ackley, S. F. and Yuan, Y.: Limiting diameter of pancake ice, J. Geophys. Res. C Ocean., 109, doi:10.1029/2003JC002123, 2004.

Smith, L. C. and Stephenson, S. R.: New Trans-Arctic shipping routes navigable by midcentury, P. Natl. Acad. Sci. USA, 110, E1191–E1195, https://doi.org/10.1073/pnas.1214212110, 2013.

Spreen, G., Kwok, R. and Menemenlis, D.: Trends in Arctic sea ice drift and role of wind forcing: 1992-2009, Geophys. Res. Lett., 38, 1–6, doi:10.1029/2011GL048970, 2011.

Squire, V. A., Duggan, J. P., Wadhams, P., Rottier, P. J. and Liu, A. J.: Of ocean waves and sea ice, Annu. Rev. Fluid Mech., 27(3), 115–168, doi:10.1146/annurev.fl.27.010195.000555, 1995.

Squire, V. A.: Of ocean waves and sea-ice revisited, Cold Reg. Sci. Technol., 49, 110–133, https://doi.org/10.1016/j.coldregions.2007.04.007, 2007.

Squire, V. A.: A fresh look at how ocean waves and sea ice interact, Philos. Trans. R. Soc. A Math. Phys. Eng. Sci., 376(2129), doi:10.1098/rsta.2017.0342, 2018.

Stammerjohn, S., Massom, R., Rind, D. and Martinson, D.: Regions of rapid sea ice change: An inter-hemispheric seasonal comparison, Geophys. Res. Lett., 39, 1–8, doi:10.1029/2012GL050874, 2012.

Steele, M.: Sea ice melting and floe geometry in a simple ice-ocean model, J. Geophys. Res.-Oceans, 97, 17729–17738, https://doi.org/10.1029/92JC01755, 1992.

Steer, A., Worby, A., and Heil, P.: Observed changes in sea-ice floe size distribution during early summer in the western Weddell Sea, Deep-Sea Res. Pt. II, 55, 933–942, https://doi.org/10.1016/j.dsr2.2007.12.016, 2008.

Stern, H. L., Schweiger, A. J., Zhang, J., and Steele, M.: On reconciling disparate studies of the sea-ice floe size distribution, Elem. Sci. Anth., 6, p. 49, https://doi.org/10.1525/elementa.304, 2018a.

Stern, H. L., Schweiger, A. J., Stark, M., Zhang, J., Steele, M., and Hwang, B.: Seasonal evolution of the sea-ice floe size distribution in the Beaufort and Chukchi seas, Elem. Sci. Anth., 6, p. 48, https://doi.org/10.1525/elementa.305, 2018b.

Stopa, J. E., Ardhuin, F., and Girard-Ardhuin, F.: Wave climate in the Arctic 1992–2014: seasonality and trends, The Cryosphere, 10, 1605–1629, https://doi.org/10.5194/tc-10-1605-2016, 2016.

Strey, S. T., Chapman, W. L. and Walsh, J. E.: The 2007 sea ice minimum: Impacts on the Northern Hemisphere atmosphere in late autumn and early winter, J. Geophys. Res. Atmos., 115(23), 1–13, doi:10.1029/2009JD013294, 2010.

Stroeve, J. C., Serreze, M. C., Holland, M. M., Kay, J. E., Malanik, J. and Barrett, A. P.: The Arctic's rapidly shrinking sea ice cover: A research synthesis, Clim. Change, 110, 1005–1027, doi:10.1007/s10584-011-0101-1, 2012.

Stroeve, J. and Notz, D.: Changing state of Arctic sea ice across all seasons, Environ. Res. Lett., 13, 103001, https://doi.org/10.1088/1748-9326/aade56, 2018.

Stroeve, J. C., Schroder, D., Tsamados, M., and Feltham, D.: Warm winter, thin ice?, The Cryosphere, 12, 1791–1809, https://doi.org/10.5194/tc-12-1791-2018, 2018.

Strong, C., Foster, D., Cherkaev, E., Eisenman, I., and Golden, K. M.: On the definition of marginal ice zone width, J. Atmos. Ocean. Tech., 34, 1565–1584, https://doi.org/10.1175/JTECH-D-16-0171.1, 2017.

Tilling, R. L., Ridout, A., Shepherd, A., and Wingham, D. J.: Increased arctic sea ice volume after anomalously low melting in 2013, Nat. Geosci., 8, 643–646, https://doi.org/10.1038/ngeo2489, 2015.

Tilling, R. L., Ridout, A., and Shepherd, A.: Estimating Arctic sea ice thickness and volume using CryoSat-2 radar altimeter data, Adv. Space Res., 62, 1203–1225, https://doi.org/10.1016/j.asr.2017.10.051, 2018.

Timmermans, M. L. and Marshall, J.: Understanding Arctic Ocean Circulation: A Review of Ocean Dynamics in a Changing Climate, J. Geophys. Res. Ocean., 125(4), 1–35, doi:10.1029/2018JC014378, 2020.

Thomson, J. and Rogers, W. E.: Swell and sea in the emerging Arctic Ocean, Geophys. Res. Lett., 41, 3136–3140, https://doi.org/10.1002/2014GL059983, 2014.

Thomson, J. and Lee, C.: An autonomous approach to observing the seasonal ice zone in the western Arctic, Oceanography, 30, 56–68, https://doi.org/10.5670/oceanog.2017.222, 2017.

Tolman, H.: User manual and system documentation of WAVEWATCH III-version 3.14 (Tech. rep.), NOAA / NWS / NCEP / MMAB, Technical Note-276, available at: https://polar.ncep.noaa.gov/mmab/papers/tn276/MMAB_276.pdf (last access: 09 July 2020), 2009.

Toyota, T., Takatsuji, S., and Nakayama, M.: Characteristics of sea ice floe size distribution in the seasonal ice zone, Geophys. Res. Lett., 33, 2–5, https://doi.org/10.1029/2005GL024556, 2006.

Toyota, T., Haas, C. and Tamura, T.: Size distribution and shape properties of relatively small sea-ice floes in the Antarctic marginal ice zone in late winter, Deep. Res. Part II Top. Stud. Oceanogr., 58(9–10), 1182–1193, doi:10.1016/j.dsr2.2010.10.034, 2011.

Toyota, T., Kohout, A., and Fraser, A. D.: Formation processes of sea ice floe size distribution in the interior pack and its relationship to the marginal ice zone off East Antarctica, Deep-Sea Res. Pt. II, 131, 28–40, https://doi.org/10.1016/j.dsr2.2015.10.003, 2016.

Tsamados, M., Feltham, D. L., Schroeder, D., Flocco, D., Farrell, S. L., Kurtz, N., Laxon, S. W. and Bacon, S.: Impact of Variable Atmospheric and Oceanic Form Drag on Simulations of Arctic Sea Ice*, J. Phys. Oceanogr., 44, 1329–1353, doi:10.1175/JPO-D-13-0215.1, 2014.

Tsamados, M., Feltham, D., Petty, A., Schroder, D., and Flocco, D.: Processes controlling surface, bottom and lateral melt of Arctic sea ice in a state of the art sea ice model, Philos. T. Roy. Soc. A, 17, 10302, https://doi.org/10.1098/rsta.2014.0167, 2015.

Vihma, T.: Subgrid parameterization of surface heat and momentum fluxes over polar oceans, J. Geophys. Res., 100, 22625-22646, doi:10.1029/95jc02498, 1995.

Vihma, T.: Effects of Arctic Sea Ice Decline on Weather and Climate: A Review, Surv. Geophys., 35, 1175–1214, https://doi.org/10.1007/s10712-014-9284-0, 2014.

Virkar, Y. and Clauset, A.: Power-law distributions in binned empirical data, Ann. Appl. Stat., 8, 89–119, doi:10.1214/13-AOAS710, 2014.

Voermans, J. J., Babanin, A. V., Thomson, J., Smith, M. M. and Shen, H. H.: Wave Attenuation by Sea Ice Turbulence, Geophys. Res. Lett., 46(12), 6796–6803, doi:10.1029/2019GL082945, 2019.

Wadhams, P., Lange, M. A. and Ackley, S. F.: The ice thickness distribution across the atlantic sector of the Antarctic ocean in midwinter, J. Geophys. Res. Ocean., 92, 14535–14552, doi:10.1029/JC092iC13p14535, 1987.

Wadhams, P., Squire, V. A., Ewing, J. A., and Pascal, R. W.: The Effect of the Marginal Ice Zone on the Directional Wave Spectrum of the Ocean, J. Phys. Oceanogr., 16, 358–376, https://doi.org/10.1175/1520-0485(1986)016<0358:teotmi>2.0.co;2, 2002.

Wang, Y., Hwang, B., Basu, R., and Ren, J.: Regional differences in processes controlling Arctic sea ice floe size distribution in Chukchi Sea, East Siberian and Fram Strait during pre-ponding season, EGU General Assembly 2020, Online, 4–8 May 2020, EGU2020-5208, https://doi.org/10.5194/egusphere-egu2020-5208, 2020.

Wassmann, P., Duarte, C. M., Agustí, S. and Sejr, M. K.: Footprints of climate change in the Arctic marine ecosystem, Glob. Chang. Biol., 17(2), 1235–1249, doi:10.1111/j.1365-2486.2010.02311.x, 2011.

Weeks, Wilford F., and Stephen F. Ackley.: The growth, structure, and properties of sea ice, In The geophysics of sea ice, pp. 9-164. Springer, Boston, MA, https://doi.org/10.1007/978-1-4899-5352-0_2, 1986.

Weiss, J.: Fracture and fragmentation of ice: A fractal analysis of scale invariance, Eng. Fract. Mech., 68, 1975-2012, doi:10.1016/S0013-7944(01)00034-0, 2001.

Weiss, J. and Schulson, E. M.: Coulombic faulting from the grain scale to the geophysical scale: Lessons from ice, J. Phys. D. Appl. Phys., 42, 214017, doi:10.1088/0022-3727/42/21/214017, 2009.

Wenta, M. and Herman, A.: Area-averaged surface moisture flux over fragmented Sea Ice: Floe size distribution effects and the associated convection structure within the

atmospheric boundary layer, Atmosphere (Basel)., 10, 1–19, doi:10.3390/atmos10110654, 2019.

Wilchinsky, A. V. and Feltham, D. L.: Modelling the rheology of sea ice as a collection of diamond-shaped floes, J. Nonnewton. Fluid Mech., 138, 22–32, doi:10.1016/j.jnnfm.2006.05.001, 2006.

Wilchinsky, A. V., Feltham, D. L., and Hopkins, M. A.: Effect of shear rupture on aggregate scale formation in sea ice, J. Geophys. Res.-Oceans, 115, C10002, https://doi.org/10.1029/2009JC006043, 2010.

Williams, T. D., Bennetts, L. G., Squire, V. A., Dumont, D., and Bertino, L.: Wave-ice interactions in the marginal ice zone. Part 1: Theoretical foundations, Ocean Model., 71, 81–91, https://doi.org/10.1016/j.ocemod.2013.05.010, 2013a.

Williams, T. D., Bennetts, L. G., Squire, V. A., Dumont, D., and Bertino, L.: Wave-ice interactions in the marginal ice zone. Part 2: Numerical implementation and sensitivity studies along 1D transects of the ocean surface, Ocean Model., 71, 92–101, https://doi.org/10.1016/j.ocemod.2013.05.011, 2013b.

Williams, G. D., Fraser, A. D., Lucieer, A., Turner, D., Cougnon, E., Kimball, P., Toyota, T., Maksym, T., Singh, H., Nitsche, F. and Paget, M.: Drones in a cold climate, Eos, 97, doi:10.1029/2016eo043673, 2016.

Williams, T. D., Rampal, P. and Bouillon, S.: Wave-ice interactions in the neXtSIM sea-ice model, Cryosphere, 11, 2117–2135, doi:10.5194/tc-11-2117-2017, 2017.

Winton, M.: Amplified Arctic climate change: What does surface albedo feedback have to do with it?, Geophys. Res. Lett., 33, 1–4, https://doi.org/10.1029/2005GL025244, 2006.

Winton, M.: Sea ice – Albedo feedback and nonlinear Arctic climate change, in: Arctic Sea Ice Decline: Observations, Projections, Mechanisms, and Implications, edited by: DeWeaver, E. T., Bitz, C. M., and Tremblay, L.-B., American Geophysical Union, Washington, D.C., 180, 111–131, https://doi.org/10.1029/180GM09, 2008.

WMO: WMO Sea-Ice Nomenclature, Tech. Rep. 259, The Joint Technical Commission for Oceanography and Marine Meteorology (JCOMM), available at: https://www.jcomm.info/index.php?option=com_oe&task=viewDocumentRecord&docID=14598 (last access: 02 September 2020), 2020.

Wu, B., Handorf, D., Detloff, K., Rinke, A. and Hu, A.: Winter weather patterns over northern eurasia and arctic sea ice loss, Mon. Weather Rev., 141, 3786–3800, doi:10.1175/MWR-D-13-00046.1, 2013.

Young, I. R., Zieger, S., and Babanin, A. V.: Global trends in wind speed and wave height, Science, 332, 451–455, https://doi.org/10.1126/science.1197219, 2011.

Yumashev, D., van Hussen, K., Gille, J. and Whiteman, G.: Towards a balanced view of Arctic shipping: estimating economic impacts of emissions from increased traffic on the Northern Sea Route, Clim. Change, 143, 143–155, doi:10.1007/s10584-017-1980-6, 2017.

Zhang, J. L. and Rothrock, D. A.: Modelling global sea ice with a thickness and enthalpy distribution model in generalized curvilinear coordinates, Mon. Weather Rev., 131, 845–861, https://doi.org/10.1175/1520-0493(2003)131<0845:MGSIWA>2.0.CO;2, 2003.

Zhang, J., Lindsay, R., Schweiger, A., and Rigor, I.: Recent changes in the dynamic properties of declining Arctic sea ice: A model study, Geophys. Res. Lett., 39, L20503, https://doi.org/10.1029/2012GL053545, 2012.

Zhang, J., Schwinger, A., Steele, M., and Stern, H.: Sea ice floe size distribution in the marginal ice zone: Theory and numerical experiments, J. Geophys. Res., 120, 3484–3498, https://doi.org/10.1002/2015JC010770, 2015.

Zhang, J., Stern, H., Hwang, B., Schweiger, A., Steele, M., Stark, M. and Graber, H. C.: Modeling the seasonal evolution of the Arctic sea ice floe size distribution, Elem. Sci. Anthr., 4, 000126, doi:10.12952/journal.elementa.000126, 2016.